

THÈSE présentée par :
Olzhas A. Ibraikulov

soutenue le : 01 Décembre 2016

pour obtenir le grade de : **Docteur de l'université de Strasbourg**

Discipline/ Spécialité : **Physics of organic semiconductors and devices**

**Bulk heterojunction solar cells based on low
band-gap copolymers and soluble fullerene
derivatives**

THÈSE dirigée par :

M. HEISER Thomas

Professeur, Université de Strasbourg, France

CO-ENCADRANT:

M. LÉVÊQUE Patrick

Maitre de conferences, Université de Strasbourg, France

RAPPORTEURS :

M. WÜRFEL Uli

Docteur, Chef de departement, Fraunhofer ISE, Université de
Freiburg, Allemagne

M. BONNASSIEUX Yvan

Professeur, Ecole Polytechnique, Paris, France

AUTRES MEMBRES DU JURY :

M. ALEKSEEV Alexander

Docteur, Chef du laboratoire photovoltaïque, Université de
Nazarbayev, Kazakhstan

M. HAACKE Stephane

Professeur, Université de Strasbourg, France

I know only one thing: that is I know nothing

Socrates

Never give up!



In bright memory of my grandfather, Kurmanbay Sadykhanovich Yegemberdiyev
(1940-2010)

I dedicate this thesis

To

My parents, family members and relatives,

- **for unconditional love, immutable support and provided opportunities**

My wife and daughters,

- **for their deep inspirations, infinite love and joy**

Bulk heterojunction solar cells based on low band-gap copolymers and soluble fullerene derivatives

Résumé

La structure chimique des semiconducteurs organiques utilisés dans les cellules photovoltaïques à base d'hétérojonction en volume peut fortement influencer les performances du dispositif final. Pour cette raison, une meilleure compréhension des relations structure-propriétés demeure cruciale pour l'amélioration des performances. Dans ce contexte, cette thèse fait état d'études approfondies du transport des charges, de la morphologie et des propriétés photovoltaïques sur de nouveaux copolymères à faible bande interdite. En premier lieu, l'impact de la position des chaînes alkyles sur les propriétés opto-électroniques et morphologiques a été étudié sur une famille de polymères. Les mesures du transport de charges ont montré que la planéité du squelette du copolymère influe sur l'évolution de la mobilité des charges avec la concentration de porteurs libres. Ce comportement suggère que le désordre énergétique électronique est fortement impacté par les angles de torsion intramoléculaire le long de la chaîne conjuguée. Un second copolymère à base d'unités accepteur de [2,1,3] thiadiazole pyridique, dont les niveaux d'énergie des orbitales frontières sont optimales pour l'application photovoltaïque, a ensuite été étudié. Les performances obtenues en cellule photovoltaïque sont très inférieures aux attentes. Des analyses de la morphologie et du transport de charge ont révélé que l'orientation des lamelles cristallines est défavorable au transport perpendiculaire au film organique et empêche ainsi une bonne extraction des charges photo-générées. Enfin, les propriétés opto-électroniques et photovoltaïques de copolymères fluorés ont été étudiées. Dans ce cas, les atomes de fluor favorisent la formation de lamelles orientées favorablement pour le transport. Ces bonnes propriétés nous ont permis d'atteindre un rendement de conversion de puissance de 9,8% avec une simple hétérojonction polymère:fullerène.

Mots-clé : Cellules solaires organiques, transport de charges, semi-conducteurs organiques, transistors organiques à effet de champ, diodes à courant limité à charge spatiale

Summary

The chemical structure of organic semiconductors that are utilized in bulk heterojunction photovoltaic cells may strongly influence the final device performances. Thus, better understanding the structure-property relationships still remains a major task towards high efficiency. Within this framework, this thesis reports in-depth material investigations including charge transport, morphology and photovoltaic studies on various novel low band-gap copolymers. First, the impact of alkyl side chains on the opto-electronic and morphological properties has been studied on a series of polymers. Detailed charge transport investigations showed that a planar conjugated polymer backbone leads to a weak dependence of the charge carrier mobility on the carrier concentration. This observation points out that the intra-molecular torsion angle contributes significantly to the electronic energy disorder. Solar cells using another novel copolymer based on pyridal[2,1,3]thiadiazole acceptor unit have been studied in detail next. Despite the almost ideal frontier molecular orbital energy levels, this copolymer did not perform in solar cells as good as expected. A combined investigation of the thin film microstructure and transport properties showed that the polymers self-assemble into a lamellar structure with polymer chains being oriented preferentially "edge-on", thus hindering the out-of-plane hole transport and leading to poor charge extraction. Finally, the impact of fluorine atoms in fluorinated polymers on the opto-electronic and photovoltaic properties has been investigated. In this case, the presence of both flat-lying and standing lamellae enabled efficient charge transport in all three directions. As a consequence, good charge extraction was possible and allowed us to achieve a maximum power conversion efficiency of 9.8%

Keywords : Organic solar cells, charge transport, organic semiconductors, organic field-effect transistors, space-charge limited current diodes

Table of Contents

Table of Contents	1
1 General introduction	7
2 Scientific background	15
2.1 Introduction.....	15
2.2 Organic semiconductors	15
2.3 Working principle of organic solar cells	17
2.3.1 Light absorption and exciton generation	18
2.3.2 Exciton diffusion and dissociation at the D/A interface.....	19
2.3.3 Charge carrier transport.....	20
2.3.4 Charge carrier extraction.....	24
2.4 Device structures used in this thesis.....	25
2.5 Current – voltage characteristics.....	26
2.6 Main parameters of organic solar cells.....	27
2.6.1 J_{sc} – the short circuit current density.....	27
2.6.2 V_{oc} – the open circuit voltage.....	28
2.6.3 FF – the fill factor	29
2.7 State-of-the-art in Organic Photovoltaics	32
2.8 Thesis in context	34
3 Materials and experimental methods	39
3.1 Introduction.....	39
3.2 Materials and substrates.....	39
3.3 Experimental details and analytical methods	41
3.3.1 Photovoltaic device elaboration	41
3.3.2 Solar cell device characterizations	42
3.3.2.1 Current-voltage measurements	42
3.3.2.2 Quantum efficiency (QE) measurements	43
3.3.2.3 Transient photovoltage and charge extraction measurements.....	45
3.3.2.3.1 Transient photovoltage.....	45
3.3.2.3.2 Charge extraction	47
3.3.3 Charge carrier mobility measurements.....	49

3.3.3.1 Space-charge limited current.....	49
3.3.3.2 SCLC device elaboration and characterization.....	51
3.3.3.3 Organic field-effect transistors	52
3.3.3.4 OFET fabrication and characterization	56
3.3.4 Ultraviolet-visible spectroscopy.....	56
3.3.4 Morphological characterizations	58
3.3.4.1 Atomic-force microscopy.....	58
3.3.4.2 Grazing-incidence wide angle X-ray scattering.....	59
4 Results: Thieno-pyrroledione based copolymers	63
4.1 Introduction.....	63
4.2 Electrochemical and optical properties of <i>TPD-DTP</i> polymers.....	65
4.2 Charge transport investigations	67
4.2.1 OFET devices.....	67
4.2.2 Space-charge limited diodes.....	69
4.3 Microstructure characterizations	71
4.4 DFT calculations.....	72
4.5 Photovoltaic devices based on TPD-DTP copolymers.....	74
4.6 Conclusion	76
5 Results: Pyridal[2,1,3]thiadiazole based copolymer	81
5.1 Introduction.....	81
5.2 Summary of the article: “Using pyridal[2,1,3]thiadiazole as an acceptor unit in a low band-gap copolymer for photovoltaic applications”	83
5.3 Article: “Using pyridal[2,1,3]thiadiazole as an acceptor unit in a low band-gap copolymer for photovoltaic applications”	85
5.4 Supporting information: “Using pyridal[2,1,3]thiadiazole as an acceptor unit in a low band-gap copolymer for photovoltaic applications”	94
5.4 Conclusion	107
6 Results: Di-fluorinated vs non-fluorinated copolymer.....	111
6.1 Introduction.....	111
6.2 Investigations on di-fluorinated copolymers	113
6.2.1 UV-Vis and electrochemical characterizations	113
6.2.2 Photovoltaic results.....	115

6.2.3 Charge transport investigations.....	118
6.2.4 GIWAXS results	123
6.3 Study on non-fluorinated copolymer.....	126
6.3.1 UV-Vis and electrochemical measurements.....	127
6.3.2 Photovoltaic properties.....	129
6.3.3 Charge transport study.....	132
6.3.4 Morphological characterizations	135
6.3.4.1 GIWAXS measurements.....	135
6.3.4.2 Atomic force microscope characterizations	137
6.4 Charge-carrier recombination dynamics in photovoltaic devices based on fluorinated and non-fluorinated copolymers	138
6.5 Conclusion	143
7 General conclusion	147
References	151
8 Résumé de la thèse	161
8.1 Introduction.....	163
8.2 Copolymères à base de thiéno-pyrroledione (TPD).....	164
8.3 Copolymère à base de pyridino [2,1,3] thiadiazole	166
8.4 Copolymères à base de di-fluoro benzothiadiazole	167
8.5 Conclusions.....	170
8.6 Contributions scientifiques	171
8.6.1 Contributions par affiche.....	171
8.6.2 Contribution orale.....	171
8.6.3 Publications	171
8.7 Références.....	172
8 Acknowledgements	175

Chapter 1: General introduction

1 General introduction

One of the cutting-edge steps towards the progress of mankind began with the industrialization era. That revolution along with the substantial growth of world population in turn was followed by a dramatic rise for energy demand. And nowadays, this energy issue, more than ever remains as a global task for a wide range of audience from politicians to scientific community.

Until now, most of the energy needs have been met by conventional hydrocarbons (oil, gas, coal). However, burning of fossil fuels followed by emission of greenhouse gases to atmosphere causes vital damage to environment and contributes significantly to global climate change. Additionally, hydrocarbon is a finite source of energy. And the shortage of these fossil fuel resources, unfortunately, stays as one of the important reasons for political and societal crises at the different places of today's world.

Within this framework of challenges, solar power offers many privileges as a clean and renewable source of energy. The first and main motivation to further develop solar energy research is the fact that everyday Sun delivers enormous amount of energy to the surface of Earth. Taking into consideration simple assumptions and rough estimations it has been reported that by covering 2% of land area with an average power conversion efficiency (PCE) of about 12%, the solar plants realistically could supply up to 67 TW power which is more than twice of world's energy demand by 2050 [1]. Another strong and solid advantage of solar energy utilization is the widespread availability of the sunshine almost everywhere on Earth. This, in turn, could potentially give rise to a decentralized energy supply which is beneficial for distant places.

Solar cells, also referred to as photovoltaic cells are the devices which convert sunlight directly into electricity. They can be produced from different types of materials (organic, inorganic, etc.) and their performance evolution with time is shown in National Renewable Energy Laboratory chart (Fig. 1.1)^a. To date, silicon solar cells (mono- and multi-crystalline silicon) are the market leaders. They hold almost 90% of all produced solar power today and reach a PCE of 22.9% for mono-crystalline and 18.5% for multi-crystalline silicon in commercial modules [2]. However, silicon-based solar cells have

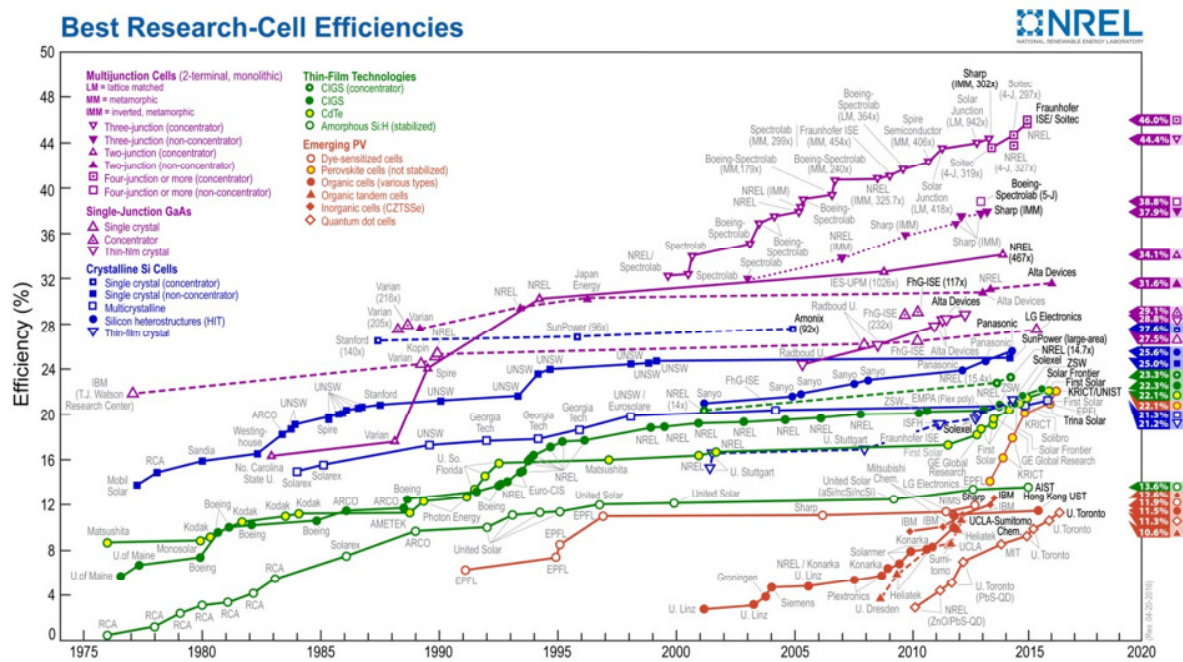


Fig. 1.1: Evolution of power conversion efficiencies of different types of solar cells versus time. Reproduced from reference [a].

significant drawbacks which reduce their competitiveness with fossil fuels. They suffer from high production costs, heavy weight and fragility. To reduce the production costs, different technologies based on thin films are under intensive development. For instance, perovskite solar cells achieved very remarkable improvement in PCEs ($\approx 20\%$ at the laboratory scale) in the last 2 years (Fig. 1), though they mainly suffer from short term stability and from the presence of lead (Pb) as toxic component [3]. Organic photovoltaics

^a http://www.nrel.gov/ncpv/images/efficiency_chart.jpg, National Renewable Energy Laboratory, Date accessed: April, 2016.

is another interesting and promising technology, due firstly to its expected low production costs and ease of processing. Also, their light weight, semi-transparency and high flexibility can potentially offer a much wider application range, from covering windows and various displays up to clothes.

It is generally considered that the history of organic electronics started with the discovery of conductive π -conjugated polymers in the late 70s, with the work of Shirakawa, MacDiarmid and Heeger [4]. The presence of delocalized π -electrons is responsible for the polymer semiconducting properties. The first organic solar cell with a PCE close to 1% was reported by Tang in 1986 [5]. An important breakthrough was achieved by Yu, Heeger and coworkers in 1995. These authors achieved improved conversion efficiencies by introducing the concept of a donor-acceptor bulk heterojunctions [6]. In the following years the PCEs of solution-processed bulk heterojunction solar cells rose up to roughly 3% [7-10]. However, despite their low-cost and facile fabrication methods, these rather low efficiency values remained a major bottleneck for the industrial development of the organic technology. Therefore, many efforts have been put by various scientific communities (chemists, physicists, physico-chemists and etc.) to push forward the fundamental understanding of the organic devices and to increase their photovoltaic performances. Today, organic photovoltaic cells with efficiencies up to $\approx 12\%$ in single junctions have been reported recently [11,12] showing that this technology has the potential to take a solid niche at the solar market in the near future.

To push this field even further, better understanding the relationships between the molecular structure of the active materials, the material opto-electronic properties and the device performances is still an important issue. Therefore, this work is focused on in-depth investigations of the physical properties of several newly designed low band-gap polymers and on their application in polymer:fullerene bulk heterojunction solar cells. In particular, correlations between the copolymer molecular structure, charge transport properties and thin film morphologies are studied in detail. The results have allowed us to rationalize the link between material properties that are crucial to the device performances and the polymer structure. In parallel, significant efforts were put into the optimization of the

device elaboration procedures with these new materials and allowed us to continuously increase the power conversion efficiency, approaching 10%.

Due to the multidisciplinary nature of this field, the work has been realized within the framework of multi-team collaboration. All the polymers studied were synthesized by the group of N. Leclerc from the Institut de chimie et procédés pour l'énergie, l'environnement et la santé (ICPEES). Structural analyzes by Grazing-incidence wide angle X-Ray scattering (GIWAXS) were performed by Dr. Benoit Heinrich from the Institut de Physique et Chimie des Matériaux de Strasbourg (IPCMS). Temperature-dependent optical characterizations of copolymers in solutions were carried out at Institut Charles Sadron (ICS) with the assistance of Dr. Laure Biniek. Density functional theory (DFT) calculations were conducted by Dr. Patrick Leveque, co-supervisor of this thesis.

This manuscript is organized in several chapters as follows:

Chapter 2 presents the fundamentals of organic semiconductors and organic solar cells. Current understanding of charge carrier generation, transport and recombination mechanisms along with the state-of-the-art knowledge on latest outstanding results in polymer photovoltaics are described.

In chapter 3 main methods and detailed experimental procedures used throughout the thesis are featured.

Chapter 4 reports in-depth charge transport, morphological and photovoltaic investigations on two copolymers based on the thieno-pyrrole-dione acceptor unit. The effect of the alkyl side chain position on opto-electronic properties of the copolymers are studied and discussed.

In chapter 5 investigations on pyridal[2,1,3]thiadiazole based copolymers are presented. It includes a summary of the work that has been published in the peer-reviewed Organic Electronics journal. The corresponding article and supporting information are fully displayed.

Chapter 6 is dedicated to the study of highly efficient backbone-fluorinated copolymers. Opto-electronic, photovoltaic and morphological investigations on fluorinated copolymers as a function of molecular weights are presented. To elucidate the impact of the fluorine

substitution and/or alkyl side chains on the charge transport, morphology and photovoltaic performances, the results on non-fluorinated equivalent polymers are discussed in the second part of this chapter.

Chapter 2: Scientific background

2 Scientific background

2.1 Introduction

In everyday life, the word *organic* is associated with living things. In organic chemistry, an organic material is a synthesized compound containing mainly carbon and hydrogen atoms. Thereby, in organic solar cells the active layer, where the light is absorbed to generate charges, is composed of a special class of organic materials, i.e. π -conjugated molecules which do behave as semiconductor in the solid state. In general, organic semiconductors can be often easily processed from solution by spin-coating, drop-casting, doctor blading etc. In thin films they can be arranged either in semi-crystalline or in amorphous phases. Mostly, they are recognized as a disordered and bulky class of materials with relatively low relative dielectric constants ($3 < \epsilon_r < 4$).

This chapter will mainly focus on the current understanding of physical processes governing the operation of organic solar cells as well as on the main parameters defining the overall cell efficiency. First, the physics of organic semiconductors is briefly presented. Then, crucial physical steps occurring during the photon energy conversion process are detailed. After that, the main solar cell parameters are described. The chapter ends with the state-of-the-art in the field along with the motivation of the work presented in my thesis.

2.2 Organic semiconductors

Carbon atoms (C) play a major role in the electrical properties of organic semiconducting materials. In its ground state with $[He]2s^22p^2$ electron configuration, the C atom can form up to 4 covalent bonds. In π -conjugated molecules such as alkenes, each C atom forms a double bond with a neighboring C atom: one s and two p orbitals form three sp^2 hybridized orbitals. These sp^2 orbitals are arranged in the same plane to form σ -bonds that are separated from each other at an angle of 120° . The fourth valence electron resides in p_z orbital, which is perpendicular to sp^2 plane and participates in the formation of π -bonds. Note that the "alternation" of single and double bonds in conjugated molecules (Fig.2.1)

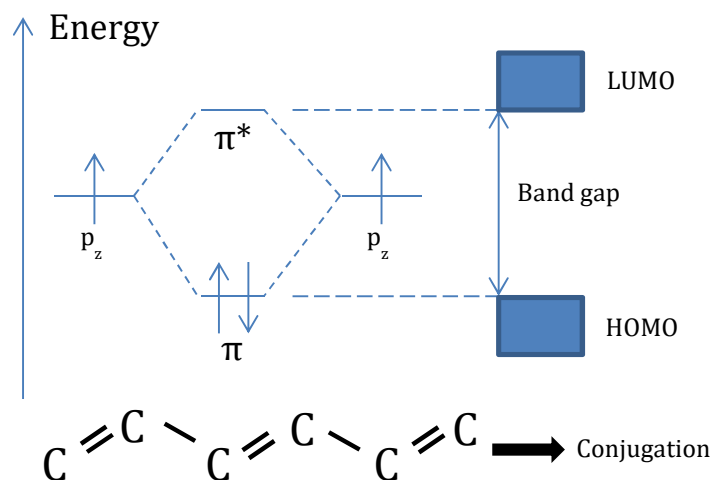


Figure 2.1: p_z orbital overlap to form π (bonding) and π^* (anti-bonding) band in C-C system

points out small periodic changes in the C-C distance. The π -electrons are highly delocalized and are at the origin of the opto-electronic properties of organic semiconductors (Fig. 2.1). This delocalization allows electrons to move freely along the conjugated backbone up to a distance referred to as conjugation length.

The overlap of p_z orbitals of C atoms result in bonding (π) and anti-bonding (π^*) orbitals (Fig. 2.1). The bonding one which is lower in energy and occupied with electrons is defined as the highest occupied molecular orbital (HOMO). The anti-bonding one, higher in energy and non-occupied is called the lowest unoccupied molecular orbital (LUMO). In thin films, the electron energy levels are broadened but remain strongly correlated to the molecular HOMO and LUMO levels. The corresponding HOMO and LUMO "bands" are analogs of the valence and conduction bands, respectively, in conventional inorganic semiconductors. The energy offset between the HOMO and the LUMO levels is called the energy band gap. If the conjugation length is increased, the energy bands shift slightly (upwards for the HOMO and downwards for the LUMO) and the band gap is reduced. For instance, while a single ethylene molecule has a band gap of ≈ 7.6 eV, butadiene, a conjugated system with four C atoms, has a gap of ≈ 5.7 eV and hexatriene ≈ 5 eV [13]. For energy band gaps lower than roughly 3 eV, the organic materials are expected to behave as a semiconductor.

In inorganic semiconductors, the position of Fermi level can be adjusted by controlling the amount of dopants in the material during the production process. In organic semiconductors, the nature of the materials (referred to as p- or n-type for inorganic semiconductors), are rather described by the positions of the HOMO and LUMO levels with respect to the charge injecting electrodes. If the HOMO level of a semiconductor is close to the work function of an injecting electrode, then this material is classified as a hole conductor, since the correspondingly small energy barrier allows efficient hole injection. In contrast, if the LUMO level is close to the work function of the electrode, then the semiconductor is recognized as an electron transporter. In organic solar cells, the active layer is generally composed of two organic semiconducting materials. They can be processed either layer by layer (bilayer solar cells) or from already intermixed solutions giving rise to bulk heterojunction (BHJ) structures. The presence of two materials in these devices is crucial and will be discussed in detail in upcoming sections. Here, I would like to describe shortly how the materials are recognized as electron-donor or electron-acceptor in terms of frontier energy levels. In a blend, a semiconductor whose HOMO and LUMO levels are lying above the HOMO and LUMO levels of the second component (i.e. are lower in absolute values) is called an electron-donor or donor (D) material. Accordingly, a semiconductor with deeper lying HOMO and LUMO levels is referred to as an electron-acceptor or acceptor (A) material. In polymer-fullerene systems, polymer materials act generally as donors while fullerene derivatives stand for acceptor materials.

2.3 Working principle of organic solar cells

The working principle of an organic solar cell can be briefly described by the following steps: (i) formation of an exciton upon light absorption, (ii) diffusion of the exciton to the interface between two materials, (iii) subsequent exciton dissociation into free charges, and (iv) transport of free charges (electrons and holes) followed by (v) their extraction at the respective electrodes. Although they are seemingly trivial, all these processes have very strict limitations. First, photo-induced excitons need to reach the D/A interface prior to their recombination. As the exciton diffusion length is quite small (generally less than 10

nm; see below), both materials should be well intermixed in the film. Second, in order to successfully dissociate the excitons, the energy level offset between the D and A materials should be sufficient to drive the charge (see below). Then, generated free charges must be transported via their respective domains in the active layer. Here, charge transport properties of both materials in blends play an important role. Finally, charges need to be extracted to be able to contribute to the current. Namely, alignment of the energy levels of contact materials must be considered. The above-mentioned physical processes are shown schematically in Fig. 2.2 and will be discussed in more detail in the following sections.

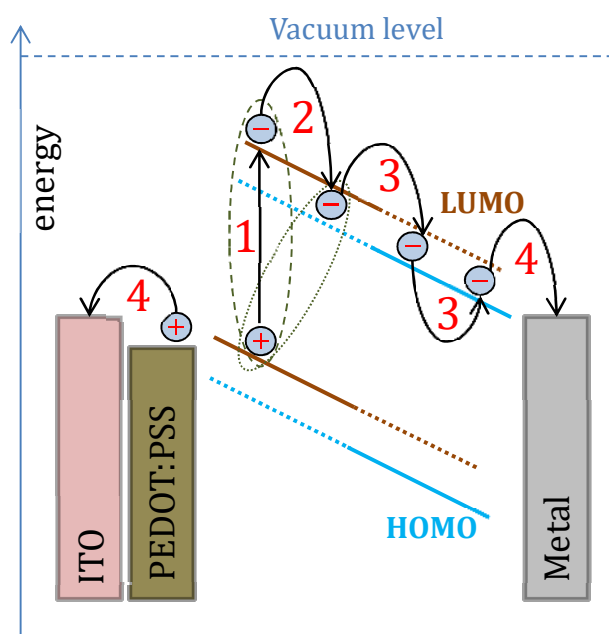


Figure 2.2: Schematic view of four crucial physical steps in organic solar cells: 1) light absorption and exciton generation; 2) exciton diffusion and dissociation at the donor/acceptor interface; 3) charge transport; 4) charge collection at the electrodes. The brown color refers to the electron-donor material and the blue color to the electron-acceptor material.

2.3.1 Light absorption and exciton generation

The generation of a photocurrent in an organic solar cell starts with the absorption of light. In general, photoactive organic materials have very high molar absorption coefficients (α) that are typically around 10^5 cm^{-1} . This important feature allows a thin organic layer ($d = 150\text{-}200 \text{ nm}$) to absorb a sufficient amount of photons within a given spectrum diapason [6]. For comparison, the absorption coefficients of conventional inorganic semiconductors

like polycrystalline silicon are in the range of 10^3 - 10^4 cm^{-1} in the visible wavelength range which requires much thicker films to absorb the same amount of light for a given wavelength. Upon absorption, electrons in the active layer (mainly in donor material for the systems using fullerene derivatives as acceptors) are excited from the HOMO to the LUMO and neutral species called excitons (bound intra-molecular electron-hole pairs) are formed. Due to the low dielectric constants and localized electronic states in organic semiconductors, a strong Coulombic attraction exists between an electron-hole pair, which does not allow direct generation of free charges. These bound electron-hole pairs have exciton binding energy of 100-1400 meV [14-17] unlike their inorganic counterparts that have exciton binding energy of around a few meV. For instance, for the well-known and widely used P3HT (poly(3-hexylthiophene-2,5-diyl)), used as donor material, an exciton binding energy of ≈ 700 meV has been reported [18]. Therefore, ambient thermal energy is not enough to separate the electron-hole pairs. As the lifetime of excitons is of the order of nanoseconds [19,20], a fast and efficient way is needed to avoid geminate recombination. A solution to this issue has been proposed by Tang et al. in 1986, who demonstrated an organic solar cell based on two different materials with properly aligned energy levels [5].

2.3.2 Exciton diffusion and dissociation at the D/A interface

After an exciton is formed it needs to travel towards the D/A interface in order to be dissociated. This distance needs to be less than the exciton diffusion length. The energy offset between the D and A materials should allow to overcome the exciton binding energy and efficiently dissociate electron-hole pairs. It is generally believed that this value must be larger than 0.3 eV [21,22]. Currently, in solution-processed BHJs, soluble fullerene derivatives like [6,6]-phenyl-C₆₁/C₇₁ butyric acid methyl ester (PC₆₁BM/PC₇₁BM) remain as the most frequently used acceptor material. Though, today non-fullerene rivals are under extensive investigation and show high efficiencies as well [23-25]. Recent literature data suggest that for the systems using fullerene derivatives as acceptor materials a ΔLUMO as low as 0.1 eV can be sufficient [26-30].

The charge transfer (CT) process in conjugated polymer-fullerene system is known to occur in a very short timescale (< 100 fs) [31,32], which is roughly 10 000 times smaller than the exciton lifetime and thus much faster and relatively efficient. When the CT step is successfully realized, hole and electron reside in neighboring donor and acceptor molecules, respectively. The resulting CT states are intermediate species between coulombically bound exciton and free charges (Fig. 2.2). At this stage, due to the delocalized nature of holes and electrons on their respective molecules, the binding energy between them is notably weaker. Therefore, they can either be thermally dissociated or separated by an electric field. The underlying mechanism of electron-hole pair dissociation is not fully understood yet and remains an important issue in organic photovoltaics (OPVs). For instance, the energy losses in CT states strongly affects the open circuit voltage [33-35] and thus the power conversion efficiency of the final solar cell. In-depth reviews on charge generation process in organic solar cells can be found in references [17,36].

2.3.3 Charge carrier transport

Once the electron-hole pairs are dissociated, the free charge-carriers must be transported towards their respective electrodes to participate to the photocurrent. Here, charge transport within the organic semiconductor plays an essential role. The fundamentals of charge transport in disordered organic materials are totally different from their inorganic counterparts. The crystal structure, which is present in classical crystalline inorganic semiconductors, allows delocalization of the electron wave function. This in turn permits electrons and holes to behave as quasi-free particles (band transport). In organic semiconductors the electronic states are more localized. While the intra-molecular charge transport is considered to be fast, the inter-molecular transport within the localized states is a rate-limiting factor and is thermally activated. Such a charge carrier hopping mechanism is strongly influenced by the presence of energetic and structural disorder.

A first hopping model among localized states was proposed by Miller and Abrahams in 1960 [37]. It was mainly oriented to describe the transport of charges in amorphous

inorganic semiconductors. According to this model, the hopping rate (v_{ij}) between localized sites (from the occupied site i to the empty site j) is given by the following equation [37]:

$$v_{ij} = v_0 \exp(-2\alpha R_{ij}) \begin{cases} 1 & E_i > E_j \\ \exp\left(-\frac{E_j - E_i}{k_B T}\right) & E_i < E_j, \end{cases} \quad (2.1)$$

where α is localization length, E_i the energy of the i state and R_{ij} the distance between the initial and final states and determines the orbital overlap. If the E_i is higher than E_j , the probability of charges to hop is only limited by the R_{ij} . On the other hand, when $E_i < E_j$, thermal energy is needed to induce the hopping of charges. As a result, hopping of charges is a trade-off between the number of available sites (or density of states, DOS) and the transition probability. For instance, when electrons are injected into an organic semiconductor characterized by a Gaussian DOS, they will quickly relax into a stationary distribution in energy, centered around the so-called equilibration energy E_∞ . The latter is located σ^2/kT below the maximum of the Gaussian DOS, with σ being the width of the Gaussian distribution [38-40]. This is known as energy relaxation process (Fig. 2.3). Subsequent hopping events are most likely to occur towards states whose energy level corresponds to the highest hopping probability (best trade-off mentioned above). This energy level is called the transport level (E_{tr}) and is located slightly below the center of the Gaussian distribution (Fig. 2.3).

In 1969, Mott first reported that in a disordered system at low temperatures charges

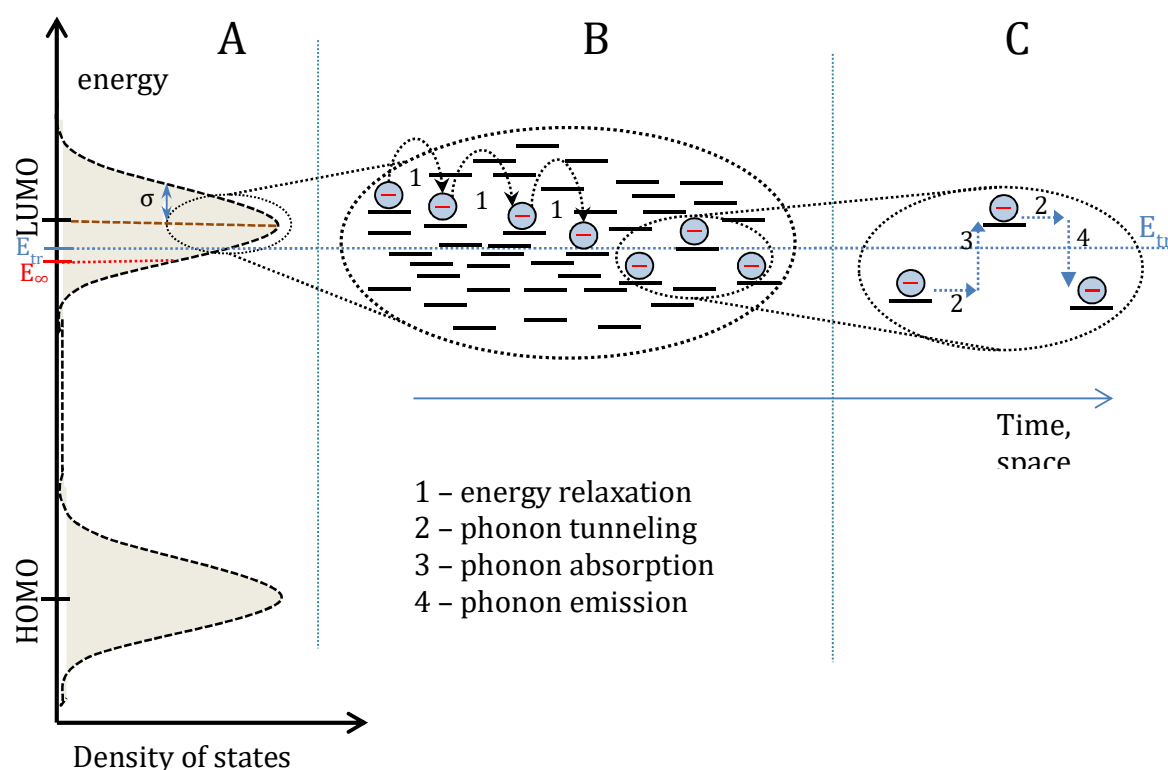


Figure 2.3: A) Distribution of density of states, inset: density of occupied states (DOOS) B) energy relaxation of an electron in excited state by hopping to energetically favorable sites; C) electron transport within the transport energy level (E_{tr}). σ and T_0 - width of Gaussian and Exponential DOS, respectively.

within the localized states would not necessarily hop to the closest neighbor if an energetically more favorable site is available at a longer distance [41]. According to Mott's variable range hopping (VRH) model, an electron or a hole would look for a compromise between the lowest activation energy (ΔE) and the shortest hopping length. Mott showed that, if the DOS can be considered as constant over the energy range where transport occurs, then the electrical conductance (G) follows:

$$G \propto \exp\left(-\frac{B}{T^{1/4}}\right) \quad (2.2)$$

where B is a constant term and T the absolute temperature.

Bässler developed the VRH model further and in 1993 presented an important extension by Monte Carlo simulations [38]. He described the density of states as well as the positional disorder by Gaussian distributions. In his so-called Gaussian disorder model (GDM), the site distribution in energy is supposed to follow:

$$g(E) = (2\pi\sigma^2)^{-1/2} \exp\left(-\frac{E^2}{2\sigma^2}\right) \quad (2.3)$$

where the Gaussian width σ represents the degree of energy disorder. Bässler showed that the charge carrier mobility μ in a disordered material at low carrier concentrations follows the empirical law:

$$\mu = \mu_0 \exp\left[-\left(\frac{2\sigma}{3k_B T}\right)^2 + C \left(\left(\frac{\sigma}{k_B T}\right)^2 - \gamma^2\right) F^{\frac{1}{2}}\right] \quad (2.4)$$

where γ represents the positional Gaussian disorder, and F the electric field. A main conclusion from the GDM is the fact that the mobility is independent of the charge carrier concentration as long as the Fermi level remains below the equilibration energy E_∞ [42]. At higher charge carrier concentrations ($E_F > E_\infty$), the charge carrier mobility starts to increase as the density of states contributing to transport increases and the effective energy barrier for transport reduces to $E_{tr} - E_F$.

Another way to describe the charge transport in disordered solids via VRH concept was introduced by Vissenberg and Matters in 1998 [43]. They applied a percolation model to describe transport in field-effect transistors. Their model is based on an exponential rather than a Gaussian density of states ($g(E) = \exp\left(-\frac{E}{kT_0}\right)$). Although such a distribution does not lead to an equilibrium level [40] and therefore cannot explain the existence of charge carrier density independent mobility often observed at low carriers densities, P. Blom et al. [44] showed that it can be considered as an approximation of the Gaussian distribution around the Fermi level ($E_F \pm kT$).

According to Vissenberg's model the field-effect mobility μ should depend on the gate voltage (V_G is directly proportional to charge carrier density) and temperature (T) following:

$$\mu_{FE}(T, T_0, \alpha, \varepsilon, \sigma_0, B_c) \propto V_G^{2\left(\frac{T_0}{T}-1\right)} \quad (2.5)$$

where T_0 is representative parameter for the degree of energy disorder (i.e. width of the DOS). This result allowed them to rationalize the charge carrier density dependence of the field-effect mobility observed in various semiconducting polymers [44]. More detailed discussions on charge transport in disordered organic semiconductors can be found in references [40,45,46].

2.3.4 Charge carrier extraction

The last step to complete the solar energy conversion in a PV system is the extraction of charge carriers at the respective electrodes. The selection of contact materials plays a key role in the charge extraction process. In particular, the work functions of the anode and cathode need to be aligned with the HOMO energy level of the donor and LUMO energy level of the acceptor materials, respectively, in order to avoid any energy barrier. If a barrier exists, the extraction/injection rate of charge carriers will be hindered. This may lead to the accumulation of charges close to the active layer/contact interface and result in low device performances, especially low fill factors (FF). It has been shown by numerical simulations that the formation of space-charges near the surface could result in deformed (S-shaped) current-voltage curves [47]. Additionally, the misalignment of active layer/electrode energy levels may strongly affect the open circuit voltage (V_{oc}) of the final solar cell [48-50]. Another factor which hampers the device performances is the collection of charges at the wrong electrodes i.e. electrons at the anode or holes at the cathode. To overcome this issue electron/hole transporting layers (ETL/HTL), also referred to as “buffer layers”, are often implemented between the active layer and the electrode, improving the selectivity of the contacts. Extended and comprehensive reviews on ETL/HTL materials and their roles in organic solar cells are reported in references [51-54].

2.4 Device structures used in this thesis

In this thesis I used two different bulk heterojunction (BHJ) solar cell architectures, “standard” and “inverted” devices. In the standard structure, holes are collected at the transparent bottom electrode (and electrons on the back electrode) while in the “inverted” solar cells electrons are extracted at the transparent electrode (and holes at the back contact). In case of “standard” devices, a low work function metal electrode (for electron extraction) is used as a top contact i.e. aluminum (Al), calcium/aluminum (Ca/Al) etc. This in turn brings a significant drawback: these metals are easily oxidized in the air resulting in poor stability. Furthermore, a widely used interfacial layer poly(3,4-ethylenedioxythiophene)-poly(styrenesulfonate) (PEDOT:PSS), to modify the work function and improve the surface uniformity of indium-tin-oxide (ITO) transparent electrode in “standard” devices, have acidic properties. Thus, it degrades the ITO that lies below. In the “inverted” structure, a high work function metal (for hole extraction) that is more resistant to the oxidation in air, such as silver (Ag) or gold (Au) is utilized as a back contact, while the front electrode is composed of electron transporting layers such as zinc oxides (ZnO_x) [54-59] or titanium oxides (TiO_x) [60-64]. Additionally, it has been reported that a thin layer of a polymer called ethoxylated polyethyleneimine (PEIE) can drastically reduce the work function of ITO converting it from hole transporting layer (HTL) to

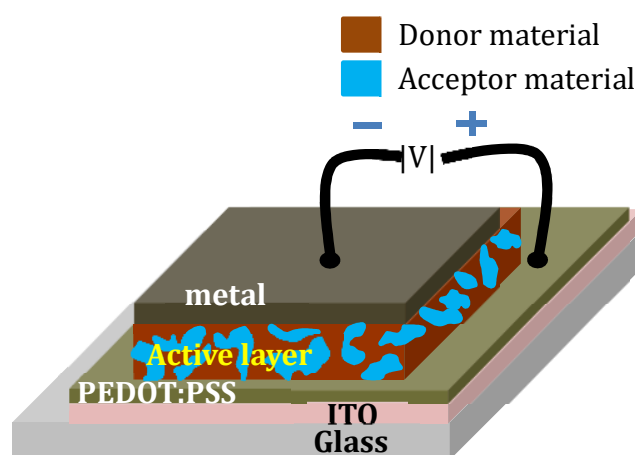


Figure 2.4: Schematic view of a standard BHJ solar cell used in this work

electron collecting layer (cathode) [65,66]. Due to the reasons mentioned above, “inverted” device structures are accepted to be more stable than the “standard” ones and they have been shown to perform much better [67,68]. More details on device architecture differences can be found in Ref [69]. The device structure of a “standard” bulk heterojunction organic solar cell used throughout this work is shown in Fig. 2.4.

2.5 Current – voltage characteristics

The main parameter that describes a solar cell is its power conversion efficiency (or PCE), denoted as η . It is defined by the ratio of obtained maximum electrical power from the cell P_{max} to the power of incident light P_{in} :

$$\eta \% = \frac{P_{max}}{P_{in}} \times 100\% \quad (2.6)$$

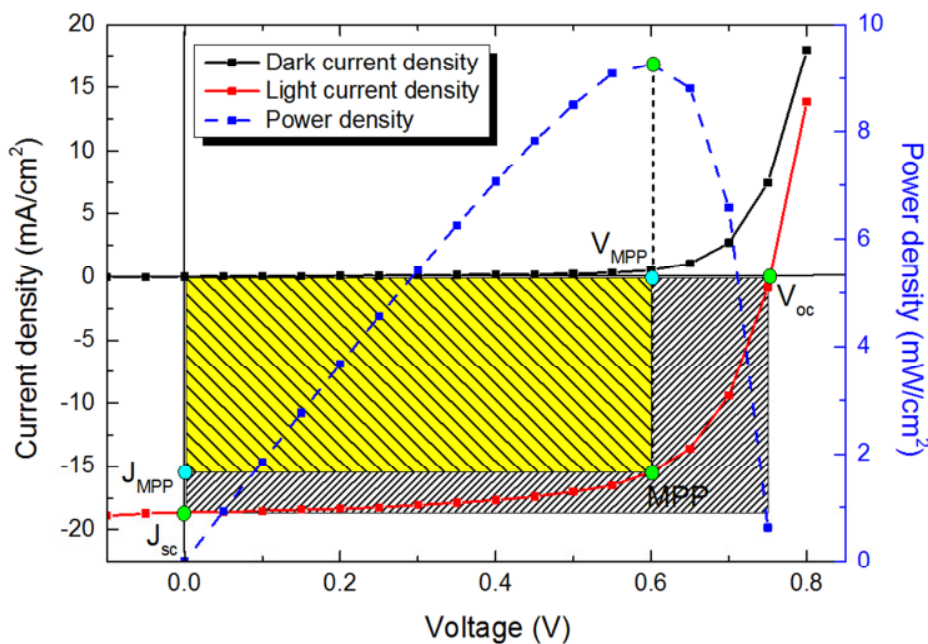


Figure 2.5: J - V characteristics of a high efficient organic solar cell investigated in this thesis. Black line and red line with symbols represent dark and illuminated curves, respectively. Blue dashed line with symbols shows the power density of the cell with its maximum power point (MPP) at around 0.62V (V_{MPP}). Green points are the open circuit voltage V_{oc} and the short circuit current density J_{sc} of the solar cell. The fill factor (FF) is evaluated by the area ratio of the yellow rectangle to the dashed grey rectangle.

To quantitatively evaluate the solar cell efficiency, a current – voltage (I - V) or current density – voltage (J - V) characteristic should be measured under a standard light power P_{in} . Illustrative dark and illuminated J - V curves are shown in Fig. 2.5. The main parameters that determine the final efficiency of a solar cell are: the short circuit current density (J_{SC}), the open circuit voltage (V_{OC}) and the fill factor (FF), which characterizes how “rectangle” the illuminated J - V curve is and is estimated as follows:

$$FF = \frac{V_{MPP} \cdot J_{MPP}}{V_{OC} \cdot J_{SC}} \quad (2.7)$$

where the V_{MPP} and J_{MPP} are determined by the maximum power (MPP) point of the cell (Fig. 2.5). Finally, the power conversion efficiency of the solar cell is given by:

$$\eta = \frac{V_{OC} \cdot J_{SC} \cdot FF}{P_{in}} \times 100 \quad (2.8)$$

In order to determine the solar cell efficiencies in a comparable way among the interested research community, standard testing conditions (STC) have been developed and accepted. This standard represents a radiant density of 100 mW/cm² with the sun spectrum of an AM 1.5G and a temperature of 25°C. The details on accurate determination of the organic solar cell efficiency can be found in references [70-72].

2.6 Main parameters of organic solar cells

In this section I will briefly discuss the main parameters of organic solar cells that determine the efficiency: J_{SC} , V_{OC} and FF . In particular, I will describe the current understanding of the parameters and highlight the factors influencing them.

2.6.1 J_{SC} – the short circuit current density

J_{SC} is the current density obtained from the solar cell under short circuit conditions ($V = 0$ V). The J_{SC} is determined by the amount of charge-carriers extracted at the electrodes and is thus directly proportional to the amount of absorbed photons in the active layer. It is

generally considered that to optimize photon absorption, and correspondingly increase J_{sc} , the band gap of the photon absorbing material should be close to the optimum value (≈ 1.3 eV) calculated by Shockley and Queisser (SQ limit) for single absorber p-n junction solar cells [73]. A more recent model, taking into account the non-abrupt DOS of disordered organic semiconductors, suggests the optimum band gap of an absorber to be slightly higher (by 0.1eV) than the SQ limit [74].

Besides the band gap, the morphology of the BHJ active layer has as well a significant influence on the amount of photo-generated charge carriers in the device [75,76]. The larger the D/A interfaces area is, the more photons will be absorbed within a distance from the D/A interface that is below the exciton diffusion length and the more excitons can be dissociated into free charge carriers [77-79].

After free charges have been formed, they need to find ways to reach their respective electrodes in order to contribute to the current. Hence, interconnected donor and acceptor pathways must be present within the active layer [80,81]. Moreover, in order to reduce the monomolecular recombination in the bulk, the purity of the domains needs to be as high as possible [82,83]. Finally, to maximize the photo-current, the efficiencies of each step mentioned above should be close to unity.

2.6.2 V_{oc} – the open circuit voltage

V_{oc} is the maximum possible voltage that can be generated in a photovoltaic (PV) cell. Namely, under open circuit conditions and constant light illumination the free charge carriers that are formed in the active layer will accumulate in the bulk of the materials and at their respective electrodes, holes at the anode and electrons at the cathode. This process generates a potential within the cell that cancels out the built-in potential. Under such conditions charge carrier generation and recombination compensate each other resulting in a net zero current at any part of the device [84-86].

It has been reported in literature that V_{oc} is related to the difference between the HOMO energy level of the donor and the LUMO energy level of the acceptor material [22,87-90].

Moreover, taking into account the behavior of various materials used in BHJs, Scharber et al. derived the following relationship [22]:

$$V_{OC} = \frac{1}{q} (|E_{Donor}^{HOMO}| - |E_{Acceptor}^{LUMO}|) - 0.3V, \quad (2.9)$$

where q is the elementary charge. This work provided an important guideline for the design of new materials with optimized energy levels. However, the origin of the empirical 0.3V loss factor in equation (2.9) is still not well understood and remains an important open issue today.

On the whole, in case of perfect ohmic contacts, V_{OC} arises from the difference of electron and hole quasi-Fermi energy levels, E_{Fn} and E_{Fp} , respectively as follows [73]:

$$V_{OC} = \frac{1}{q} (E_{Fn} - E_{Fp}) \quad (2.10)$$

Crystalline silicon solar cells based on p-n junctions show well-defined quasi-Fermi energy levels that can lie close to conduction and valence band edges, while in organic semiconductors, due to the high energetic disorder, the quasi-Fermi levels can be pinned to the tail energy states. These tail states lead to a downshift of the electron and an upshift of the hole quasi-Fermi levels and thereby result in a reduced V_{OC} [91].

Recently Widmer et al. by analyzing various donor-acceptor material combinations suggested a pathway to quantify the energy level distributions in blends [92]. Factors such as energetic and structural disorder, CT states, D-A interface quality in the bulk, microstructure, work function of electrodes and active layer-electrode interface quality strongly influence the DOS and significantly impact V_{OC} . Recent reviews on the V_{OC} of organic solar cells can be found in Refs. [33,93].

2.6.3 FF – the fill factor

FF is the most complex parameter that determines along with J_{sc} and V_{oc} the power conversion efficiency of the solar cell. Up to date, the underlying physical processes defining the FF are less well understood than those for two other parameters. The FF can

be considered as a measure of how efficiently photo-generated charge carriers can be extracted under the maximum power point operating conditions. A recent study by Koster et al. showed that the FF is indeed governed by the competition between recombination and extraction rates of free charges [94].

In the ideal case of negligible contributions from the series (R_s) and parallel or shunt (R_{sh}) resistances, the ideal fill factor FF_0 can be expressed via the expression [95]:

$$FF_0 = \frac{v_{OC} - \ln(v_{OC} + 0.72)}{v_{OC} + 1} \quad (2.11)$$

where v_{OC} is a dimensionless open circuit voltage ($qV_{OC}/nk_B T$) and n is an ideality factor. In an ideal p-n junction Si solar cell, where only diffusion currents exist, the factor $n \approx 1$. In contrast, for organic solar cells (OSCs) this factor deviates from unity. It has been reported to be around 1.3-1.6 for different material systems [96,97]. The equation (2.11) is quite accurate, especially when the $v_{OC} > 10$, and applies well for OPV as well. For instance, for P3HT:PCBM system (assuming $V_{OC} \approx 0.6$ V and $n \approx 1.5$) the normalized voltage ≈ 16 and $FF_0 \approx 77\%$. However, we know from literature that this value is far away from most reported experimentally measured FFs (≈ 60 - 65%) for optimized devices. This offset of almost 15% between the experimental and theoretically estimated data suggest that solar cells in practice experience substantial losses. These losses are often caused by R_S and R_{SH} that cannot be neglected [6]. R_S mainly originates from the electrodes (especially ITO), the organic layer and interfacial contacts between them. R_{SH} represents different types of leakage currents: in the bulk (imperfect organic layer quality, aggregates, pinholes etc.), from the edge of the device and even can be caused by impurities.

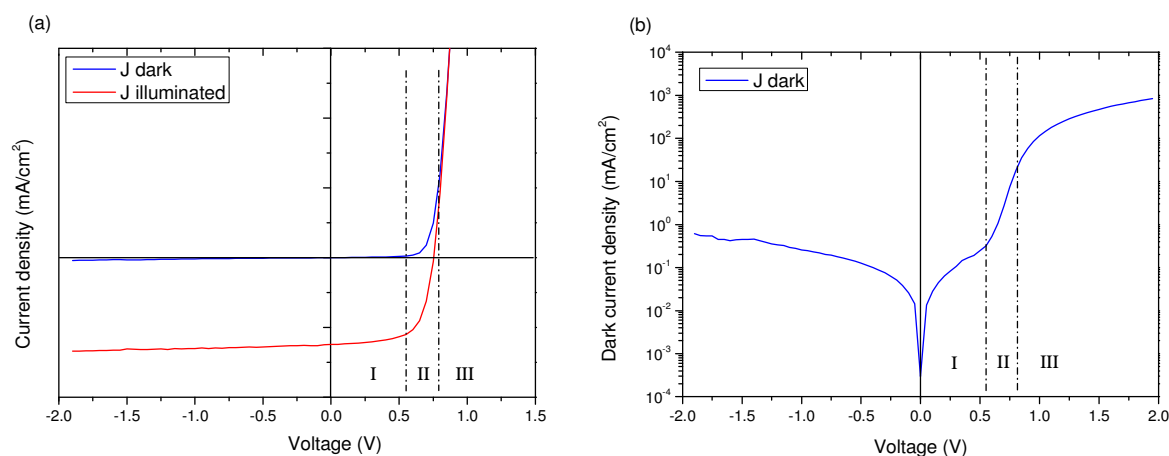


Figure 2.5: (a) An exemplary current density-voltage curves under dark (blue) and illuminated (red) conditions; (b) the dark current density of a solar cell plotted versus voltage using absolute values in a semi-logarithmic scale. Three different regions I, II and III can be distinguished where the behavior is dominated by R_{sh} (I) R_s (III) or where a perfect diode can be assumed (II), respectively.

Figure 2.5 clarifies the role of these resistances in the determination of FFs. If we plot the dark J-V curve in a semi-logarithmic scale, we can clearly distinguish 3 different regions (Fig. 2.5b) that are extrapolated to J-V curves plotted in linear scale (Fig. 2.5a). In region I (Fig. 2.5a), at relatively low positive applied bias the J-V curves stays almost horizontal with a slope of $1/R_{SH}$. The straighter the lines are (representing dark and illuminated curves in Fig. 2.5a) means a higher R_{SH} and a high FF. However, it should be noted that in organic solar cells R_{SH} under dark and illumination near short circuit conditions can be different. This could be due for instance to electric field dependent charge carrier generation and/or recombination. As a consequence, R_{SH} values estimated from illuminated J-V curves may differ from the one estimated from the J-V curves in the dark. In this case, the parallel resistances estimated from the illuminated curves do not reflect the reality [98]. In region II, the current density increases exponentially. This part is representative of a diode-like character of the device. In the region III, when $V > V_{OC}$, the J-V curve again looks like a straight line but with a slope of $1/R_s$. Therefore, to obtain a good FF value the R_s value should be as small as possible. The more extended reviews on fundamentals of Fill Factor in organic solar cells can be found elsewhere [99,100].

2.7 State-of-the-art in Organic Photovoltaics

More than 20 years have already passed since the first BHJ solar cell was reported [6]. Although those cells evolved slowly in terms of PCEs at the beginning [101-103], interest for this field was far from being stewed. On the contrary, the efficiencies of BHJ devices have experienced a strong evolution within the last decade achieving remarkable efficiencies of more than 10% [11,104,105]. This impressive progress owes much to the design and development of new organic semiconducting materials with optimized opto-electronic properties as well as to the optimization and control of the active layer morphology. Copolymers with quinoidal structure [106] or with alternating electron-donor (D) and electron-acceptor (A) moieties [107,108] have shown to perform well in solar cells as both synthetic strategies allow adjusting precisely the frontier molecular orbital (FMO) energy levels. In addition to that, other structural modifications like the planarity of the polymer backbone and nature and position of substituted side-chains have also been reported to influence the polymer opto-electronic properties [109,110].

In this regard, various D and A unit combinations have been used to synthesize high efficient copolymers. Today, compared to the large diversity of D-units offered, the number and nature of A-units are relatively limited. Besides widely utilized benzo[2,1,3]thiadiazole (BT) and pyridal[2,1,3]thiadiazole [111-114], diketopyrrolopyrrole (DPP) [115-117] and thieno[3,4-c]pyrrole-4,6-dione (TPD) [118-120] remain as other good examples of A-units used in efficient polymer solar cells.

TPD was first utilized as A-unit in a D-A alternating copolymer in organic solar cells in 2010. Intuitively, its relatively compact and planar structure could facilitate the electron delocalization and enhance the intra- and interchain interactions. In addition to that, also taking into account its strong electron-withdrawing effect, the FMO energy levels (HOMO and LUMO) of final copolymer could be decreased. Leclerc and co-workers [118], who first used TPD for OPV applications, combined it with benzodithiophene (BDT) D-unit and synthesized a low band-gap copolymer PBDTTPD. Using a “standard” architecture, without any additive and annealing optimizations they achieved a comparatively high PCE of 5.5% for that time. Interestingly, the UV-Vis absorption profiles of PBDTTPD in solution and in

thin films were almost identical. This observation suggests that the PBDTPD polymer revealed strong aggregation behavior even in solutions that could be indeed due to enhanced polymer interchain interactions. Reynolds and So et al. demonstrated a PCE of more than 8% in “inverted” solar cells for dithienogermole-TPD based copolymer in 2012 [120]. Though that work was mainly focused on the optimization of the electron transport layer (ETL), this does not diminish the role of the used TPD-based polymer.

Pyridal[2,1,3]thiadiazole (PyT) block as a good alternative for BT unit to strengthen the electron affinity was suggested by the group of Leclerc in 2008 [111]. The copolymer composed of carbazole dithiophene (CDT) as D-unit and PyT as A-unit (PCDTPT) had a deeper LUMO and thus a lower band-gap compared to its BT derivative. This was mainly attributed to the electron withdrawing strength of PyT that is higher than BT. However, solar cells based on PCDTPT did not perform better conceivably due to the low molecular weight and poor solubility of the copolymer. You and colleagues came over this issue by introducing two alkylated thiophene rings from both sides of PyT unit [121]. A new dithiophene-Py (DTPyT) moiety was successfully combined with different D units and led to several relatively high molecular weight low band-gap copolymers with deep LUMO levels. The respectable PCE of > 6.3% was reached using a copolymer incorporating benzo[1,2-b:4,5b']dithiophene (BnDT) as a D unit.

Recently, fluorination of the conjugated polymer backbone turned out to be another perspective strategy towards highly efficient polymer solar cells (PSCs) [122-124]. In pioneering works on the conjugated backbone fluorination of polymers for OPVs, incorporation of fluorine atoms was mainly stated to reduce FMO energy levels. Thereby, Yu and colleagues were among the first to present efficient PSCs based on backbone fluorinated polymers [124]. In their work, introduction of the fluorine atom into the 3rd position of thieno[3,4-b]thiophene unit led to the significant decrease of both HOMO and LUMO levels while the band-gap kept almost unchanged. As expected, due to the lowered HOMO level the V_{OC} of the BHJ solar cells based on fluorinated derivative (PTB4) were slightly higher than for non-fluorinated one (PTB5). The improvements on the other OPV parameters (J_{sc} and FF) were not clear at that time and were attributed to the difference in

the active layer morphology. In the following years, similar tendencies have been observed upon fluorination of various polymers by the other research groups [125,126].

Along with molecular energy engineering, active layer morphology is well-known to be another key parameter in BHJ solar cells as it mainly governs the charge carrier generation, transport and collection efficiencies. Mostly, fluorination of polymer backbone has been reported to have dramatic and often positive impact on the thin film morphology often leading to better photovoltaic performances [127-130]. As a consequence, one of today's record PCE (> 11.5%) in OPV belongs to the fluorinated copolymer [12].

2.8 Thesis in context

From the above, it is obvious that lots of efforts are put on better understanding the key parameters starting from material design up to devices which affect the final performance of photovoltaic cells. Many different types of semiconducting low-bandgap materials have been synthesized and successfully utilized in photovoltaic applications [131,132]. Though, the optimization of energy levels of compounds and lowering their bandgaps for better light harvesting itself is far not enough to obtain well-working final solar cell devices. It is well-known that organic materials generally suffer from low charge carrier mobility which highly depends on thin film microstructure. Moreover, organization of molecules in solution-processed thin films varies with different materials and results in diverse morphologies in non-trivial ways. Therefore, besides the development of novel organic semiconductors, one of the crucial routes to boost the efficiencies of solar cells even further remains the control of the morphology and deeper understanding of the basic processes.

In the present context, this thesis addresses in-depth study of the charge transport, microstructure and photovoltaic performances of different polymer families. π -conjugated copolymers studied within the scope of this thesis were based on three different widely used electron-deficient units. They are: benzothiadiazole (BT), pyridal[2,1,3]thiadiazole (PyT) and thienopyrrole dione (TPD). Opto-electronic and photovoltaic properties of TPD based copolymers are studied as a function of alkyl side chain positions. Based on the

results, polymer backbone torsion is suggested to have strong impact on energy disorder and charge transport. Studies on PyT-based copolymer show how morphology is critical for device performances. Though, the copolymer has almost ideal FMO energy levels unfavorable backbone orientations in thin films strongly limit the charge transport and thus the efficiency of photovoltaic cells. Investigations on BT-based copolymer versus difluorinated BT-based copolymer reveal very big differences in opto-electronic, structural and photovoltaic properties for both materials. As morphological studies clearly indicate, a favorable backbone “face-on” orientation is mainly driven by long alkyl side chains. Yet significant differences in charge transport and photovoltaic performances are attributed to the presence of fluorine atoms in the polymer backbone. Finally, combination of all these methods and findings described in this work, gives some ways to better understand structure-property relationships in conjugated low band-gap copolymers and their impact on photovoltaic performances.

Chapter 3: Materials and experimental methods

3 Materials and experimental methods

3.1 Introduction

Several polymer families with different optoelectronic properties were investigated in various device types throughout this thesis. In order to have deeper insights into the material properties different experimental techniques were applied. The information on materials, experimental and analytical methods is summarized in this chapter.

After a brief description of the materials and substrates used, the elaboration procedures of “standard” and “inverted” photovoltaic device structures and the device characterization methods are presented. The next section focuses on vertical and horizontal charge transport measurements and details the analytical expressions used to extract the charge carrier mobilities. Then, the ultraviolet-visible spectroscopy set-up that was used to get absorption profiles of polymers and blends in different phases (solid state and solutions) is described. The final section of the chapter briefly presents the morphological characterization methods of polymers and blends in thin films.

3.2 Materials and substrates

All the polymers used in this thesis were synthesized by chemists from Institut de chimie et procédés pour l'énergie, l'environnement et la santé (ICPEES) under the supervision of Dr. Nicolas Leclerc. The polymers were based on widely used A-units such as TPD, PyT and di-fluorinated BT. The polymer molecular structures are described in more detail in the corresponding chapters. PC[61]BM and PC[71]BM were purchased from Solenne B.V. and utilized as received. Two different types of PEDOT:PSS emulsions were used. One was purchased from Heraeus Clevis PH and the other from Ossila. Both were used as received. Polyethyleneimine, 80% ethoxylated (PEIE) solution (average Mw = 70 000 g/mol) and 2-methoxyethanol 99.8% were purchased from Sigma-Aldrich and utilized as received. The solvents (1,2-dichlorobenzene, chloroform) and the processing additive (1,8-diiodooctane)

were purchased from Sigma-Aldrich and used as received. Indium tin oxide (ITO) coated glass substrates, utilized in photovoltaic and space-charge limited diodes were purchased from Luminescence Technology (LumTech) Corporation. The dimensions of substrates were 20 x 20 x 1 mm (L x W x H). The sheet resistance was around 10 Ω /sq.

Bottom contact bottom gate (BC/BG) organic field-effect transistors (OFETs) were fabricated on commercially available silicon substrates with photo-lithographically defined electrodes, purchased from Fraunhofer Institut Photonische Mikrosysteme. Specifications of the substrates are listed below:

- N-doped silicon ($\approx 3 \times 10^{17} \text{ cm}^{-3}$) used as the gate
- $230 \pm 10 \text{ nm}$ of thermally grown SiO_2 used as gate-dielectric
- 30 nm of Au with 10 nm of high work function ITO as an adhesion layer for source and drain electrodes
- channel lengths of 2.5, 5, 10 and 20 μm (4 of each per substrate) with a width of 10 mm

Figure 3.1a shows a scheme of 15 mm x 15 mm Fraunhofer substrates with 16 incorporated source and drain electrodes. The layout of a single transistor is depicted in figure 3.1b. All the substrates were covered with a protective layer upon receive.

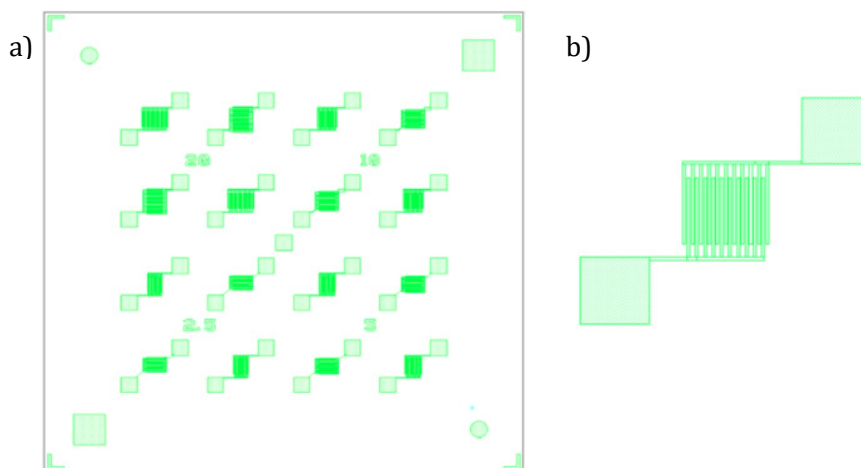


Figure 3.1: a) Scheme of a substrate with source and drain electrodes; b) a single transistor

3.3 Experimental details and analytical methods

3.3.1 Photovoltaic device elaboration

ITO coated glass substrates were cleaned at 45°C for 20 minutes for each step in ultrasonic bath in the following order: deionized water, acetone and 2-propanol. After that, UV/Ozone treatment has been performed to remove residual organic contaminants. Then, depending on device architecture, either 30-40 nm of the hole transporting PEDOT:PSS (for standard device structures) or 7-10 nm of the polyelectrolyte PEIE (for inverted devices) layers were deposited by spin-coating.

Spin-coating conditions for PEDOT-PSS (\approx 30-40 nm) were as follows:

- filtering the PEDOT:PSS suspension (nylon filter pore diameter = 0.45 μ m);
- spin-coating at 5000 rpm, with acceleration of 1000 rpm/s, during 90 sec;
- cleaning of the PEDOT:PSS with water from part of the substrate (Fig. 3.2);
- annealing of PEDOT:PSS layer at 140°C for 30 minutes in nitrogen-filled glove box.

Spin-coating conditions for PEIE (\approx 7-10 nm) were:

- preparation of PEIE solution diluted in 2-methoxyethanol (0.6% of PEIE by mass);
- spin-coating at 5000 rpm, with acceleration of 1000 rpm/s, during 60 sec;
- cleaning the PEIE with ethanol from part of the substrate (Fig. 3.2);
- annealing of PEIE layer at 100°C for 15 minutes in nitrogen-filled ambient (glove box) to remove the residual solvent.

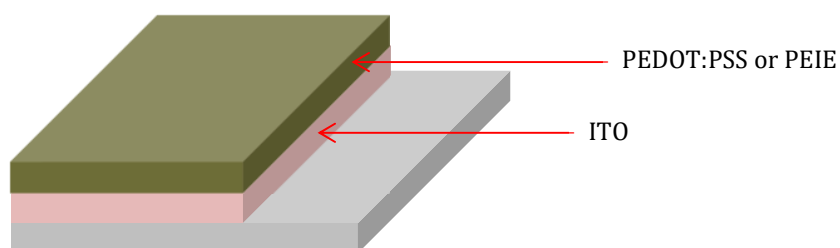


Figure 3.2: Schematic view of interfacial layers coated on ITO after cleaning from one side

After the annealing step the active layer was spin-coated. Depending on the polymers used, spin-coating conditions were varied to obtain homogenous films. Thin film deposition parameters employed for each polymer will be given in the appropriate chapters. To complete the photovoltaic devices, metal electrodes were thermally evaporated in vacuum (Pressure $\approx 1 \times 10^{-6}$ mbar). For standard device structures, either Al (120 nm) or Ca (20 nm)/Al (120 nm) bilayers were used, while for inverted devices MoO₃ (7 nm)/Ag (120 nm) bilayers were used as top electrodes (Fig. 3.3).

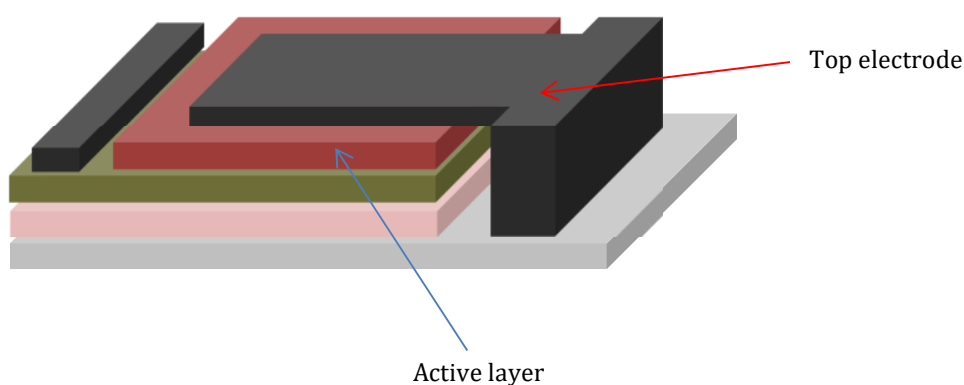


Figure 3.3: Schematic view of final photovoltaic device

3.3.2 Solar cell device characterizations

3.3.2.1 Current-voltage measurements

Current-voltage (I-V) characteristics of solar cells were measured using a LabView-controlled Keithley 2400 SMU. Measurements were performed in the dark and under light using an ABET Technologies Sun 3000 solar simulator with an AM1.5G filter. The standard light-intensity condition (100 mW/cm^2) was controlled by a calibrated Si solar-cell, while for the measurements under different light intensities, neutral optical filters with various transmittances were employed.

All the main parameters of solar devices (V_{OC} , J_{SC} , FF and PCE) as well as R_{SH} and R_S were extracted using the LabView software. The details on measured (I-V) curves and main solar

cell parameters are given in chapter 2. As has been stated before, series and shunt resistances play a major role in the FFs of solar cells. The values of R_{SH} given in this thesis were extracted from inverse slopes of dark (I-V) curves at $V \approx 0$ V:

$$R_{SH} = \left(\frac{dV}{dI} \right)_{V=0} \quad (3.1)$$

Additionally, the values for R_S were estimated from the slopes of dark (I-V) characteristics close to the solar cell operating conditions, at $V \approx V_{oc}$ [133,134]:

$$R_S = \left(\frac{dV}{dI} \right)_{V=V_{oc}} \quad (3.2)$$

3.3.2.2 Quantum efficiency (QE) measurements

As has been said in previous sections, once the charges are generated within a solar cell they have to be collected at the electrodes in order to contribute to the current. However,

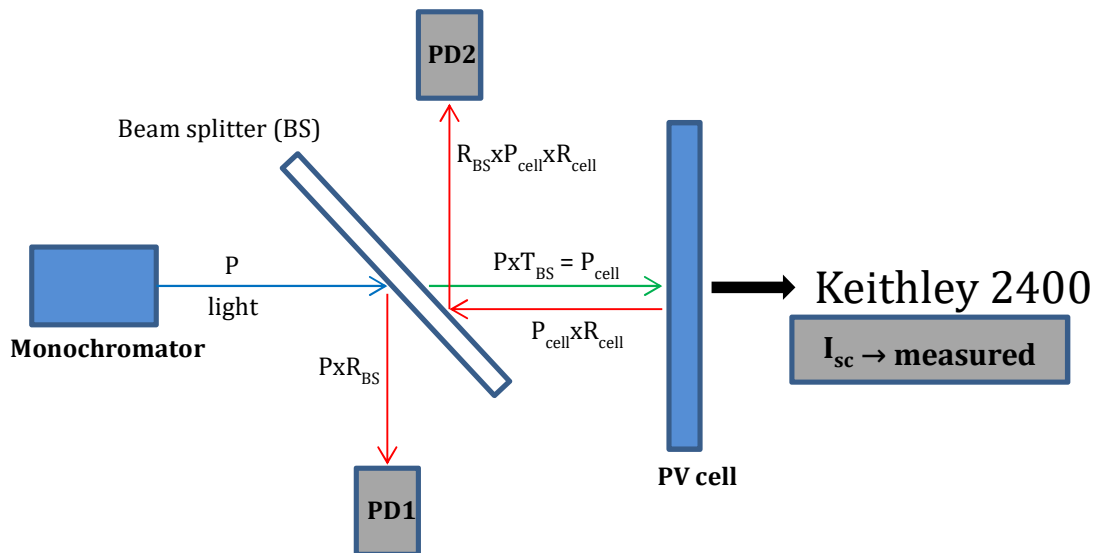


Figure 3.4: Schematic view of EQE/IQE measurement setup at ICube. P – power of incident light; PD1 – photodiode 1; PD2 – photodiode 2; T_{BS} and R_{BS} – transmittance and reflectance of the beam splitter, respectively; P_{cell} and R_{cell} – light power incident to PV cell and reflectance of PV cell, respectively; I_{sc} – measured short circuit current.

the carriers at this stage may also recombine without contributing to the external circuit. Here, quantum efficiency is a powerful tool to assess quantitatively the amount of photons that are finally converted into collected charges. Two types of QE are often determined for solar cells. They are:

- The external quantum efficiency (EQE), which is the ratio of the number of collected charge carriers to the number of incident photons at short-circuit conditions.
- The internal quantum efficiency (IQE), which is the ratio of the number of collected charge carriers to the number of photons absorbed by the PV device at short-circuit conditions.

Fig. 3.4 illustrates the EQE/IQE measurement setup scheme used in this work. In general, EQE is expressed as follows:

$$EQE = \frac{\text{Measured current}(A)/\text{elementary charge } (C)}{\text{Power of incident light}(W)/\text{energy of a single photon}(E_{PH})} \quad (3.3)$$

If we convert equation 3.3 to what we measure with the setup depicted in Fig. 3.4, we obtain:

$$EQE = \frac{I_{sc}}{q_e} \frac{hc}{P_{cell}\lambda} \quad (3.4)$$

Keeping in mind the following:

$$IQE = \frac{EQE}{(1 - R_{cell})} \quad (3.5)$$

We get an analytical expression for IQE as well:

$$IQE = \frac{I_{sc}}{q_e} \frac{hc}{P_{cell}(1 - R_{cell})\lambda} \quad (3.6)$$

where I_{sc} is measured current from the PV cell, q_e is elementary charge, P_{cell} is the light power received by the PV cell, R_{cell} is the reflectance estimated from the specularly reflected light intensity from the PV cell (recorded by PD2), h is Planck's constant, c is the velocity of light in vacuum and λ is wavelength. It should be noted that the so measured IQE

is only an approximation of the actual IQE as it does not take into account the contribution of diffused light.

All the EQE and IQE data reported in this thesis were calculated according to equations (3.4) and (3.6), respectively.

3.3.2.3 Transient photovoltage and charge extraction measurements

Transient photovoltage (TPV) is a powerful technique to assess the charge carrier lifetime after exciton dissociation. This method is based on measuring a photovoltage decay caused by a small optical perturbation under a given light power. The charge extraction (CE) method allows monitoring the charge carrier density accumulated within a solar device under open-circuit conditions for different illumination intensities. Combining both techniques can provide a deep insight into the dominating recombination mechanisms. Both methods are briefly presented in the following sub-sections.

3.3.2.3.1 Transient photovoltage

Figure 3.5a presents a simplified scheme of the setup utilized to perform TPV measurements. To ensure open circuit conditions, the investigated solar cell is connected to the oscilloscope via a high resistance ($\approx 5 \text{ M}\Omega$). A constant bias white light is provided by a high performance array of light emitting diodes (LED) with a light spectrum close to the solar spectrum and with a light intensity varying from 0.01 to 1.2 suns. The intensity of white light is tuned by a voltage applied to LED via a power source. In addition to the white light, a green LED ($\lambda = 535 \text{ nm}$) to deliver a low intensity light pulse with an adjustable duration is used. As a consequence of this small optical perturbation, additional charges are generated resulting in a voltage transient with a maximum amplitude ΔV . The intensity of the pulsed green light is adjusted to maintain the condition $\Delta V \leq 0.05 \times V_{oc}$ (small perturbation regime). As no external current flows, the photo-generated charges remain within the device. The corresponding splitting of the quasi-Fermi level determines the

value of V_{oc} . Thus, following the voltage drop allows assessing the charge carrier recombination lifetime $\tau_{\Delta n}$ (Fig. 3.5b) [135].

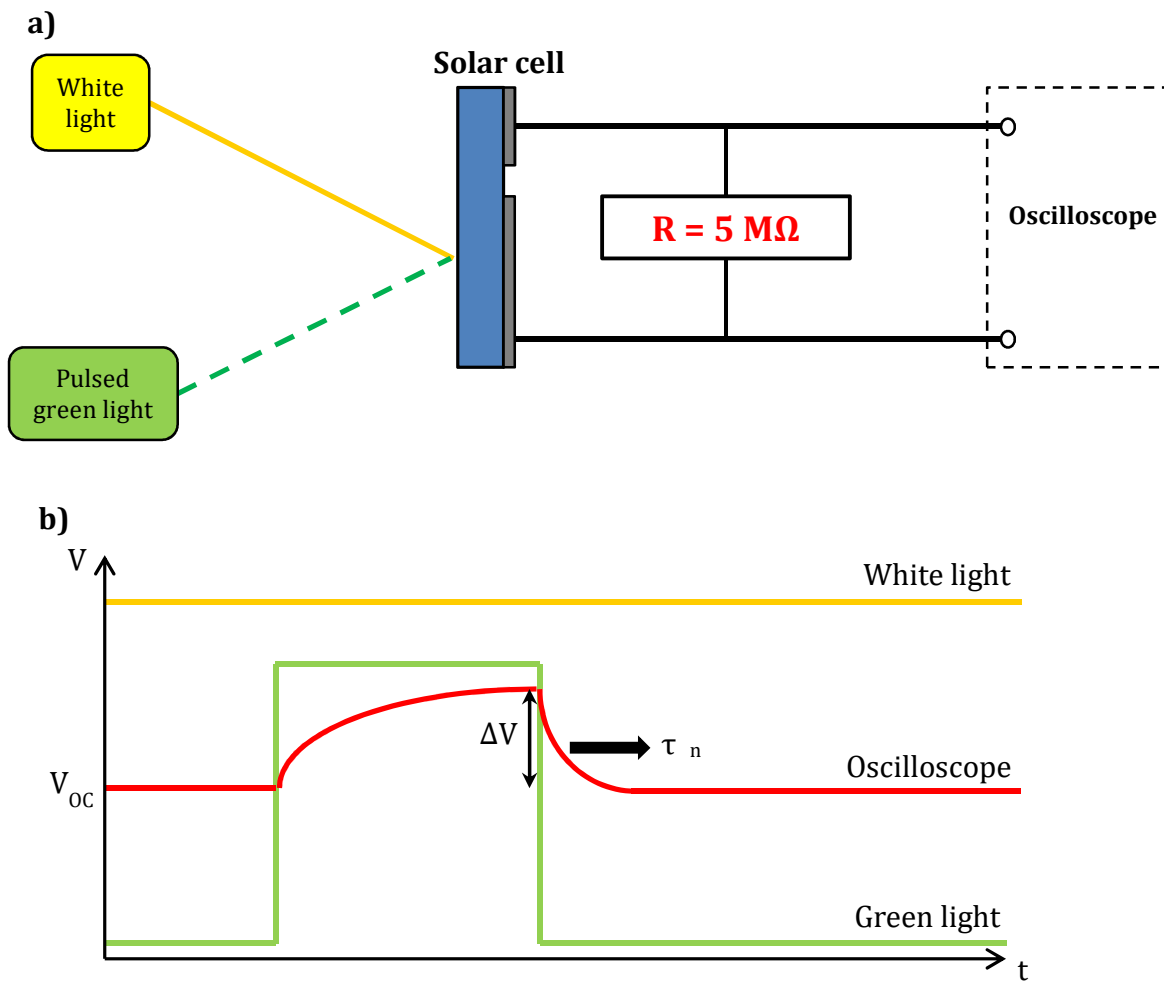


Figure 3.5: Scheme of a) TPV setup at the ICube; b) measured voltage drop after the green light pulse

In the limit of the small-perturbation regime, the voltage transient can be described by a single exponential decay as follows:

$$\frac{d\Delta V}{dt} \propto \frac{d\Delta n}{dt} = -k_{rec}\Delta n = -\frac{\Delta n}{\tau_{\Delta n}} \quad (3.7)$$

where k_{rec} is the recombination rate, Δn is the change in the carrier density caused by pulsed green light, and $\tau_{\Delta n}$ is the corresponding charge carrier lifetime. By integrating the equation (3.7) we get:

$$\Delta n(t) = \Delta n_0 e^{-\frac{t}{\tau_{\Delta n}}} \quad (3.8)$$

3.3.2.3.2 Charge extraction

Charge extraction (CE) is a common technique that is used to study the charge carrier density in an operating solar cell under various conditions. The experiments start with the

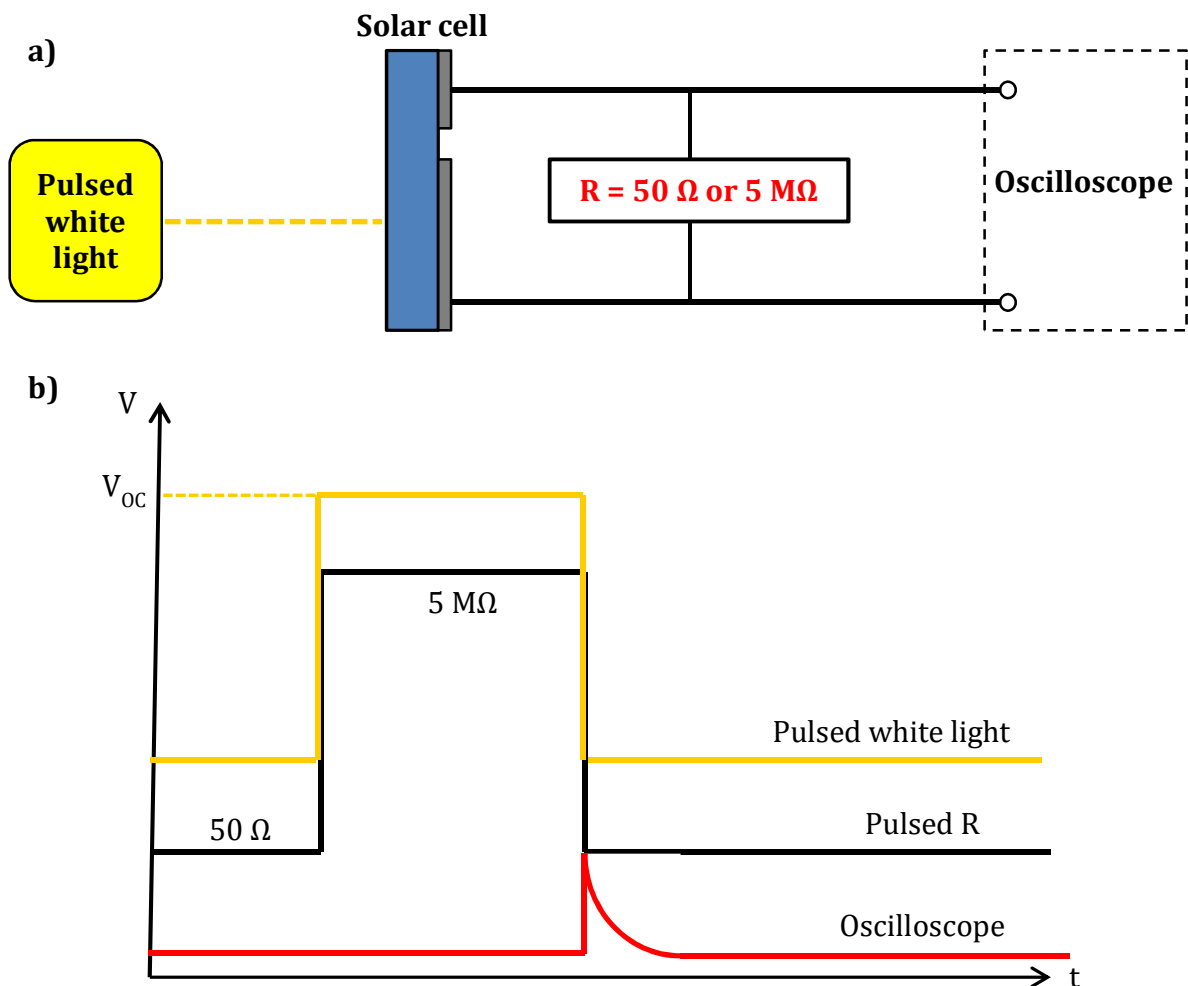


Figure 3.6: Scheme of a) CE setup at the ICube; b) measured current drop (in red) after switching to short circuit condition

illumination of solar cells with pulsed white light provided by the same LED array used for TPV measurements. To combine CE data with TPV results, the same LED light intensities were used. The scheme of the CE setup is depicted in Fig. 3.6a. When the light is turned on, a fast C-MOS transistor is switched to the off-state with a resistance to 5 M Ω ensuring the open circuit condition. Here, as no current flow is possible, the charge generation and recombination rates are equalized. When the V_{OC} has reached its stationary value the white light is turned off and the fast transistor is switched to its on-state (switching time smaller than 200 ns), corresponding to an input resistance of 50 Ω that brings the solar cell into a "short-circuit" condition. This step allows photo-generated charges to drift out causing a current flow across the 50 Ω resistance that is recorded by the oscilloscope (Fig 3.6b). By integrating the measured transient current flow over time gives the total charge carrier density (n_{total}) as follows:

$$n_{total} = \frac{1}{Adq_{e-}} \int_{t_0}^{t_1} I(t)dt \quad (3.9)$$

where A is the illuminated area, d is the active layer thickness and q_{e-} is the elementary charge. Here, it should be noted that the total amount of charge carriers (Q_{total}) is the sum of photo-generated charges in the bulk (Q_{bulk}) and non-negligible amount of capacitive charges at the electrodes (Q_{geo}). As we are interested in charge carrier density in the bulk (n_{bulk}), n_{total} should be corrected by geometric capacitance as follows:

$$n_{bulk} = \frac{Q_{total} - Q_{geo}}{Adq_{e-}} \quad (3.10)$$

This allows us to estimate the variation of the free charges in the bulk (n_{bulk}) of the photovoltaic device as a function of white-light intensity [136].

From the data extracted from both TPV and CE measurements, we can write the charge-carrier dynamics as:

$$\frac{dn}{dt} = -kn^\alpha \quad (3.11)$$

k being a pre-factor and α a parameter depending on the dominant charge-carrier recombination mechanism occurring in the solar-cell.

3.3.3 Charge carrier mobility measurements

In contrast to inorganic semiconductors, the relatively low charge carrier mobilities of organic semiconductors remain one of the main bottlenecks towards high power conversion efficiencies, since photo-generated charges are likely to recombine prior to being collected by their respective electrodes. This non-geminate recombination strongly limits the FFs of organic photovoltaic devices. Therefore, charge transport studies can give important insight into the intrinsic material properties. In this thesis, charge transport investigations were performed in vertical and horizontal directions using space-charge limited current (SCLC) devices and organic field-effect transistors (OFETs), respectively. Both methods will be discussed in the coming sub-sections below.

3.3.3.1 Space-charge limited current

The space-charge limited current (SCLC) method is widely used to estimate the vertical (out-of-plane) charge carrier mobility in thin semiconductor films. When charges (positive and/or negative) are injected into a low conductivity semiconductor, a space-charge is formed that affects the current flow. The resulting device current-voltage characteristic does not follow Ohm's law any more, but depends on the charge carrier mobility.

SCLC devices in this thesis are elaborated by sandwiching the semiconductor film between two electrodes that are chosen to allow either electron injecting (electron-only device) or hole-injection (hole-only device).

The theoretical basis of space-charge limited currents for a single carrier device was first described by Mott and Gurney in 1940 and used to describe charge transport in resistive semiconductors [137]. The current is limited by the space-charge if: a) the dielectric relaxation time, given by $\epsilon_0 \epsilon_r / \sigma$, where ϵ_r is the dielectric constant and σ the conductivity of

the semiconductor, is longer than the "time-of-flight" of the carriers across the device, b) the current is not limited by an injection barriers (i.e. ohmic contacts). Under these conditions the current density will be given as:

$$J = \frac{9}{8} \varepsilon_r \varepsilon_0 \mu \frac{V^2}{L^3} \quad (3.12)$$

where V is the applied bias, L the thickness of the semiconductor film and μ the charge-carrier mobility. Equation 3.12 neglects the diffusion currents, background carriers and traps in the semiconductor. Furthermore, the charge-carrier mobility according to equation 3.12 is assumed to be independent of electric field and charge carrier density. However, in disordered materials such as most organic semiconductors, the charge carrier mobility can depend on the electric field (Poole-Frenkel effect) and on the carrier concentration [44]. An extension to Mott-Gurney equation, describing the field dependence of the mobility by a Poole-Frenkel type effect, has been proposed by Murgatroyd [138]:

$$J = \frac{9}{8} \varepsilon_r \varepsilon_0 \mu_0 e^{0.89\gamma\sqrt{E}} \frac{V^2}{L^3} \quad (3.13)$$

Where μ_0 is zero-field mobility and γ is a dependency factor of mobility to the electric field.

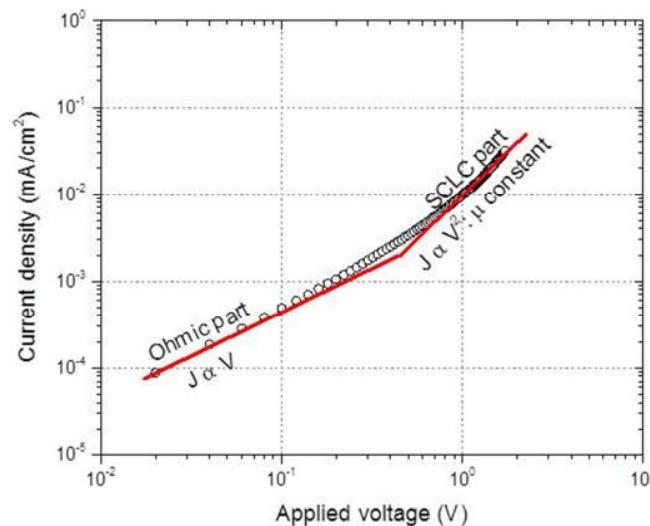


Figure 3.8: (J-V) curve of an SCLC diode indicating two different regimes: Ohmic and SCLC behaviors

Figure 3.8 presents an exemplary current voltage characteristic of an SCLC device plotted in log-log scale. Two different regimes can be distinguished. At low applied voltages the curve follows Ohm's law where the current density (J) is directly proportional to the applied voltage (V). At higher bias, the current density deviates from $J \propto V$ dependence and becomes limited by the space-charge. In this regime J is proportional to V^2 (equation 3.12) in the case of constant charge-carrier mobility.

In this thesis, I used single-carrier SCLC devices either with pure polymer films or with polymer-fullerene blends to investigate out-of-plane carrier mobilities (i.e. perpendicular to the substrate).

3.3.3.2 SCLC device elaboration and characterization

The substrate cleaning procedure was identical to the one used for solar devices (see section 3.3.1). Depending on the type of devices, either PEDOT:PSS (for hole-only devices) or PEIE (electron-only devices) layers were spin-coated under ambient atmosphere. PEDOT:PSS and PEIE spin-coating conditions were the same as for solar cell elaboration described in section 3.3.1. Various polymers and polymer/fullerene blends were deposited by spin-coating in a nitrogen-filled glove box. To finalize single-carrier devices, multi-layer electrodes were thermally evaporated onto the semiconductor film. For hole-only devices MoO_3 (7 nm)/Ag (140 nm) or Au (50 nm) were used, while Ca (20 nm)/Al (120) was used for electron-only devices. Each glass substrate could accommodate up to 20 SCLC diodes

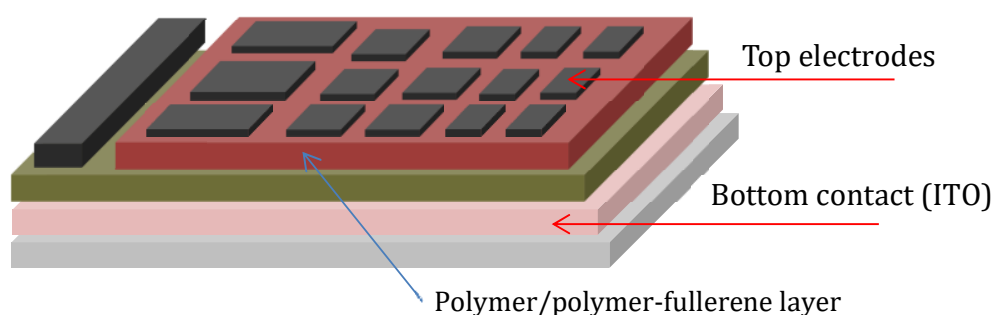


Figure 3.7: Schematic view of SCLC device substrate with various area diodes

with various device areas as shown schematically in Fig. 3.7.

The devices were characterized on a probe station equipped with an optical microscope. Round tips were employed as a probe to contact the top electrodes. This was done in order to avoid penetration of the tips into the studied film and destroying the device. The current-voltage responses were recorded by a Semiconductor Characterization System 4200 from Keithley.

3.3.3.3 Organic field-effect transistors

The structure of bottom-contact-bottom-gate (BC-BG) organic field-effect transistors (OFETs) used throughout this thesis is depicted in Fig. 3.8. The gate composed of n-doped silicon substrate is separated by the SiO₂ dielectric layer from the organic layer and the source and drain electrodes. The channel length and width (Section 3.2) are defined in accordance with Fig. 3.8. This structure has the drawback to lead to relatively high contact resistances due to an enhanced morphology disorder close to the contacts [139]. However, it benefits from facile device fabrication and testing and is often sufficient to compare charge transport in different materials.

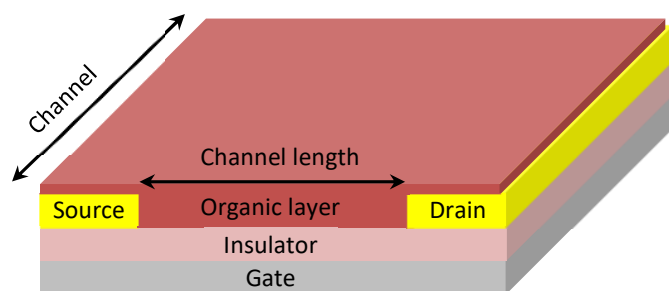


Figure 3.8: Scheme of an organic field-effect transistor in BC-BG configuration with channel length and width

When a bias is applied to the gate, the charges with opposite polarity will accumulate in the organic layer close to the semiconductor/insulator interface [140]. A negative voltage applied to the gate will cause the accumulation of positive charges (holes) while a positive gate voltage will promote negative charges (electrons) as shown in Fig. 3.9a and b, respectively. As the local charge carrier density in a semiconductor channel is controlled by the gate voltage, the electric conductivity of that channel can be varied by the gate bias. Thus, for a given voltage (V_{DS}) applied between the drain and source electrodes, the current

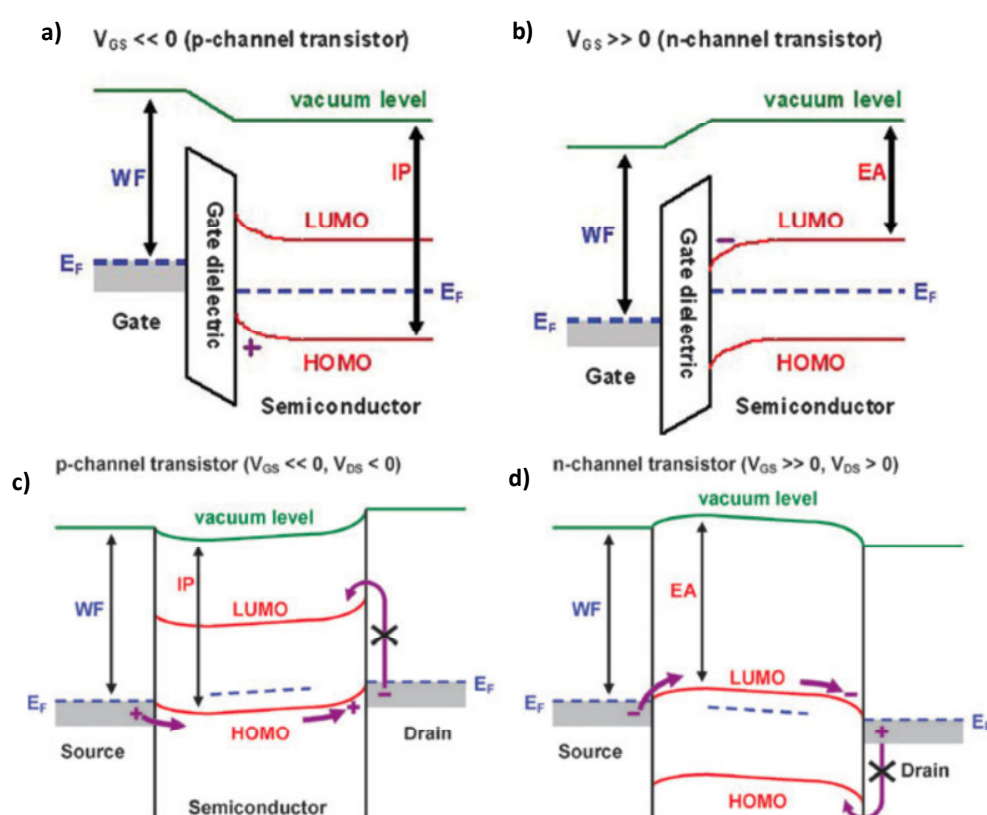


Figure 3.9: Energy-level diagrams a) and b) after applying V_G via organic layer/dielectric interface, showing the accumulation of holes and electrons, respectively; c) and d) along the channel after applying the V_{DS} showing the drift of holes and electrons, respectively. Reproduced from Ref [141].

flowing in the channel is adjusted by tuning the gate voltage (Fig. 3.9c and d) [141].

However, in the presence of traps not all the accumulated charges are mobile. Upon applying the gate voltage, these traps are filled first. For this reason, the gate voltage (V_G)

has to be greater than a given threshold voltage (V_{th}). The effective gate bias that controls the gate current is therefore given by the difference between the applied voltage and V_{th} . On the other hand, residual (uncontrolled) doping of the organic semiconductor layer results in the accumulation of charges even at zero gate voltage. In this case, an opposite bias must be applied to turn the transistor off [142-144].

The I_D - V_{DS} characteristics of an operating OFET (often referred to as output characteristics) shown in Fig. 3.10a exhibits two different regimes: the linear and the saturation regime (Fig 3.10b and c, respectively). To explain the charge transport in OFETs in terms of the measured current-voltage characteristics, the electric field created by the gate bias must be much larger than the field induced by the drain voltage. As a result of this gradual channel approximation, charge transport in OFETs is limited to the organic layer/dielectric interface. Assuming a constant mobility the current flow in the channel can be described as:

$$I_D = \frac{WC_i\mu}{L} \left[(V_G - V_{Th}) - \frac{V_{DS}}{2} \right] V_{DS} \quad (3.14)$$

Where I_D is the drain-source current, C_i is the capacitance per area of the insulator, μ is the charge carrier mobility, W and L are the channel width and length, respectively.

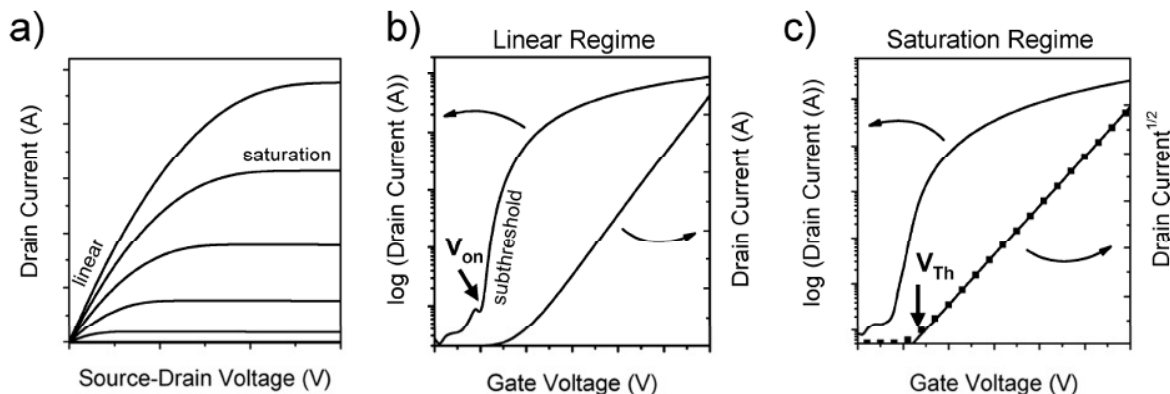


Figure 3.10: Current-voltage characteristics for OFETs: a) Output characteristics with the linear and saturation regimes; Transfer characteristics in b) linear regime with onset voltage (V_{on}) and c) saturation regime indicating threshold voltage (V_{Th}). Reproduced from Ref. [142].

In the linear regime, when $V_D \ll |V_G - V_{Th}|$, the equation 3.14 becomes:

$$I_D = \frac{WC_i\mu_{lin}}{L}(V_G - V_{Th})V_{DS} \quad (3.15)$$

In the limit when $V_{DS} \approx |V_G - V_{Th}|$, the gradient of accumulated charges in the channel concentrates at the source electrode. As a consequence, the depletion zone is formed and the source and drain electrodes are no more connected. Starting from this so-called pinch-off point, the current does not increase anymore and becomes independent of the drain voltage (saturation regime). Equation 3.14 can then be re-written as:

$$I_D = \frac{WC_i\mu_{sat}}{L}(V_G - V_{Th})^2 \quad (3.16)$$

Exemplary transfer characteristics in linear and saturation regimes are shown in Fig. 3.10 b) and c), respectively. Assuming that the mobility is constant across the channel, the μ values for different regimes can be directly extracted from transfer curves as a function of the slope:

in the linear regime (see Eq. 3.15):

$$\mu_{lin} = \frac{L}{WC_iV_{DS}} \left(\frac{\partial I_D}{\partial V_G} \right) \quad (3.17)$$

and in the saturation regime (see Eq. 3.16):

$$\mu_{sat} = \frac{2L}{WC_i} \left(\frac{\partial \sqrt{I_D}}{\partial V_G} \right)^2 \quad (3.18)$$

It should be noted however that the assumption of a constant field-effect mobility for disordered organic semiconductors is generally not valid as the mobility increases with the applied gate voltage (i.e. with charge carrier density) [114,145]. Therefore, mobilities estimated in saturation regime are often higher compared to the linear regime.

To go further in the analysis, for polymer transistors that showed negligible injection barriers, complementary I_D - V_G measurements were performed at low V_D . Due to the fact that in linear regime charges are uniformly distributed in the channel, estimated mobility

values from I_D - V_G curves in this regime are considered to reflect better the intrinsic material properties. Hole mobilities were calculated using Eq. 3.17 from the slopes of transfer curves corresponding to each data point and were plotted versus V_G .

3.3.3.4 OFET fabrication and characterization

Fraunhofer substrates (see Section 3.2 and Fig. 3.1) were used to fabricate OFETs. To remove the protective layer and other contaminants from the substrate surface, samples were cleaned in ultrasonic baths for at least 15 minutes at each step in the following order: deionized water with detergent, acetone and 2-propanol. During the cleaning process the temperature of ultrasonic bath was set to 45°C. The following UV/Ozone treatment for additional 15 minutes ensured elimination of residual organic contaminants. After this step samples were transferred into the glove box and various organic layers were deposited by spin-coating. Spin-coating conditions varied according to the polymers used. Precise film deposition conditions will be described in appropriate chapters dedicated to each polymer. At last, samples were left under vacuum (10^{-6} mbar) overnight to remove the residual solvent.

Finalized devices were characterized on the probe station assembled with an optical microscope. As the source and drain electrodes are located below the organic layer (bottom-contact), sharp tips were used to pierce the layer and establish electrical contacts. The gate voltage was applied to a conducting plate in contact with the n-doped Si substrate. All the output and transfer characteristics were recorded by a Semiconductor Characterization System 4200 from Keithley. Device transfers between the glove boxes were realized using a sealed container to prevent samples from air exposure.

3.3.4 Ultraviolet-visible spectroscopy

Ultraviolet-visible (UV/Vis) spectroscopy is a technique used to measure quantitatively the absorption or reflectance of a material either in solution (absorption) or in thin films. The working principle is based on shining a monochromatic light on the sample and analyzing

the transmitted or reflected fraction of the light. The equipment used in UV/Vis spectroscopy is a UV/Vis spectrophotometer that usually includes a radiation source, an adjustable sample holder, a monochromator for light dispersion, and a photodetector. The light source is a tungsten wire, a xenon arc lamp (160-2000 nm), and a deuterium lamp that is continuous in the 190-400 nm wavelength range. The detector is generally a photodiode or a charge-coupled device. In our case, the UV/Vis spectrophotometer measures the transmitted light intensity (I_n) and compares it to the incident light intensity (I_{n0}) as a function of the wavelength. The corresponding ratio $T=I_n/I_{n0}$ gives the transmittance. If the reflectance and non-specular light diffusion are negligible, the absorbance (Ab) can be estimated using:

$$Ab = \log\left(\frac{1}{\%T}\right) \quad (3.19)$$

Furthermore, according to Beer-Lambert's law, the absorbance of light passing through a solution is directly proportional to the material concentration (C_n) and to its path length (L):

$$Ab = \epsilon C_n L \quad (3.20)$$

where ϵ is so-called molar attenuation coefficient. This value describes a specific absorptive property of a material and is constant under a given wavelength and temperature.

In this thesis, all the absorption profiles of neat polymers or polymer/fullerene blends in solid state were characterized using a Shimadzu 082395 spectrophotometer at ICPEES with the assistance of Dr. Nicolas Leclerc. In-situ temperature dependent UV/Vis measurements in solutions were carried out with the help of Dr. Laure Biniek at ICS on the Agilent Cary 60 UV-VIS spectrophotometer.

3.3.4 Morphological characterizations

To further understand the results obtained from OPV measurements and charge transport investigations, morphological characterizations were carried out. In particular, atomic-force microscopy (AFM) and grazing incidence wide-angle x-ray scattering (GIWAXS) techniques were applied to thin films composed of either polymer/fullerene blends or pure polymer materials.

3.3.4.1 Atomic-force microscopy

The AFM technique is used in the so-called tapping mode to measure the surface morphology. The measurement is based on the small-distance interactions between the

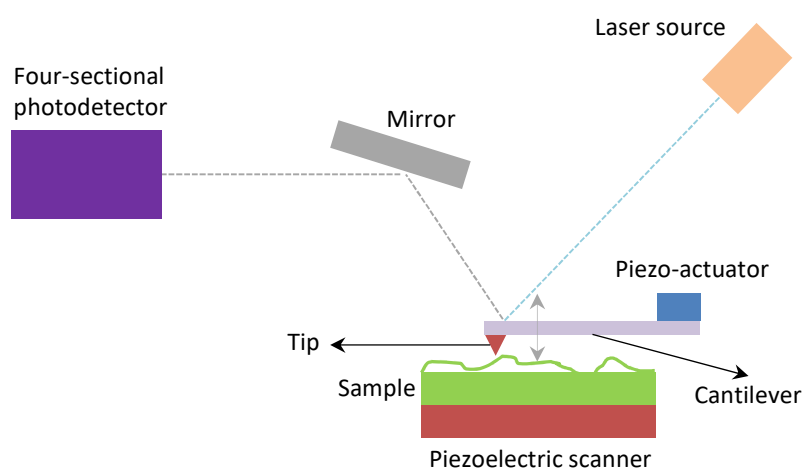


Figure 3.11: A simplified scheme of an AFM assembly

scanning probe and the sample surface. Figure 3.11 presents a simplified scheme of the AFM tapping mode principle. A sharp tip (probe) mounted to a free edge of a cantilever is brought close to the sample surface. Vibrations transmitted from the piezo-actuator make the cantilever oscillate close to its resonant frequency (f). The signal detection is realized by four-sectional photodiodes that catch the reflection of the laser beam focused on the edge of the cantilever. In order to tune the spacing between the tip and surface, a feedback

mechanism is used that keeps the amplitude of vibrations constant while the tip is scanned over the sample surface. As a consequence the surface topography can be built-up.

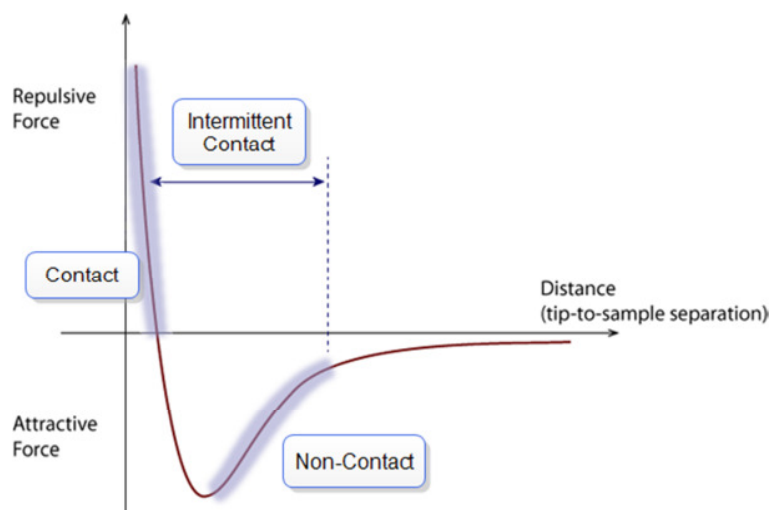


Figure 3.12: Tip-sample interaction as a function of spacing

In the tapping mode it is also possible to measure the phase shift between the probe oscillations and the electrical signal applied to the piezo-actuator. The latter depends on the inelastic interaction between the tip and the sample and allows one to distinguish between the materials or different phases (e.g. crystalline versus amorphous domains in a semi-crystalline polymer).

We used the technique to characterize the surface morphologies of bulk heterojunctions. Besides the thin film roughness, AFM allows to assess the approximate domain sizes of both donor and acceptor materials.

3.3.4.2 Grazing-incidence wide angle X-ray scattering

X-ray diffraction is a common technique used to analyze the crystal structure of a material at atomic or molecular level. Lattice structures formed by atoms cause the incident x-rays to diffract in different directions that are detected. By measuring the angles and intensities of diffracted beams, a 3-D crystal structure of a given material can be reconstructed. As

interatomic distances are in the 0.1 nm scale, interested scattering vectors q are located above 1 \AA^{-1} . In soft matter, molecular segments act as authentic objects without internal structure. These self-organized structures therefore lie in the nanometer scale and giving rise to scattering signals and periodicities in the q range of Small-Angle X-ray Scattering (SAXS) technique (acquisition range: 0.001 to 0.5 \AA^{-1}).

SAXS usually applies to bulk samples probed in transmission, but a variation consists in the Grazing Incidence Small-Angle X-ray Scattering (GISAXS) technique, for which a beam arrives in grazing incidence on a film of tens of nanometers' thick, deposited on a flat substrate such as silicon wafer. The signal scattered inside and outside the specular plane then gives information on the size, shape and self-organization of the studied object. Though the resolution and accuracy of q -vectors are well below SAXS this technique ensures access to the angles between crystallographic directions with respect to the substrate, providing information on molecular orientation. As a consequence, GISAXS characterization gives more insight into the orientation of objects and domains on the surface. As the signal scattered out of the specular plane is of low intensity, synchrotron radiation is often required for GISAXS. On several instruments, the GISAXS set-ups were designed to allow the detection of scattering peaks up to the limit of 2 \AA^{-1} . In this case, the denomination Grazing-incidence wide angle X-ray scattering (GIWAXS) is often used.

Structural characterizations of either polymer or polymer:fullerene thin films presented in this work were performed using a GIWAXS configuration. Measurements were conducted by Dr. Benoit Heinrich from the Institut de Physique et Chimie des Matériaux de Strasbourg (IPCMS) at U-SAXS line 9A of synchrotron PL-II of Pohang Accelerator Laboratory (PAL) in Korea. The monochromatic X-ray beam was produced with a vacuum undulator (IVU), a Si(111) double-crystals monochromator, and focused on the detector using K-B type mirrors. Patterns were recorded with a 2D CCD detector (Rayonix SX165). The sample-to-detector distance was about 225 mm for energy around 11.1 keV (wavelength: $\lambda = 1.12 \text{ \AA}$).

Chapter 4: Results: Thieno- pyrroledione based copolymers

4 Results: Thieno-pyrroledione based copolymers

4.1 Introduction

One of the significant drawbacks of organic semiconductors compared to their inorganic analogues is their relatively poor charge transporting ability. Indeed, structural and energetic disorders that are highly present in organic materials impede charges to move easily by creating trap states. Depending on different material systems, various models that are mostly adapted from the studies of inorganics semiconductors are as well applied to organics to describe charge transport [141]. Due to weak Van der Waals forces that exist between single polymer chains they may have relatively large spatial freedom. As a result, these macromolecules may self-organize in different microstructures from pure amorphous to highly crystalline phases. Relying on the findings that inorganic crystalline semiconductors usually transport charges much better than their amorphous counterparts, considerable efforts were dedicated to develop polymers that adapt crystalline-like microstructures. However, recent studies on various polymer systems enforce the community to revise the established views. For instance, some structurally disordered or even almost amorphous polymers seem to allow charge carrier mobilities as high as semi-crystalline ones [131,146]. Moreover, recently Noriega et al. found that existing structural disorder would not necessarily impact the energetic disorder. In particular, activation energies for charge transport in semi-crystalline and poorly ordered semiconducting polymers were shown to be comparable or less than 100 meV [80]. By analyzing polymers such as P3HT, PBTTT, PCDTBT along with the literature data they suggested a general relationship between disorder, aggregation and charge transport. The main outcome of their work was that charge transport in poorly ordered polymers was governed by the interconnectivity of the disordered aggregates. The next year another research group reported almost low energy disorder transport in conjugated polymers [147]. Surprisingly, charge transport properties of one of the investigated polymers based on indacenodithiophene (IDT) unit approached intrinsic disorder-free limit despite its near-amorphous microstructure. One of the clear evidences of this disorder-free transport was

the fact that the field-effect charge carrier mobility of that polymer was only weakly depending on the applied gate bias. Venkateshvaran et al. attributed this unique feature of IDT-based polymer to its molecular structure. By performing quantum chemical and molecular dynamics calculations along with pressure-dependent Raman spectroscopy they found that IDT-based polymer had a near-torsion-free conjugated backbone. As a result, high mobility and low energetical disorder of IDT-based polymers were attributed to the backbone planarity. Both of the mentioned studies therefore suggest that structural disorder does not necessarily cause energetic disorder and low mobility, and that the intramolecular torsion angles are of significant importance [148]. These recent findings could be beneficial for photovoltaics as the morphology control for such disordered materials may be less restraining.

In this context, this chapter mainly describes the observations on charge transport, morphology and photovoltaic properties of two different polymers of the same family based on thieno-pyrroledione (TPD) and dithienopyrrole (DTP) building blocks. The monomers of both polymers have four ethyl-hexyl (EH) side-chains, two of which are grafted on the TPD and DTP blocks and the two others are grafted on two thiophene units

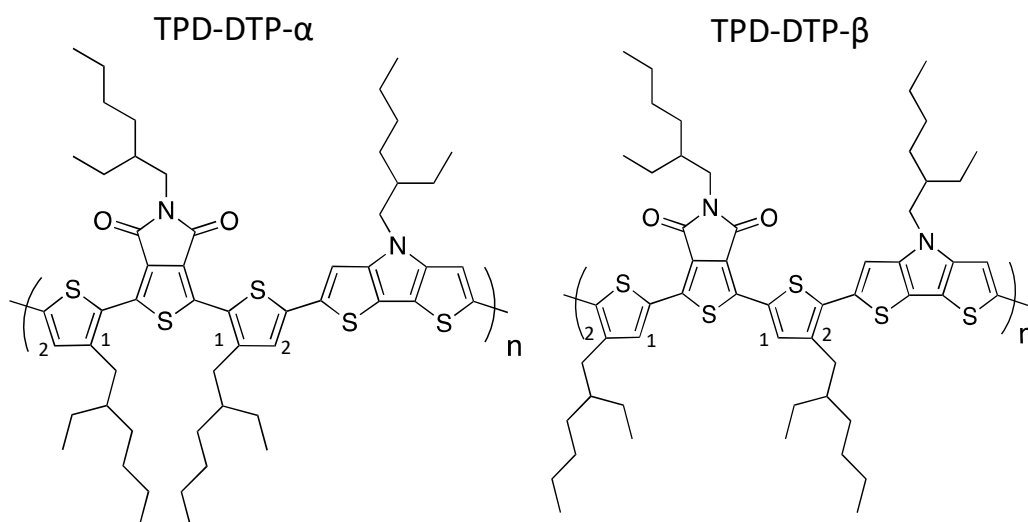


Figure 4.1: Chemical structures of TPD-DTP- α (left) and TPD-DTP- β (right) polymers. Positions 1 and 2 on the thiophene correspond to the α and β polymers, respectively.

(Fig. 4.1). The only difference between the two polymers is the position of the two EH side-

chains that are grafted on thiophenes. For the first polymer, side-chains are grafted on the thiophene at the position 1 (**TPD-DTP- α**). For the other, EH side-chains are located at the position 2 (**TPD-DTP- β**). First, **TPD-DTP- β** polymer, which has been initially designed for its electrochemical (HOMO, LUMO levels) and optical properties, was studied in detail. Charge transport properties of **TPD-DTP- β** were found to be of particular interest (details are in the following sections). Following these results, and in order to investigate the influence of the torsion angle between TPD and DTP units (induced by the thiophene-grafted EH side-chains) on charge transport, the polymer **TPD-DTP- α** was synthesized. To facilitate the reading, I will describe the results for both polymers together in the following sections. This chapter starts with the description of the electrochemical and optical measurements for **TPD-DTP- α** and for **TPD-DTP- β** . Charge transport properties along with GIWAXS measurements for both materials are described in section 4.3. Section 4.4 highlights the difference between both polymers in terms of backbone torsion angle as estimated from Density Functional Theory (DFT) calculations. Performances of both polymers in photovoltaic devices are reported in section 4.5.

Both polymers were synthesized by the former PhD student Dr. Ibrahim Bulut under the supervision of Dr. Nicolas Leclerc at ICPEES. Electrochemical measurements were done at ICPEES as well. DFT calculations were performed by the co-supervisor of my thesis, Dr. Patrick Leveque.

4.2 Electrochemical and optical properties of *TPD-DTP* polymers

Cyclic voltammetry (CV) was performed to assess the oxidation potentials for both materials. As the solubility of polymers was limited in dichloromethane the CV experiments were carried out in solid state. The HOMO energy levels of both copolymers were calculated from oxidation potentials with respect to ferrocene as a standard. As the reduction potentials were not clear, the LUMO levels were estimated taking into account optical band gaps. The change in alkyl side chain positions from β to α led to slight upshift of LUMO and significant downshift of HOMO energy levels. Opto-electronic properties are listed in Table 4.1.

Table 4.1: Opto-electronic properties of TPD-DTP based copolymers

	M_n (kg/mol)	E_{HOMO} (eV)	E_{LUMO} (eV)	E_g^{opt} (eV)
TPD-DTP-α	22	-5.66	3.82	1.84
TPD-DTP-β	20	-5.41	3.78	1.63

Figure 4.2 illustrates UV-Vis absorption spectra of **TPD-DTP- α** and **TPD-DTP- β** copolymers in solution and in solid state. We clearly observe a significant red shift both in solutions and thin films when switching from α to β position. For both polymers, a strong

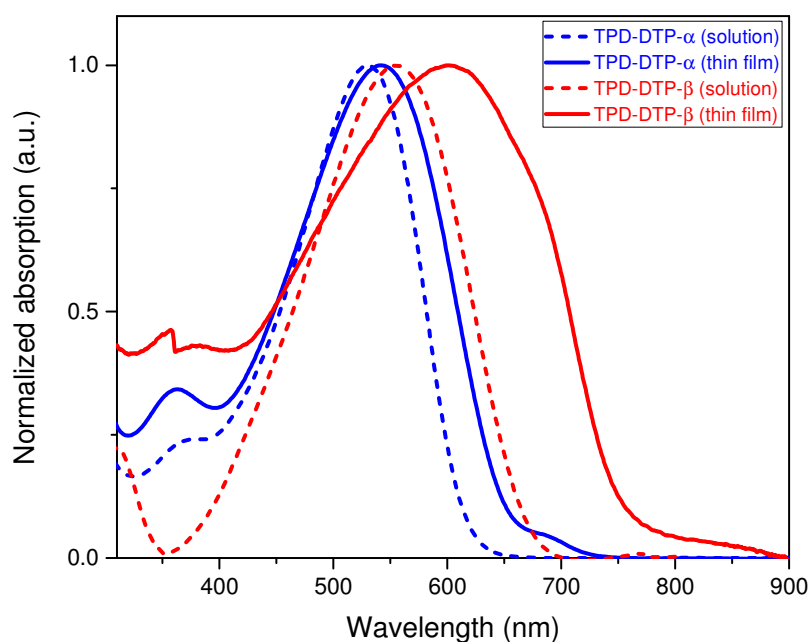


Figure 4.2: UV-Vis absorption profiles of **TPD-DTP- α** (blue) and **TPD-DTP- β** (red) copolymers in solutions (dashed lines) and thin films (solid lines)

red-shift is also observed when going from solution to thin film (40 nm for α and 100 nm for β). This red-shift is indicative of a stronger molecular interaction in solid-state. The larger red-shift observed for **TPD-DTP- β** suggests that the organization in solid-state of this polymer leads either to an enhanced backbone planarity and/or to stronger intermolecular π - π interactions.

4.2 Charge transport investigations

4.2.1 OFET devices

Thin films of **TPD-DTP- β** were spin coated onto Fraunhofer substrate from warm 5 mg/ml o-DCB solutions. After that, the substrates were left overnight under vacuum for drying. All the devices were characterized under nitrogen atmosphere using Keithley 4200 Semiconductor characterization system. In-plane hole mobility values were estimated from

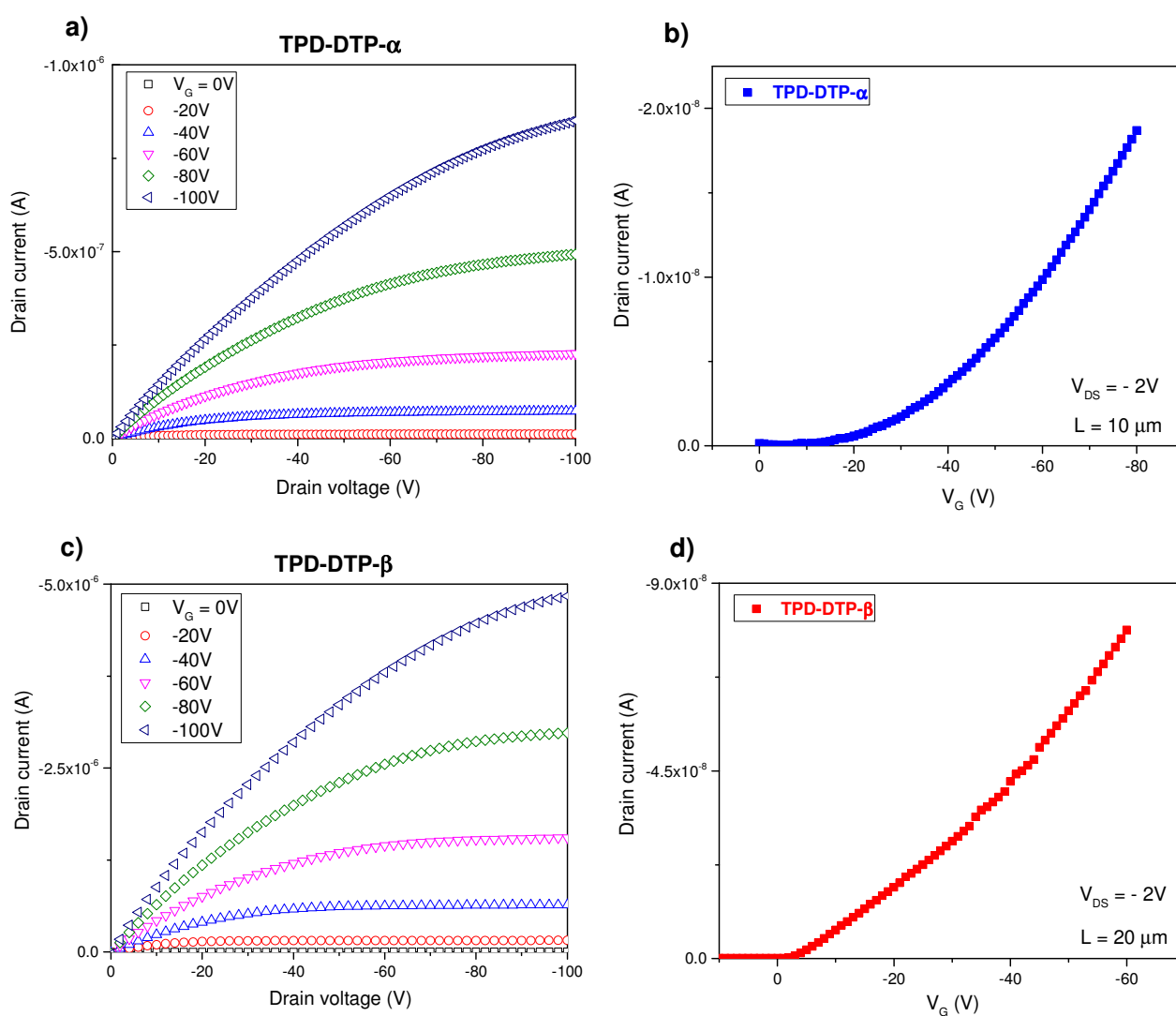


Figure 4.3: Output (a, c) and linear regime transfer (b, d) characteristics of BC-BG OFETs based on pure TPD-DTP- α (a, b) and β (c, d) polymers

the slopes of transfer curves in linear regime ($V_{DS} = -2V$).

Figure 4.3 shows output (left) and linear regime transfer curves (right) of OFETs based on pristine **TPD-DTP** copolymers, respectively. The average hole mobilities for **TPD-DTP- α** and **TPD-DTP- β** in linear regime ($\mu_{h,lin}^{FET}$) were found to be $7 \pm 1 \times 10^{-6}$ and $1.8 \pm 0.5 \times 10^{-4}$ cm^2/Vs , respectively. Interestingly, though the M_n of both copolymers were similar, $\mu_{h,lin}^{FET}$ of **TPD-DTP- β** was more than 25 times higher than for **TPD-DTP- α** .

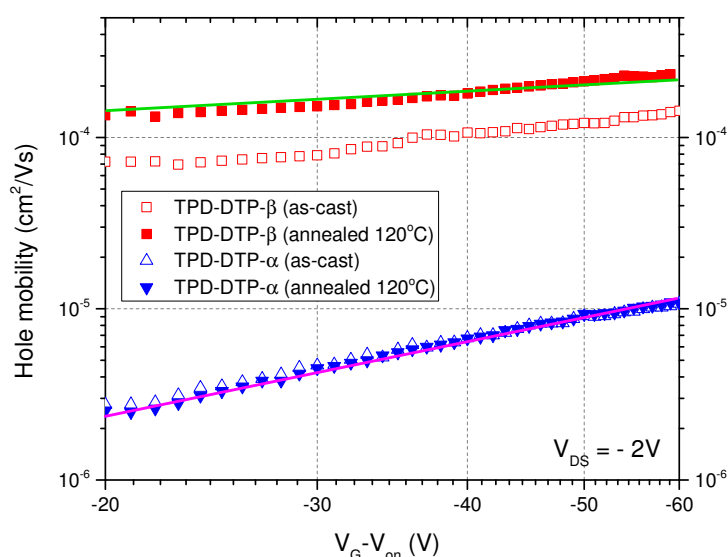


Figure 4.4: Evolution of $\mu_{h,lin}^{FET}$ vs effective gate voltage for **TPD-DTP- β** (red) and **TPD-DTP- α** (blue) as-cast (open symbols) and annealed for 30 min at 120°C (closed symbols) devices. Solid lines stand as eye guides for the mobility dependence on the gate voltage

Moreover, $\mu_{h,lin}^{FET}$ of both copolymers extracted from the linear transfer curves are plotted as a function of gate voltage in Fig. 4.4. Two different slopes for both polymers can be clearly distinguished. For **TPD-DTP- α** , $\mu_{h,lin}^{FET}$ shows a strong dependence to the applied V_G (from 2×10^{-6} up to 1.1×10^{-5} cm^2/Vs) that is rather expected for a highly disordered system. In contrast to that, for **TPD-DTP- β** the $\mu_{h,lin}^{FET}$ evolution in the same V_G range was much less pronounced (by factor of 1.8). This behavior is not the general trend for disordered organic materials for which the carrier mobility is often found to strongly increase with the charge carrier concentration (i.e. gate voltage) [44].

According to the model developed by Vissenberg et al. [43] for the field-effect mobility, the gate voltage dependence is linked to the width of density of states (details are in Chapter 2). Therefore, the slopes of the curves plotted in Fig. 4.4 can be associated to the level of energy disorder in the material: the stronger the slope, the higher the energy disorder and the broader the DOS. Interestingly, thermal annealing at 120°C led to slightly improved $\mu_{h,lin}^{FET}$ for **TPD-DTP- β** with a small decrease in gate-voltage dependence, while $\mu_{h,lin}^{FET}$ of **TPD-DTP- α** was not affected by the thermal treatment.

4.2.2 Space-charge limited diodes

Hole mobilities in the out-of-plane direction for both materials were estimated from hole-only space-charge limited (SCL) diodes. The details on device elaboration are presented in Chapter 3. In order to correctly evaluate the SCLC hole mobilities, diodes with various

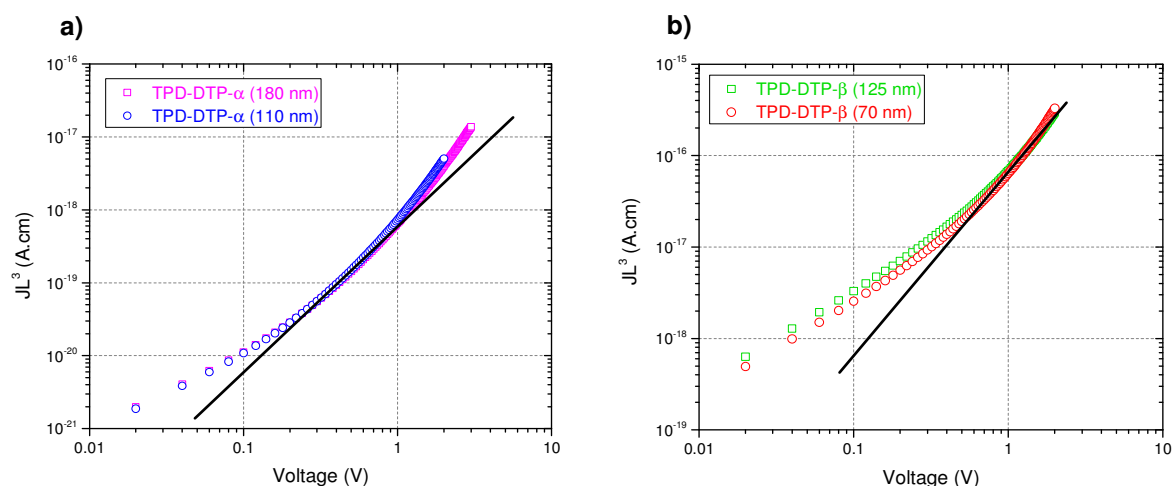


Figure 4.5: Current-voltage characteristics of hole-only SCL diodes based on a) **TPD-DTP- α** and b) **TPD-DTP- β** for 2 different polymer layer thicknesses

thicknesses were fabricated and tested. Figure 4.5 depicts current-voltage curves of hole-only devices based on pure polymer films with two different thicknesses. As it is shown, the curves almost collapse when the measured current density is multiplied by the cubic thickness (L^3) indicating that the current is space-charge limited and not injection-limited. Thickness-scaled J-V curves for both polymers are shown in Fig. 4.6. Vertical hole mobilities (μ_h^{SCLC}) for **TPD-DTP- β** and **TPD-DTP- α** were estimated to be around $1.5 \pm 0.2 \times 10^{-4}$ and $2 \pm 0.6 \times 10^{-6}$ cm^2/Vs , respectively. Moreover, the deviation from Mott-Gurney law at higher applied voltages is more pronounced for **TPD-DTP- α** copolymer. This could be due to electric field or charge carrier density dependent mobility [44]. Surprisingly, though the molecular weights of both polymers were similar [149], the in-plane and out-of-plane mobilities were found to be very different (up to two orders of magnitude difference). On the other hand, μ_h^{FET} at the lowest gate voltage and μ_h^{SCLC} for **TPD-DTP- β** are very close, suggesting that the charge carrier mobility increases only at high carrier densities (roughly above $\approx 1.6 \times 10^{18}$ cm^{-3}) and that transport is isotropic. For convenience, all hole mobility values are listed below in Table 4.2.

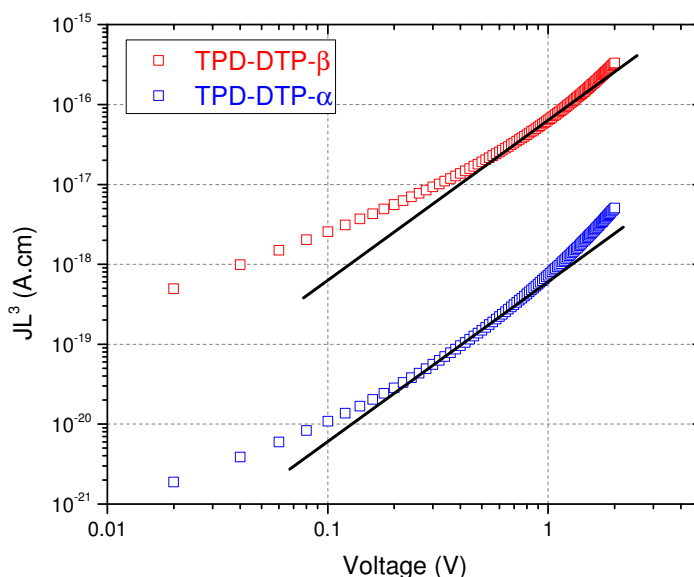


Figure 4.6: Current-voltage characteristics of hole-only SCL diodes based on **TPD-DTP- β** (red) and **TPD-DTP- α** (blue) scaled with thicknesses of the polymer layers

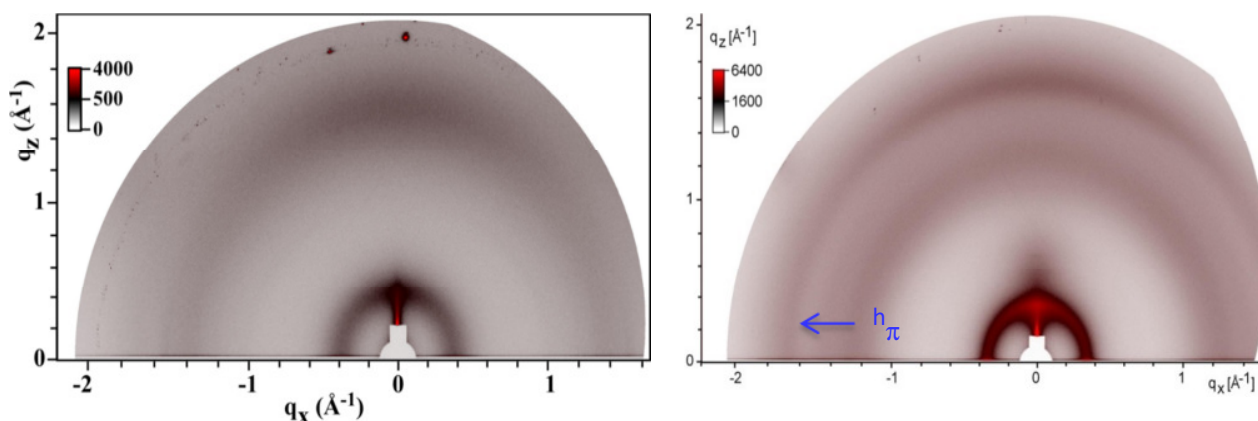
Table 4.2: In-plane and out-of-plane hole mobilities for pristine **TPD-DTP- α** and **TPD-DTP- β** polymer films

	$\mu_{h,FET}, \text{cm}^2/\text{V}\cdot\text{s}$	$\mu_{h,SCLC}, \text{cm}^2/\text{V}\cdot\text{s}$
TPD-DTP-α	$7 \pm 1 \times 10^{-6}$	$2 \pm 0.6 \times 10^{-6}$
TPD-DTP-β	$1.8 \pm 0.5 \times 10^{-4}$	$1.5 \pm 0.2 \times 10^{-4}$

Although the energy disorder for **TPD-DTP- β** polymer is rather low, the 3-D hole mobility is still limited. This could be due to the relatively low molecular weight of this copolymer ($M_n \approx 20 \text{ kg/mol}$, Table 4.1) that may hinder intermolecular connectivity. It has indeed recently been reported that efficient connection between short-range aggregates plays a major role in maintaining high charge carrier mobilities [150-152].

4.3 Microstructure characterizations

In order to better understand the charge transport results on both polymers, GIWAXS measurements have been performed on thin films. The results show that both polymer thin films are quasi-amorphous. Though the scattering profile of **TPD-DTP- β** has some

**Figure 4.7:** GIWAXS patterns of as-deposited **TPD-DTP- α** (left) and **TPD-DTP- β** (right) pristine polymer films.

signature of π - π^* stacking in the direction parallel to the substrate, the scattering rings are

rather continuous indicating poorly ordered polymer chains (Fig. 4.7). The **TPD-DTP- α** polymer is totally disordered and amorphous as it only gives rise to a broad and also continuous scattering rings without any signature of π - π^* stacking.

Except for the weak signature of π - π^* stacking for **TPD-DTP- β** , the structural disorder for both polymers are similar, while their charge transport behavior is rather dissimilar. For amorphous **TPD-DTP- α** , the charge transport results correlate well with its microstructure. Indeed, the structural disorder for this copolymer should give rise to a high energy disorder and to low hole mobilities. On the other hand, the poorly ordered **TPD-DTP- β** resulted in surprisingly low energy disorder and significantly higher hole mobilities in both horizontal and vertical directions compared to its **TPD-DTP- α** counterpart. At this stage, the difference in energy disorder is still unclear. However, similar observations have been reported recently by Venkateshvaran et al. [147]. In their work, seemingly structurally disordered polymer had low energy disorder. According to these authors' findings, the low energy disorder was mainly due the small torsion angle between neighboring units along the polymer backbone.

4.4 DFT calculations

DFT calculations were used as a tool to estimate the possible impact of alkyl side-chain position on the torsion angle of the polymer backbone. In order to keep reasonable calculation times, DFT calculations were performed on dimers with much shorter alkyl side chains. Ethyl (C2) side chains were grafted to α and β positions of the thiophenes. Calculations were performed using the B3LYP/6-31G* level in vacuum.

The simulation results for **TPD-DTP- β** dimers are shown in Fig. 4.8. The most pronounced

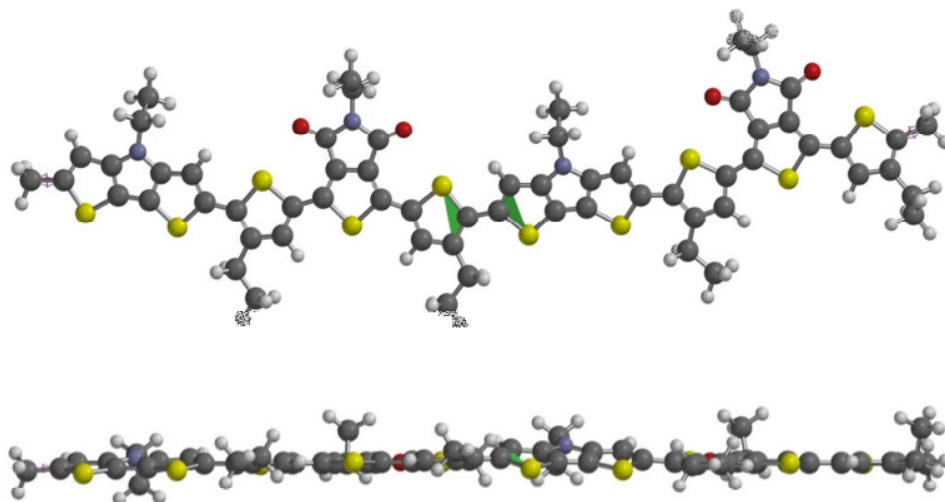


Table 4.8: a) Front and b) side view of **TPD-DTP- β** dimer calculated by SPARTAN

backbone torsion angle was around 20° . This value is not enough to break the conjugation along the single backbone. Therefore this molecule stays relatively planar. The calculated HOMO and LUMO energy levels were around -4.54 eV and -2.37 eV, respectively. For the **TPD-DTP- α** dimer, DFT calculations show that, due to the steric hindrance brought by the side chains in the α position, the backbone is far less planar with the tendency to adopt a helicoidal structure (Fig. 4.9). The relatively high torsion angle ($\approx 48^\circ$) is large enough to considerably disturb the backbone conjugation. Practically, the α isomer is less conjugated with the a slight downwards shift in the HOMO position and an upwards shift for the LUMO position resulting in a higher calculated band-gap. The corresponding HOMO and LUMO energy levels for **TPD-DTP- α** dimer are -4.64 eV and -2.28 eV, respectively.

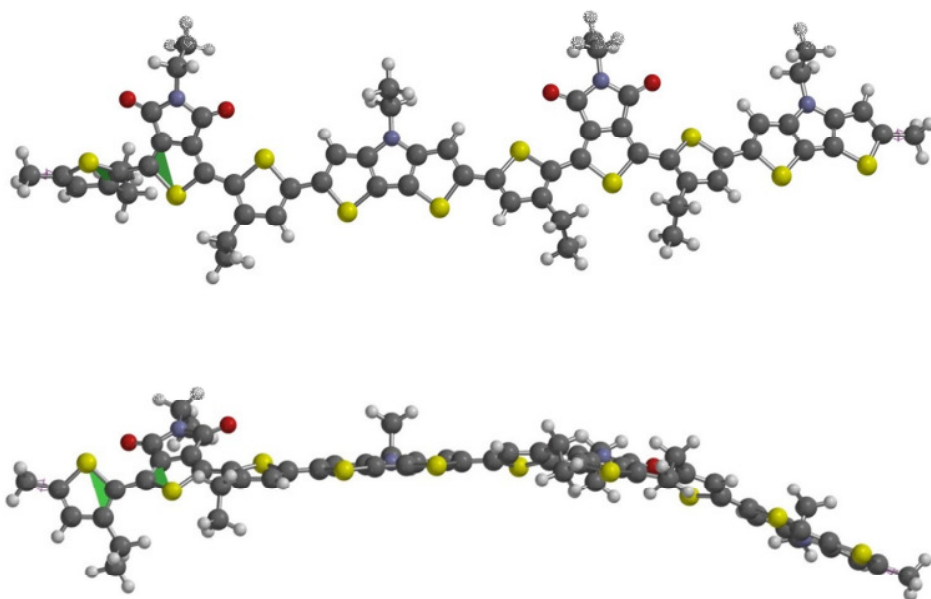


Table 4.9: a) Front and b) side view of **TPD-DTP- α** dimer simulated by SPARTAN

The calculated DFT results are well in-line with UV-Vis spectroscopy measurements where **TPD-DTP- α** was blue shifted compared to its **TPD-DTP- β** counterpart. In addition, we may conclude that high backbone torsion for **TPD-DTP- α** should significantly hamper the intra-chain charge transport and lead to the observed high energy disorder and low hole mobilities, while the highly planar conjugated backbone of **TPD-DTP- β** is in accordance with measured low energy disorder and significantly higher mobility.

4.5 Photovoltaic devices based on TPD-DTP copolymers

Finally, the polymers were tested in bulk heterojunction solar devices. PC[71]BM, was used as an acceptor material. All the details on device fabrication procedure are given in Chapter 3. Optimized solar cells were elaborated from polymer/PC[71]BM at a ratio of 1/1 in a solvent mixture of 50/50 (v/v) o-DCB/CHCl₃. Optimum concentrations of the solutions were around 10 mg/ml. In finalized standard device architecture, a bilayer Ca (20nm)/Al

(120nm) was used as a cathode. All the photovoltaic results are listed below in Table 4.3. Corresponding (J-V) curves are shown in Fig. 4.10.

Table 4.3: Photovoltaic results of BHJ cells based on **TPD-DTP- α** and **TPD-DTP- β** / PC[71]BM in standard device architectures

	Additive DIO (%)	V_{oc} (mV)	J_{sc} (mA/cm ²)	FF (%)	PCE (%)	Thickness (nm)
TPD-DTP-α	-	530 \pm 10	1.3 \pm 0.1	23 \pm 2	0.14 \pm 0.02	118 \pm 5
	2	593 \pm 15	2.5 \pm 0.2	31 \pm 1	0.46 \pm 0.04	118 \pm 5
TPD-DTP-β	-	578 \pm 7	9.1 \pm 0.4	49 \pm 1	2.6 \pm 0.1	125 \pm 10
	2	582 \pm 5	10.1 \pm 0.1	51 \pm 1	3.0 \pm 0.1	125 \pm 8

The photovoltaic results are clearly in-line with previous charge transport observations. In particular, **TPD-DTP- α** based devices strongly suffer from low J_{sc} and FFs. The low

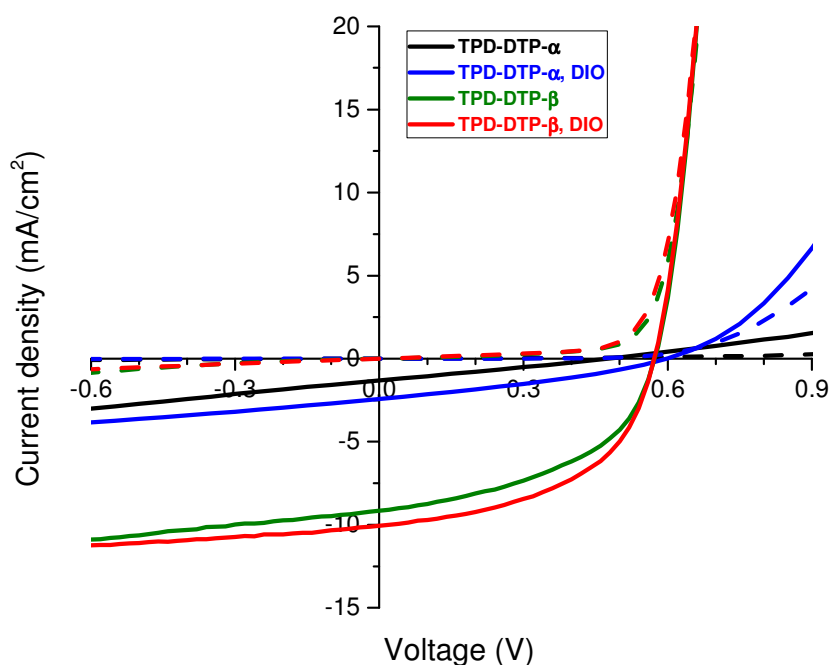


Figure 4.10: J-V characteristics of BHJ cells based on **TPD-DTP- α** and **TPD-DTP- β** / PC[71]BM in standard device architectures

photocurrent likely results from the reduced photon absorption (larger band-gap) and poorer charge extraction (as pointed out by the significant increase in photo-current under reverse bias). As the charge carriers are less mobile they could in turn strongly recombine in the active layer and thus limit the FFs of the final cells [98]. The PCEs of **TPD-DTP- β** /PC[71]BM based photovoltaic devices were also limited by FFs that are hardly higher than 50%. It seems that the out-of-plane hole mobility of $\approx 10^{-4}$ cm²/Vs measured for this polymer was still not enough to achieve high FFs even in relatively thin active layer devices. On the other hand, V_{oc} of the PV cells clearly followed the trend obtained from electrochemical measurements and DFT calculations. Indeed, V_{oc} is believed to be mainly driven by the effective band-gap. As the HOMO energy level of **TPD-DTP- α** was found to be slightly deeper than that of **TPD-DTP- β** , optimized **TPD-DTP- α** based devices resulted in higher V_{oc} values compared to the **TPD-DTP- β** one. The presence of a processing additive (1,8-diiodooctane or DIO) had significant effect for both copolymer-based devices. We attribute these improvements to the possible well-intermixed polymer and PC[71]BM phases in the active layer, as has been reported for other fullerene-based systems [153-155].

4.6 Conclusion

To sum up, within the present chapter, two different low band-gap copolymers of the same family based on a thieno-pyrroledione (TPD) acceptor unit were studied. The impact of the alkyl side chain position on the opto-electronic properties of the copolymers has been investigated. Charge transport studies on **TPD-DTP- β** revealed an unusual behavior with the hole field-effect mobility being only weakly dependent on applied gate voltage (charge carrier concentration). In contrast to **TPD-DTP- β** copolymer, the hole mobility of **TPD-DTP- α** in the identical OFET structures showed a rather strong gate voltage dependence. In addition, both in-plane and out-of-plane hole mobilities of **TPD-DTP- α** were considerably lower than for **TPD-DTP- β** . Surprisingly, though the structural disorder, measured by GIWAXS, for both materials were similar (poorly ordered) the degree of energy disorder is quite different. Furthermore, DFT calculations on the corresponding dimers indicated

significant differences in torsion angles of the conjugated backbone. While for **TPD-DTP- α** dimer the calculated torsion angle was around 48° (enough to impede the conjugation) the **TPD-DTP- β** dimer, with a torsion angle of about 20° , stayed rather planar. These results suggest that the torsion angles along the molecular backbone contribute significantly to the energy disorder, in agreement with previous reports. As a consequence, photovoltaic cells based on both copolymers performed very differently. While the maximum power conversion efficiency (PCE) for optimized **TPD-DTP- β** based devices reached 3%, the PCE for **TPD-DTP- α** barely reached 0.5%.

Chapter 5: Results:
Pyridal[2,1,3]thiadiazole based
copolymer

5 Results: Pyridal[2,1,3]thiadiazole based copolymer

5.1 Introduction

One of the efficient and strategic approaches to engineer FMO energy levels of polymers involves the alternation of electron-rich (D) and electron-poor (A) moieties along the conjugated backbone [107,156,157]. It is believed that in such D-A alternating copolymers, the HOMO level is primarily defined by the ionization potential of D-moiety while the LUMO level is mostly adjusted by the electron affinity of the A-moiety [108]. Considering this, the polymer band-gap can be controlled almost independently from the HOMO level by simply varying the strength of the A-moiety. A-unit with stronger electron affinity would deepen the LUMO level and thus lower the band-gap. For instance, benzothiadiazole (BT), one of the widely utilized A-unit, is recognized for its relatively strong electron affinity. Many of the low band-gap copolymers having BT moiety are successfully utilized in efficient organic solar cells [158,159]. Pyridal[2,1,3]thiadiazole (Py), as an alternative for BT, was recently demonstrated in different polymer systems by several research groups. It has been shown that polymers using Py-unit instead of BT performed better in photovoltaic devices [111,121,160]. In an earlier work of Prof. T. Heiser's group, Biniek et al. reported series of polymers based on BT acceptor unit [161]. The best performing low band-gap copolymer backbone was comprised of BT acceptor surrounded by four alkylated thiophenes (T, two from each side) and a thienothiophene unit (TT) (PPBzT², inset of Fig. 5.1).

Based on that work, this chapter mainly focuses on deep opto-electronic investigations of a new low band-gap copolymer including Py instead of BT unit. The molecular structure of this new copolymer marked as **PPPyT²** is shown in Fig. 5.1. All the observations and results obtained on this material during my PhD have been published in the Organic Electronics journal from Elsevier. Accordingly, this chapter is organized in a following way. Section 5.2 presents the summary of the article, highlighting the most important results. The article

and supporting information are fully displayed in sections 5.3 and 5.4, respectively. The summary of the chapter with concluding remarks is presented in Section 5.5.

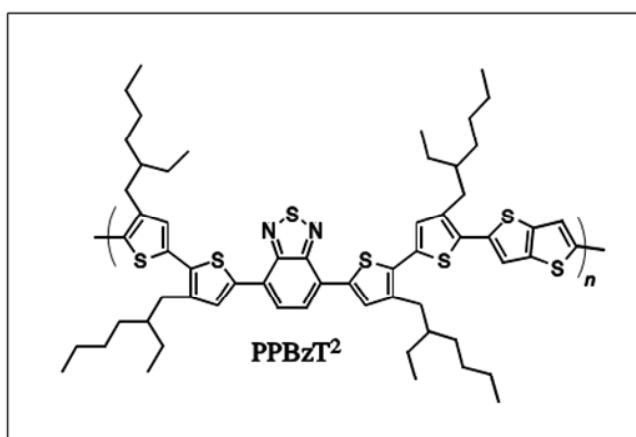
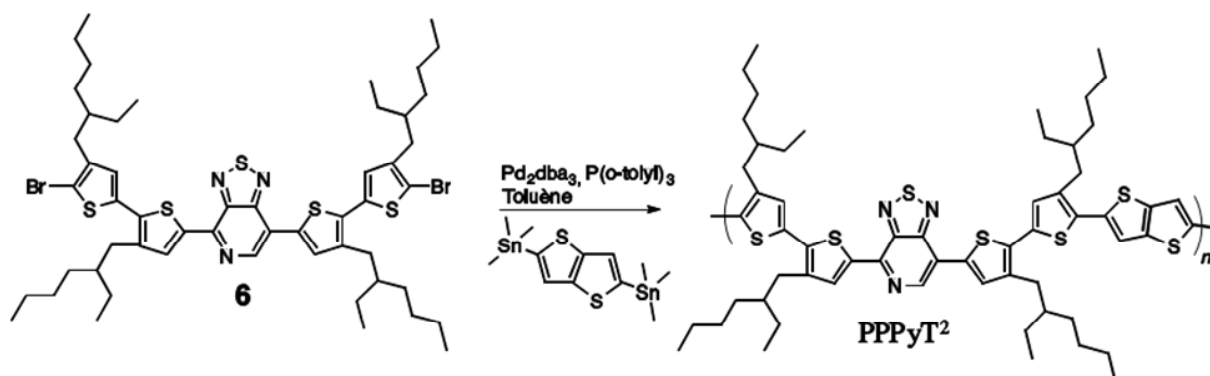


Table 5.1: Synthesis and chemical structure of **PPPyT²**. The inset shows the structure of **PPBzT²**

5.2 Summary of the article: “Using pyridal[2,1,3]thiadiazole as an acceptor unit in a low band-gap copolymer for photovoltaic applications”

The results of this extensive study on charge transport, morphology and photovoltaic devices were published in Organic Electronics journal from Elsevier. All the optimized thin polymer and polymer/fullerene blend films were spin-coated from 1,2-dichlorobenzene and chloroform solvent mixture with the volume ratio of 1:1. As **PPPyT²** polymer tend to form aggregates in solutions, the solution and the substrates were heated up to 80-90°C shortly prior to spin-coating. The thin-film device elaboration was done according to the procedures described in Materials and Experimental details chapter.

Initial DFT calculations to assess the FMO energy levels showed the interest of replacing the BT by Py unit. Though DFT calculations do not allow a precise estimation of the energy level values, it can provide deeper insights to the variations caused by the given structural changes. Calculated HOMO and LUMO energy levels for single units and building blocks are shown in Table 2 of the displayed article in Section 5.3. Due to the large LUMO energy offsets (> 2 eV) followed by weak orbital hybridization between BT/Py and surrounding T-units, the LUMOs of the trimers (T-BT-T and T-Py-T) will lie close to the LUMOs of both acceptor units. However, relatively small HOMO energy offsets between BT/Py and T units offer a more pronounced hybridization with the trimer HOMO's lying above the T HOMO level. Therefore, to a certain extent, HOMO can be spread over both donor and acceptor moieties, while the LUMO is predominantly localized on acceptor units (see Fig. S1 in supporting information, Section 5.4). In this sense, DFT evaluations confirm the interest for BT to Py replacement as this should lower both the band-gap and the HOMO energy level of the resulting copolymer.

Electrochemical and optical measurements confirm the trend going from BT to Py given by initial DFT calculations. The HOMO energy level of **PPPyT²** estimated from cyclic voltammetry experiments was slightly deeper than of **PPBzT²** (-5.1 eV vs -5.05 eV). Though

the value of 0.05 eV lies within the uncertainty range of CV measurements, the general trend is rather obvious. Figure 2a in the article clearly shows the significant reduction of the band-gap by almost 0.14 eV in solution switching from BT to Py. Moreover, for **PPPyT²** more than 100 nm red shift is recorded going from solution to thin films leading to an optical band-gap (E_g^{opt}) of ≈ 1.5 eV. Putting these experimental data (E_g^{opt} and E_{HOMO}) as initial input parameters into the empirical model developed by Scharber et al. [22] one can estimate the potential of this polymer in solar cells. According to this model, when **PPPyT²** polymer is blended with PC[60]BM, the theoretically achievable PCE gives the value of > 10%.

Apart from the energy level engineering, charge transport and morphology control remain as other important key challenges towards high efficiency organic solar cells. To better understand the charge transport anisotropy and the energy disorder present in the **PPPyT²** and **PPPyT²/fullerene** blends, charge carrier behaviors in horizontal and vertical directions were evaluated. In-plane charge transport was studied using BC-BG field-effect transistors. According to the Vissenberg model [43], developed to describe the charge transport in disordered organic semiconductors, the power law exponent should increase with the width of the DOS. Thus in the present case, the slopes of the curves in Fig. 3 of the attached article (solid lines) can be directly related to the degree of energy disorder. Field-effect hole mobilities ($\mu_{h,FET}$) in pristine **PPPyT²** films reached the value 0.3×10^{-2} cm²/Vs in the linear regime. Though the $\mu_{h,FET}$ decreased after adding PC[71]BM, the degree of energy disorder was not altered. This surprising result can be clearly seen from the slopes of the curves (Fig. 3) that are similar for pure polymer and blend films. On the other hand, annealing resulted both in improved hole mobility and reduced energetic disorder as would be expected [162,163]. Out-of-plane hole mobilities ($\mu_{h,SCLC}$) for both pure **PPPyT²** and **PPPyT²:PC[71]BM** films were estimated from current-voltage characteristics of single-carrier SCLC diodes. Interestingly, $\mu_{h,SCLC}$ increased by almost factor of 4 (from 2×10^{-5} to 8×10^{-5} cm²/Vs) after introducing PC[71]BM into the pure polymer film. This finding suggests that the presence of PC[71]BM slightly reduces the charge transport anisotropy leading to higher vertical and lower horizontal mobility. To clarify these charge transport observations microstructure analyses have been carried out by Dr. Benoit Heinrich from

the Institut de Physique et Chimie des Matériaux de Strasbourg (IPCMS). Pure **PPPyT²** film showed in-plane π - π^* stacking with an ordered lamellar packing. The latter was even enhanced after thermal annealing treatment that is evidenced from the narrowing of diffraction peaks in 001 direction (Fig. 4a and b, Section 5.3). Furthermore, GIWAXS patterns in Fig. 4c and d in Section 5.3 demonstrate that the addition of PC[71]BM did not significantly affect the **PPPyT²** self-organization in the film. This observation is in line with the charge transport results where the energy disorder in polymer domains was not considerably disturbed. However, it does not clarify the question of reduced hopping anisotropy in **PPPyT²:PC[71]BM** blends. We therefore attribute the origin of the four time increase in $\mu_{h,SCLC}$ after blending to the amorphous polymer domains. The signature of these amorphous fractions can be seen from the absorption spectrum of **PPPyT²:PC[71]BM** blend thin film (Fig. 2b, Section 5.3). The arrow in the Fig. 2b indicates the shoulder at around 580 nm that corresponds to the maximum of charge transfer peak in pure polymer solution.

Optimized bulk heterojunction devices showed a maximum PCE of 4.5%. It is clear that this value lies far below the theoretically estimated PCE according to Scharber's model [22]. According to this study, non-favorable polymer morphology is likely to be responsible for the limited PCEs. Indeed, dominantly "edge-on" orientation of polymer lamellas impedes the charge transport in the vertical direction. This in turn could strongly confine the fill factors of the solar cells that hardly reached the value of 50%.

5.3 Article: "Using pyridal[2,1,3]thiadiazole as an acceptor unit in a low band-gap copolymer for photovoltaic applications"



Contents lists available at ScienceDirect

Organic Electronics

journal homepage: www.elsevier.com/locate/orgel

Using pyridal[2,1,3]thiadiazole as an acceptor unit in a low band-gap copolymer for photovoltaic applications



Olzhas A. Ibraikulov^{a,b}, Rony Bechara^a, Patricia Chavez^c, Ibrahim Bulut^c, Dias Tastanbekov^b, Nicolas Leclerc^c, Anne Hebraud^c, Benoît Heinrich^d, Solenn Berson^e, Noëlla Lemaitre^e, Christos L. Chochos^{f,g}, Patrick Lévêque^a, Thomas Heiser^{a,*}

^a Laboratoire ICube, Département ESSP, Université de Strasbourg, CNRS, 23 rue du Loess, Strasbourg 67037, France

^b Nazarbayev University Research and Innovation System, Nazarbayev University, 53 Kabanbay Batyr Ave., Astana 010000, Kazakhstan

^c Institut de Chimie et Procédés pour l'Énergie, l'Environnement et la Santé, Université de Strasbourg, CNRS, 25 rue Becquerel, 67087 Strasbourg, France

^d Institut de Physique et Chimie des Matériaux de Strasbourg, Université de Strasbourg, CNRS, 23 rue du Loess, Strasbourg 67034, France

^e LMPO, CEA Grenoble, INES, 50 avenue du Lac Léman, 73375 Le Bourget du Lac, France

^f Department of Materials Science and Engineering, University of Ioannina, Ioannina 45110, Greece

^g Advent Technologies SA, Patras Science Park, Stadiou Street, Platani-Rio, 26504 Patra, Greece

ARTICLE INFO

Article history:

Received 20 February 2015

Received in revised form 17 April 2015

Accepted 18 April 2015

Available online 21 April 2015

Keywords:

Polymer solar cells

Energy disorder

Charge transport

Field-effect mobility

Space-charge-limited current

Morphology

ABSTRACT

In this report, we explore the optoelectronic properties of a low band-gap copolymer based on the alternation of electron rich (thiophene and thienothiophene units) and electron deficient units (pyridal[2,1,3]thiadiazole (Py)). Initial density functional theory calculations point out the interest of using the Py unit to optimize the polymer frontier orbital energy levels. A high molecular weight ($M_n = 49$ kg/mol) solution-processable copolymer, based on Py, thiophene and thienothiophene units, has been synthesized successfully. From cyclic-voltammetry and UV-visible absorption measurements a relatively deep HOMO level (-5.1 eV) and an optical band-gap (1.48 eV) have been estimated. Charge transport both in horizontal and vertical directions were extracted from field-effect transistors and space charge limited current diodes, respectively, and led to a relatively high in-plane hole mobility in pure polymer films ($0.7 \times 10^{-2} \text{ cm}^2 \text{ V}^{-1} \text{ s}^{-1}$). GIWAXS results showed almost identical in-plane lamellar morphologies, with similar average size and orientation of the polymer crystalline domains in both, pure polymer films and polymer:fullerene blends. Also, the gate-voltage dependence of the field-effect mobility revealed that the energy disorder in the polymer domains was not altered by the introduction of fullerenes. The nevertheless significantly higher out-of-plane hole mobility in blends, in comparison to pure polymer films, was attributed to the minor amorphous polymer phase, presumably localized close to the donor/acceptor interface, whose signature was observed by UV-vis absorption. Promising photovoltaic performances could be achieved in a standard device configuration. The corresponding power conversion efficiency of 4.5% is above the value achieved previously with a comparable polymer using benzo [2,1,3]thiadiazole instead of Py as acceptor unit.

© 2015 Elsevier B.V. All rights reserved.

1. Introduction

Polymer solar cells are considered as a promising low-cost technology for renewable production of electricity from solar light. Significant progress in their power conversion efficiency (PCE) has been achieved over the last decade [1–5]. The continuously growing knowledge of the material parameters, which are critical for the device performances, as well as the collective experimental

data achieved by methodical investigations of numerous molecular systems, have been essential to this positive development. It is in particular recognized today that polymers used as electron-donor material in a donor/acceptor bulk heterojunction (BHJ) device should match the following requirements: an energy offset of about 0.3 eV between the polymer lowest unoccupied molecular orbital (LUMO) level and the electron-acceptor LUMO level, to allow efficient charge transfer at the donor/acceptor interface [6]; an energy band-gap lying within the optimum window defined by Queisser et al. for single absorber photovoltaic devices (i.e., between 1.1 and 1.5 eV) [7]; and a high ionization potential (below 5 eV versus vacuum) so as to maximize the device open-circuit

* Corresponding author.

E-mail address: thomas.heiser@unistra.fr (T. Heiser).

voltage (V_{oc}) and to enhance the polymer stability in ambient conditions. In addition to these desired electronic properties, the polymer, when blended with the acceptor component, must adopt a morphology that allows efficient charge generation and transport towards the collecting electrodes. The latter features depend on the polymer molecular structure in a non-trivial way and are more difficult to foresee [8–10].

A well-known approach to engineer the polymer energy levels consists in designing a conjugated backbone that comprises alternating electron rich (D) and electron deficient units (A) [11–13]. In such D–A co-polymers, the HOMO level is mostly controlled by the D ionization potential, while the LUMO level is mainly fixed by the A unit electron affinity [13]. Accordingly, the polymer band-gap can be fine-tuned almost independently from the HOMO level by varying the acceptor unit. Benzothiadiazole (Bz) for instance is a very common A unit, known for its strong electron affinity. It has been frequently associated to various D moieties to synthesize low band-gap polymers [14–17]. Replacing Bz with fluorinated benzothiadiazole (higher electron affinity) allowed Zhou et al. to reduce the band-gap of PBnDT–DTBT even further by 0.1 eV [17]. Another recent example reported by Leclerc et al. [18], You et al. [19] and Bazan et al. [20–23] is Pyridal [2,1,3]thiadiazole (Py). It has been used as high electron affinity acceptor group in replacement of Bz in low band-gap polymers and small molecules and led to improved photovoltaic performances.

Our group has recently reported the synthesis, materials and device properties of low band-gap donor–acceptor copolymers based on Bz acceptor units and thiophene (T) and thienothiophene (TT) donor units. The optical band-gap and HOMO level of the best performing polymer (labeled **PPBzT²** in Ref. [16], and shown in the insert of Fig. 1) were 1.6 eV and -5.05 eV, respectively [16]. According to the design rules mentioned above, a gain in performance can be expected for this material family if the band-gap is further reduced without diminishing its ionization potential. We therefore initiated the development of a new polymer whose molecular structure is similar to **PPBzT²**, except that Bz is being replaced by a Py electron-acceptor unit. Although such a change

along the molecular backbone may at first glance appear as a minor modification, it is likely that the frontier orbital energy levels are not the only important material property that is impacted by this alteration. It is therefore desirable to analyze in-depth all the material parameters that are crucial to the photovoltaic device performances.

In this report, we present an extensive investigation of the optoelectronic material and device properties of the new D–A copolymer based on a Py acceptor unit and T as well as TT donor units. The molecular structure of this polymer, labeled **PPPyT²**, is given in Fig. 1. Density functional theory (DFT) calculations are presented in order to anticipate the potential impact of Py on the polymer frontier orbitals. The electrochemical and optical properties of the newly synthesized **PPPyT²** copolymer, in solution and in thin films, are described. Charge carrier mobilities in pristine **PPPyT²** films and in **PPPyT²:PCBM** blends, were investigated as active layers in either field-effect transistors or space-charge limited current devices. The obtained results of the charge carrier mobilities are correlated with the structural conformation of the polymer chains acquired by utilizing in-situ grazing incidents wide-angle X-ray (GIWAXS) diffraction data. Finally, the performances of bulk heterojunction devices based on **PPPyT²:PCBM** blends are discussed. It is shown that using Py as an electron deficient building block reduces the band-gap by more than 0.1 eV. The resulting improved photon harvesting of **PPPyT²** in comparison to **PPBzT²** contributes to the higher power conversion efficiency of **PPPyT²**-based bulk heterojunctions.

2. Experimental details

2.1. Material investigations

2.1.1. Molecular properties

Size exclusion chromatography (SEC) measurements were performed with a Waters Alliance GPCV 2000 instrument (Milford/MA) that incorporates a differential refractive index and a

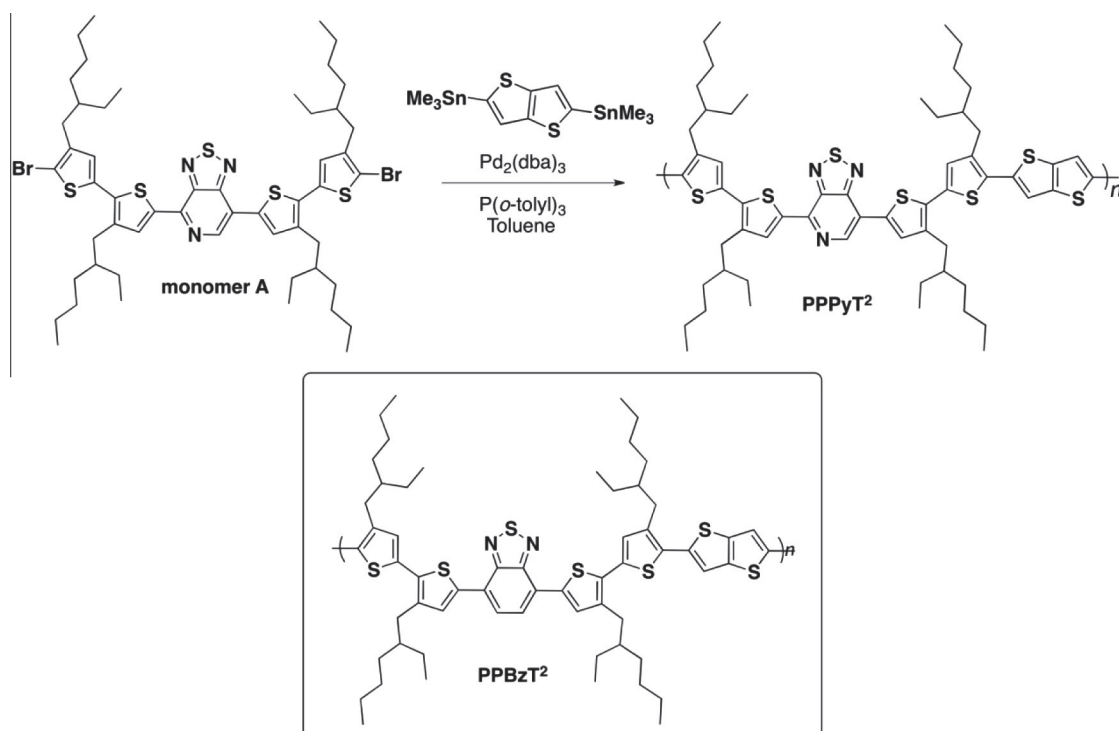


Fig. 1. Synthesis and chemical structure of **PPPyT²**. The insert shows the structure of **PPBzT²**.

viscosimeter. 1,2,4 trichlorobenzene (TCB) was used as the mobile phase at a flow rate of 1 mL/min at 150 °C. It was stabilized with 2,6-di(tert-butyl)-4-methylphenol. All polymers were injected at a concentration of 1 mg/mL. The separation was carried out on three Agilent columns (PL gel Olexis 7 × 300 mm) and a guard column (PL gel 5 μm). Columns and detectors were maintained at 150 °C. The Empower software was used for data acquisition and data analysis. The molecular weight distributions were calculated with a calibration curve based on narrow polystyrene standards (from Polymer Standard Service, Mainz), using only the refractometer detector. ¹H and ¹³C NMR spectra were recorded on a Bruker 300 Ultrashield™ 300 MHz NMR spectrometer and a Bruker 400 Ultrashield™ 400 MHz NMR spectrometer, with an internal lock on the 2H-signal of the solvent (CDCl₃).

2.1.2. Computational study

Density functional theory (DFT) was used at the B3LYP/6-311+G* level of theory in vacuum (using Spartan 10) to anticipate the impact of Py on the material optoelectronic properties [24]. To estimate the HOMO and LUMO energy level positions and spatial distributions of the polymer **PPPyT²**, we considered two monomers with methyl groups replacing the side-chains to keep the computational time within a reasonable range. CH₃ were placed at both ends of the backbone and the dihedral angle between the last carbon atom and the methyl group was kept fixed to mimic the polymer rigidity.

2.1.3. Electrochemical and optical properties

Cyclic voltammetry analyzes were carried out with a BioLogic VSP potentiostat using platinum electrodes at scan rates of 20 mV/s. The measurements were performed on thin films drop-casted from chloroform solutions onto a platinum working electrode. A Pt wire was used as counter electrode and Ag/Ag⁺ as reference electrode in acetonitrile containing 0.1 mol/L of tetrabutylammonium tetrafluoroborate. Ferrocene was used as internal standard to convert the values obtained in reference to Ag/Ag⁺ to the saturated calomel electrode scale (SCE). An ionization potential value of −4.4 eV for the F_c/F_c⁺ redox system has been used.

For optical measurements in solution, **PPPyT²** was dissolved in *o*-DCB at a sufficiently low concentration (0.025–0.03 mg/ml) to maintain transparency. Optical properties in solid state were studied on as-deposited thin films obtained by spin-coating **PPPyT²** *o*-DCB solutions (4–5 mg/ml) at 1500 rpm during 180 s under ambient conditions on glass substrates. Absorption measurements for both in solution and in solid state were performed on Shimadzu UV-2101PC scanning spectrophotometer.

2.1.4. Charge transport

As charge transport is often anisotropic in conjugated polymers, two different methods were used to estimate the charge carrier mobility: field-effect transistor (FET) measurements and space-charge limited single carrier (SCLC) device characterizations for in-plane and out-of-plane transport studies, respectively. Note that the large variations in charge carrier density in these measurements need to be taken into account when comparing both results (see below) [25].

Bottom contact field-effect transistors (FET) were elaborated using commercially available FET test structures on silicon with lithographically defined Au (30 nm)/ITO (10 nm) bilayers as source and drain electrodes and 230 nm thick SiO₂ as gate insulator. The channel length and width were $L = 20 \mu\text{m}$ and $W = 10 \mu\text{m}$, respectively. The substrates were cleaned in successive ultrasonic baths at 45 °C for 15 min using soapsuds, acetone and isopropanol and followed by a 15 min cleaning step in a UV-ozone chamber. Hexamethyldisilazane (HMDS) was then spin-coated on top of the silicon dioxide, followed by an annealing step at 135 °C for

10 min. At last, pre-heated 3 mg/ml solutions of either **PPPyT²** or **PPPyT²:PC₇₁BM** blends (1:1 weight ratio) in an *o*-DCB/CHCl₃ (50/50 by volume) solvent mixture were spin-coated to complete the FET devices. OFET devices were characterized before and after thermal annealing at 150 °C for 15 min. The transistor output and transfer characteristics were measured using a Keithley 4200 semiconductor characterization system. The hole mobility was then extracted in the linear regime as a function of gate voltage using a standard device model [26].

For the hole injecting SCLC devices, we used ITO coated glass as a substrate, onto which a thin poly(ethylenedioxythiophene):polystyrene sulfonate (PEDOT:PSS) layer was spin-coated and used as bottom electrode. Pre-heated **PPPyT²** *o*-DCB/CHCl₃ (50:50 vol. ratio) solutions were deposited by spin-coating. Different layer thicknesses were obtained by varying the polymer concentration in solution. Thermal annealing (150 °C, 15 min) was performed prior to top electrode deposition. The devices were completed by a thermally evaporated 50 nm thick gold layer. SCLC diode (surface area: 0.01 cm²) transfer characteristics were measured using a Keithley 4200 semiconductor characterization system. All devices exhibited symmetrical current–voltage curves.

2.1.5. Morphology

X-ray diffraction measurements were performed on **PPPyT²** and **PPPyT²:PC₇₁BM** thin films that were deposited on PEDOT:PSS pre-coated Si substrates. The thin films were obtained by spin-coating a 5 mg/ml solution with respect to the polymer concentration in an *o*-DCB/CHCl₃ mixture with 1:1 volume ratio. As a reference sample a PEDOT:PSS coated Si substrate was used. Grazing incidence wide angle X-ray scattering (GIWAXS) measurements were carried out at PLS-II 9A U-SAXS beamline of Pohang Accelerator Laboratory (PAL) in Korea. The X-rays coming from the vacuum undulator (IVU) were monochromated using Si(111) double crystals and focused on the detector using K–B type mirrors. Patterns were recorded using a 2D CCD detector (Rayonix SX165). The sample-to-detector distances were about 221 and 225 mm for energies of 11.105 and 11.06 keV (1.1165 and 1.121 Å).

Tapping-mode atomic force microscope (AFM) measurements were performed on a Nanoscope IIIa system commercialized by Veeco®. **PPPyT²:PC₇₁BM** thin films were spin-coated from *o*-DCB/CHCl₃ solvent mixture with 1:1 volume ratio onto PEDOT:PSS coated ITO/Glass substrates. The active layer surface morphologies were investigated before and after annealing.

2.2. Bulk heterojunction devices

Bulk heterojunction solar cells were elaborated using blends of **PPPyT²** as electron donor and **PC₇₁BM** as an electron acceptor. The blends were processed in a 1,2-Dichlorobenzene (*o*-DCB) and chloroform mixture with solvent volume ratios varying between 1:1 and 3:2. The polymer concentration was kept at 5 mg/ml to avoid aggregation. Different polymer:fullerene weight ratios were explored. Solutions were left and stirred at room temperature (500 rpm) for two days in nitrogen ambient and heated up to 120 °C for 10 min before coating. All solutions were spin-coated on cleaned ITO/glass substrates with a pre-coated PEDOT:PSS layer (1500 rpm; 40 nm). Different top electrodes consisting of either Al (120 nm), Ca/Al (20 nm/120 nm) bilayers or TiO_x/Al (10 nm/200 nm) were used to complete the devices. The metallic layers were deposited by thermal evaporation under a 4×10^{-7} mbar vacuum. The TiO_x nanoparticles layer was spin-coated from acetone solution prior to evaporation of Al. Four diodes, with a 12 mm² active surface area, were elaborated on each substrate, while two substrates (8 diodes) were elaborated with identical conditions. Device characterizations were done in nitrogen

atmosphere under dark and simulated AM1.5G irradiation (100 mW/cm², Lot Oriel Sun 3000 solar simulator).

3. Results and discussion

3.1. Polymer synthesis

The synthesis route and chemical structure of the **PPPyT**² copolymer are shown in Fig. 1, along with the structure of **PPBzT**² copolymer (figure inset) for comparison. More details on the experimental conditions for the monomer and polymer synthesis are given in the Electronic Supporting Information (ESI). Two successive Stille cross-coupling steps have been carried out to obtain the Py-based pentamer (compound **6** in ESI). The first step involves a Stille coupling between the 2-(trimethylstannyl)-4-(2-ethylhexyl)thiophene and the 4,7-dibromo-[1,2,5]thiadiazolo [3,4-*c*]pyridine unit followed by a dibromination reaction using *N*-bromosuccinimide (NBS) agent. The second step consists in the extension of the conjugation by a Stille coupling between this dibromo-derivative (compound **4** in ESI) and the 2-(trimethylstannyl)-4-(2-ethylhexyl)thiophene. A further dibromination step using again NBS in a mixture of CHCl₃ and DMF allows the synthesis of compound **6**. **PPPyT**² was synthesized by a Stille coupling reaction between **6** and the 2–5-bis-trimethylstannyl-thieno[3,2-*b*] thiophene unit, using Pd₂dba₃/P(*o*-tolyl)₃ as catalyst and toluene as solvent. A Soxhlet extraction in chlorobenzene leads to a fraction of soluble polymers. The molecular weight of this polymer fraction was estimated by gel permeation chromatography in hot trichlorobenzene, using polystyrene as reference polymer. The molecular weight and polydispersity index are given in Table 1.

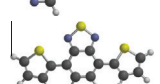
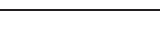
3.2. Material properties

3.2.1. DFT calculations

We used DFT to evaluate the influence of replacing the benzene ring in Bz by the pyridine ring in Py on the frontier orbital energy levels. The HOMO/LUMO levels were calculated for the major copolymer building blocks and are given in Table 2. DFT calculations do not allow a precise assessment of the absolute energy values of electronic states but they permit to anticipate relative variations induced by structural modifications. In the present case, the DFT results clarify the impact of Py on the polymer electronic energy levels. Indeed, from the large energy offset (above 2 eV) between the LUMO levels of T with Bz and Py, respectively, found by DFT, we may conclude that the hybridization of both orbitals remains weak and that the trimer LUMO level will follow closely the electron-acceptor moiety LUMO. The same trend is observed after adding two T and one TT units to the trimer. As a consequence, **PPPyT**² is expected to have a LUMO level deeper than **PPBzT**². On the other hand, the smaller HOMO energy offset between T and the acceptor units (0.3 and 0.8 eV for Bz and Py, respectively) suggests a more pronounced hybridization, with the trimer HOMO level lying above the T HOMO level. Correspondingly, the HOMO delocalizes to some extent over both the donor and acceptor units, while the LUMO spatial distribution remains localized on the acceptor unit (see ESI, Fig. S1). As the HOMO hybridization is less pronounced for Py (due to the larger

Table 2

Calculated HOMO and LUMO energy levels for separate building blocks using DFT.

Building block/trimer	HOMO (eV)	LUMO (eV)	
	T	-6.3	-0.2
	Bz	-6.6	-2.3
	Py	-7.1	-2.8
	T-Bz-T	-5.3	-2.6
	T-Py-T	-5.5	-2.9
	PPBzT ²	-4.7	-2.7
	PPPyT ²	-4.7	-2.9

energy offset), a slightly deeper HOMO level is expected for the Py-based molecules. Adding the TT unit enhances the electron delocalization and raises the HOMO level further upwards. Finally, the DFT calculations show that replacing Bz with Py should lower the band-gap and deepen the HOMO level, as previously reported on other systems [20,21]. Both expected trends are of interest for photovoltaic devices.

3.2.2. Electrochemical and optical properties

Cyclic voltammetry was used to estimate the oxidation potential of **PPPyT**² in thin films. The poor solubility of this copolymer in dichloromethane inhibited the experiment to be performed in solution. Therefore, the measurement has been performed in solid state. The reduction and oxidation waves are both quasi-reversible (see ESI, Fig. S2). The HOMO and LUMO energy levels were calculated from the oxidation and reduction onset potentials relative to ferrocene as the internal standard. The results led to a **PPPyT**² HOMO level of -5.1 eV, which is about 0.05 eV deeper than the **PPBzT**² HOMO level reported in [16]. It should be noted however that the observed variation in HOMO level is in the same range as the uncertainty associated with cyclic voltammetry.

The UV–Vis spectrum of **PPPyT**² in *o*-DCB is shown in Fig. 2 and compared to the results obtained previously on **PPBzT**² [16]. For both polymers, two absorption bands can be clearly distinguished. Such a configuration is frequently observed in donor–acceptor low band-gap polymers [27]. The higher energy band (400 nm) is generally attributed to a π - π^* (HOMO \rightarrow LUMO+1) transition on the donor segment while the lower energy band (580 nm) is related to a charge transfer transition (i.e., HOMO localized on the donor \rightarrow LUMO localized on the acceptor unit). Our results confirm this interpretation. Indeed, switching from Bz to Py affects significantly the low energy band transition [20,21], as would be expected from a D/A charge transfer transition, while the higher energy band remains almost unchanged, confirming that the latter transition is set by the donor unit. The 30 nm shift in the charge

Table 1
Molecular weights, polydispersity indexes and major optoelectronic properties of **PPPyT**².

	M_n (g/mol)	PDI	E_g^{opt} (eV) (thin film)	HOMO (eV)	Field-effect mobility (cm ² /V s)		SCLC hole mobility (cm ² /V s)
					Holes	Electrons	
PPPyT ²	49,000	4.1	1.48	-5.1	7×10^{-3} ($\pm 7 \times 10^{-4}$)	-	2.2×10^{-5} ($\pm 5 \times 10^{-6}$)
PPPyT ² /PC ₇₁ BM (ratio 1:1)	-	-	-	-	1.4×10^{-3} ($\pm 2 \times 10^{-4}$)	1×10^{-3} ($\pm 1 \times 10^{-3}$)	8×10^{-5} ($\pm 6 \times 10^{-6}$)

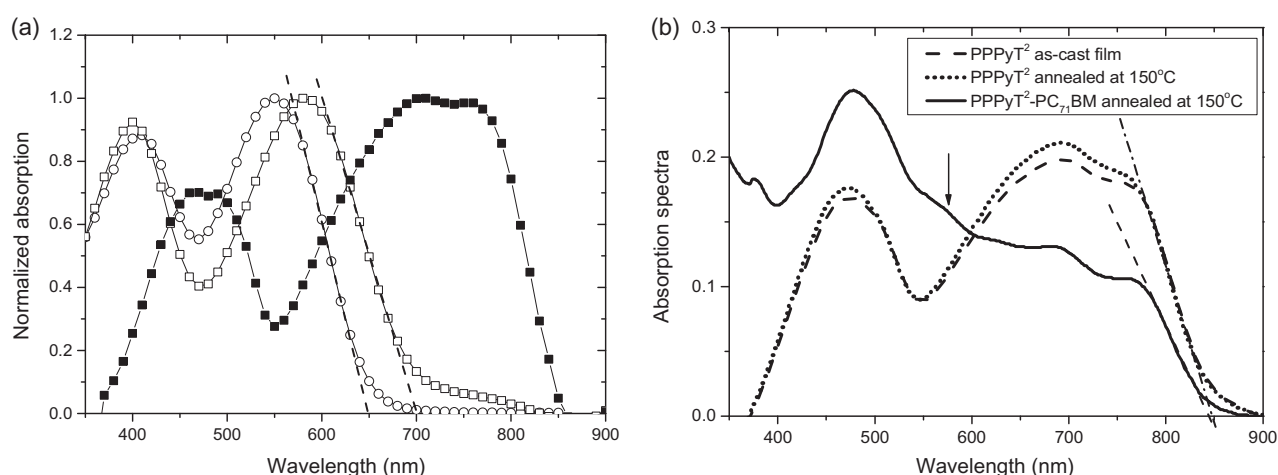


Fig. 2. (a) Normalized absorption spectra for **PPBzT²** (open circles) and **PPPyT²** (open squares) in solution. **PPBzT²** was dissolved in *o*-DCB while **PPPyT²** was dissolved in CHCl_3 . The thin film absorption spectrum of **PPPyT²** is represented by closed symbols; (b) Absorption spectra of pure **PPPyT²** (as-cast and annealed at 150 °C for 15 min) and **PPPyT²**-**PC₇₁BM** (ratio 1:1) film annealed at 150 °C for 15 min. The arrow indicates the position of the **PPPyT²** absorption maximum in solution (580 nm). Dashed lines are extrapolation of each curves used to estimate band gaps.

transfer peak position corresponds to a 0.12 eV drop in HOMO/LUMO gap, following the trend from DFT [20,21].

The optical band-gap of **PPPyT²** in solution is 0.14 eV lower than the **PPBzT²** band-gap. For **PPPyT²** a significant bathochromic shift is observed when passing from solution to thin films, leading to a E_g^{opt} of 1.48 eV that lies within Queisser's optimum window (Fig. 2a). Also noteworthy are the enhanced broadness of the charge transfer band and the clear appearance of a second peak at the lower energy edge as well as a shoulder at the high energy edge. These spectral features could possibly be due to vibronic transitions, similar to those observed for other conjugated polymers [28]. The small shoulder appearing in the solution spectrum at around 750 nm may be due to the presence of some residual polymer aggregates. Additional optical measurements performed on annealed pure polymer films and on **PPPyT²**:**PC₇₁BM** films are shown in Fig. 2b. For the pure polymer, the spectral features (band gap, shapes of the spectra) did not change with annealing. However, a small increase in the absorption rate is observed which suggests a more pronounced in-plane orientation of the polymer chains [29–31]. The observation of the vibronic features in the blend film indicates that self-organization in **PPPyT²** is still feasible in the presence of 50 wt% of **PC₇₁BM** (see below) [30,31]. Importantly, the small peak occurring at 580 nm, close to the charge-transfer peak observed in solution, points out the presence of a small fraction of amorphous polymers in the blend (see below).

Using the experimental E_g^{opt} and HOMO levels as input parameters of the empirical model developed by Scharber et al. [1] we estimate the potentially achievable power conversion efficiency of **PPPyT²**:**PC₆₁BM** blends to roughly 11%. It should even be higher when using **PC₇₁BM**, due to improved photon harvesting of this acceptor molecule (in comparison to **PC₆₁BM**).

3.2.3. Charge transport

We have investigated the charge transport in as-deposited and annealed (150 °C, 15 min) **PPPyT²** films using both field-effect-mobility (FET) measurements and space charge limited current devices. As mentioned previously, this combination allows us to get a better insight into the charge transport anisotropy and on the degree of energy disorder. In-plane charge transport can be studied by monitoring the current–voltage characteristics of field-effect transistors at room temperature. The hole mobilities $\mu_{\text{h,FET}}$, extracted from the slope of the current–voltage transfer

curve in the linear regime for both pristine **PPPyT²** films and for **PPPyT²**-**PC₇₁BM** blends, are shown in Fig. 3 as a function of $V_g - V_{\text{th}}$, where V_{th} is a threshold voltage.

For both, as-deposited and annealed films, $\mu_{\text{h,FET}}$ increases with V_g , reaching $0.3 \times 10^{-2} \text{ cm}^2 \text{ V}^{-1} \text{ s}^{-1}$ in the pure polymer film at $V_g - V_{\text{th}} = -60 \text{ V}$ (the transistor output, transfer characteristics and equations used to estimate $\mu_{\text{h,FET}}$ are given in the ESI). Moreover, for $V_g - V_{\text{th}} \gtrsim 20 \text{ V}$, $\mu_{\text{h,FET}}$ follows approximately the power law dependence (constant slope in Fig. 3) expected for hopping transport in a disordered semiconductor [32]. A slight deviation from the power law is observed at lower gate voltages and is most pronounced for the as-cast blend film, for which the mobility is lowest. A possible origin of this effect could be space charge accumulation at low gate voltages, as reported by Weis [33]. The space charge in the channel is indeed expected to increase with decreasing mobility and to lead to an overestimated mobility value using the standard gradual channel approximation (Eq. (S1)).

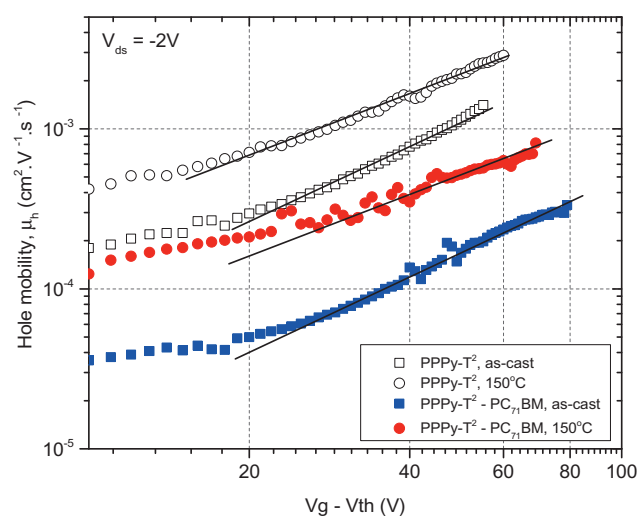


Fig. 3. Hole mobility (μ_{h}) as a function of $V_g - V_{\text{th}}$ for pure **PPPyT²** films (open symbols) and for **PPPyT²**-**PC₇₁BM** blends (closed symbols) before (squares) and after annealing (circles). V_{th} for as-cast and annealed polymer films are +4 and 0 V, for blends are +7 and +17 V, respectively. Solid lines represent slopes to each of the curves.

According to the percolation model developed by Vissenberg et al. [34] for the field-effect mobility in amorphous organic semiconductors, the power law exponent is expected to increase with the width of the density of state distribution. The slopes of the curves in Fig. 3 (solid lines) can therefore be considered as representative for the degree of energy disorder in the films. We note that for both, pure **PPPyT²** and **PPPyT²:PC₇₁BM** blend films, the slopes are reduced after annealing. This observation corroborates the expectation that the polymer ordering is enhanced during the heat treatment [35–37]. Interestingly, the slopes observed for blends are close to those seen in pristine polymer films for the same processing conditions. In other words, the domains that support hole transport seem not affected by the presence of fullerenes. The significantly lower mobility values observed in the blend in comparison to the pure polymer film must therefore be due to a reduced percolation of the hole transporting domains, rather than to increased disorder within the domains (see below).

The FET devices have also been used to investigate electron mobilities in **PPPyT²:PC₇₁BM** (1:1 wt% ratio) blends, before and after annealing. The electron mobility, $\mu_{e,FET}$, in **PPPyT²:PC₇₁BM** blends has been estimated from the transistor characteristics under a positive gate voltage. Note that the significant contact resistance impedes mobility extraction from the linear regime and leads to underestimated electron mobility values (see ESI, Fig. S8 for the current–voltage curves) [9]. We find a $\mu_{e,FET} \gtrsim 10^{-3} \text{ cm}^2 \text{ V}^{-1} \text{ s}^{-1}$, which is only one order of magnitude lower than the $\mu_{e,FET}$ in pure PC₆₁BM layers and reveals a good ambipolar charge transport in the blend. This result is in-line with our previous findings on PPBzT²:PC₆₁BM blends where it was shown that the branched side-chains allow a reasonable electron mobility to be obtained at a relatively low fullerene loading [9].

At this stage, we would like to emphasize that high field-effect mobility does not necessarily lead to better OPV device performances, as the underlying polymer assembly may enhance the charge transport anisotropy and result in a lower out-of-plane mobility [38]. It is therefore essential to study the out-of-plane hole mobility as well. This can be achieved by measuring the current–voltage characteristics of single carrier space-charge-limited current (SCLC) diodes. The SCLC results obtained on annealed **PPPyT²** devices for two different thicknesses [39,40] are shown in the ESI, Fig. S9. The resulting $\mu_{h,SCLC}$ is found to be $2.2 \times 10^{-5} \text{ cm}^2 \text{ V}^{-1} \text{ s}^{-1}$. Note that the current scales with the film thickness as predicted for SCLC in the absence of injection barriers. At higher voltages, the current increases more rapidly than predicted by Mott–Gurney's law. This effect may be caused either by a field-dependent mobility or by the charge carrier density dependence [32]. Moreover, the two orders of magnitude difference between SCLC and OFET mobility values in pristine polymer films could be due either to the large difference in charge carrier densities in both devices [33,41] or to a strong anisotropy in charge transport. The charge carrier density dependence is expected to be important in highly disordered materials, while transport anisotropy should be more pronounced in ordered structures [42]. SCLC hole mobilities were estimated in **PPPyT²:PC₇₁BM** blends as well. The $\mu_{h,SCLC}$ in the blend after annealing at 150 °C is found to be $8 \times 10^{-5} \text{ cm}^2 \text{ V}^{-1} \text{ s}^{-1}$ which is significantly higher than for the pure polymer film. This observation suggests that the additional structural disorder induced by the presence of PC₇₁BM, attenuates the hopping anisotropy, leading to a higher out-of-plane hole mobility and a lower in-plane mobility. However, as the in-plane hole mobility in polymer:fullerene blends was found to be controlled by a similar energetic disorder (and thus structural disorder) than that of pure polymer films, the nature of the additional structural disorder remains unclear at this stage and will be further addressed below.

3.2.4. Morphology

The microstructures of pure **PPPyT²** film and **PPPyT²:PC₇₁BM** blend (as-deposited and annealed) were investigated by GIWAXS. The diffraction patterns obtained on as-cast and annealed samples are shown in Fig. 4.

For pure **PPPyT²** a film microstructure consisting in flat lying lamellae of ca. 15 Å thickness, formed by layers of π -stacked polymer backbones alternating with molten aliphatic chains (h_{ch}), is observed before (Fig. 4a) and after (Fig. 4b) annealing. The lamellae are formed by the polymer conjugated backbone oriented edge-on and the π stacking direction parallel to the surface (as illustrated in Fig. 4e). The scattering h_{π} at ca. 3.8 Å, which is associated to π -stacking, is already visible as a well-defined arc located on the equator in the as-deposited film pattern. The softening of the sample during the annealing mainly improves the regularity of lamellae, as evidenced by the sharpening and the enhancement of (001) reflections. The observed lamellar morphology with in-plane π - π^* stacking clarifies the charge transport measurements described above. Indeed, the annealing-induced lowering of energy disorder and increased field-effect mobility in pristine polymer films correlate well with the enhanced structural order inferred from the narrowing diffraction peaks. Also the orientation of the π - π^* stacking axis substantiates the high $\mu_{h,FET}$ value and proves the transport to be highly anisotropic in pristine polymer films. Moreover, as evidenced from Fig. 4c and d, the GIWAXS patterns of the blend are similar to those of pure polymer films. We may therefore conclude that the average size and orientation of the polymer crystalline domains is not significantly altered by the presence of PC₇₁BM. This result is in line with our observation that the energy disorder in the polymer domains is not significantly increased upon blending with PC₇₁BM. On the other hand however, it leaves open the question about the origin of the reduced charge transport anisotropy observed in the blends. Considering the fact that the lamellar morphology impedes out-of plane transport, we believe that the four times higher hole mobility observed in the blend is due to the presence of an amorphous fraction of the polymer. The latter is presumably at the origin of the small shoulder observed at 580 nm in the thin film absorption spectrum, close to the position of the absorption maximum of **PPPyT²** in solution (Fig. 2a and b). It is likely that the amorphous polymer chains are located near the D/A interface, forming a mixed polymer/PC₇₁BM phase. A similar three phase morphology (D/mixed D:A/A) has been reported previously for other polymer:fullerene systems [43–45].

Finally, the **PPPyT²:PC₇₁BM** blend morphology was also investigated by AFM (see Fig. S10 in the ESI). This was specifically done to detect the presence of eventual larger D or A domains that may result from a poor miscibility or phase separation. The AFM results show a low film roughness (8–10 nm) and a granular morphology composed of nanometer-sized domains with negligible macro-phase separation (before and after thermal annealing).

3.3. Photovoltaic device properties

The photovoltaic properties of **PPPyT²** were investigated by using **PPPyT²:PC₇₁BM** as photoactive layer. Due to the strong polymer aggregation tendency in solution, good quality thin films could only be obtained by using solvent mixtures (*o*-DCB and CHCl₃) [46]. The best film quality was obtained for a solvent *o*-DCB:CHCl₃ volume ratio between 2:1 and 3:2. Three different polymer:PC₇₁BM weight ratios (1:0.7, 1:1 and 1:1.5) have been tested using a standard device structure (ITO/PEDOT:PSS/blend/Al). The best performances were found at a ratio of 1:1 (see ESI Table S1 for the device characteristics versus different D:A ratios), which is in accordance with the relatively high ambipolar field-effect mobilities observed for this blend composition. It also corroborates our previous finding that ethyl–hexyl side chains reduces fullerene

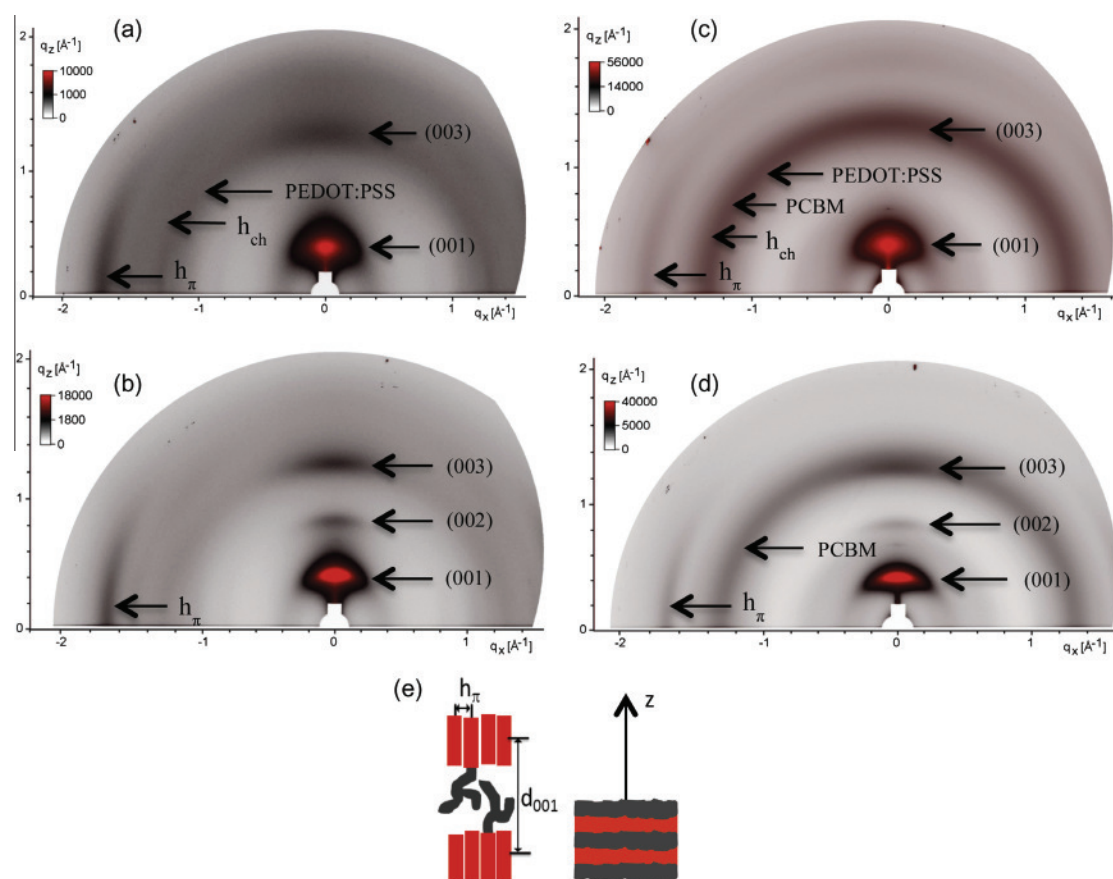


Fig. 4. GIWAXS patterns of as-cast (a) and annealed (b) **PPPyT²** as well as as-cast (c) and annealed (d) **PPPyT²:PC₇₁BM** films. A schematic view of the polymer microstructure is also represented, where red blocks correspond to polymer backbones and gray to aliphatic side chains (e). *z* is the direction perpendicular to the substrate. (For interpretation of the references to color in this figure legend, the reader is referred to the web version of this article.)

intercalation and allows percolation of electron transporting domains at relatively low fullerene contents [9].

The device optimization was further carried out by inserting an additional interfacial layer (Ca or TiO_x) between the Al and the active layer. The TiO_x layer is believed to reduce the interface recombination and to behave as an optical spacer. Table 3 summarizes the best performances of devices using either Ca/Al or TiO_x/Al bilayers as cathode. The highest efficiency of 4.5% was obtained on devices with a 10 nm thin TiO_x layer. The corresponding dark and light current–voltage curves are given in Fig. 5. The higher *J*_{sc} value observed for the **PPPyT²** devices leads to an increase in PCE in comparison to **PPBzT²** devices [16] and can be attributed at least partly to the better photon harvesting of the **PPPyT²** (Fig. 2). External quantum efficiency (EQE) measurements have also been carried out (see ESI, Fig. S11). The band gap deduced from the EQE correlates well with the optical band-gap. Moreover, the short circuit current calculated by integrating the EQE data (*J*_{sc, EQE}) matches well with the experimental *J*_{sc} (see ESI for details).

Although the higher efficiency achieved with the **PPPyT²** corroborates the positive impact of the Py unit on the photovoltaic performances, the overall power conversion efficiency remains

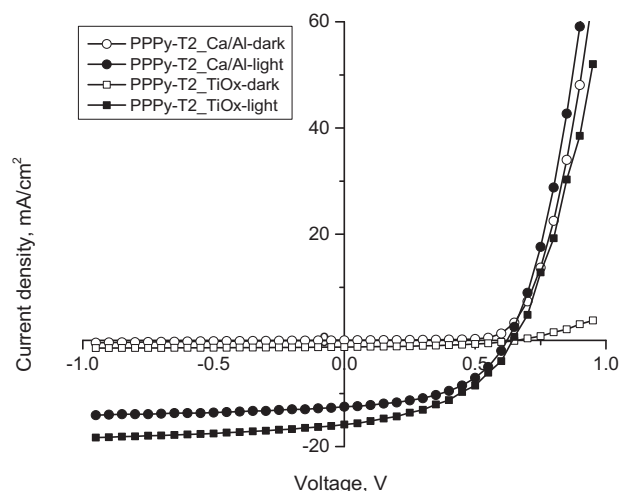


Fig. 5. Current–voltage curves of best photovoltaic devices under illumination (1.5AM) and dark conditions.

Table 3

Average photovoltaic parameters obtained for **PPPyT²:PC₇₁BM** devices, D:A ratio: 1:1.

	Cathode	<i>V</i> _{oc} (V)	<i>J</i> _{sc} (mA/cm ²)	FF (%)	PCE (%)
PPPyT ² :PC ₇₁ BM	Ca/Al	0.61 ± 0.01	12.2 ± 0.3	49.1 ± 0.9	3.74 ± 0.16
	TiO _x /Al	0.64 ± 0.01	15.2 ± 0.6	42.6 ± 1.3	4.15 ± 0.35

well below the estimated achievable value of 11%. According to the GIWAXS results and transport measurements discussed above, the lamellar morphology of PPPyT² could be responsible for this behavior. The in-plane π -stacking leads to anisotropic charge transport, with a relatively low out-of plane mobility. The anisotropy, although less pronounced in the presence of PC₇₁BM, is likely to be at the origin of the low fill factor and constitutes a remaining bottleneck towards higher efficiencies.

4. Conclusions

In the present work, a solution-processable copolymer utilizing pyridal [2,1,3]thiadiazole as an electron deficient moiety was successfully synthesized. The new polymer has a relatively deep HOMO level of 5.1 eV and exhibits a strong bathochromic red-shift in the solid state, leading to an optimal optical band gap of 1.48 eV. Charge transport in pure polymer films was found to be highly anisotropic with a high in-plane mobility and low out-of plane mobility, and correlates well with the ordered lamellar morphology observed by X-ray diffraction. The transport anisotropy was significantly reduced upon blending with fullerenes, while the X-ray diffraction spectra remained almost unaffected. Also the energy disorder, estimated from the gate voltage dependence of the field effect mobility, did not change notably upon blending. The higher out-of-plane mobility observed in blends was attributed to the presence of polymers in an amorphous state, whose signature could be seen in the UV–visible absorption spectrum. Bulk heterojunction solar cell devices fabricated using this new copolymer demonstrated a PCE of 4.5% with a high J_{sc} of around 15.8 mA/cm². Further studies are under way to examine the influence of alkyl side chains with different types and lengths in order to control and drive the structural conformation of the polymer chains to a more appropriate orientation.

Acknowledgements

We thank the Centre National de la Recherche Scientifique (CNRS), Total E&P Kazakhstan and Rhin-Solar project supported by the European Fund for Regional Development (FEDER) in the framework of the Programme INTERREG IV Upper Rhine for financial support. We want to thank as well Pohang Accelerator Laboratory (PAL) for giving us the opportunity to perform the GIWAXS measurements, MEST and POSTECH for supporting these experiments, Dr. Tae Joo Shin for adjustments and help, and other people from 9A U-SAXS beamline for assistance. This research was supported by Leading Foreign Research Institute Recruitment Program through the National Research Foundation of Korea (NRF) funded by the Ministry of Science, ICT & Future Planning (NRF-2010-00453).

Appendix A. Supplementary data

Supplementary data associated with this article can be found, in the online version, at <http://dx.doi.org/10.1016/j.orgel.2015.04.018>.

References

- [1] M.C. Scharber, N.S. Sariciftci, *Prog. Polym. Sci.* 38 (2013) 1929–1940.

- [2] G. Li, R. Zhu, Y. Yang, *Nat. Photon.* 6 (2012) 153–161.
 [3] Z. He, C. Zhong, S. Su, M. Xu, H. Wu, Y. Cao, *Nat. Photon.* 6 (2012) 591–595.
 [4] K. Li, Z. Li, F. Feng, X. Xu, L. Wang, Q. Peng, *J. Am. Chem. Soc.* 135 (2013) 13549–13557.
 [5] J. You, L. Dou, K. Yoshimura, T. Kato, K. Ohya, T. Moriarty, K. Emery, C.-C. Chen, J. Gao, G. Li, Y. Yang, *Nat. Commun.* 4 (2013) 1446.
 [6] J.-L. Bredas, D. Beljonne, V. Coropceanu, J. Cornil, *Chem. Rev.* 104 (2004) 4971–5003.
 [7] W. Shockley, H.J. Queisser, *J. Appl. Phys.* 32 (1961) 510–519.
 [8] Z. Li, Y. Zhang, S.-W. Tsang, X. Du, J. Zhou, Y. Tao, J. Ding, *J. Phys. Chem. C* 115 (2011) 18002–18009.
 [9] S. Fall, L. Biniek, N. Leclerc, P. L ev eque, T. Heiser, *Appl. Phys. Lett.* 101 (2012) 123301.
 [10] B. Fu, J. Baltazar, A.R. Sankar, P.-H. Chu, S. Zhang, D.M. Collard, E. Reichmanis, *Adv. Funct. Mater.* 24 (2014) 3734–3744.
 [11] S. Beaupre, M. Leclerc, *J. Mater. Chem. A* 1 (2013) 11097–11105.
 [12] L. Biniek, C.L. Chochos, N. Leclerc, G. Hadziioannou, J.K. Kallitsis, R. Bechara, P. Leveque, T. Heiser, *J. Mater. Chem.* 19 (2009) 4946–4951.
 [13] H. Zhou, L. Yang, W. You, *Macromolecules* 45 (2012) 607–632.
 [14] N. Blouin, A. Michaud, M. Leclerc, *Adv. Mater.* 19 (2007) 2295–2300.
 [15] J. Hou, H.-Y. Chen, S. Zhang, G. Li, Y. Yang, *J. Am. Chem. Soc.* 130 (2008) 16144–16145.
 [16] L. Biniek, S. Fall, C.L. Chochos, N. Leclerc, P. Leveque, T. Heiser, *Org. Electron.* 13 (2012) 114–120.
 [17] H. Zhou, L. Yang, A.C. Stuart, S.C. Price, S. Liu, W. You, *Angew. Chem. Int. Ed.* 50 (2011) 2995–2998.
 [18] N. Blouin, A. Michaud, D. Gendron, S. Wakim, E. Blair, R. Neagu-Plesu, M. Belletete, G. Durrocher, Y. Tao, M. Leclerc, *J. Am. Chem. Soc.* 130 (2008) 732–742.
 [19] H. Zhou, L. Yang, S.C. Price, K.J. Knight, W. You, *Angew. Chem. Int. Ed.* 49 (2010) 7992–7995.
 [20] G.C. Welch, G.C. Bazan, *J. Am. Chem. Soc.* 133 (2011) 4632–4644.
 [21] C.J. Takacs, Y. Sun, G.C. Welch, L.A. Perez, X. Liu, W. Wen, G.C. Bazan, A.J. Heeger, *J. Am. Chem. Soc.* 134 (2012) 16597–16606.
 [22] Y. Sun, G.C. Welch, W.L. Leong, C.J. Takacs, G.C. Bazan, A.J. Heeger, *Nat. Mater.* 11 (2012) 44–48.
 [23] J.E. Coughlin, Z.B. Henson, G.C. Welch, G.C. Bazan, *Acc. Chem. Res.* 47 (2014) 257–270.
 [24] www.wavefun.com.
 [25] W.F. Pasveer, J. Cottaar, C. Tanase, R. Coehoorn, P.A. Bobbert, P.W.M. Blom, D.M. de Leeuw, M.A.J. Michels, *Phys. Rev. Lett.* 94 (2005) 206601.
 [26] J. Zaumseil, H. Sirringhaus, *Chem. Rev.* 107 (2007) 1296.
 [27] N. Banerji, E. Gagnon, P.-Y. Morgantini, S. Valouch, A.R. Mohebbi, J.-H. Seo, M. Leclerc, A.J. Heeger, *J. Phys. Chem. C* 116 (2012) 11456–11469.
 [28] C. Winder, N.S. Sariciftci, *J. Mater. Chem.* 14 (2004) 1077–1086.
 [29] R. Peng, J. Zhu, W. Pang, Q. Cui, F. Wu, K. Liu, M. Wang, G. Pan, *J. Macromol. Sci. Part B Phys.* 50 (2011) 624–636.
 [30] Y. Kim, S.A. Choulis, J. Nelson, D.D.C. Bradley, S. Cook, J.R. Durrant, *Appl. Phys. Lett.* 86 (2005) 063502.
 [31] Y. Kim, S. Cook, S.M. Tuladhar, S.A. Choulis, J. Nelson, J.R. Durrant, D.D.C. Bradley, M. Giles, I. McCulloch, C.-S. Ha, M. Ree, *Nat. Mater.* 5 (2006) 197–203.
 [32] C. Tanase, E.J. Meijer, P.W.M. Blom, D.M. de Leeuw, *Phys. Rev. Lett.* 91 (2003) 216601.
 [33] M. Weis, *J. Appl. Phys.* 111 (2012) 054506.
 [34] M.C.J.M. Vissenberg, *Phys. Rev. B* 57 (1998) 12964–12967.
 [35] X. Yang, J. Loos, S.C. Veenstra, W.J.H. Verhees, M.M. Wienk, J.M. Kroon, M.A.J. Michels, R.A.J. Janssen, *Nano Lett.* 5 (2005) 579–583.
 [36] H. Hoppe, N.S. Sariciftci, *J. Mater. Chem.* 16 (2006) 45–61.
 [37] S. Ebadian, B. Gholamkhass, S. Shambayati, S. Holdcroft, P. Servati, *Sol. Energy Mater. Sol. Cells* 94 (2010) 2258–2264.
 [38] S. Fall, PhD thesis (2013), University of Strasbourg.
 [39] D.H. Apaydin, D.E. Yildiz, A. Cirpan, L. Toppare, *Sol. Energy Mater. Sol. Cells* 113 (2013) 100–105.
 [40] V.N. Savvateev, M. Tarabia, H. Chayet, E.-Z. Farragi, G.-B. Cohen, S. Kirstein, D. Davidov, Y. Avny, R. Neumann, *Synth. Met.* 85 (1997) 1269–1270.
 [41] Y. Roichman, N. Tessler, *Synth. Met.* 135 (2003) 443–444.
 [42] V.D. Mihailetchi, H. Xie, B. de Boer, L.J.A. Koster, P.W.M. Blom, *Adv. Funct. Mater.* 16 (2006) 699–708.
 [43] N.D. Treat, M.A. Brady, G. Smith, M.F. Toney, E.J. Kramer, C.J. Hawker, M.L. Chabincyn, *Adv. Energy Mater.* 1 (2011) 82–89.
 [44] W. Yin, M. Dadmun, *ACS Nano* 5 (2011) 4756–4768.
 [45] J.-M.Y. Carrillo, R. Kumar, M. Goswami, B.G. Sumpter, W.M. Brown, *Phys. Chem. Chem. Phys.* 15 (2013) 17873–17882.
 [46] G. Fang, J. Liu, Y. Fu, B. Meng, B. Zhang, Z. Xie, L. Wang, *Org. Electron.* 13 (2012) 2733–2740.

5.4 Supporting information: “Using pyridal[2,1,3]thiadiazole as an acceptor unit in a low band-gap copolymer for photovoltaic applications”

O.A. Ibraikulov^{a,b}, R. Bechara^a, P. Chávez^c, I. Bulut^c, D. Tastanbekov^b, N. Leclerc^c, A. Hebraud^c, B. Heinrich^d, S. Berson^e, N. Lemaitre^e, C.L. Chochos^{f,g}, P. Lévêque^a and T. Heiser^{a*}

^a Laboratoire ICube, CNRS – Université de Strasbourg, 23 rue du Loess, Strasbourg, 67037, France.

^b Nazarbayev University Research and Innovation System, Nazarbayev University, 53 Kabanbay Batyr Ave., Astana 010000, Kazakhstan.

^c Institut de Chimie et Procédés pour l’Energie, l’Environnement et la Santé, Université de Strasbourg, CNRS, 25 rue Becquerel, 67087 Strasbourg, Cedex 02, France.

^d Institut de Physique et Chimie des Matériaux de Strasbourg (IPCMS), Université de Strasbourg, CNRS, 23 rue du Loess, Strasbourg, 67034, France.

^e LMPO, CEA Grenoble, INES, 50 avenue du Lac Leman, 73375 Le Bourget du Lac, France.

^f Department of Materials Science and Engineering, University of Ioannina, Ioannina 45110, Greece.

^g Advent Technologies SA, Patras Science Park, Stadiou Street, Platani-Rio, 26504, Patra, Greece.

*Corresponding author’s e-mail: thomas.heiser@unistra.fr

Supporting Information

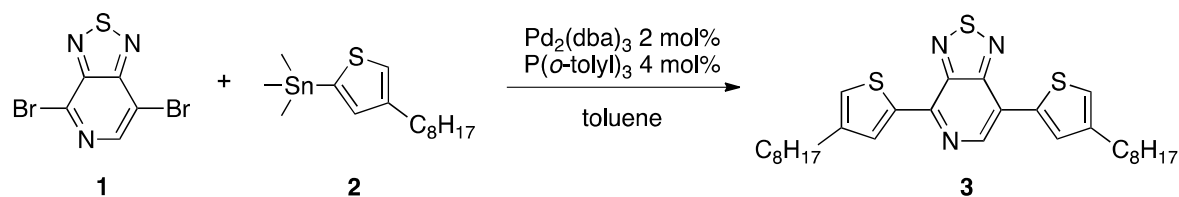
1, Synthesis

General Procedure

All reagents and chemicals were purchased. THF and Toluene (ACS grade) were distilled from Na / benzophenone. The synthesis of 4,7-dibromo-[1,2,5]thiadiazolo[3,4-*c*]pyridine (**1**), 2-(trimethylstannyl)-4-(2-ethylhexyl)thiophene (**2**) and 2-5-bis-trimethylstannyl-thieno[3,2-*b*]thiophene (**7**) have been prepared as described in the literature.¹

1. J. Mater. Chem., 2011, 21, 13247

Procedure A: Stille type cross-coupling

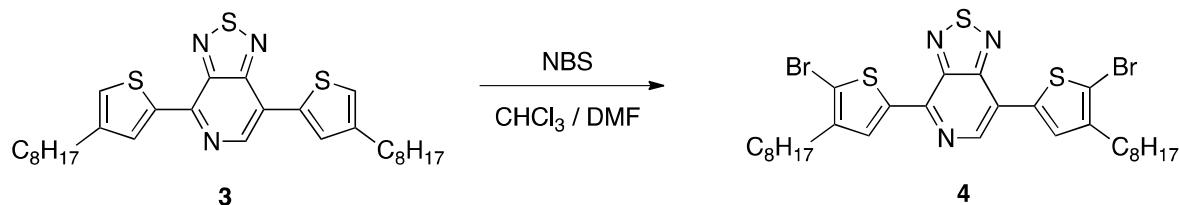


4,7-bis(4-octylthiophen-2-yl)-[1,2,5]thiadiazolo[3,4-c]pyridine (**3**)

A flame dried Schlenck was charged with 4,7-dibromo-[1,2,5]thiadiazolo[3,4-c]pyridine (**1**) (1.0 equiv). Anhydrous and degassed toluene (0.1M) was added under inert gas followed by 2-(trimethylstannyl)-4-(2-ethylhexyl)thiophene (**2**) (2.2 equiv). Finally, the $\text{Pd}_2(\text{dba})_3$ (2 mol%) and $\text{P}(o\text{-tolyl})_3$ (8 mol%) were added in one portion and the mixture was stirred 18 hours at 120°C. After cooling to room temperature the reaction mixture was filtered through a pad of celite and the toluene solution was evaporated under reduced pressure. Then, the crude material was purified by column chromatography (silica gel, $\text{CH}_2\text{Cl}_2/\text{PE}$: 30/70). Yield (78%).

mol. wt.: 525.84 g/mol. Orange dark solid. ^1H NMR (300 MHz, CDCl_3) δ = 8.81 (s, 1H), 8.50 (d, J = 1.2 Hz, 1H), 7.92 (d, J = 1.2 Hz, 1H), 7.18 (s, 1H), 7.05 (s, 1H), 2.65 (dd, J = 4.6, 6.7 Hz, 4H), 1.68-1.62 (m, 2H), 1.39-1.27 (m, 16H), 0.95-0.88 (m, 12H). ^{13}C NMR (75 MHz, CDCl_3) δ = 148.7, 146.8, 144.5, 143.8, 142.4, 141.0, 136.9, 134.2 (x2), 130.6, 127.7, 124.3, 121.4, 41.3, 41.2, 35.2 (x2), 33.3 (x2), 33.2 (x2), 26.4 (x2), 23.7 (x2), 14.4 (x2), 11.1 (x2).

Procedure B: Di-Bromination

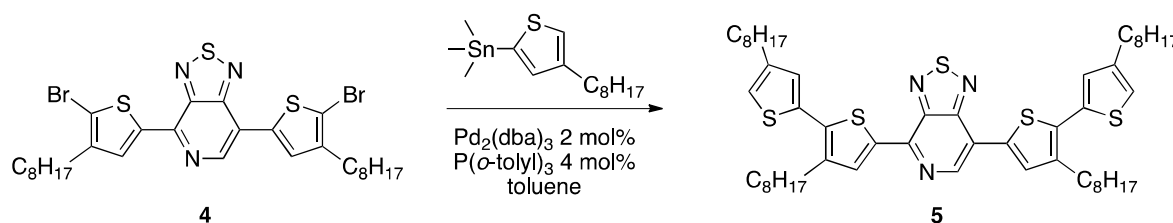


4,7-bis(5-bromo-4-octylthiophen-2-yl)-[1,2,5]thiadiazolo[3,4-c]pyridine (**4**)

Compound **(3)** (1.0 equiv) was solubilized in CHCl_3 (0.15 M) and DMF (0.05 M) under argon in the dark. NBS (2.0 equiv) was added portion wise. The resulting solution was stirred at room temperature under argon overnight. Water and diethylether were added and the resulting solution was stirred for 2h. The organic phase was separated from the water phase and extracted with brine (3x100 mL). The organic phase was dried with sodium sulfate, filtered and the solvent evaporated under reduced pressure. The crude product was purified by column chromatography (silica gel, $\text{CH}_2\text{Cl}_2/\text{PE}$: 10/90). Yield (68%).

mol. wt.: 683.63 g/mol. Red solid. ^1H NMR (300 MHz, CDCl_3) δ = 8.60 (s, 1H), 8.25 (s, 1H), 7.69 (s, 1H), 2.56 (dd, J = 3.1, 7.1 Hz, 4H), 1.72-1.68 (m, 2H), 1.39-1.25 (m, 16H), 0.95-0.89 (m, 12H). ^{13}C NMR (75 MHz, CDCl_3) δ = 154.5, 147.6, 145.3, 143.4, 142.5, 140.8, 140.0, 135.7, 133.0, 129.0, 119.8, 117.1, 112.6, 40.0 (x2), 34.0, 33.8, 32.5 (x2), 28.8 (x2), 25.7 (x2), 23.1 (x2), 14.2 (x2), 10.9 (x2).

Procedure A: Stille type cross-coupling



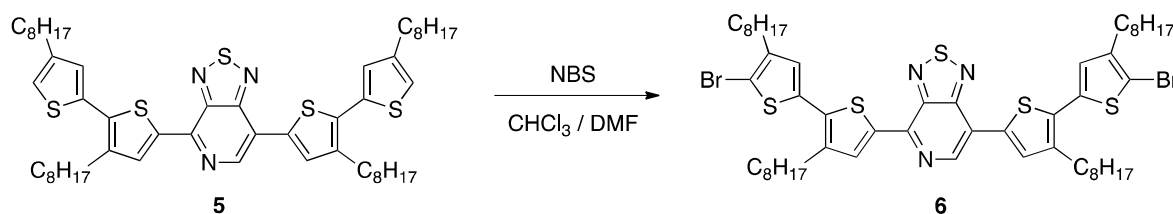
4,7-bis(3,4'-dioctyl-[2,2'-bithiophen]-5-yl)-[1,2,5]thiadiazolo[3,4-c]pyridine (**5**)

A flame dried Schlenck was charged with trimere **4** (1.0 equiv). Anhydrous and degassed toluene (0.1M) was added under inert gas followed by 2-(trimethylstannyl)-4-(2-ethylhexyl)thiophene (2.2 equiv). Then, the $\text{Pd}_2(\text{dba})_3$ (2 mol%) and $\text{P}(\text{o-tolyl})_3$ (8 mol%) were added in one portion and the mixture was stirred 18 hours at 120°C . After cooling to room temperature the reaction mixture was filtered through a pad of celite and the toluene solution was evaporated under reduced pressure. Finally, the crude material was purified by column chromatography (silica gel, $\text{CH}_2\text{Cl}_2/\text{PE}$: 20/80). Yield (70%)

mol. wt.: 914.51 g/mol. Red dark oil..

^1H NMR (300 MHz, CDCl_3) δ = 8.78 (s, 1H), 8.48 (s, 1H), 7.92 (s, 1H), 7.12 (d, J = 0.7 Hz, 1H), 7.05 (d, J = 0.7 Hz, 1H), 6.94 (s, 1H), 6.92 (s, 1H), 2.80 (dd, J = 7.5, 9.9 Hz, 4H), 2.56 (d, J = 6.8 Hz, 4H), 1.72-1.80 (m, 2H), 1.55-1.58 (m, 2H), 1.36-1.29 (m, 32H), 0.85-0.92 (m, 24H). ^{13}C NMR (75 MHz, CDCl_3) δ = 154.8, 148.2, 145.7, 142.6 (x2), 142.4 (x2), 140.4, 140.2, 139.6, 138.2, 135.5, 135.4, 135.2, 133.9, 133.8, 131.5, 128.7 (x2), 128.5 (x2), 40.4, 40.3, 40.2, 40.1, 34.6, 34.5, 33.8 (x2), 33.5 (x2), 32.6 (x2), 29.0 (x2), 28.9 (x2), 28.7 (x2), 25.8 (x2), 25.7 (x2), 23.1 (x2), 23.0 (x2), 14.1 (x2), 10.9 (x2), 10.7 (x2). MS ESI-TOF m/z (%) $\text{C}_{53}\text{H}_{75}\text{N}_3\text{S}_5$: 914.5 [M-H] (100). HRMS ESI-TOF m/z calculated for $\text{C}_{53}\text{H}_{75}\text{N}_3\text{S}_5$ [M-H]: 914.4592; found: 914.4582.

Procedure B: Di-Bromination



4,7-bis(5'-bromo-3,4'-dioctyl-[2,2'-bithiophen]-5-yl)-[1,2,5]thiadiazolo[3,4-c]pyridine (6)

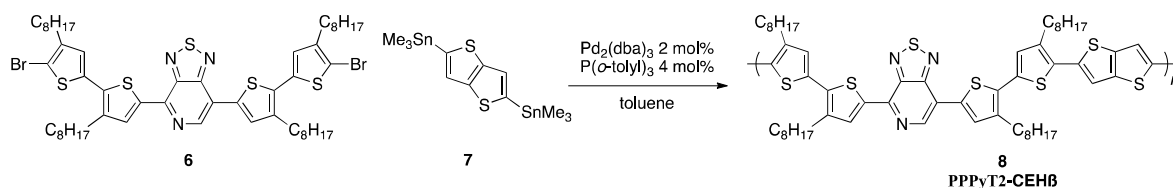
Compound (**5**) (1.0 equiv) was solubilized in CHCl_3 (0.15 M) and DMF (0.05 M) under argon in the dark. NBS (2.0 equiv) was added portion wise. The resulting solution was stirred at room temperature under argon overnight. Water and CHCl_3 were added and the resulting solution was stirred for 2h. The organic phase was separated from the water phase and extracted with brine (3x100 mL). The organic phase was dried with sodium sulfate, filtered and the solvent evaporated under reduced pressure. The crude product was purified by column chromatography (silica gel, $\text{CH}_2\text{Cl}_2/\text{PE}$: 20/80). Yield (52%).

mol. wt.: 1072.30 g/mol. Red dark oil.

^1H NMR (300 MHz, CDCl_3) δ = 8.60 (s, 1H), 8.28 (s, 1H), 7.80 (s, 1H), 6.93 (s, 1H), 6.86 (s, 1H), 2.69 (pseudo t, J = 6.1 Hz, 4H), 2.51 (d, J = 6.0 Hz, 4H), 1.73-1.66 (m, 4H), 1.40-1.33 (m, 32H), 0.97-0.88 (m, 24H). ^{13}C NMR (75 MHz, CDCl_3) δ = 154.4, 147.8, 145.2, 141.7, 141.6, 140.3, 140.2, 139.8, 138.7, 136.2, 135.3, 135.2, 135.1, 134.1, 132.6, 131.2, 127.8, 127.6, 119.6, 110.3, 109.8, 39.9 (x2), 33.8, 33.7, 32.6 (x2), 32.5 (x2), 32.4 (x2), 28.9 (x2), 28.8 (x2), 28.6 (x2), 26.89 (x2), 25.7 (x2), 23.1 (x2),

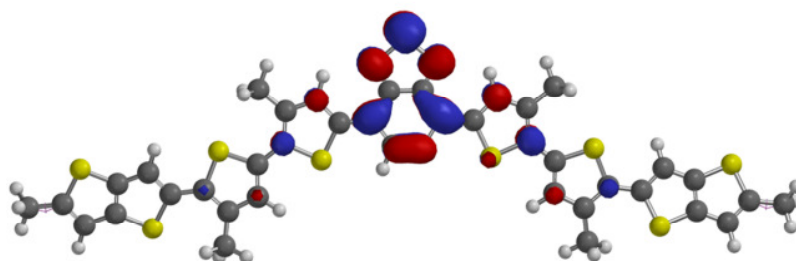
23.0 (x2), 22.9 (x2), 14.1 (x2), 10.8 (x2), 10.7 (x2). MS ESI-TOF m/z (%) $C_{53}H_{73}Br_2N_3S_5$: 1072.3 [M-H] (100). HRMS ESI-TOF m/z calculated for $C_{53}H_{73}Br_2N_3S_5$ [M-H]: 1072.2845; found: 1072.3385.

Polymerization: PPPyT² (**8**)



Thieno[3,2-*b*]thiophene derivative (**7**) (1.0 equiv) and compound (**6**) (1.0 equiv) were dissolved in dry toluene (0.0125 M) in flame dried Schlenck. Then, $Pd_2(dba)_3$ (2 mol%) and $P(o-tolyl)_3$ (8 mol%) were added and the reaction mixture was stirred at 110°C under argon atmosphere for 15min. The reaction was quenched with 2-(Me_3Sn)thiophene (0.6 equiv) during 1 hour followed by 2-Brthiophene (0.6 equiv). Then, the polymer crude was purified by precipitation in methanol, filtered and separated by Soxhlet extraction with methanol, cyclohexane and chlorobenzene. Then, the *sodium diethyldithiocarbamate* solution was added in the chlorobenzene fraction and the mixture was stirred at 60°C during 1 hour. The organic phase was separated and evaporated under reduced pressure. Finally, the polymer was precipitated in methanol, filtered and dried under reduced pressure at 40°C overnight, providing a film with a metallic shine with 85% of yield.

2. DFT calculations



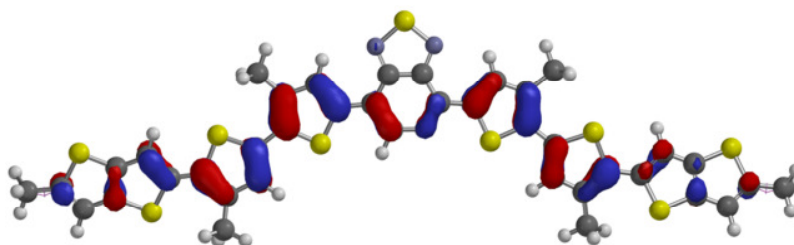


Fig. S1. Calculated HOMO (bottom) and LUMO (top) for PPPyT²

3. Cyclic Voltammogram

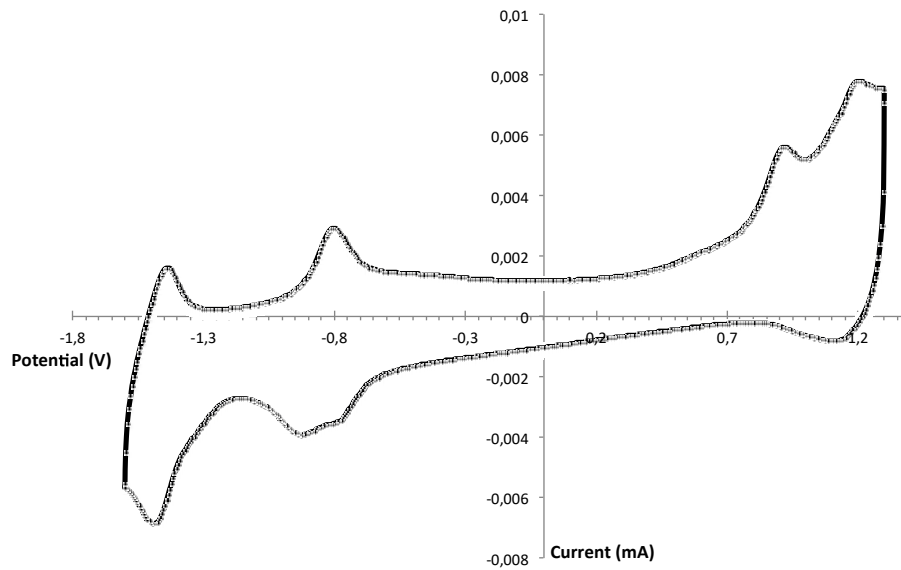
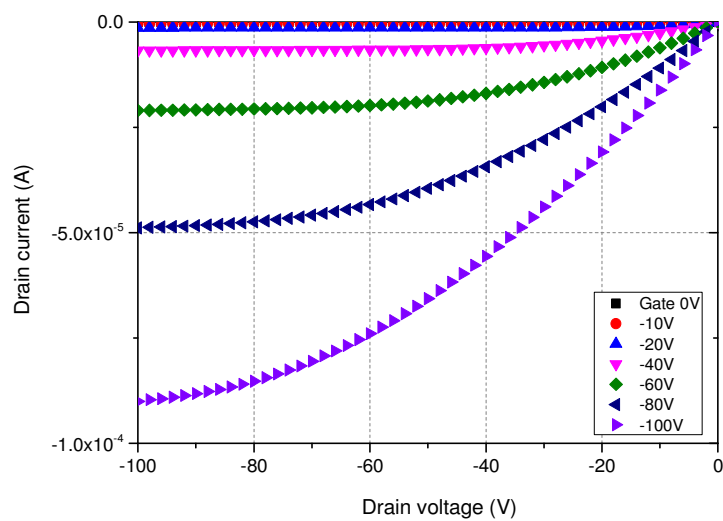
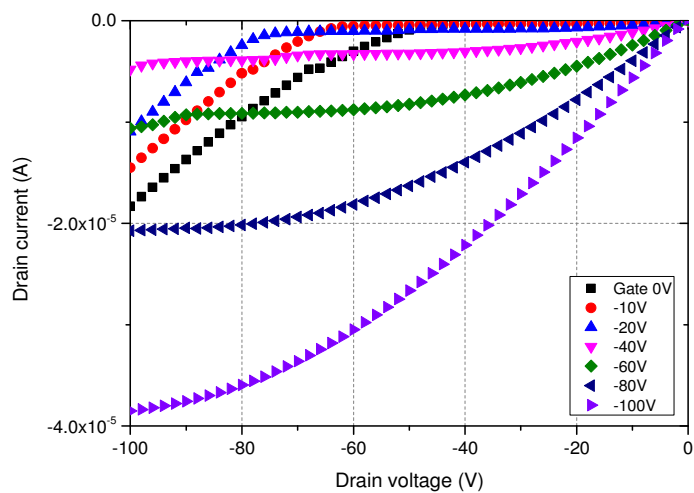


Fig. S2. Cyclic voltammogram of PPPyT² in solid state

4. Charge transport characteristics

Fig. S3. Output characteristics of pure PPPyT² film annealed at 150°C for 15 min.Fig. S4. Output characteristics of PPPyT²:PC₇₁BM blend annealed at 150°C for 15 min at negative gate voltages.

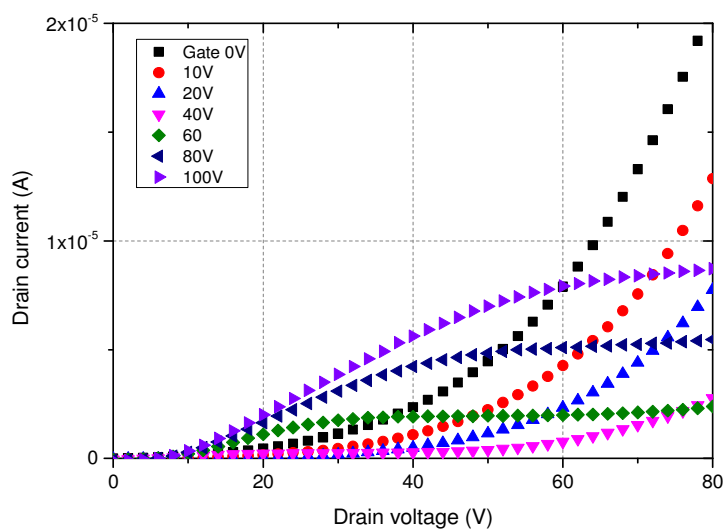


Fig. S5. Output characteristics of PPPyT²:PC₇₁BM blend annealed at 150°C for 15 min at positive drain and gate voltages.

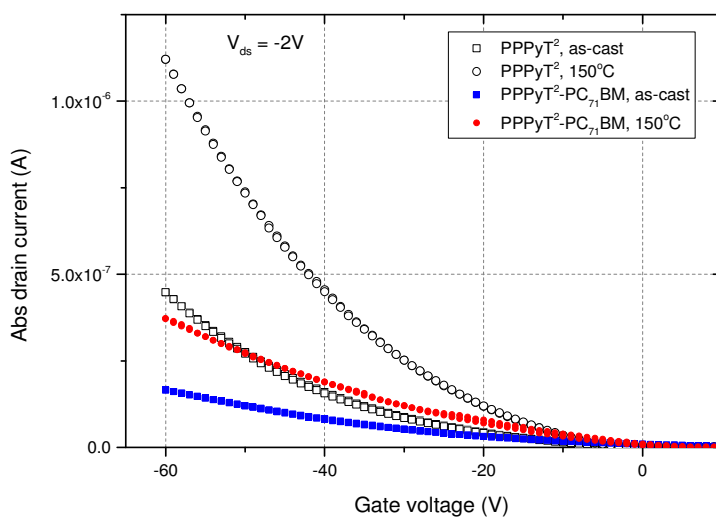


Fig. S6. Transfer characteristics of pure PPPyT² film and PPPyT²:PC₇₁BM blend as-cast and annealed at 150°C for 15 mins. Drain-source voltage V_{ds} is set to -2V

Hole mobilities in the linear regime (low V_{DS}) were extracted from the following expression:

$$\mu_{h+} = \frac{L}{W \cdot C_i \cdot V_{DS}} \left(\frac{\partial I_{DS}}{\partial V_{GS}} \right) \quad (S1)$$

W = width of the channel; L = length of the channel; C_i = capacitance per unit area; V_{DS} = drain-source voltage.

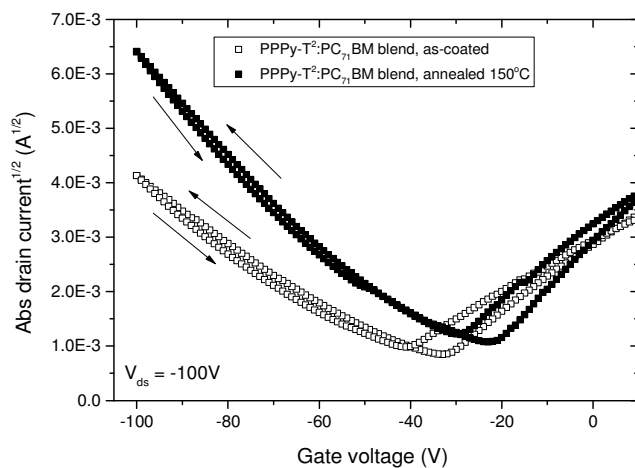


Fig. S7. Current-voltage characteristics of PPPy-T²:PC₇₁BM blends wt% ratio: 1/1 before and after annealing at negative gate voltages (for hole mobility in blends). Upper arrows show forward directions.

For extracting the field-effect hole mobility the currents in forward directions were used.

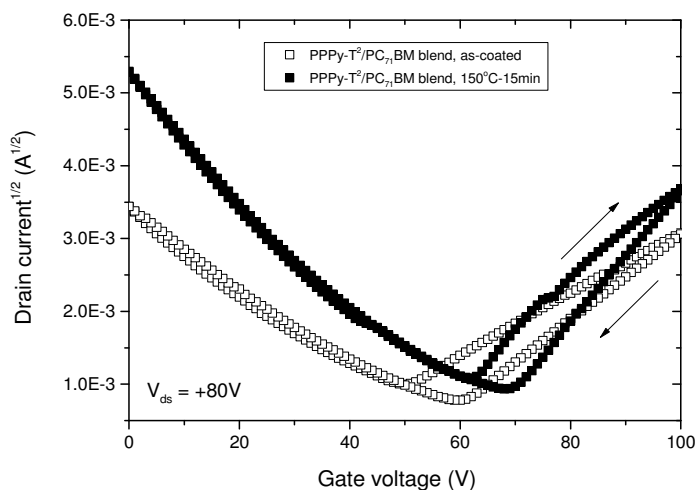


Fig. S8. Current-voltage characteristics of PPPy-T²:PC₇₁BM blends at positive gate voltages (for electron mobility). Upper arrow indicates the forward direction, and the below one backward direction

To extract the field-effect electron mobility the currents in forward direction were used.

Charge mobility in the saturation regime was extracted from the following formula:

$$\mu = \frac{2.L}{W.C_i} \left(\frac{\partial I_{DS}^{1/2}}{\partial V_{GS}} \right)^2 \quad (S2)$$

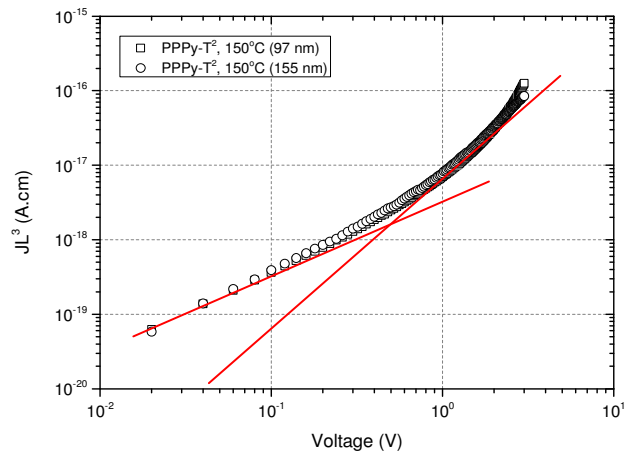


Fig. S9. SCLC characteristics of pure, annealed PPPyT² films (open symbols) with two different thicknesses. Solid lines represent ohmic part ($J \propto V$) and space-charge limited part ($J \propto V^2$) dependence

5. Morphology

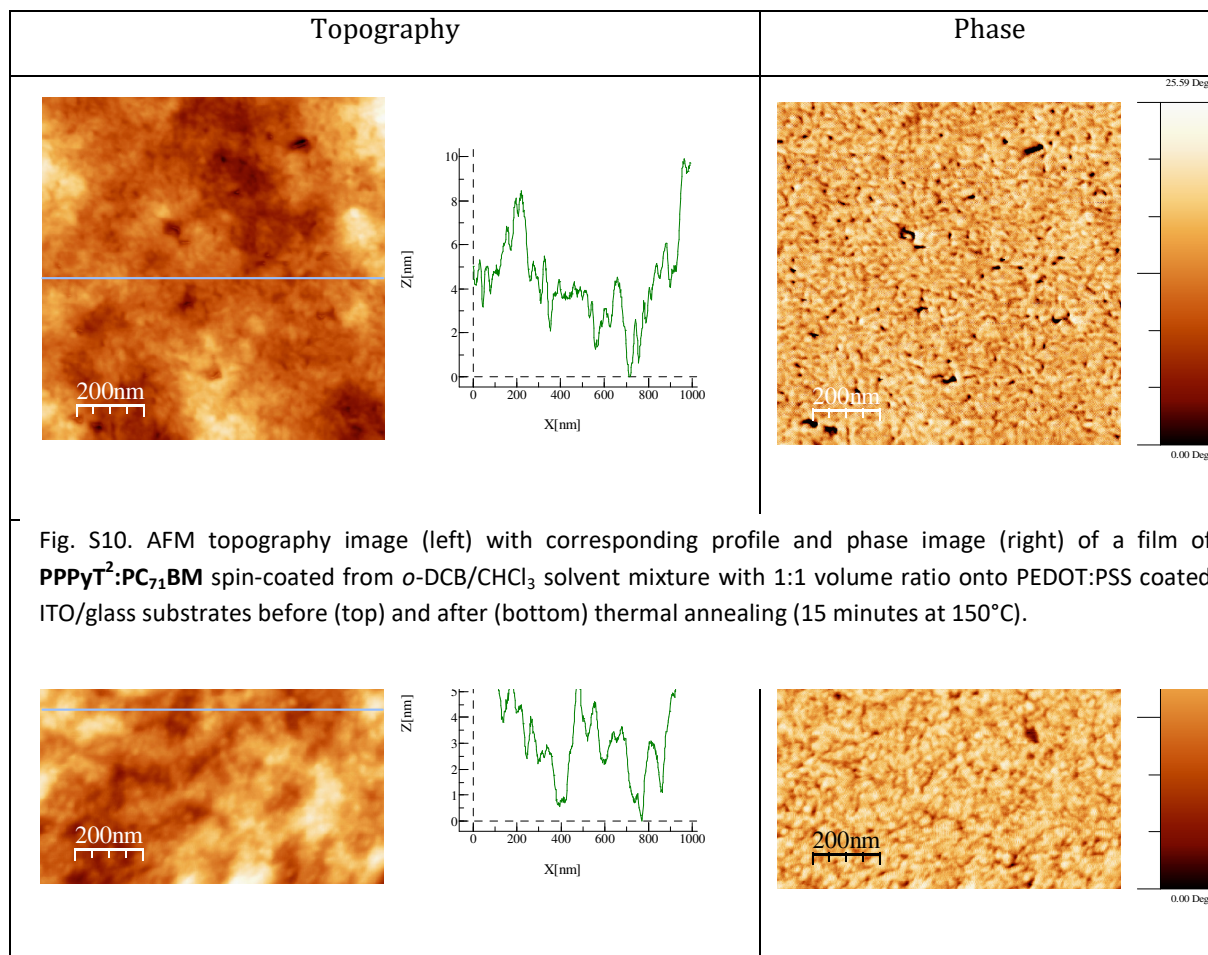


Fig. S10. AFM topography image (left) with corresponding profile and phase image (right) of a film of **PPP_yT²:PC₇₁BM** spin-coated from *o*-DCB/CHCl₃ solvent mixture with 1:1 volume ratio onto PEDOT:PSS coated ITO/glass substrates before (top) and after (bottom) thermal annealing (15 minutes at 150°C).

6. Photovoltaic properties

Table S1. Average photovoltaic device parameters as a function of D/A ratio. Device structure: Glass/ITO/PEDOT:PSS/Active layer/Ca-Al.

	<i>D/A ratio</i>	<i>V_{oc} (V)</i>	<i>J_{sc} (mA/cm²)</i>	<i>FF (%)</i>	<i>PCE (%)</i>
PPPyT²:PC₇₁BM	1:0.7	0.62±0.01	8.96±0.2	47.5±1.2	2.6±0.20
	1:1	0.62±0.01	12.3±0.2	49.1±0.9	3.74±0.16
	1:1.5	0.61±0.01	10.7±0.4	47±1	3.08±0.11

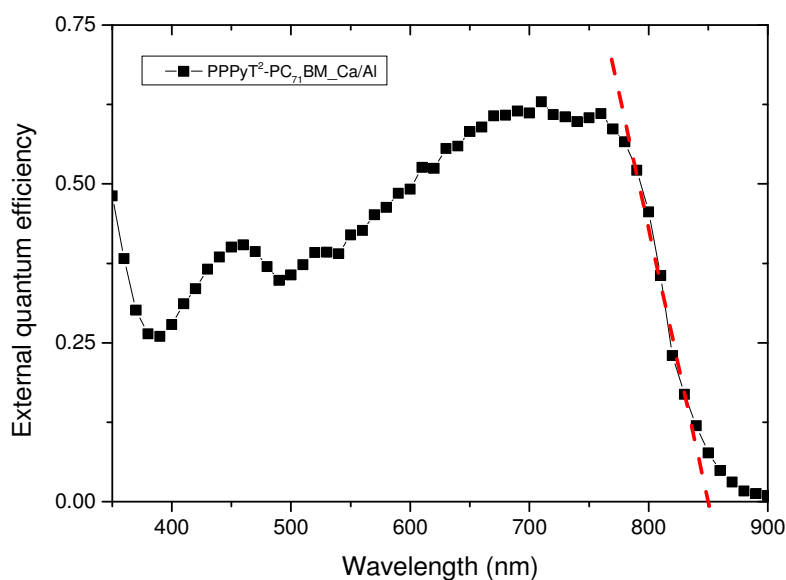


Fig. S11. EQE spectrum of best PPPyT²:PC₇₁BM device with Ca/Al cathode. Dashed red line represents the extrapolation of the onset to estimate the band gap

Short circuit current can be easily estimated from EQE data. Assuming that one photon generates one electron:

$$J_{sc} = \sum_{\lambda} \frac{S_{EQE,\lambda} S_{Solar,\lambda}}{ch/\lambda q} \quad (S3)$$

$q = 1.6 \times 10^{-19}$ Coulombs, elementary charge;

$S_{EQE,\lambda}$ – EQE at wavelength λ ;

$S_{\text{Solar}, \lambda}$ – Solar spectrum, AM1.5G;

c – Velocity of light in vacuum;

h – Planck's constant;

λ – Wavelength of incident light.

Using measured EQE data and equation S3 estimated J_{sc} was found to be around 13.9 mA/cm². While measured J_{sc} for the same cell is 12.5 mA/cm².

5.4 Conclusion

In summary, we have investigated a new low band-gap copolymer based on pyridal[2,1,3]thiadiazole as an acceptor unit. In-depth charge transport studies were carried out. In-plane and out-of-plane charge transport studies showed high anisotropy. Hole mobility in SCLC diodes (vertical direction) were almost 2 orders of magnitude lower than horizontal mobility in pristine polymer films. Surprisingly, blending **PPPyT²** polymer with PC[71]BM at a ratio of 1:1 lead to increased vertical hole mobility and slightly decreased OFET hole mobility. GIWAXS measurements were performed to understand the structural self-organization of **PPPyT²** in pure and blend films. These results revealed the semi-crystalline nature of the **PPPyT²** in thin films and clearly explained the charge transport findings in pure polymer films. In particular, polymer lamellas were organized in “edge-on” orientation that was not even disturbed in the presence of PC[71]BM. To further understand the evolution of hole mobilities, additional UV-Vis absorption measurements were performed for polymer:fullerene blends in solid state. These results showed the increase of the amorphous polymer fractions after blending with PC[71]BM. The almost four times larger out-of-plane hole mobility was attributed to these amorphous fractions.

Despite its initial promising features from the FMO energy level point of view **PPPyT²** did not perform in BHJ solar cells as expected. The relatively low out-of-plane hole mobility caused by non-favorable orientation of polymer lamellas strongly limits the fill factors (FF) of final solar devices.

Chapter 6: Results: Di-fluorinated vs non-fluorinated copolymer

6 Results: Di-fluorinated vs non-fluorinated copolymer

6.1 Introduction

Although the polymers investigated in previous chapters were very promising in terms of FMO energy level positioning, it was not possible to reach with them the theoretically expected high PCE in BHJ solar cells. Poorly ordered **TPD-DTP- β** (Chapter 4) showed surprisingly low energy disorder but still suffered from relatively low both in-plane and out-of-plane hole mobilities. On the other hand, the semi-crystalline nature of **PPPyT²** (Chapter 5) was not enough to prevail this barrier either, primarily due to non-favorable orientation of polymer lamellas in thin films that hampered out-of-plane charge transport. As a consequence, the PCEs of BHJ solar devices were strongly limited by the corresponding FFs.

Very recently, polymer backbone fluorination has been proposed to be another perspective way in designing efficient polymers for organic photovoltaics [124]. Though fluorination was initially considered to fine-tune the FMO energy levels, other positive side effects have been evidenced by different research groups. Introduction of fluorine atoms into the conjugated polymer backbone resulted, for instance, in reduced domain size [127,128,164], improved domain purity [127,165], enhanced crystallinity and structural ordering [166,167]. Additionally, most of the fluorinated polymers have been found to have strong π - π^* interactions [166,168] and self-organize into lamellas with a mixed "face-on" or "edge-on" molecular orientation. The latter rather unexpected property led to increased out-of-plane hole mobilities [130,169]. Yet, the reasons for such preferable self-organization of polymers in thin films are still under debate.

In this context, we decided to apply the backbone fluorination strategy to our polymer families. Polymers based on thienothiophene, difluorinated and non-fluorinated benzothiadiazole moiety and two thiophenes substituted by two octyl-dodecyl alkyl side chains at the β -position were synthesized (Fig. 6.1a and b). The choice of this material was based on one of the previously investigated non-fluorinated copolymers with shorter alkyl

side chains (Fig. 6.1c) published by Pr. Thomas Heiser's group [145]. It should be noted that very recently, while our group was intensively studying this fluorinated copolymer, the same polymer structure has been published in the literature and gave rise to promising photovoltaic performances [170].

Accordingly, this chapter focuses on the investigations of backbone fluorinated and non-fluorinated low band-gap copolymers with identical side-chains. Section 6.2 focuses on the results obtained from various studies (OPV, charge transport, morphology) of di-fluorinated polymers with different molecular weights. Results and discussions on non-fluorinated counterpart are presented in section 6.3. To go further, charge-carrier dynamics in solar cells based on fluorinated and non-fluorinated copolymers were investigated and are discussed in Section 6.4. This chapter is finalized by the conclusion in Section 6.5.

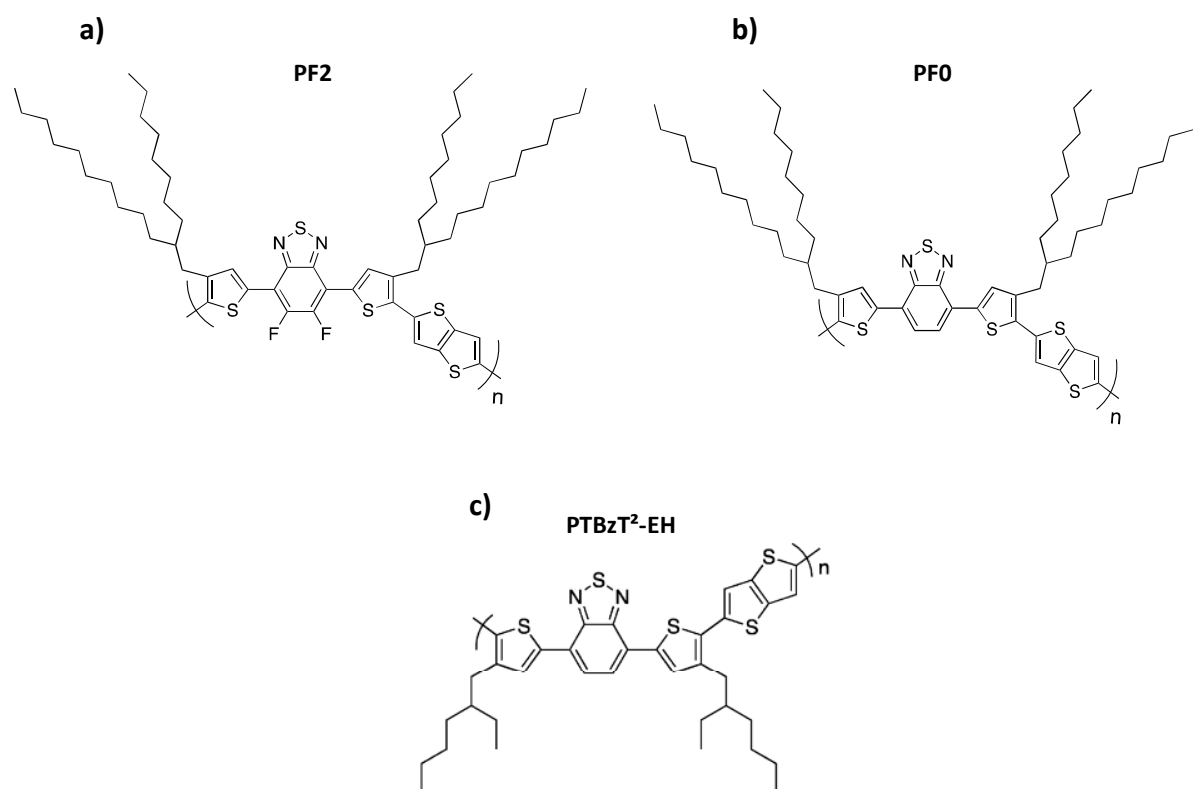


Figure 6.1: Chemical structures of a) di-fluorinated copolymer studied within this work b) its non-fluorinated counterpart and c) the copolymer recently published by Pr. Thomas Heiser group [144]

6.2 Investigations on di-fluorinated copolymers

Di-fluorinated copolymers (**PF2**) with three different molecular weights have been synthesized and studied in this section. The copolymers with highest, medium and lowest molecular weights are denoted as **PF2-HM**, **PF2-MM** and **PF2-LM**, respectively.

6.2.1 UV-Vis and electrochemical characterizations

Figure 6.1a shows the absorption spectra of pure **PF2-HM** in diluted o-DCB solution at different temperatures and compares them to the absorption spectrum in solid state. **PF2-HM** shows substantial temperature dependent aggregation in solution. Similar

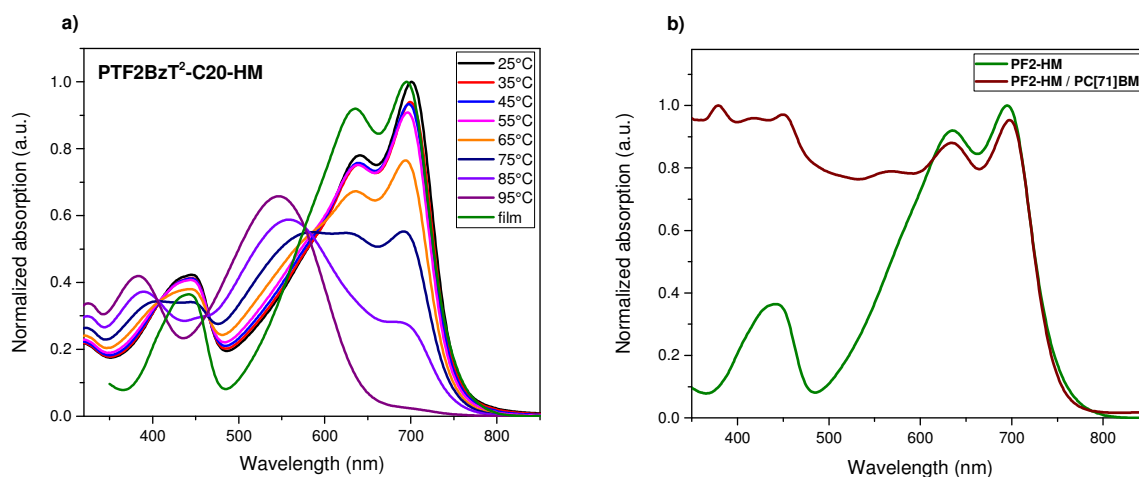


Figure 6.2: UV-Vis absorption spectra of a) **PF2-HM** in solution as a function of temperature and in thin film b) pure **PF2-HM** and **PF2-HM/PC[71]BM** (ratio: 1/1.5) blend films

observations have been reported for other fluorinated polymers [11,12]. The shapes of the solution absorption spectra at relatively low temperatures (25°C-55°C) are similar to the one measured in solid state with two marked low-energy peaks for all, pointing out strong and similar intermolecular interactions in solution and in thin films. On the other hand, a significant blue shift and a solution-like absorption spectrum is observed when the temperature is increased up to 95°C. Additionally, absorption measurements of **PF2-HM/PC[71]BM** blends in thin films at a ratio of 1/1.5 were performed (Fig. 6.1b). Compared to the pure copolymer film, a significantly broader band in the 350-500 nm

wavelength range is detected for the blend indicating the contribution of PC[71]BM to the total absorption spectrum. Interestingly, the low-energy double-peak is preserved in the blend despite the large PCBM content (60wt%), pointing out that the **PF2-HM** crystallinity

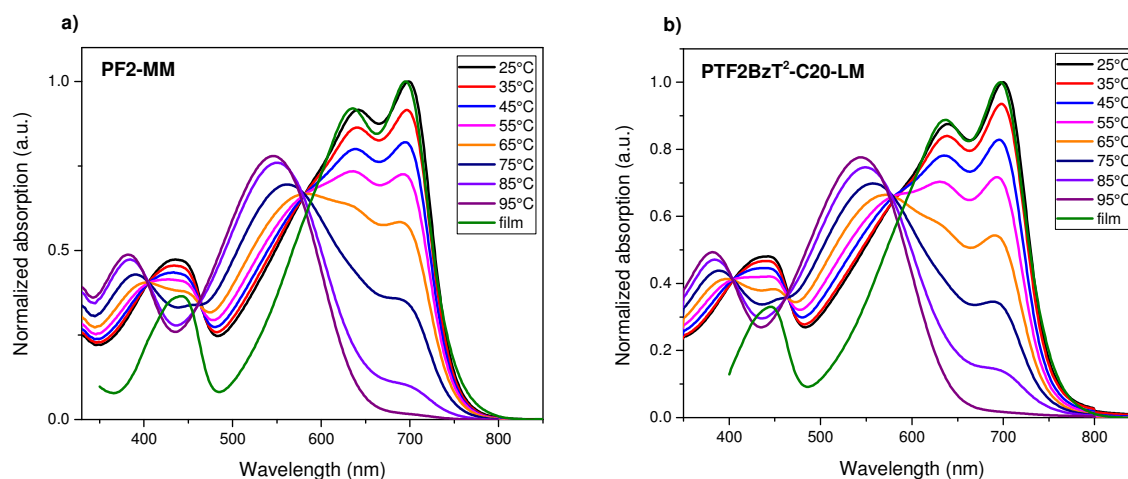


Figure 6.3: UV-Vis absorption spectra of a) **PF2-MM** and b) **PF2-LM** in solution for different temperatures and in thin films

in the film is not significantly altered by PC[71]BM. Other copolymers with medium (**PF2-MM**) and low (**PF2-LM**) molecular weights have been tested as well. As shown in Fig. 6.3, the general trend of aggregation in solution at low temperature is observed for all **PF2** copolymers. The transition temperature from “solid-state like” to “solution-like” spectrum is observed to slightly decrease with the copolymer molecular weight M_n . This is in accordance with the generally observed decrease of a conjugated polymer solubility with increasing molecular weight. From the onset on the UV-visible absorption in solid-state, an optical band-gap of 1.59 eV was estimated for all **PF2** copolymers.

CV measurements were performed for all **PF2** copolymers in thin films. The HOMO levels were estimated from the measured oxidation potential, while the LUMO levels were calculated by taking into account the optical band gap (E_g^{opt}). Table 6.1 below lists some opto-electronic properties of respective polymers. As expected, the FMO energy levels do not depend on the molecular weights.

Table 6.1: Opto-electronic properties of PF2 copolymers

	HOMO (eV)	LUMO (eV)	E_g^{opt} (eV)	M_n (g/mol)	PDI
PF2-HM	-5.42	-3.83	1.59	35 000	1.7
PF2-MM	-5.42	-3.83	1.59	29 000	2.0
PF2-LM	-5.42	-3.83	1.59	17 000	2.6

6.2.2 Photovoltaic results

In order to obtain homogeneous films and avoid aggregates and gel formation, the polymer/PC[71]BM blends were spin-coated from hot o-DCB solutions onto pre-heated substrates (both were heated up to $\approx 100^\circ\text{C}$). Spin coating speed, acceleration and time were set to 600 rpm, 200 rpm/s and 180 s, respectively. Before top electrode deposition, all the substrates were left overnight under high vacuum. The OPV device structure used in this study was as follows: Glass/ITO/PEIE/polymer:PC[71]BM/MoO₃/Ag. All the solar cells were tested under standardized AM1.5G (100 mW/cm²) conditions. The active area of 0.12 cm² was defined with a shadow mask.

Fluorinated copolymers with different molecular weights have been tested in OPV devices. Various conditions including different additive concentrations, annealing conditions were tested. The best performances for all polymers could be achieved without any additive and thermal treatment at a D:A weight ratio of 1:1.5. To achieve similar thicknesses, various concentrations of 20 mg/ml, 14 mg/ml and 13 mg/ml were used for **PF2-LM**, **PF2-MM** and **PF2-HM**, respectively.

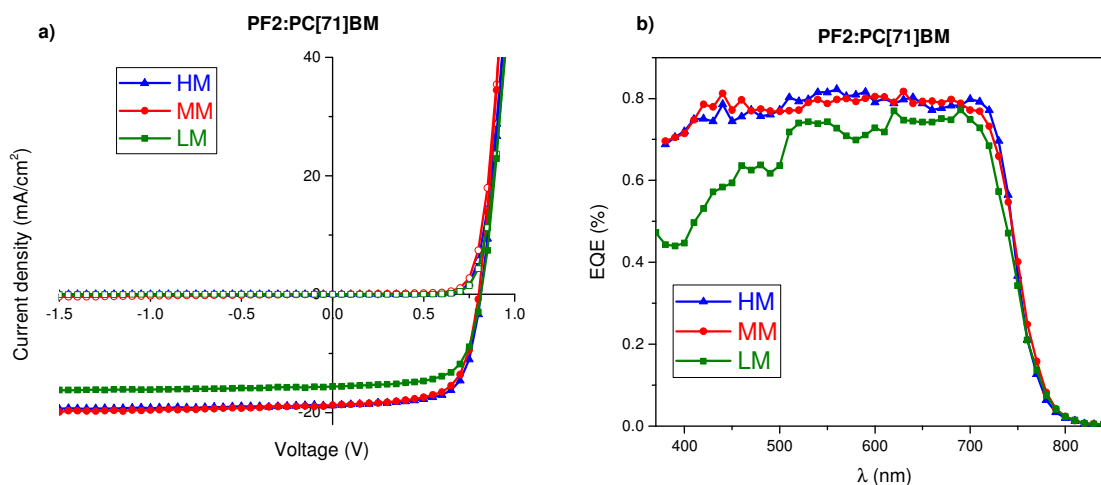
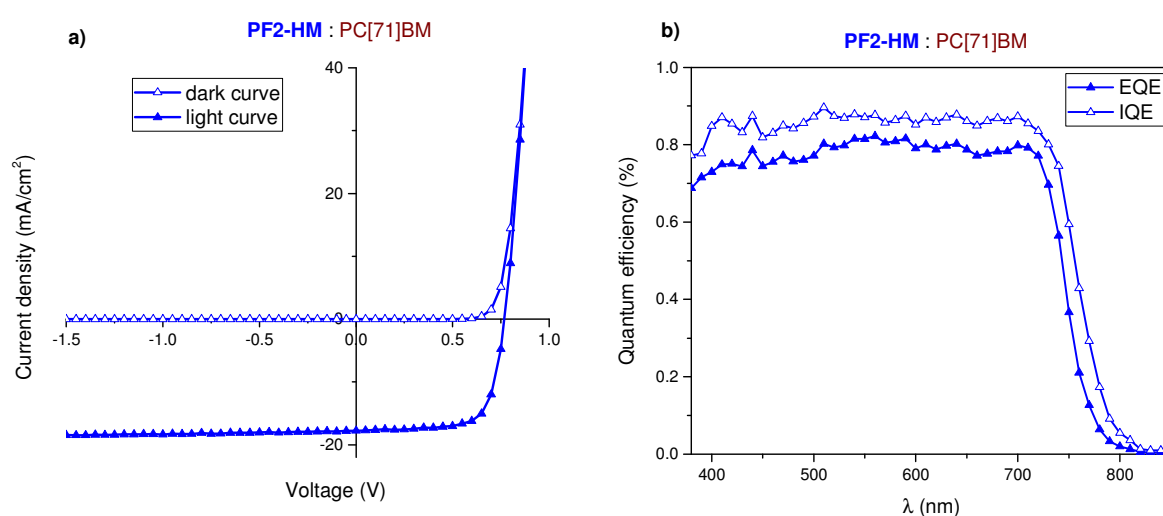


Figure 6.4: a) (J-V) characteristics in the dark (open symbols) and under AM1.5G (100 mW/cm²) conditions (closed symbols) and b) EQE curves of BHJ devices based on different molecular weight fluorinated polymers

Figure 6.4a and b represents current density-voltage and EQE curves, respectively, of the best performing devices for each isomer. Average photovoltaic values are summarized in Table 6.2. Devices based on all the polymers showed rather high efficiencies. Performances of **PF2-LM** copolymer devices were mainly limited by a lower J_{sc} in comparison to the other two materials. The corresponding EQE measurement indicates that the main current density losses could come from photons absorbed in the low wavelength range. As these photons are mainly absorbed by PC[71]BM, **PF2-LM** solar cells may suffer from and inadequate PC[71]BM average domain size that could limit the exciton dissociation. As expected, V_{oc} 's of all solar cells were almost identical, confirming that the FMO energy levels are not affected by the molecular weight. Average PCEs of BHJ cells based on medium and high M_n copolymers exceeded the value of 9%. The main differences between both copolymer-based devices are the corresponding FFs. The average FF of **PF2-HM**:PC[71]BM devices was the highest among all and reached the value of 69%. As a consequence, the highest PV performances could be achieved for these PV cells. PV parameters of the best performing cell were as follows: $J_{sc} = 17.9$ mA/cm², $V_{oc} = 0.770$ V, FF = 71.3 % and PCE = 9.8%.

Table 6.2: Average photovoltaic parameters for optimized BHJ devices based on different molecular weight fluorinated copolymers

	V_{oc} (mV)	J_{sc} (mA/cm ²)	FF (%)	PCE (%)	R_s (Ω)	R_{SH} (Ω)	Thickness (nm)
PF2-HM	770±5	17.8±0.4	69.3±2	9.54±0.3	50.5±4	5x10 ⁵	265±5
PF2-MM	760±5	17.8±0.5	66.1±1.5	9.02±0.2	58.5±5	3x10 ⁴	250±10
PF2-LM	768±5	15.3±0.3	66.0±1	7.75±0.15	66.7±2.5	10 ⁶	235±10

**Figure 6.5:** Best recorded a) (J-V) characteristics and b) quantum efficiency curves of solar cells based on PF2-HM:PC[71]BM blends

Best recorded J-V characteristics and quantum efficiency curves are shown in Fig. 6.5. The dark J-V curve shows negligible leakage currents, while the illuminated curve exhibits a good diode characteristic and stays almost parallel to the dark one, suggesting negligible geminate recombination and efficient charge extraction. The EQE values of PF2-HM based BHJ devices are above 80% between 510-590 nm with a maximum of 82.3% at 560 nm (Fig. 6.5b). The calculated value of J_{sc} from EQE spectrum is 18.1 mA/cm², which is consistent with J_{sc} obtained from the J-V measurement.

6.2.3 Charge transport investigations

Charge transport studies have been carried out in horizontal and vertical directions. The BC-BG OFET device elaboration procedure was as follows: pre-cleaned Fraunhofer substrates (details are in Chapter 3) were transferred into the glove box. Organic layer spin-coating procedure was identical to solar device elaboration. The devices were left overnight under high vacuum to remove solvent traces before starting device testing. Figure 6.6 represents the output and transfer curves of OFET devices based on **PF2** copolymers with different molecular weights. It should be noted that due to high contact resistances, the hole mobilities (μ_h^{OFET}), estimated from the slopes of saturation transfer curves in Fig. 6.6, need to be considered as minimum values for the respective materials. Thus, extracted saturation μ_h^{OFET} were around $(1.3 \pm 0.3) \times 10^{-2}$, $(1.2 \pm 0.2) \times 10^{-2}$ and $(1.2 \pm 0.2) \times 10^{-2}$ cm²/Vs for **PF2-LM**, **PF2-MM** and **PF2-HM**, respectively. Interestingly, the average μ_h^{OFET} was almost independent on the polymer molecular weight.

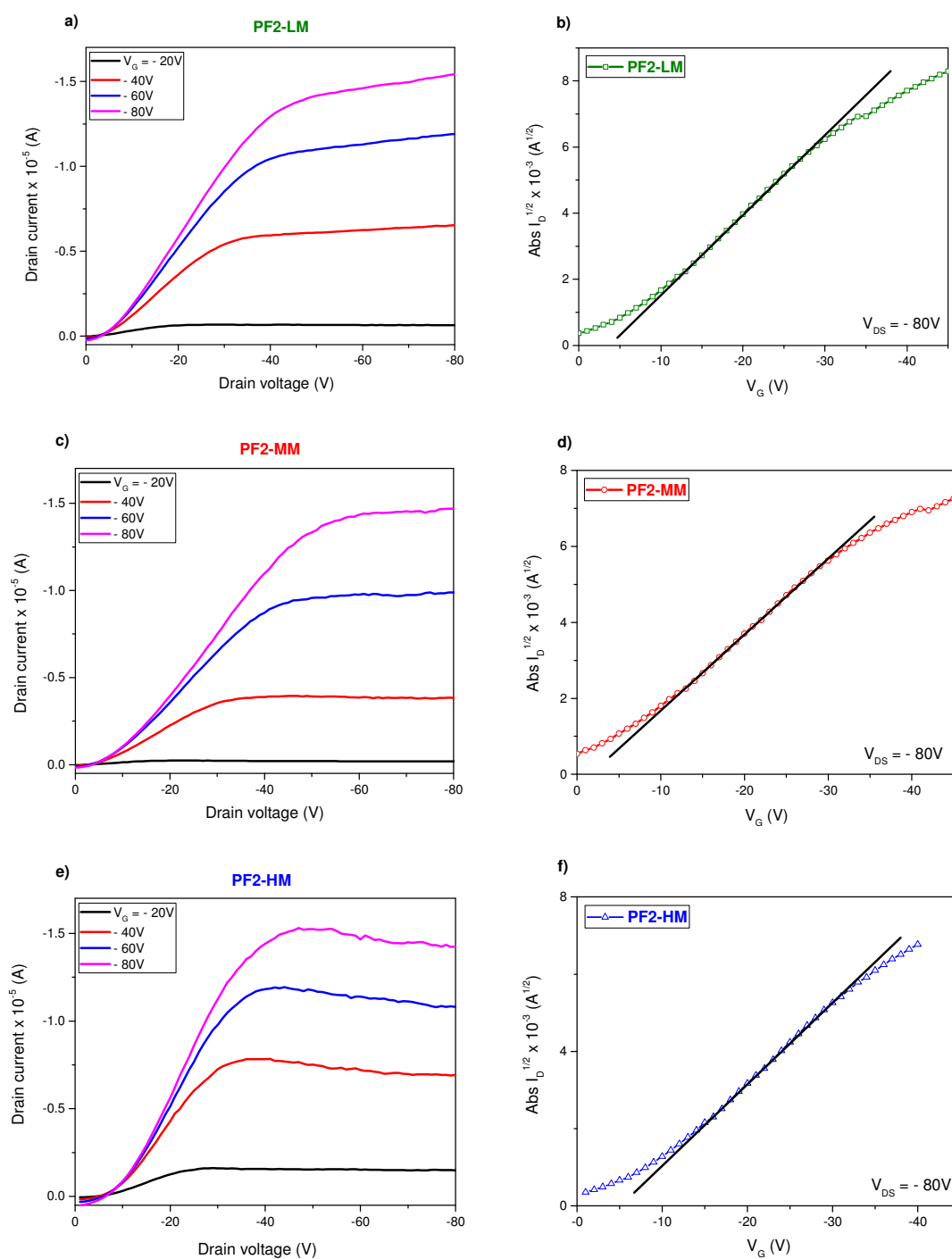


Figure 6.6: Output (left) and transfer (right) characteristics of **PF2** copolymers of different molecular weights. Black solid lines represent the slopes used to estimate hole mobility values

Vertical charge transport was measured using SCLC devices. Polymer thin layers were spin-coated inside the glove box using an identical procedure as for OFETs and solar cell devices.

The structure of hole-only diodes was as follows: Glass/ITO/PEDOT:PSS/polymer or polymer:PC[71]BM/MoO₃/Ag. Furthermore, out-of-plane electron mobilities in polymer:fullerene blends were estimated using electron-only devices based on Glass/ITO/PEIE/ polymer:PC[71]BM/Ca/Al structures. Prior to the thermal evaporation of the top electrodes, organic layer deposited substrates were dried under high vacuum for at least 16 hours.

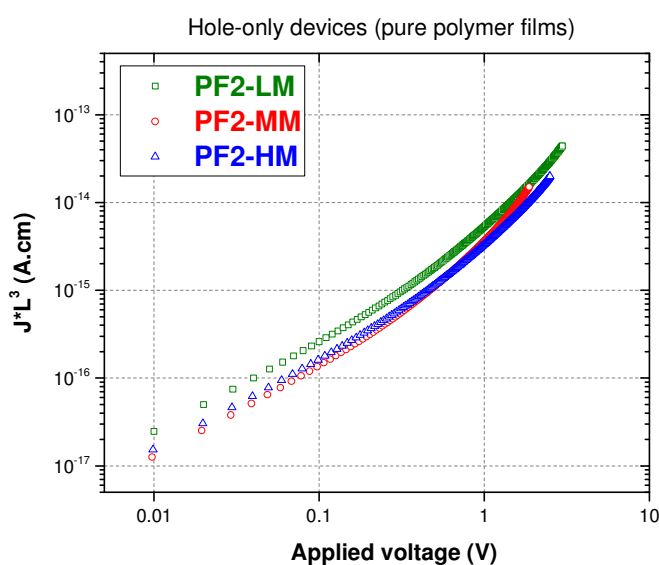


Figure 6.7: Current density-voltage characteristics of hole-only diodes based on pure polymer films scaled with cubic thickness

Figure 6.7 shows thickness-scaled current-voltage curves of devices based on three fluorinated copolymers. According to the measurements, the SCLC hole mobilities (μ_h^{SCLC}) for **PF2-LM**, **PF2-MM** and **PF2-HM** were calculated to be around $(1.3 \pm 0.1) \times 10^{-2}$, $(1.03 \pm 0.06) \times 10^{-2}$ and $(0.85 \pm 0.05) \times 10^{-2} \text{ cm}^2 \text{V}^{-1} \text{s}^{-1}$, respectively. These vertical mobility values are relatively high for organic semiconducting materials. Though the values were close to each other (same order of magnitude), surprisingly, the average hole mobility slightly increased with decreasing the molecular weight of the copolymer. Moreover, the vertical and horizontal hole mobilities are in the same range. This observation of a 3-D charge transport behavior suggest that interconnectivity of charge transporting domains in pure polymer films is not hampered even at low molecular weights [80,152]. On the other hand, charge transport anisotropy seems to be slightly more pronounced in polymers with higher M_n

(Fig. 6.8). However, it should be noted that values estimated for μ_h^{OFET} are slightly underestimated.

Hole and electron mobilities were also measured in polymer:PC[71]BM blends at a ratio of 1:1.5. Respective current-voltage characteristics are shown in Fig. 6.9.

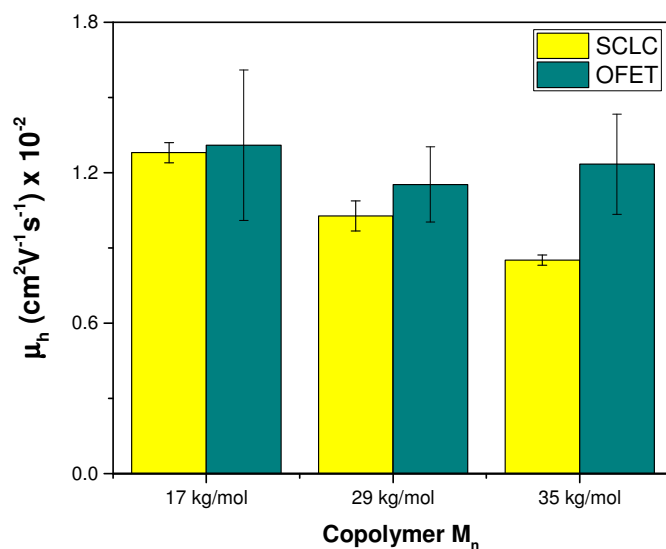


Figure 6.8: Comparison of vertical (SCLC) and horizontal (OFET) hole mobilities in pure polymer films versus respective M_n

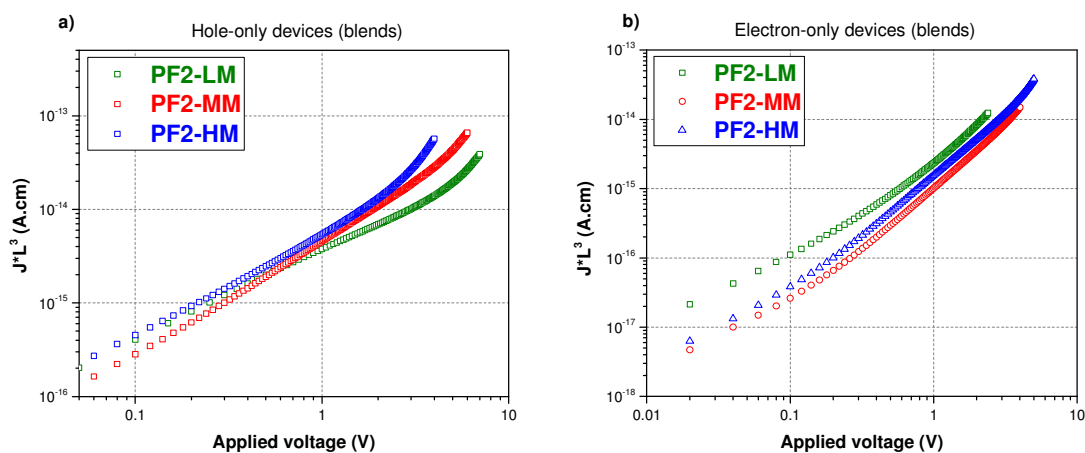


Figure 6.9: Thickness-scaled current-voltage characteristics of a) hole-only and b) electron-only devices based on polymer:fullerene blends (ratio: 1:1.5)

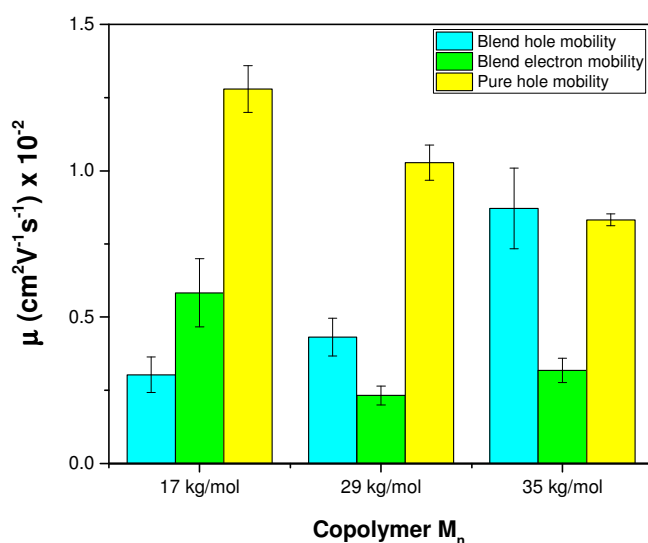


Figure 6.10: Comparison of hole and electron mobility values in pure polymer films and polymer:PC[71]BM blends

It should be noted that the measured current-voltage curves of hole-only devices slightly deviated from the $J \propto V^2$ dependence at moderate applied bias (Fig. 6.9a). The ohmic parts (slope =1) are particularly long, suggesting the presence of residual dopants [171]. Namely in blends, the presence of polymer (or PC[71]BM) could generate holes (or electrons) that in turn would act as traps for injected electrons (or holes) and thus postpone the formation of electron (or hole) space-charge. Interestingly, **PF2-LM** copolymer is most affected by the addition of PC[71]BM (Fig. 6.10) with a hole mobility almost divided by 4 in blends compared to the one measured for the pure polymer. This finding corroborates with EQE measurements. The possible presence of larger PC[71]BM domains could indeed alter polymer chain interconnectivity and prevent holes to move easily (see below). In contrast, μ_h^{SCLC} in **PF2-HM**:PC[71]BM blends slightly increases in the presence of PC[71]BM. This could be the reason for the highest recorded FFs in BHJ devices based on the high M_n copolymer. These observations in out-of-plane blend hole mobilities ($\mu_{h,blend}^{SCLC}$) suggest that polymer with the highest M_n is less affected with PC[71]BM loading. Electron mobilities ($\mu_{e,blend}^{SCLC}$) in all blends were in the same order of magnitude and were relatively balanced with the respective ($\mu_{h,blend}^{SCLC}$). The less balanced charge carrier mobility in blends is

observed for **PF2-HM** where the hole mobility is twice the electron one. Highest average $\mu_{e,blend}^{SCLC}$ was found for **PF2-LM:PC[71]BM** composition confirming the existence of larger acceptor domains (see above). For convenience, all the average hole and electron mobility values are listed in Table 6.3.

Table 6.3: Average hole and electron mobilities in pure materials and in blends

	Pure materials		blends	
	μ_h^{OFET} (cm ² /Vs)	μ_h^{SCLC} (cm ² /Vs)	μ_h^{SCLC} (cm ² /Vs)	μ_e^{SCLC} (cm ² /Vs)
PF2-LM	$(1.3 \pm 0.3) \times 10^{-2}$	$(1.3 \pm 0.1) \times 10^{-2}$	$(3.0 \pm 0.6) \times 10^{-3}$	$(5.8 \pm 1.2) \times 10^{-3}$
PF2-MM	$(1.1 \pm 0.2) \times 10^{-2}$	$(1.03 \pm 0.06) \times 10^{-2}$	$(4.3 \pm 0.7) \times 10^{-3}$	$(2.3 \pm 0.3) \times 10^{-3}$
PF2-HM	$(1.2 \pm 0.2) \times 10^{-2}$	$(0.85 \pm 0.05) \times 10^{-2}$	$(8.7 \pm 1.3) \times 10^{-3}$	$(3.2 \pm 0.4) \times 10^{-3}$

6.2.4 GIWAXS results

Further structural characterizations were performed to get deeper insights into photovoltaic and charge transport findings. For GIWAXS measurements, silicon wafers with native silicon dioxide (SiO₂) layer were used as substrates. Thin polymer films were spin coated in the glove box onto PEIE pre-deposited Si-wafer to be close to the solar cells structure. Applied polymer and blend thin film processing conditions were identical to that

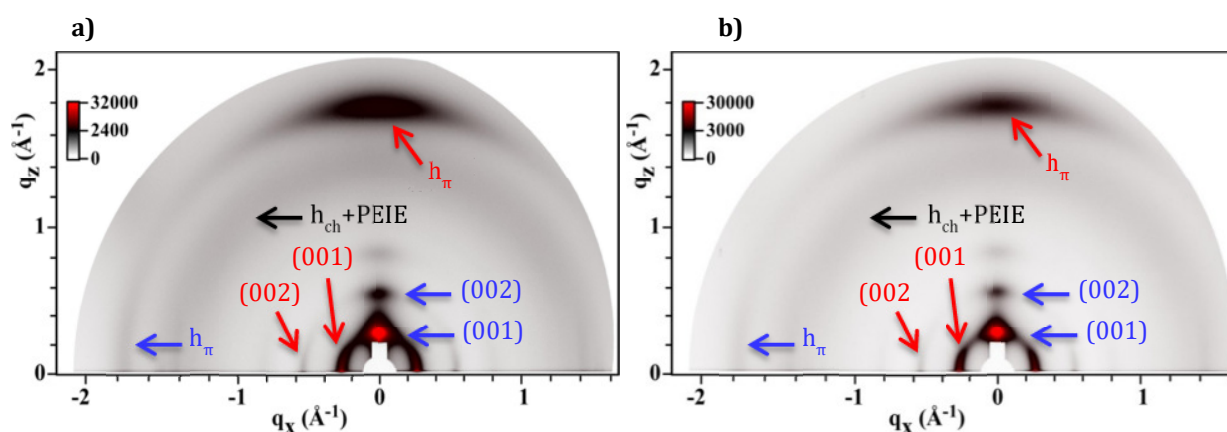


Figure 6.11: GIWAXS patterns of pure a) **PF2-HM** and b) **PF2-MM** polymer films

of thin film elaboration for photovoltaic and charge transport studies (Sections 6.2.2, 6.2.3). Figure 6.11 presents GIWAXS profiles of pristine **PF2-MM** and **PF2-HM** polymer films. Both

polymers are organized in relatively high crystalline forms. The (00N) reflections reveal the presence of regularly stacked lamellas, while the large angle reflection (h_π) corresponds to polymer π -stacking. Two major populations of well-aligned lamellar packings can be clearly distinguished for both materials: flat-lying lamellae with the π -stacking direction parallel to the substrate plane shown with blue arrows in Fig. 6.11 (“edge-on” orientation) and standing lamellae with π -stacking perpendicular to the substrate plane (red arrows in Fig. 6.11, “face-on” orientation). For both polymers, the edge-on and face-on orientation predominate over intermediate domain orientations. Moreover, layer spacings ($d_{HM} = 22.6 \text{ \AA}$ vs $d_{MM} = 22.5 \text{ \AA}$), π -stacking distances ($h_{\pi,HM} = 3.53 \text{ \AA}$ vs $h_{\pi,MM} = 3.52 \text{ \AA}$) and correlation lengths ($\xi_{HM} = 4 \text{ nm}$ vs $\xi_{MM} = 4 \text{ nm}$) for both isomers were almost identical meaning that the molecular weight has almost no influence on the polymer self-organization in pure thin films. Similar observations have also been reported for other fluorinated copolymers [11,168]. It should also be noted that the presence of mixed phase orientations are well in-line with charge transport findings where balanced in-plane and out-of-plane hole mobilities in pure polymer films were found for both materials (Section 6.2.3).

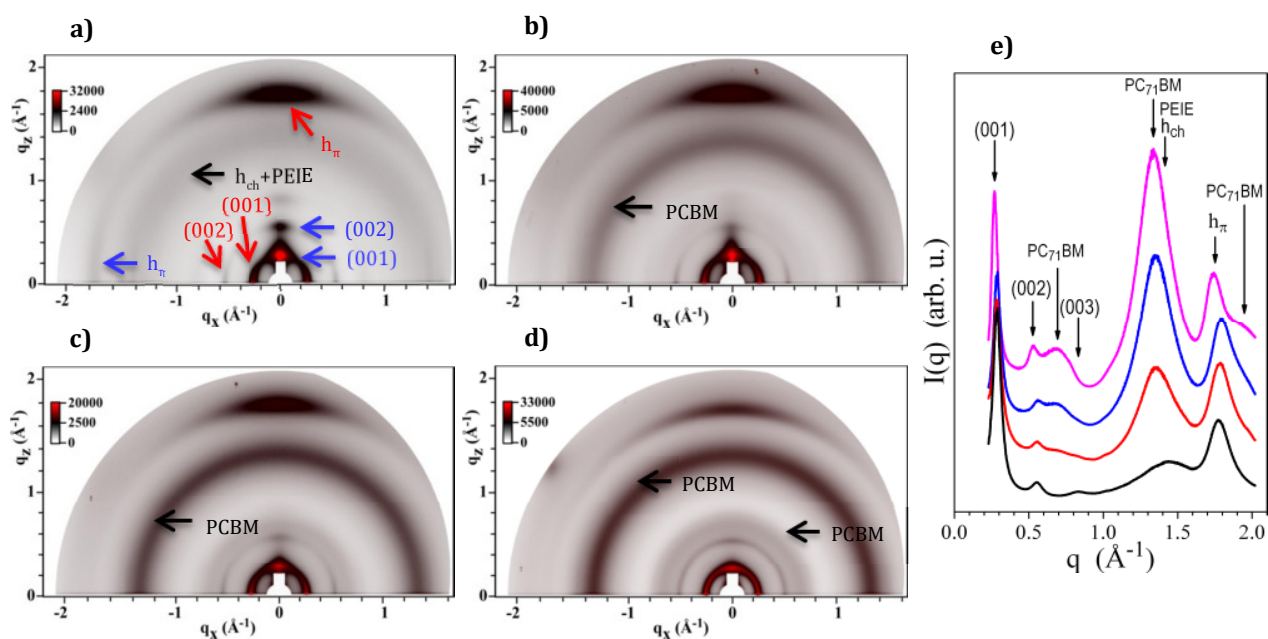


Figure 6.12: GIWAXS patterns of a) pure **PF2-HM** copolymer; b) **PF2-HM**:PC[71]BM at 1:1 ratio; c) 1:1.5 ratio; and d) 1:2 ratio. e) Radial profiles of GIWAXS patterns pure polymer film (black), polymer:fullerene blend film ratio of 1:1 (red), 1:1.5 (blue) and 1:2 (magenta)

Further GIWAXS measurements on polymer:fullerene blend films were performed only for **PF2-HM**:PC[71]BM composition at various weight ratios. Blend films were tested to elucidate the influence of PC[71]BM on the **PF2-HM** polymer microstructure. As can be seen in Fig. 6.12, the presence of PC[71]BM has only a limited impact on the structure. In particular, increasing the PC[71]BM content up to 60% (ratio 1:1.5) does not change the diffraction peak corresponding to the standing lamellae. However, the lamellar alignment blurs out towards an unoriented film morphology when the PC[71]BM content is further increased.

These structural observations clarify the charge transport results in polymer:fullerene blends. From out-of-plane charge transport investigations it was found that μ_h^{SCLC} in a 1:1.5 ratio **PF2-HM**:PC[71]BM blend was slightly increased compared for pure polymer one (Table 6.3). This could be explained by the almost unchanged standing lamellae (i.e. face-on polymer orientation) in the presence of 60% of PC[71]BM, which provide the holes an efficient pathway perpendicular to the substrate.

As stated above, similar mixed, edge-on or face-on, polymer orientations in thin films have been reported before for fluorinated copolymers [128,129]. However, the reasons that are leading to this favorable polymer organization are still under debate [172]. For instance, Zhou et al. suggested that owing to the strong tendency of fluorinated copolymers to form aggregates, preferable lamellar orientations could be controlled by the thin film processing conditions [11]. In the work of Zhao et al., the authors stated that processing additives could promote “face-on” polymer backbone orientation [12]. In order to address this question further, we performed a similar study on a non-fluorinated analog of **PF2**. The results will be described in the following.

6.3 Study on non-fluorinated copolymer

To explore the influence of fluorine atoms on the polymer opto-electronic properties a non-fluorinated counterpart (**PF0**) with identical backbone and alkyl side chains than **PF2** has been synthesized by the group of Dr. Nicolas Leclerc. Chemical structures of **PF0** and **PF2** are illustrated in Fig. 6.13. The M_n of the final non-fluorinated copolymer was estimated to be around 43 kg/mol. We therefore compare the results with those obtained on the

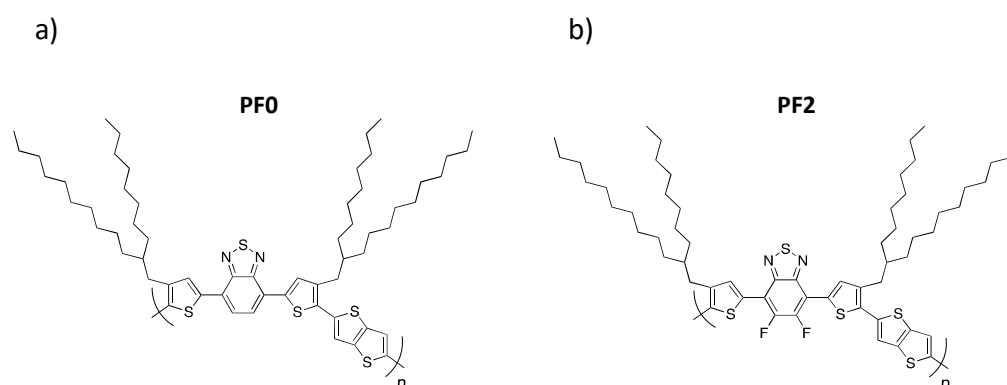


Figure 6.13: Chemical structures of a) non-fluorinated **PF0** and b) fluorinated **PF2**

fluorinated copolymer with the highest M_n (35 kg/mol).

6.3.1 UV-Vis and electrochemical measurements

Figure 6.14b illustrates the absorption profiles of **PF0** in diluted o-DCB solutions vs different temperatures and in thin films. The absorption spectra for **PF2-HM** in the same conditions are included for comparison (Fig. 6.14a).

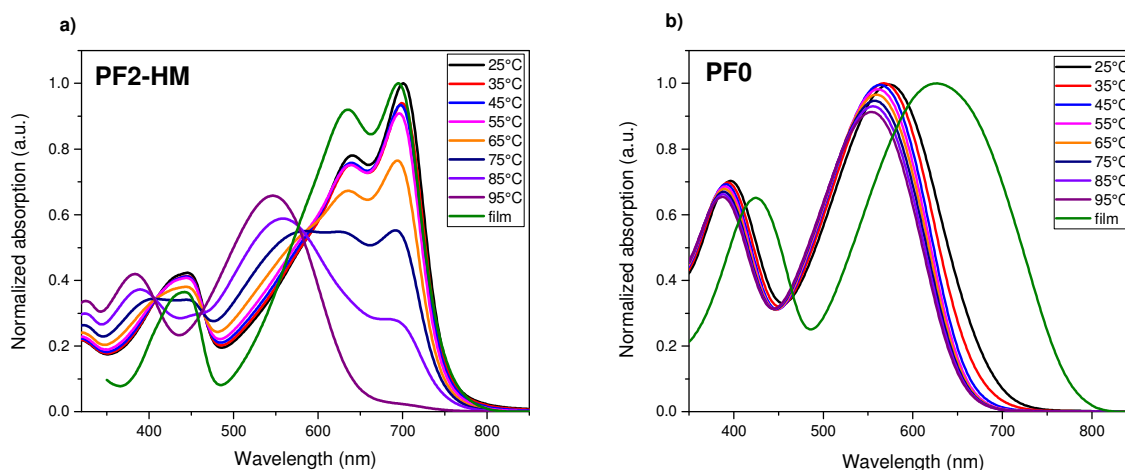


Figure 6.14: Absorption spectra of a) **PF2-HM** and b) **PF0** in solutions vs temperatures and thin films

In contrast to the fluorinated copolymer, **PF0** does not show any signature of aggregation in solution. Increasing the temperature of the solution led to a slight blue shift without a notable change in the spectral shape. On the other hand, a significant red shift was observed when going from solution to solid state indicating that intermolecular interactions exist in **PF0** and are more pronounced in solid state. These results reveal that incorporation of fluorine atoms into the polymer backbone leads to much stronger chain interactions that reduce its solubility in o-DCB. Moreover, although the E_g^{opt} in thin films for both were close to each other, the spectral features were quite different. The double peak at high wavelength seen for **PF2-HM** points out that the presence of fluorine atoms in the backbone considerably enhances the crystallinity.

UV-Vis absorption measurements were also performed for polymer:PC[71]BM BHJ blends and compared to pure polymer spectra (Fig. 6.15). The absorption profiles demonstrate very different behaviors for both polymers when PC[71]BM is present in the film. The still

observed low energy double peak for **PF2-HM**:PC[71]BM indicates that the polymer crystallinity is not disturbed by the PC[71]BM presence. However, for **PF0** copolymer the spectral shape after blending with PC[71]BM is more substantially altered, pointing out a stronger impact of PC[71]BM on the polymer organization.

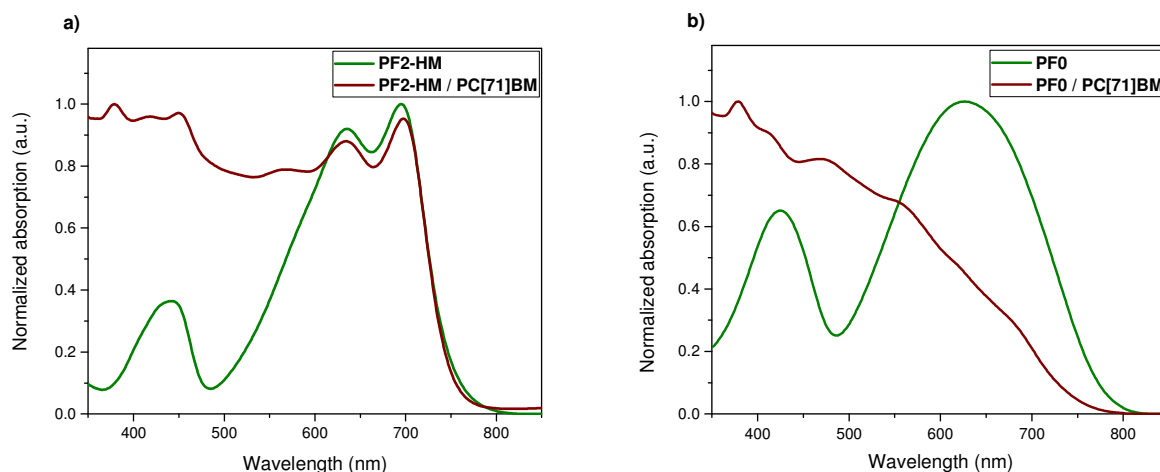


Figure 6.15: Absorption profiles of thin films based on a) **PF2-HM** and b) **PF0** copolymers in pure materials (green) and BHJ blends (brown) at a polymer:fullerene ratio of 1:1.5

CV measurements clearly demonstrate the effect of two fluorine atoms on FMO energy levels. As expected, both HOMO and LUMO levels of **PF20-HM** are deeper about 0.2 eV than those of **PF0** [123,124].

Table 6.4: Opto-electronic properties of **PF2-HM** and **PF0** copolymers

	HOMO (eV)	LUMO (eV)	E_g^{opt} (eV)	M_n (g/mol)	PDI
PF2-HM	-5.42	-3.83	1.59	35 000	1.7
PF0	-5.20	-3.63	1.57	43 000	1.4

6.3.2 Photovoltaic properties

As concluded from the UV-Vis measurements, non-fluorinated copolymer does not show any aggregation tendency in solution. Thus, spin-coating from hot or warm solutions should in principle not affect thin film quality. However, in order to maintain similar conditions as for fluorinated copolymer, all the BHJ layers were cast from hot solutions. PV devices were fabricated in “inverted” architectures (Glass/ITO/PEIE/polymer:PC[71]BM/MoO₃/Ag), identical to that of fluorinated solar cells. Spin-coating speed, acceleration and time were set to 600 rpm, 200 rpm/s and 180 s, respectively. All the solar cells were tested under standardized AM1.5 conditions. The active area of 0.12 cm² was defined with a shadow mask.

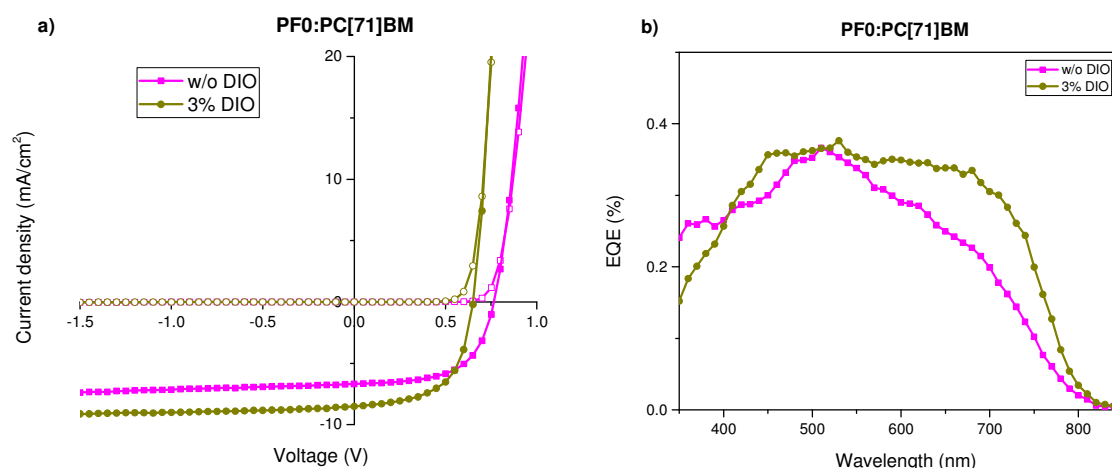


Figure 6.16: a) (J-V) characteristics in the dark (open symbols) and under standard AM1.5G (100 mW/cm²) illumination (closed symbols) and b) EQE curves of **PF0:PC[71]BM** solar cells processed with or without additives (D:A ratio is 1:1.5)

Figure 6.16 represents best obtained (J-V) and EQE curves for **PF0:PC[71]BM** devices. The addition of a small amount of co-solvent (3% v/v DIO) slightly enhanced the final solar cell performance mainly due to an improvement in J_{sc} . This could be due to less pronounced phase separation and smaller domains caused by the additive [83,153,154]. On the other hand, the gain in J_{sc} was partially compensated by the loss in V_{oc} of the devices. The observed decrease in V_{oc} of the devices processed with DIO could be due to an increase of **PF0** crystallinity in blends that in turn could promote a reduction in effective optical band

gap [173]. It should be noted that the active layer thicknesses of optimized devices based on non-fluorinated copolymer were significantly thinner than for fluorinated devices. To compare both polymers in similar conditions, keeping the D:A ratio constant, the concentration of **PF0**:PC[71]BM solutions were increased up to 20 mg/ml with respect to copolymer content. Average organic layer thicknesses of fabricated solar cells were measured to be ≈ 210 nm. All the average PV parameters are listed below in Table 6.5. For comparison, data for **PF2-HM**:PC[71]BM are also included.

Table 6.5: Average PV parameters of BHJ devices based on fluorinated and non-fluorinated copolymers. Acceptor material: PC[71]BM. D:A ratio 1/1.5.

	Additive	V _{oc} (mV)	J _{sc} (mA/cm ²)	FF (%)	PCE (%)	R _s (Ω)	R _{SH} (Ω)	Thickness (nm)
PF2-HM	-	770 \pm 5	17.9 \pm 0.4	69.2 \pm 2	9.54 \pm 0.3	50.5 \pm 4	5 \times 10 ⁵	265 \pm 5
PF0	-	765 \pm 5	6.7 \pm 0.1	58.6 \pm 2	3.01 \pm 0.1	210 \pm 10	5 \times 10 ⁴	140 \pm 10
	3% DIO	650 \pm 5	8.6 \pm 0.2	59.2 \pm 1	3.30 \pm 0.1	110 \pm 20	7 \times 10 ⁶	140 \pm 10
	-	700 \pm 5	5.2 \pm 0.5	46.1 \pm 1	1.70 \pm 0.1	500 \pm 20	3 \times 10 ⁴	210 \pm 10

As seen from Table 6.5, performances of thicker **PF0** based devices were considerably lower compared to thinner ones and suffered mainly from FFs. This decrease in FF when going for thick active layers could probably due to impeded charge carrier mobilities in blends. The importance of carrier mobility for device FFs was recently illustrated [98,174,175]. These PV results clearly demonstrate the importance of fluorine substitution into the copolymer backbone. The V_{oc} values of solar cells well corroborate with the HOMO energy level differences of both copolymers. Significant differences in PCEs of devices based on both materials arise from different J_{sc}s and FFs. This could be related to the discrepancies in active layer morphologies and in polymer microstructures. Possible reasons causing such considerable differences in device performances will be addressed in the coming sub-sections. Solar cell parameters for the best devices are summarized in Table 6.6. For visual comparison, J-V curves of the best devices are given in Fig. 6.17.

Table 6.6: Best PV parameters of BHJ devices based on fluorinated and non-fluorinated copolymers. Acceptor material: PC[71]BM. D:A ratio 1/1.5.

	Additive	V _{oc} (mV)	J _{sc} (mA/cm ²)	FF (%)	PCE (%)	R _s (Ω)	R _{sh} (Ω)	Thickness (nm)
PF2-HM	-	770	17.9	71.3	9.80	47	6x10 ⁵	265±5
PF0	-	760	6.77	60.3	3.1	200	6x10 ⁴	140±10
	-	700	5.55	46.6	1.81	509	5x10 ⁴	210±10

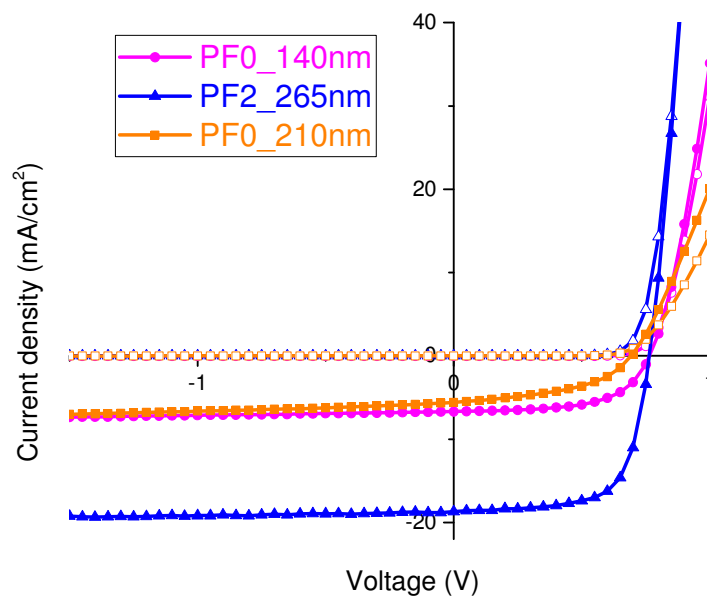


Figure 6.17: (J-V) characteristics in the dark (open symbols) and under standard AM1.5G (100 mW/cm²) illumination (closed symbols) for the best BHJ devices for the fluorinated polymer and two active layer thicknesses for the non-fluorinated one.

6.3.3 Charge transport study

To better understand the influence of backbone fluorination on the copolymer properties 3-D charge transport study has been carried out. Device elaboration procedures for both were identical (Section 6.2.3). Figure 6.18 shows output (left) and saturation transfer (right) curves of BC-BG OFETs based on pure fluorinated (a, b) and non-fluorinated (c, d) copolymers.

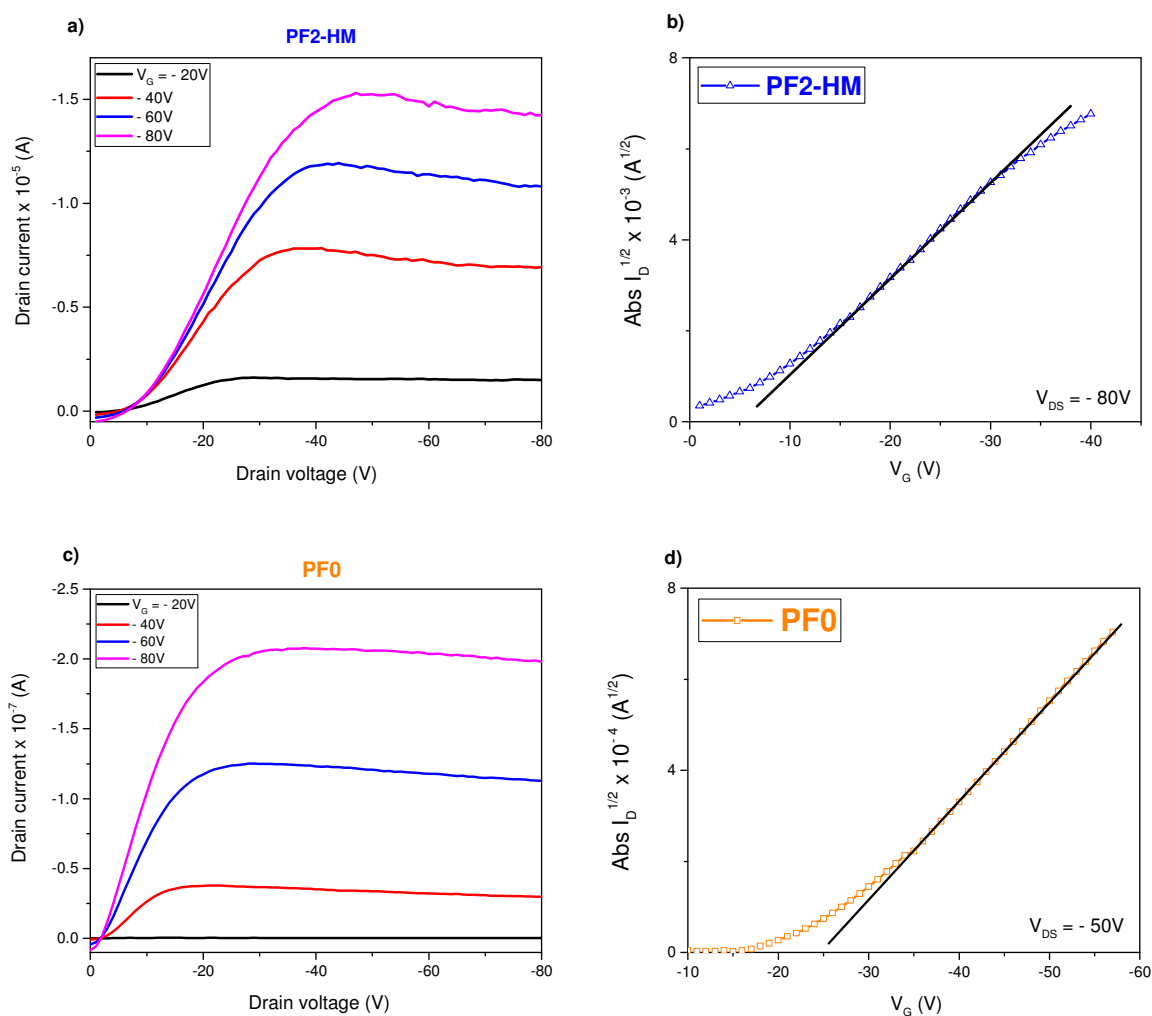


Figure 6.18: Output (left) and transfer (right) characteristics of OFETs based on **PF2-HM** and **PF0** copolymers. Black solid lines represent the slopes used to estimate hole mobility values

Extracted μ_h^{OFET} values in saturation regime were around $(1.2 \pm 0.2) \times 10^{-2}$ and $(1.3 \pm 0.3) \times 10^{-4}$ cm^2/Vs for **PF2-HM** and **PF0**, respectively, pointing out that copolymer backbone fluorination led to an almost two orders of magnitude improvement in horizontal hole mobility.

Out-of-plane hole mobilities were probed in pure copolymers and in blends using SCLC diodes.

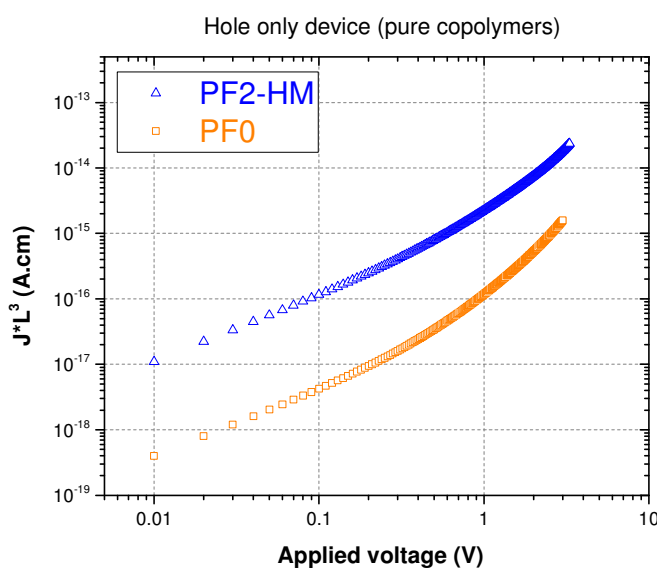


Figure 6.19: Thickness-scaled current-voltage characteristics of hole-only SCLC devices based on **PF2-HM** and **PF0** copolymers

Figure 6.19 compares current density-voltage curves of SCLC diodes based on pure fluorinated and non-fluorinated copolymers. Calculated μ_h^{SCLC} values were $(0.85 \pm 0.05) \times 10^{-2}$ and $(2.7 \pm 0.8) \times 10^{-4}$ cm^2/Vs , respectively. Here, we also found very significant differences for both materials. These observations suggest that backbone fluorination indeed strongly influence the electronic properties of the final copolymer. Interestingly, charge transport anisotropy was low for both copolymers.

In order to maintain similar conditions to OPV devices, out-of-plane hole mobilities of both copolymers were tested in polymer:fullerene BHJ blends at a ratio of 1:1.5. The presence of 60% of PC[71]BM in blends resulted in opposite tendencies for both materials (Fig. 6.20).

While μ_h^{SCLC} of the fluorinated copolymer slightly increased after blending, the non-fluorinated counterpart μ_h^{SCLC} significantly dropped in blends. This lies in agreement with solid state UV-Vis measurements in blends where it has been shown that the addition of PC[71]BM substantially changed the absorption spectrum of **PF0** in the low energy part. Moreover, the significantly decreased FF in **PF0** based devices when going to thicker films could also be due to low μ_h^{SCLC} in polymer:fullerene blends. All these observations could indicate that the microstructure of the fluorinated copolymer is more resistant to the presence of PC[71]BM than the one of its non-fluorinated counterpart. For convenience, all the in-plane and out-of-plane hole mobility values are summarized in Table 6.7.

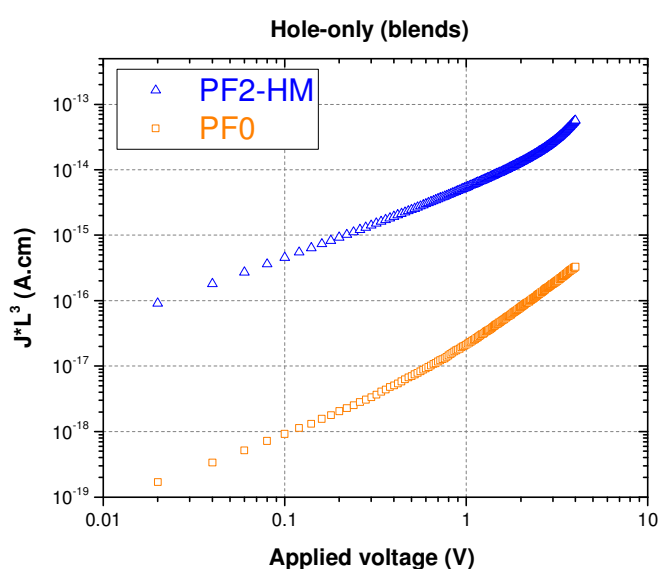


Figure 6.20: Thickness-scaled current-voltage characteristics of hole-only SCLC devices based on polymer:PC[71]BM blends at a ratio of 1:1.5

Table 6.7: Average hole mobilities in pure copolymers and in polymer:fullerene blends

	Pure materials		BHJ blends
	μ_h^{OFET} (cm ² /Vs)	μ_h^{SCLC} (cm ² /Vs)	μ_h^{SCLC} (cm ² /Vs)
PF2-HM	$(1.2 \pm 0.2) \times 10^{-2}$	$(0.85 \pm 0.05) \times 10^{-2}$	$(8.7 \pm 1.3) \times 10^{-3}$
PF0	$(1.3 \pm 0.3) \times 10^{-4}$	$(2.7 \pm 0.8) \times 10^{-4}$	$(5.7 \pm 0.7) \times 10^{-5}$

6.3.4 Morphological characterizations

6.3.4.1 GIWAXS measurements

In order to deeply understand the influence of backbone fluorination on copolymer microstructure, GIWAXS characterizations were performed. Device preparation procedures were the same for fluorinated and non-fluorinated copolymers (see section 6.2.4). Figure 6.21 below illustrates GIWAXS patterns of pure **PF2-HM** and **PF0** copolymers. The non-fluorinated polymer shows a lower degree of alignment compared to the fluorinated one. Nevertheless, two preferred lamellar orientations can be clearly distinguished: flat-lying lamellae (“edge-on”) with in-plane π -stacking direction (blue arrows in Fig. 6.21b) and standing lamellae (“face-on”) with out-of-plane π -stacking direction (blue arrows in Fig.

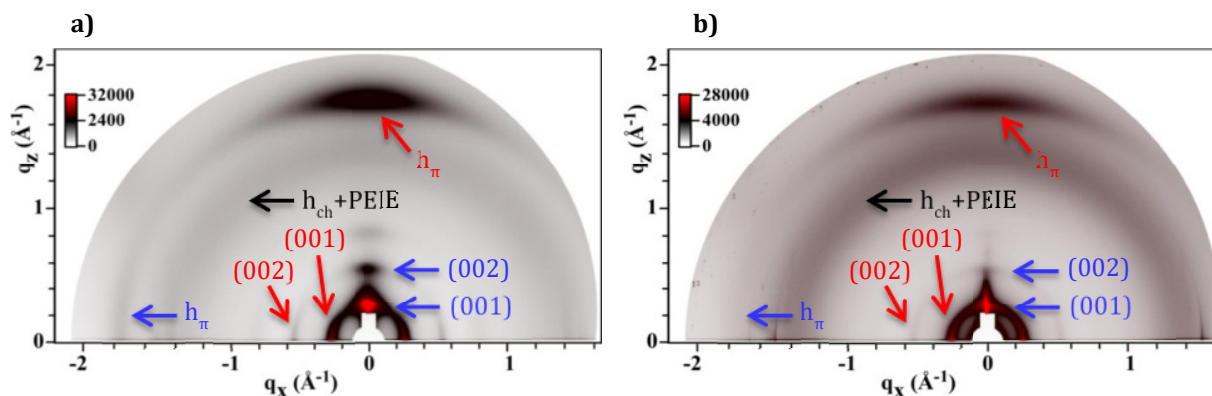


Figure 6.21: GIWAXS patterns of pure a) **PF2-HM** and b) **PF0** copolymers

6.21b). Interestingly, though the self-organization of polymer chains in non-fluorinated copolymer was less pronounced, both of them showed similar set of oriented lamellae in pure thin films. These results clearly indicate that fluorination is not the major driving force for the very particular mixed lamellae. Moreover, in a recent work by Prof. Thomas Heiser's team [145] the morphology of a copolymer (T_b) with the same backbone than **PF0** but with much shorter alkyl side chains (Fig. 6.1c) was investigated. In that study, GIWAXS experiments showed less ordered but exclusively flat-lying lamellae (“edge-on”) with π -stacking direction parallel to the substrate. Comparing this study with our results, we can conclude that the longer alkyl side chains on **PF0** are responsible for the polymer backbone “face-on” orientation. Surprisingly, π - π^* stacking distances ($h_{\pi, \text{fluorinated}} = 3.53 \text{ \AA}$ vs $h_{\pi, \text{non-}}$

fluorinated = 3.57 Å) and correlation lengths ($\xi_{\text{fluorinated}} = 4 \text{ nm}$ vs $\xi_{\text{non-fluorinated}} = 4 \text{ nm}$) for both **PF0** and **PF2** copolymers were rather similar, which is counterintuitive if we consider that the fluorine atoms enhance the intermolecular interactions (as revealed by the absorption spectra).

These structural investigations allow nevertheless a better understanding of the charge transport properties. On one hand, the weak charge transport anisotropy for both materials can be explained by the presence of mixed phase orientations. On the other hand, the slightly lower alignment in non-fluorinated copolymer (larger angular distribution of the h_{π} diffraction peak) points out more structural disorder that may lead to the observed lower 3-D hole mobilities. In this sense, the higher crystallinity of **PF2-HM** compared to **PF0** could indeed be attributed to the fluorine atoms.

To investigate the impact of PC[71]BM on the **PF0** microstructure, copolymer:fullerene blends at various ratios were characterized by GIWAXS. Structural profiles of the **PF0**-based samples are given in Fig. 6.22. According to the results, preferable lamellar

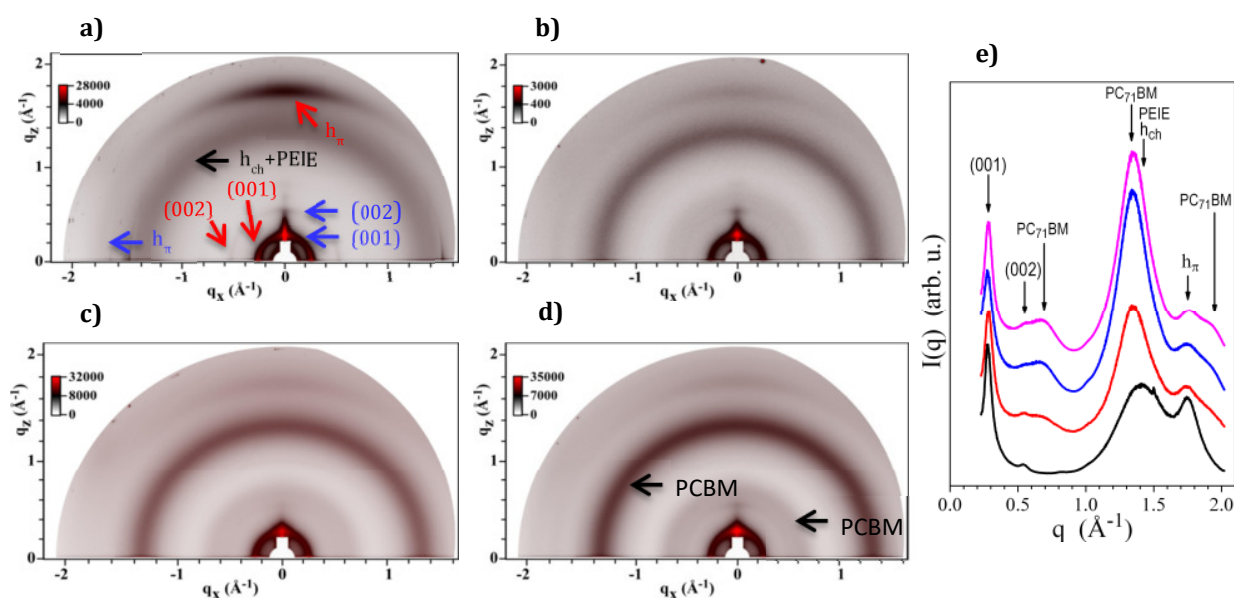


Figure 6.22: GIWAXS patterns of a) pure **PF0** copolymer; b) **PF0**:PC[71]BM at 1:1 ratio; c) 1:1.5 ratio; and d) 1:2 ratio. e) Radial profiles of GIWAXS patterns of pure polymer film (black), polymer:fullerene blend film ratio of 1:1 (red), 1:1.5 (blue) and 1:2 (magenta)

orientations were notably altered towards disordered morphology in the presence of PC[71]BM. On the other hand, as seen from the radial profiles (Fig. 6.22e) though π -stacking and lamellar reflections were less pronounced in blend compared to pure copolymer, they were still preserved in blends even at a ratio of 1:2. Therefore, decreased μ_h^{SCLC} in **PF0**:PC[71]BM blends (1:1.5) compared to the pure copolymer may be due to the increased structural disorder after adding PC[71]BM. Furthermore, the diverse behavior of fluorinated and non-fluorinated copolymers in the presence of PC[71]BM suggest that the enhanced intermolecular strength caused by the backbone fluorination improves the robustness of polymer lamellae against PC[71]BM buckyballs.

6.3.4.2 Atomic force microscope characterizations

To compare blend morphologies based on fluorinated and non-fluorinated copolymers complementary AFM measurements were performed. This was especially done to assess the sizes of D and/or A domains that could result from poor miscibility or strong phase separation. The thin film elaboration procedure was the same as for OPV devices. The AFM

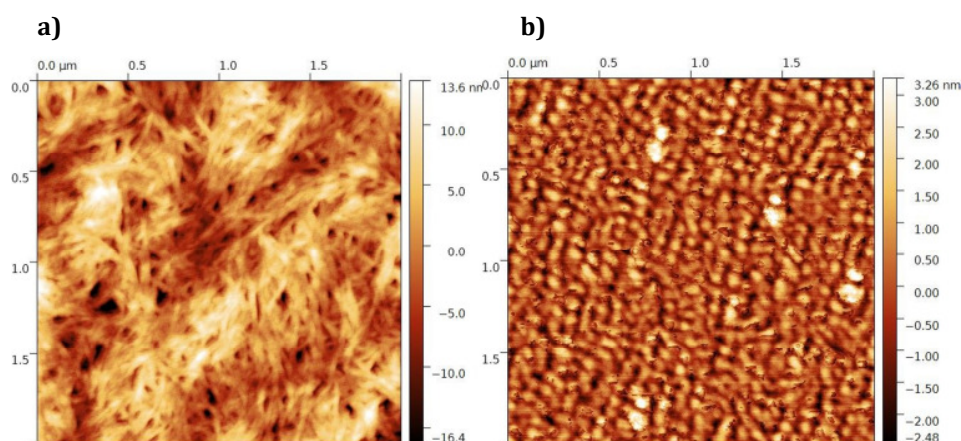


Figure 6.23: AFM images of a) **PF2-MM**:PC[71]BM and b) **PF0**:PC[71]BM thin films. D:A ratio in both cases was 1:1.5

images of **PF2-MM**:PC[71]BM and **PF0**:PC[71]BM thin films given in Fig. 6.23 reveal quite different morphologies for both blends. **PF2-MM**:PC[71]BM showed a fibrous morphology composed of well mixed nanometer-sized domains with negligible phase separation. In

contrast, **PF0**:PC[71]BM morphology was composed of granular structures. It is likely that the latter yields a lower D/A interfacial area and therefore a reduced J_{sc} .

6.4 Charge-carrier recombination dynamics in photovoltaic devices based on fluorinated and non-fluorinated copolymers

To investigate the influence of polymer backbone fluorination on the charge-carrier recombination in the corresponding photovoltaic devices, stationary and transient measurements were performed. Optimized solar cells based on the fluorinated copolymer with medium M_n (**PF2-MM**) and the non-fluorinated copolymer (**PF0**) were studied. In both cases, PC[71]BM at a D:A weight ratio of 1:1.5 was utilized. The same device architectures (ITO/PEIE/active layer/MoO₃/Ag) for both were used.

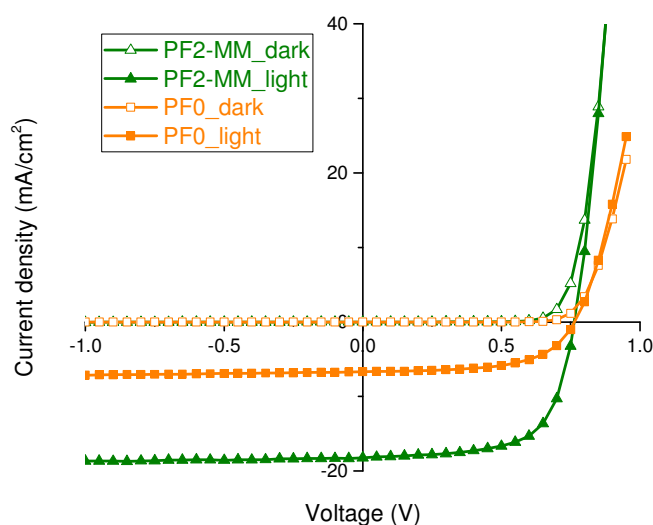


Figure 6.24: J-V characteristics of PF2-MM and PF0 based photovoltaic devices under dark (open symbols) and 1 sun conditions

Table 6.8: PV parameters of **PF2-MM** and **PF0** based photovoltaic devices under 1 sun conditions

	V_{oc} (mV)	J_{sc} (mA/cm ²)	FF (%)	PCE (%)	Thickness (nm)
PF2-MM	766	18.2	66	9.2	235
PF0	768	6.6	60	3.1	125

First, standard J-V measurements have been performed on optimized solar devices based on both copolymers. Figure 6.24 illustrates J-V curves under dark and 1 Sun illumination. As has already been discussed before, devices based on both materials perform very differently. Photovoltaic parameters under 1 sun conditions are listed in Table 6.8. The PCE of **PF2-MM** based device was almost a factor of three higher than for **PF0**. Main differences in performances came from J_{sc} and FF of the respective devices.

To go further, stationary photovoltaic measurements as a function of light intensity have been carried out on the same devices using neutral optical filters. The photo-generated current-density follows an almost linear dependence with incident light intensity (P_{in}) in

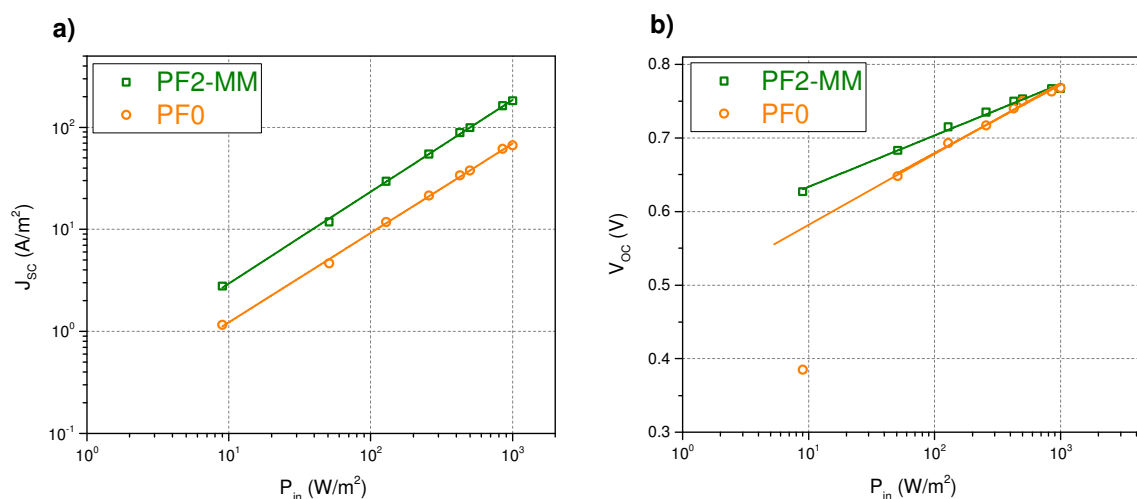


Figure 6.25: a) J_{sc} plots as a function of illuminated light power (P_{in}) in log-log scale for both materials. Solid lines represent fits using power-law dependence for J_{sc} and P_{in} with a similar power of ≈ 0.9 for both; b) V_{oc} as a function of P_{in} for both copolymers. Solid lines are fits using single logarithmic laws described by the Eq. 6.1.

log-log plot as, demonstrated in Fig. 6.25a. A power-law dependence between J_{SC} and P_{in} with a power of ≈ 0.9 reasonably fits all the experimental data points.

V_{oc} versus light intensity exhibits a different behavior depending on the copolymer, as shown in Fig. 6.25b. For both materials, at $P_{in} > 50 \text{ W/m}^2$, V_{oc} obeys the following equation [176]:

$$V_{oc} = \frac{E_{gap}}{q} - \frac{k_B T}{q} \ln \left[\frac{(1-P)\gamma N_c^2}{P} \right] + \alpha \frac{k_B T}{q} \ln(P_{in}) \quad (6.1)$$

where E_{gap} is the effective band gap, q is the elementary charge, α is a recombination pre-factor depending on the dominating charge-carrier recombination mechanism, k_B the Boltzmann constant, T the temperature and P_{in} the incident light power. One would expect α approaching one for trap-free and to be higher than one when trap-limited recombination dominates [176]. As depicted in Fig. 6.25b, V_{oc} follows Eq. (6.1) with $\alpha \approx 1.2$ for **PF2-MM** based devices studied within the whole light intensity range. As α is close to 1, we conclude that the trap-free recombination dominates in **PF2-MM** based PV cells. However, for **PF0** based cells at $P_{in} > 50 \text{ W/m}^2$, $\alpha \approx 1.6$ which is substantially higher than unity. Moreover, at low light intensities, an even higher value of α (≈ 9.7) is needed to fit Eq. (6.1) for **PF0**.

To confirm these observations, transient techniques i.e. transient photo-voltage (TPV) and charge extraction (CE) have been applied on the same devices [135,177]. The V_{oc} was controlled by the light intensity from white LEDs. An extra ΔV_{oc} , which was generated by a pulsed green LED, was fixed to be smaller than 5% of the given V_{oc} to maintain the small perturbation regime (details are in Chapter 3). Thus, charge-carrier recombination time ($\tau_{\Delta n}$) in the small perturbation regime can usually be given as [135]:

$$\tau_{\Delta n} = \tau_{\Delta n 0} e^{-\beta V_{oc}} \quad (6.2)$$

Table 6.9: Fitting parameters obtained for different devices using Eq-s. 6.2 and 6.3

	$\tau_{\Delta n0}$ (μs)	β (V^{-1})	n_0 (cm^{-3})	γ (V^{-1})	β/γ
PF2-MM	9.5×10^5	15.9	2×10^{12}	13.2	1.2
PF0	-	-	3×10^{14}	5.9	-

The dependence of $\tau_{\Delta n}$ on the V_{OC} is depicted in Fig. 6.26a. Best fitting parameters are summarized in Table 6.9. It should be noted that **PF0** based samples had two different regimes at high and low light intensities and therefore do not fit the Eq. 6.2 in the studied range. Eq. 6.2 fits the experimental data only at $V_{OC} > 600$ mV. At low light power the **PF0** $\tau_{\Delta n}$ saturates, becoming almost insensitive to the variations in V_{OC} . On the other hand, at high light intensities both samples show almost the same β factor.

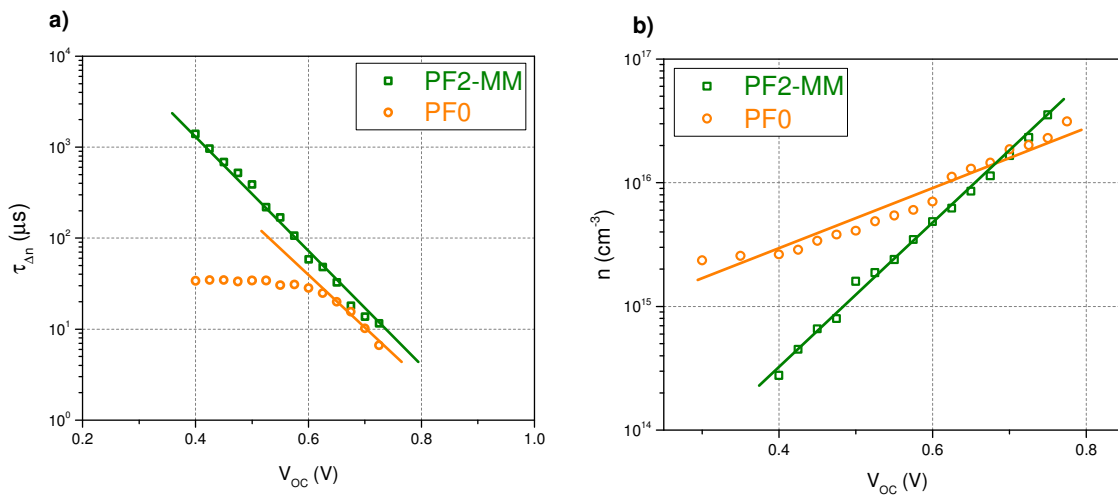


Figure 6.26: a) Dependences of charge-carrier recombination time in small perturbation regime ($\tau_{\Delta n}$) versus V_{OC} . Best fits using Eq. 6.2 are shown in solid lines with fitting parameters in Table 6.9; b) Charge-carrier concentration n as a function of V_{OC} . Solid lines are the best fits using the Eq. 6.3 with fitting parameters listed in Table 6.9.

CE measurements were performed using the same white LED pulse. To ensure the same charge-carrier concentration as in previous TPV measurements the pulse of the light was set to a relatively long time. The extracted n values were corrected taking into account the charges accumulated at the electrodes [177]. For both materials, n follows an exponential dependence as a function of V_{OC} as shown in Fig. 6.26b and given in the following:

$$n = n_0 e^{\gamma V_{oc}} \quad (6.3)$$

with fitting parameters that are summarized in Table 6.9.

Considerable differences for n_0 and γ have been found depending on the materials. The combination of both techniques allows us to plot $\tau_{\Delta n}$ as a function of n (Fig. 6.27). Namely, combination the Eq-s. 6.2 and 6.3 gives:

$$\tau_{\Delta n} = \tau_{\Delta n 0} \left(\frac{n_0}{n} \right)^{\frac{\beta}{\gamma}} \quad (6.4)$$

where β/γ for **PF2-MM** is constant and equal to 1.2 in the investigated range. In contrast, for **PF0**, high charge-carrier concentration and low charge-carrier concentration (below $7 \times 10^{15} \text{ cm}^{-3}$) regimes can be clearly distinguished. Both regimes follow the Eq. 6.4 but with different β/γ values. For **PF0**, β/γ values is ≈ 0 at charge-carrier concentrations n below $7 \times 10^{15} \text{ cm}^{-3}$ and equal to about 1.2 above this concentration. From the Eq. 6.4 charge-

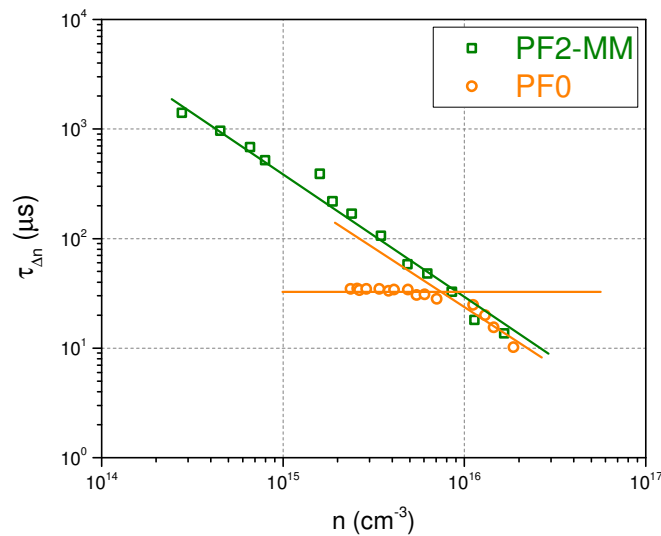


Figure 6.27: Dependence of charge-carrier recombination time in small perturbation regime ($\tau_{\Delta n}$) versus the charge-carrier concentration n for both copolymers. Solid lines are the best fits to the experimental data points using Eq. 6.4

carrier dynamics can be expressed as follows [177]:

$$\frac{dn}{dt} \approx - \frac{n^{(1+\beta/\gamma)}}{(1 + \beta/\gamma)\tau_{\Delta n_0} n_0^{\beta/\gamma}} \quad (6.5)$$

where $1+\beta/\gamma$ is the recombination order. Thus, within all the investigated range for **PF2-MM** and at $n > 7 \times 10^{15} \text{ cm}^{-3}$ for **PF0**, the recombination order is close to ≈ 2 ($\beta/\gamma \approx 1.2$) meaning that bimolecular recombination mechanism is dominant. Therefore, fill factors of solar cells under 1 sun illumination ($n \gg 7 \times 10^{15} \text{ cm}^{-3}$) did not show significant differences. On the other hand, for **PF0** at $n < 7 \times 10^{15} \text{ cm}^{-3}$, the recombination order is close to ≈ 1 ($\beta/\gamma \approx 0$) meaning that trap-limited recombination mechanism is dominant. The transition charge-concentration ($7 \times 10^{15} \text{ cm}^{-3}$) from trap-limited to bimolecular recombination regime for **PF0** is a rough estimate of the electrically-active trap-concentration present in the **PF0:PC[71]BM** blend. A possible origin for such traps could be residual PC[71]BM molecules that remain dissolved in the polymer domains.

In conclusion, both copolymers show very distinct properties in solar devices. While the fluorinated (**PF2-MM**) copolymer represents a clear trap-free recombination mechanism, the non-fluorinated (**PF0**) counterpart suffers from the trap-limited one at lower charge-carrier concentrations. It is possible that the addition of fluorine to the polymer backbone lowers the solubility of PC[71]BM in the polymer domains (higher domain purity) leading to a reduced number of recombination sites.

6.5 Conclusion

In summary, semiconducting low band-gap copolymers based on di-fluorinated (**PF2**) and non-fluorinated (**PF0**) benzothiadiazole unit have been investigated. Through the study of charge transport vs M_n for fluorinated copolymers it was found that 3-D hole mobilities in pure materials were almost insensitive to the molecular weights meaning that intermolecular connectivity could be sufficient even for a copolymer with the lowest M_n . Moreover, all the **PF2** copolymers showed relatively low charge transport anisotropy in pure films. Out-of-plane hole and electron mobilities in **PF2-MM/PF-HM:fullerene** blends

were relatively high and balanced ($\approx 10^{-2}$ cm²/Vs). Structural investigations showed ordered lamellas with mixed phase orientations (“edge-on” and “face-on”) confirming the isotropic transport of **PF2** copolymers. **PF0** showed less ordered nature but with similar set of preferred lamellar orientations supporting the isotropic hole transport for **PF0** as well. Thus, taking into account a recent report by Fall et al. [145], we clearly concluded that long alkyl side chains rather than fluorine atoms induced polymer chain “face-on” orientation. Almost two orders of magnitude difference in hole mobilities in pure materials was attributed to the stronger polymer inter-chain interactions and to higher crystallinity of **PF2-HM** compared to **PF0**. Charge-carrier dynamics study revealed different recombination mechanisms depending on the copolymer. It was found that recombination in **PF0** based photovoltaic devices in low charge-carrier concentration regime were mainly limited by traps. In contrast, in **PF2-MM** based devices trap-free or bimolecular recombination mechanism was dominating within all the investigated range.

Finally, bulk heterojunction devices based on fluorinated and non-fluorinated copolymers showed quite diverse performances. Under similar conditions, while the maximum PCE of **PF0** devices hardly reached 3%, solar cells based on **PF2-HM** showed a PCE of 9.8%.

Chapter 7: General conclusion

7 General conclusion

Photovoltaics remain an important green technology to replace traditional energy sources in the future. The attention paid in recent years in terms of research and development of main emerging photovoltaic technologies i.e. organic, hybrid, dye-sensitized and perovskite solar cells, has improved the knowledge and contributed to improve the performances of these technologies and make them economically viable. Today, in the field of organic photovoltaics, best performing solar cells are based on vapor deposited bulk heterojunctions which are composed of a blend of two different organic semiconducting materials (electron-donor and electron-acceptor). To date, polymer-fullerene blends are among the most investigated material systems. Yet, the complex interrelationships between the chemical structure and material properties that affect the device performances are still only partly understood.

Within this framework, the present thesis was dedicated to in-depth material investigations including charge transport, morphological and photovoltaic studies on a series of new low band-gap copolymers including different acceptor units. First, two different low band-gap copolymers based on the thieno-pyrrole dione (TPD) acceptor unit have been intensively studied. The main objective of this study was to elucidate the impact of alkyl side chain positions on charge transport, morphological and photovoltaic properties of copolymers. Interestingly, the field-effect hole mobility of the structurally poorly ordered TPD-DTP- β showed a weak dependence on the charge carrier concentration, a signature for low energy disorder, while the hole mobility of the similarly structurally disordered TPD-DTP- α showed a strong charge carrier concentration dependence (high energy disorder). In addition, both vertical and horizontal hole mobility values of TPD-DTP- α were significantly lower than those of TPD-DTP- β . These results point out that structural disorder does not necessary cause energy disorder. DFT calculations reveal the existence of a considerable difference in backbone torsion angles for both copolymers, suggesting that the energy disorder is dominated by the degree of backbone torsion.

The second part of this thesis was devoted to a novel low band-gap copolymer based on pyridal[2,1,3]thiadiazole as an acceptor unit (PPPyT²). The energy band-gap and HOMO level of PPPyT² fit well with the optimum values predicted by Scharber's semi-empirical law. 3-D charge transport investigations on pure polymer films revealed high transport anisotropy, with high in-plane and low out-of-plane mobilities. Introducing PC[71]BM was found to lower the anisotropy, leading to an increased vertical and slightly decreased horizontal hole mobility, without altering the energy disorder. To better understand these results, GIWAXS measurements were performed both on pure polymer and polymer/fullerene blends. Structural results revealed the semi-crystalline nature of PPPyT² with flat-lying lamellae ("edge-on" polymer orientation) that were preserved even in the presence of PC[71]BM, in accordance with the transport results (similar energy disorder for pure materials and blends). Further UV-Vis measurements showed that the amount of amorphous polymer phase increased after blending with PC[71]BM, suggesting that out-of-plane transport is occurring mostly within these disordered domains. Despite initial promising features, BHJ cells based on this material did not perform as good as expected. The relatively low vertical hole mobility caused by the preferentially "edge-on" oriented polymer lamellas strongly confined the FF (< 50%) and therefore the power conversion efficiency ($\approx 4.5\%$).

The last part of this thesis was dedicated to fluorinated copolymers and to the possible impact of backbone fluorination on the opto-electronic and photovoltaic properties. The fluorinated polymer was found to allow efficient charge transport in all three directions. Surprisingly, the hole mobility depended only weakly on the polymer molecular weight, in contrast to the dramatic increase in mobility with M_n generally observed on other polymers. On the other hand, the impact of PC[71]BM on transport was found to depend on M_n . While for the high molecular weight polymer the vertical hole mobility remained almost constant after blending with PC[71]BM, it dropped by factor of 4 for the lowest molecular weight polymer. It is likely that the interconnectivity among ordered polymer domains was more easily disrupted by the fullerenes for the lowest molecular weight polymer.

GIWAXS measurements revealed the presence of mixed edge-on / face-on lamellae orientations which clarify the origin of the balanced 3D charge transport observed in fluorinated copolymers. In order to identify the contribution of fluorine substitution to the polymer orientation, a non-fluorinated counterpart with identical alkyl side chains has been explored. Though a lower degree of alignment was observed for the non-fluorinated polymer, a mixed orientation (flat-lying and standing lamellae) of the crystalline lamellae has been detected in both polymer films. Based on this finding and taking into account previous results on similar non-fluorinated polymers with smaller side-chains, we could conclude that longer alkyl side chains diminish the driving force for preferential edge-on polymer orientation. This leads to the simultaneous presence of both, edge-on and face-on polymer orientations and to the observed isotropic charge transport in polymers with long alkyl chains (with or without fluorination). The higher mobility observed in the fluorinated polymer correlates with a higher long range structural order. In addition, the charge carrier recombination mechanism was seen to be influenced by the backbone fluorination as well. While in non-fluorinated polymer devices the carrier recombination was essentially trap-assisted, the dominating mechanism in fluorinated polymer devices followed bimolecular recombination kinetics. It is possible that the presence of fluorine atoms reduces the solubility of fullerene in the polymer domains which act as recombination sites. Finally, the good charge transport properties and light harvesting capacity of the fluorinated polymers allowed us to achieve state-of-the-art photovoltaic performances, with a FF exceeding 70% and a maximum power conversion efficiency of 9.8%.

All the experimental work and analytical tools conducted within this interdisciplinary project gave me a rewarding scientific experience. Moreover, the international collaboration (Kazakhstan-France), established on the basis of this thesis, allowed me to directly take part in the development of the new organic photovoltaics laboratory at the National Laboratory Astana, Kazakhstan. I hope that this work will help, even on a modest scale, to better understand the complex interrelation between polymer structure, thin film morphology and device properties. To achieve further progress and finally reach the market, deeper understanding of polymer chemistry and device physics remain essential. It is likely that it will require the design and synthesis of novel, still better performing and

stable materials (donors and/or acceptors) as well as advances in morphology control during device processing.

References

1. Darling, S. B.; You, F. The case for organic photovoltaics. *RSC Adv.* **2013**, *3*, 17633–17648.
2. Lewis, N. S. Research opportunities to advance solar energy utilization. *Science* **2016**, *351*, aad1920–aad1920.
3. Park, N.-G. Perovskite solar cells: an emerging photovoltaic technology. *Materials Today* **2015**, *18*, 65–72.
4. Shirakawa, H.; Louis, E. J.; MacDiarmid, A. G.; Chiang, C. K.; Heeger, A. J. Synthesis of electrically conducting organic polymers: halogen derivatives of polyacetylene, (CH)_x. *J. Chem. Soc., Chem. Commun.* **1977**, 578–580.
5. Tang, C. W. Two-layer organic photovoltaic cell. *Applied Physics Letters* **1986**, *48*, 183–185.
6. Yu, G.; Gao, J.; Hummelen, J. C.; Wudl, F.; Heeger, A. J. Polymer Photovoltaic Cells: Enhanced Efficiencies via a Network of Internal Donor-Acceptor Heterojunctions. *Science* **1995**, *270*, 1789–1791.
7. Shaheen, S. E.; Brabec, C. J.; Sariciftci, N. S.; Padinger, F.; Fromherz, T.; Hummelen, J. C. 2.5% efficient organic plastic solar cells. *Applied Physics Letters* **2001**, *78*, 841–843.
8. Padinger, F.; Rittberger, R. S.; Sariciftci, N. S. Effects of Postproduction Treatment on Plastic Solar Cells. *Advanced Functional Materials* **2003**, *13*, 85–88.
9. Rispens, M. T.; Meetsma, A.; Rittberger, R.; Brabec, C. J.; Sariciftci, N. S.; Hummelen, J. C. Influence of the solvent on the crystal structure of PCBM and the efficiency of MDMO-PPV:PCBM “plastic” solar cells. *Chemical Communications* **2003**, 2116–2118.
10. and, K. M. C.; McGehee, M. D. Conjugated Polymer Photovoltaic Cells. *Chemistry of Materials* **2004**, *16*, 4533–4542.
11. Liu, Y.; Zhao, J.; Li, Z.; Mu, C.; Ma, W.; Hu, H.; Jiang, K.; Lin, H.; Ade, H.; Yan, H. Aggregation and morphology control enables multiple cases of high-efficiency polymer solar cells. *Nature Communications* **2014**, *5*, 5293.
12. Zhao, J.; Li, Y.; Yang, G.; Jiang, K.; Lin, H.; Ade, H.; Ma, W.; Yan, H. Efficient organic solar cells processed from hydrocarbon solvents. *Nature Energy* **2016**, *1*, 15027.
13. Geoghegan, M.; Hadziioannou, G. *Polymer Electronics*; Oxford University Press, 2013.
14. Knupfer, M. Exciton binding energies in organic semiconductors. *Applied Physics A: Materials Science & Processing* **2003**, *77*, 623–626.
15. Hummer, K.; Ambrosch-Draxl, C. Oligoacene exciton binding energies: Their dependence on molecular size. *Physical Review B* **2005**, *71*, 081202.
16. van der Horst, J. W.; Bobbert, P. A.; Michels, M. A. J.; Bäessler, H. Calculation of excitonic properties of conjugated polymers using the Bethe–Salpeter equation. *The Journal of Chemical Physics* **2001**, *114*, 6950–6957.
17. Clarke, T. M.; Durrant, J. R. Charge Photogeneration in Organic Solar Cells. *Chemical Reviews* **2010**, *110*, 6736–6767.
18. Deibel, C.; Mack, D.; Gorenflot, J.; Schöll, A.; Krause, S.; Reinert, F.; Rauh, D.; Dyakonov, V. Energetics of excited states in the conjugated polymer poly(3-hexylthiophene). *Physical Review B* **2010**, *81*, 085202.
19. De, S.; Kesti, T.; Maiti, M.; Zhang, F.; Inganäs, O.; Yartsev, A.; Pascher, T.; Sundström, V. Exciton dynamics in alternating polyfluorene/fullerene blends. *Chemical Physics* **2008**, *350*, 14–22.
20. Shaw, P. E.; Ruseckas, A.; Samuel, I. D. W. Exciton Diffusion Measurements in Poly(3-hexylthiophene). *Advanced Materials* **2008**, *20*, 3516–3520.
21. Brédas, J.-L.; Beljonne, D.; Coropceanu, V.; Cornil, J. Charge-Transfer and Energy-Transfer Processes in π -Conjugated Oligomers and Polymers: A Molecular Picture. *Chemical Reviews* **2004**, *104*, 4971–5004.
22. Scharber, M. C.; Mühlbacher, D.; Koppe, M.; Denk, P.; Waldauf, C.; Heeger, A. J.; Brabec, C. J.

- Design Rules for Donors in Bulk-Heterojunction Solar Cells—Towards 10 % Energy-Conversion Efficiency. *Advanced Materials* **2006**, *18*, 789–794.
23. Lin, Y.; Zhan, X. Non-fullerene acceptors for organic photovoltaics: an emerging horizon. *Materials Horizons* **2014**, *1*, 470–488.
24. Zhan, C.; Zhang, X.; Yao, J. New advances in non-fullerene acceptor based organic solar cells. *RSC Adv.* **2015**, *5*, 93002–93026.
25. Nielsen, C. B.; Holliday, S.; Chen, H.-Y.; Cryer, S. J.; McCulloch, I. Non-Fullerene Electron Acceptors for Use in Organic Solar Cells. *Accounts of Chemical Research* **2015**, *48*, 2803–2812.
26. Vandewal, K.; Ma, Z.; Bergqvist, J.; Tang, Z.; Wang, E.; Henriksson, P.; Tvingstedt, K.; Andersson, M. R.; Zhang, F.; Inganäs, O. Quantification of Quantum Efficiency and Energy Losses in Low Bandgap Polymer:Fullerene Solar Cells with High Open-Circuit Voltage. *Advanced Functional Materials* **2012**, *22*, 3480–3490.
27. Ren, G.; Schlenker, C. W.; Ahmed, E.; Subramanian, S.; Olthof, S.; Kahn, A.; Ginger, D. S.; Jenekhe, S. A. Photoinduced Hole Transfer Becomes Suppressed with Diminished Driving Force in Polymer-Fullerene Solar Cells While Electron Transfer Remains Active. *Advanced Functional Materials* **2012**, *23*, 1238–1249.
28. Hoke, E. T.; Vandewal, K.; Bartelt, J. A.; Mateker, W. R.; Douglas, J. D.; Noriega, R.; Graham, K. R.; Fréchet, J. M. J.; Salleo, A.; McGehee, M. D. Recombination in Polymer:Fullerene Solar Cells with Open-Circuit Voltages Approaching and Exceeding 1.0 V. *Advanced Energy Materials* **2012**, *3*, 220–230.
29. Di Nuzzo, D.; Wetzelaer, G.-J. A. H.; Bouwer, R. K. M.; Gevaerts, V. S.; Meskers, S. C. J.; Hummelen, J. C.; Blom, P. W. M.; Janssen, R. A. J. Simultaneous Open-Circuit Voltage Enhancement and Short-Circuit Current Loss in Polymer: Fullerene Solar Cells Correlated by Reduced Quantum Efficiency for Photoinduced Electron Transfer. *Advanced Energy Materials* **2012**, *3*, 85–94.
30. Vandewal, K. Interfacial Charge Transfer States in Condensed Phase Systems. *Annu Rev Phys Chem* **2016**, *67*, 113–133.
31. Sariciftci, N. S.; Smilowitz, L.; Heeger, A. J.; Wudl, F. Photoinduced Electron Transfer from a Conducting Polymer to Buckminsterfullerene. *Science* **1992**, *258*, 1474–1476.
32. Brabec, C. J.; Zerza, G.; Cerullo, G.; De Silvestri, S.; Luzzati, S.; Hummelen, J. C.; Sariciftci, S. Tracing photoinduced electron transfer process in conjugated polymer/fullerene bulk heterojunctions in real time. *Chemical Physics Letters* **2001**, *340*, 232–236.
33. Elumalai, N. K.; Uddin, A. Open circuit voltage of organic solar cells: an in-depth review. *Energy Environ. Sci.* **2016**, *9*, 391–410.
34. Gao, F.; Tress, W.; Wang, J.; Inganäs, O. Temperature Dependence of Charge Carrier Generation in Organic Photovoltaics. *Physical Review Letters* **2015**, *114*, 128701.
35. Scharber, M. C. On the Efficiency Limit of Conjugated Polymer:Fullerene-Based Bulk Heterojunction Solar Cells. *Advanced Materials* **2016**, *28*, 1994–2001.
36. Pelzer, K. M.; Darling, S. B. Charge generation in organic photovoltaics: a review of theory and computation. *Mol. Syst. Des. Eng.* **2016**, *1*, 10–24.
37. Miller, A.; Abrahams, E. Impurity Conduction at Low Concentrations. *Physical Review* **1960**, *120*, 745–755.
38. Bäessler, H. Charge Transport in Disordered Organic Photoconductors a Monte Carlo Simulation Study. *physica status solidi (b)* **1993**, *175*, 15–56.
39. Oelerich, J. O.; Baranovskii, S. D. Theoretical tools for the description of charge transport in disordered organic semiconductors. *Journal of Physics: ...* **2015**.
40. Nenashev, A. V.; Oelerich, J. O.; Baranovskii, S. D. Theoretical tools for the description of charge transport in disordered organic semiconductors. *Journal of Physics: Condensed Matter* **2015**, *27*, 093201.
41. Mott, N. F. Conduction in non-crystalline materials. *Philosophical Magazine* **1969**, *19*, 835–852.
42. Gebhard, F.; Baranovskii, S. D. Energy position of the transport path in disordered organic

semiconductors. *Journal of Physics: ...* **2014**.

43. Vissenberg, M. C. J. M.; Matters, M. Theory of the field-effect mobility in amorphous organic transistors. *Physical Review B* **1998**, *57*, 12964–12967.

44. Tanase, C.; Meijer, E. J.; Blom, P. W. M.; de Leeuw, D. M. Unification of the Hole Transport in Polymeric Field-Effect Transistors and Light-Emitting Diodes. *Physical Review Letters* **2003**, *91*, 216601.

45. Oelerich, J. O.; Jansson, F.; Nenashev, A. V.; Gebhard, F.; Baranovskii, S. D. Energy position of the transport path in disordered organic semiconductors. *Journal of Physics: Condensed Matter* **2014**, *26*, 255801.

46. Bässler, H.; Köhler, A. Charge Transport in Organic Semiconductors. In *Unimolecular and Supramolecular Electronics I*; Topics in Current Chemistry; Springer Berlin Heidelberg: Berlin, Heidelberg, 2011; Vol. 312, pp. 1–65.

47. Wagenpfahl, A.; Rauh, D.; Binder, M.; Deibel, C.; Dyakonov, V. S-shaped current-voltage characteristics of organic solar devices. *Physical Review B* **2010**, *82*, 115306.

48. Rauh, D.; Wagenpfahl, A.; Deibel, C.; Dyakonov, V. Relation of open circuit voltage to charge carrier density in organic bulk heterojunction solar cells. *Applied Physics Letters* **2011**, *98*, 133301.

49. Brenner, T. M.; Chen, G.; Meinig, E. P.; Baker, D. J.; Olson, D. C.; Collins, R. T.; Furtak, T. E. Tuning zinc oxide/organic energy level alignment using mixed triethoxysilane monolayers. *Journal of Materials Chemistry C* **2013**, *1*, 5935–5943.

50. Zhang, Y.; Dang, X.-D.; Kuik, M.; Cowan, S. R.; Zalar, P.; Kim, C.; Nguyen, T.-Q. High light intensity effects on nanoscale open-circuit voltage for three common donor materials in bulk heterojunction solar cells. *Energy Environ. Sci.* **2013**, *6*, 1766–1771.

51. Po, R.; Carbonera, C.; Bernardi, A.; Camaioni, N. The role of buffer layers in polymer solar cells. *Energy Environ. Sci.* **2011**, *4*, 285–310.

52. Lattante, S. Electron and Hole Transport Layers: Their Use in Inverted Bulk Heterojunction Polymer Solar Cells. *Electronics* **2014**, *3*, 132–164.

53. Wang, F.; Tan, Z.; Li, Y. Solution-processable metal oxides/chelates as electrode buffer layers for efficient and stable polymer solar cells. *Energy Environ. Sci.* **2015**, *8*, 1059–1091.

54. Liang, Z.; Zhang, Q.; Jiang, L.; Cao, G. ZnO cathode buffer layers for inverted polymer solar cells. *Energy Environ. Sci.* **2015**, *8*, 3442–3476.

55. White, M. S.; Olson, D. C.; Shaheen, S. E.; Kopidakis, N.; Ginley, D. S. Inverted bulk-heterojunction organic photovoltaic device using a solution-derived ZnO underlayer. *Applied Physics Letters* **2006**, *89*, 143517.

56. Hau, S. K.; Yip, H.-L.; Baek, N. S.; Zou, J.; O'Malley, K.; Jen, A. K. Y. Air-stable inverted flexible polymer solar cells using zinc oxide nanoparticles as an electron selective layer. *Applied Physics Letters* **2008**, *92*, 253301.

57. Kong, J.; Hwang, I.-W.; Lee, K. Top-Down Approach for Nanophase Reconstruction in Bulk Heterojunction Solar Cells. *Advanced Materials* **2014**, *26*, 6275–6283.

58. Jagadamma, L. K.; Al-Senani, M.; El-Labban, A.; Gereige, I.; Ngongang Ndjawa, G. O.; Faria, J. C. D.; Kim, T.; Zhao, K.; Cruciani, F.; Anjum, D. H.; McLachlan, M. A.; Beaujuge, P. M.; Amassian, A. Polymer Solar Cells with Efficiency >10% Enabled via a Facile Solution-Processed Al-Doped ZnO Electron Transporting Layer. *Advanced Energy Materials* **2015**, *5*, 1500204.

59. Liao, S.-H.; Jhuo, H.-J.; Yeh, P.-N.; Cheng, Y.-S.; Li, Y.-L.; Lee, Y.-H.; Sharma, S.; Chen, S.-A. Single Junction Inverted Polymer Solar Cell Reaching Power Conversion Efficiency 10.31% by Employing Dual-Doped Zinc Oxide Nano-Film as Cathode Interlayer. *Sci Rep* **2014**, *4*, 6813.

60. Steim, R.; Choulis, S. A.; Schilinsky, P.; Brabec, C. J. Interface modification for highly efficient organic photovoltaics. *Applied Physics Letters* **2008**, *92*, 093303.

61. Hadipour, A.; Müller, R.; Heremans, P. Room temperature solution-processed electron transport layer for organic solar cells. *Organic Electronics* **2013**, *14*, 2379–2386.

62. Litzov, I.; Brabec, C. Development of Efficient and Stable Inverted Bulk Heterojunction (BHJ)

- Solar Cells Using Different Metal Oxide Interfaces. *Materials* **2013**, *6*, 5796–5820.
63. Kuwabara, T.; Sugiyama, H.; Yamaguchi, T.; Takahashi, K. Inverted type bulk-heterojunction organic solar cell using electrodeposited titanium oxide thin films as electron collector electrode. *Thin Solid Films* **2009**, *517*, 3766–3769.
64. Kim, J. Y.; Kim, S. H.; Lee, H. H.; Lee, K.; Ma, W.; Gong, X.; Heeger, A. J. New Architecture for High-Efficiency Polymer Photovoltaic Cells Using Solution-Based Titanium Oxide as an Optical Spacer. *Advanced Materials* **2006**, *18*, 572–576.
65. Zhou, Y.; Fuentes-Hernandez, C.; Shim, J.; Meyer, J.; Giordano, A. J.; Li, H.; Winget, P.; Papadopoulos, T.; Cheun, H.; Kim, J.; Fenoll, M.; Dindar, A.; Haske, W.; Najafabadi, E.; Khan, T. M.; Sojoudi, H.; Barlow, S.; Graham, S.; Bredas, J. L.; Marder, S. R.; Kahn, A.; Kippelen, B. A Universal Method to Produce Low-Work Function Electrodes for Organic Electronics. *Science* **2012**, *336*, 327–332.
66. Zhang, Y.; Chen, L.; Hu, X.; Zhang, L.; Chen, Y. Low Work-function Poly(3,4-ethylenedioxythiophene): Poly(styrene sulfonate) as Electron-transport Layer for High-efficient and Stable Polymer Solar Cells. *Sci Rep* **2015**, *5*, 12839.
67. Ameri, T.; Dennler, G.; Waldauf, C.; Denk, P.; Forberich, K.; Scharber, M. C.; Brabec, C. J.; Hingerl, K. Realization, characterization, and optical modeling of inverted bulk-heterojunction organic solar cells. *Journal of Applied Physics* **2008**, *103*, 084506.
68. Yuan, J.; Huang, X.; Dong, H.; Lu, J.; Yang, T.; Li, Y.; Gallagher, A.; Ma, W. Structure, band gap and energy level modulations for obtaining efficient materials in inverted polymer solar cells. *Organic Electronics* **2013**, *14*, 635–643.
69. Etxebarria, I.; Guerrero, A.; Albero, J.; Garcia-Belmonte, G.; Palomares, E.; Pacios, R. Inverted vs standard PTB7:PC70BM organic photovoltaic devices. The benefit of highly selective and extracting contacts in device performance. *Organic Electronics* **2014**, *15*, 2756–2762.
70. Kroon, J. M.; Wienk, M. M.; Verhees, W. J. H.; Hummelen, J. C. Accurate efficiency determination and stability studies of conjugated polymer/fullerene solar cells. *Thin Solid Films* **2002**, *403-404*, 223–228.
71. Shrotriya, V.; Li, G.; Yao, Y.; Moriarty, T.; Emery, K.; Yang, Y. Accurate Measurement and Characterization of Organic Solar Cells. *Advanced Functional Materials* **2006**, *16*, 2016–2023.
72. Gevorgyan, S. A.; Eggert Carlé, J.; Søndergaard, R.; Trofod Larsen-Olsen, T.; Jørgensen, M.; Krebs, F. C. Accurate characterization of OPVs: Device masking and different solar simulators. *Solar Energy Materials and Solar Cells* **2013**, *110*, 24–35.
73. Shockley, W.; Queisser, H. J. Detailed Balance Limit of Efficiency of p-n Junction Solar Cells. *Journal of Applied Physics* **1961**, *32*, 510–519.
74. Janssen, R. A. J.; Nelson, J. Factors Limiting Device Efficiency in Organic Photovoltaics. *Advanced Materials* **2012**, *25*, 1847–1858.
75. Vandewal, K.; Himmelberger, S.; Salleo, A. Structural Factors That Affect the Performance of Organic Bulk Heterojunction Solar Cells. *Macromolecules* **2013**, *46*, 6379–6387.
76. Ma, Z.; Sun, W.; Himmelberger, S.; Vandewal, K.; Tang, Z.; Bergqvist, J.; Salleo, A.; Andreasen, J. W.; Inganäs, O.; Andersson, M. R.; Müller, C.; Zhang, F.; Wang, E. Structure–property relationships of oligothiophene–isoindigo polymers for efficient bulk-heterojunction solar cells. *Energy Environ. Sci.* **2014**, *7*, 361–369.
77. Sharenko, A.; Proctor, C. M.; van der Poll, T. S.; Henson, Z. B.; Nguyen, T.-Q.; Bazan, G. C. A high-performing solution-processed small molecule:perylene diimide bulk heterojunction solar cell. *Adv. Mater. Weinheim* **2013**, *25*, 4403–4406.
78. Bloking, J. T.; Giovenzana, T.; Higgs, A. T.; Ponc, A. J.; Hoke, E. T.; Vandewal, K.; Ko, S.; Bao, Z.; Sellinger, A.; McGehee, M. D. Comparing the Device Physics and Morphology of Polymer Solar Cells Employing Fullerenes and Non-Fullerene Acceptors. *Advanced Energy Materials* **2014**, *4*, n/a–n/a.
79. Sharenko, A.; Gehrig, D.; Laquai, F.; Nguyen, T.-Q. The Effect of Solvent Additive on the Charge Generation and Photovoltaic Performance of a Solution-Processed Small Molecule:Perylene Diimide

- Bulk Heterojunction Solar Cell. *Chemistry of Materials* **2014**, *26*, 4109–4118.
80. Noriega, R.; Rivnay, J.; Vandewal, K.; Koch, F. P. V.; Stingelin, N.; Smith, P.; Toney, M. F.; Salleo, A. A general relationship between disorder, aggregation and charge transport in conjugated polymers. *Nat Mater* **2013**, *12*, 1038–1044.
81. Proctor, C. M.; Kher, A. S.; Love, J. A.; Huang, Y.; Sharenko, A.; Bazan, G. C.; Nguyen, T.-Q. Solar Cells: Understanding Charge Transport in Molecular Blend Films in Terms of Structural Order and Connectivity of Conductive Pathways (Adv. Energy Mater. 9/2016). *Advanced Energy Materials* **2016**, *6*.
82. Zhang, J.; Zhang, Y.; Fang, J.; Lu, K.; Wang, Z.; Ma, W.; Wei, Z. Conjugated Polymer–Small Molecule Alloy Leads to High Efficient Ternary Organic Solar Cells. *Journal of the American Chemical Society* **2015**, *137*, 8176–8183.
83. Collins, B. A.; Li, Z.; Tumbleston, J. R.; Gann, E.; McNeill, C. R.; Ade, H. Absolute Measurement of Domain Composition and Nanoscale Size Distribution Explains Performance in PTB7:PC 71BM Solar Cells. *Advanced Energy Materials* **2012**, *3*, 65–74.
84. Brabec, C. J.; Cravino, A.; Meissner, D.; Sariciftci, N. S.; Fromherz, T.; Rispens, M. T.; Sanchez, L.; Hummelen, J. C. Origin of the Open Circuit Voltage of Plastic Solar Cells. *Advanced Functional Materials* **2001**, *11*, 374–380.
85. Vandewal, K.; Tvingstedt, K.; Gadisa, A.; Inganäs, O.; Manca, J. V. On the origin of the open-circuit voltage of polymer–fullerene solar cells. *Nat Mater* **2009**, *8*, 904–909.
86. Dennler, G.; Scharber, M. C.; Brabec, C. J. Polymer-Fullerene Bulk-Heterojunction Solar Cells. *Advanced Materials* **2009**, *21*, 1323–1338.
87. Mihailetschi, V. D.; Blom, P. W. M.; Hummelen, J. C.; Rispens, M. T. Cathode dependence of the open-circuit voltage of polymer:fullerene bulk heterojunction solar cells. *Journal of Applied Physics* **2003**, *94*, 6849–6854.
88. Lemaire, V.; Steel, M.; Beljonne, D.; Brédas, J.-L.; Cornil, J. Photoinduced Charge Generation and Recombination Dynamics in Model Donor/Acceptor Pairs for Organic Solar Cell Applications: A Full Quantum-Chemical Treatment. *Journal of the American Chemical Society* **2005**, *127*, 6077–6086.
89. Kietzke, T.; Egbe, D. A. M.; Hörhold, H.-H.; Neher, D. Comparative Study of M3EH-PPV-Based Bilayer Photovoltaic Devices. *Macromolecules* **2006**, *39*, 4018–4022.
90. Veldman, D.; Meskers, S. C. J.; Janssen, R. A. J. The Energy of Charge-Transfer States in Electron Donor-Acceptor Blends: Insight into the Energy Losses in Organic Solar Cells. *Advanced Functional Materials* **2009**, *19*, 1939–1948.
91. Lange, I.; Kniepert, J.; Pingel, P.; Dumsch, I.; Allard, S.; Janietz, S.; Scherf, U.; Neher, D. Correlation between the Open Circuit Voltage and the Energetics of Organic Bulk Heterojunction Solar Cells. *The Journal of Physical Chemistry Letters* **2013**, *4*, 3865–3871.
92. Widmer, J.; Tietze, M.; Leo, K.; Riede, M. Open-Circuit Voltage and Effective Gap of Organic Solar Cells. *Advanced Functional Materials* **2013**, *23*, 5814–5821.
93. Qi, B.; Wang, J. Open-circuit voltage in organic solar cells. *Journal of Materials Chemistry* **2012**, *22*, 24315–24325.
94. Bartesaghi, D.; Pérez, I. D. C.; Kniepert, J.; Roland, S.; Turbiez, M.; Neher, D.; Koster, L. J. A. Competition between recombination and extraction of free charges determines the fill factor of organic solar cells. *Nature Communications* **2015**, *6*, 7083.
95. Green, M. A. Solar cell fill factors: General graph and empirical expressions. *Solid-State Electronics* **1981**, *24*, 788–789.
96. Wetzelaer, G. A. H.; Kuik, M.; Lenes, M.; Blom, P. W. M. Origin of the dark-current ideality factor in polymer:fullerene bulk heterojunction solar cells. *Applied Physics Letters* **2011**, *99*, 153506.
97. Tvingstedt, K.; Deibel, C. Temperature Dependence of Ideality Factors in Organic Solar Cells and the Relation to Radiative Efficiency. *Advanced Energy Materials* **2016**, *6*.
98. Würfel, U.; Neher, D.; Spies, A.; Albrecht, S. Impact of charge transport on current-voltage characteristics and power-conversion efficiency of organic solar cells. *Nature Communications*

2015, 6, 6951.

99. Qi, B.; Wang, J. Fill factor in organic solar cells. *Physical Chemistry Chemical Physics* **2013**, *15*, 8972–8982.
100. Jao, M.-H.; Liao, H.-C.; Su, W.-F. Achieving a high fill factor for organic solar cells. *J. Mater. Chem. A* **2016**, *4*, 5784–5801.
101. Park, S. H.; Roy, A.; Beaupré, S.; Cho, S.; Coates, N.; Moon, J. S.; Moses, D.; Leclerc, M.; Lee, K.; Heeger, A. J. Bulk heterojunction solar cells with internal quantum efficiency approaching 100%. *Nature Photonics* **2009**, *3*, 297–302.
102. Liang, Y.; Wu, Y.; Feng, D.; Tsai, S.-T.; Son, H.-J.; Li, G.; Yu, L. Development of New Semiconducting Polymers for High Performance Solar Cells. *Journal of the American Chemical Society* **2009**, *131*, 56–57.
103. Zhang, F.; Inganäs, O.; Zhou, Y.; Vandewal, K. Development of polymer–fullerene solar cells. *National Science Review* **2016**, *3*, 222–239.
104. Hu, H.; Jiang, K.; Yang, G.; Liu, J.; Li, Z.; Lin, H.; Liu, Y.; Zhao, J.; Zhang, J.; Huang, F.; Qu, Y.; Ma, W.; Yan, H. Terthiophene-Based D–A Polymer with an Asymmetric Arrangement of Alkyl Chains That Enables Efficient Polymer Solar Cells. *Journal of the American Chemical Society* **2015**, *137*, 14149–14157.
105. Li, S.; Ye, L.; Zhao, W.; Zhang, S.; Mukherjee, S.; Ade, H.; Hou, J. Energy-Level Modulation of Small-Molecule Electron Acceptors to Achieve over 12% Efficiency in Polymer Solar Cells. *Advanced Materials* **2016**.
106. Liang, Y.; Yu, L. A New Class of Semiconducting Polymers for Bulk Heterojunction Solar Cells with Exceptionally High Performance. *Accounts of Chemical Research* **2010**, *43*, 1227–1236.
107. Zhang, Q. T.; Tour, J. M. Alternating Donor/Acceptor Repeat Units in Polythiophenes. Intramolecular Charge Transfer for Reducing Band Gaps in Fully Substituted Conjugated Polymers. *Journal of the American Chemical Society* **1998**, *120*, 5355–5362.
108. Zhou, H.; Yang, L.; You, W. Rational Design of High Performance Conjugated Polymers for Organic Solar Cells. *Macromolecules* **2012**, *45*, 607–632.
109. Wu, J.-S.; Cheng, S.-W.; Cheng, Y.-J.; Hsu, C.-S. Donor–acceptor conjugated polymers based on multifused ladder-type arenes for organic solar cells. *Chem. Soc. Rev.* **2015**, *44*, 1113–1154.
110. Graham, K. R.; Cabanetos, C.; Jahnke, J. P.; Idso, M. N.; El-Labban, A.; Ngongang Ndjawa, G. O.; Heumueller, T.; Vandewal, K.; Salleo, A.; Chmelka, B. F.; Amassian, A.; Beaujuge, P. M.; McGehee, M. D. Importance of the Donor:Fullerene Intermolecular Arrangement for High-Efficiency Organic Photovoltaics. *Journal of the American Chemical Society* **2014**, *136*, 9608–9618.
111. Blouin, N.; Michaud, A.; Gendron, D.; Wakim, S.; Blair, E.; Neagu-Plesu, R.; Belletête, M.; Durocher, G.; Tao, Y.; Leclerc, M. Toward a Rational Design of Poly(2,7-Carbazole) Derivatives for Solar Cells. *Journal of the American Chemical Society* **2008**, *130*, 732–742.
112. Welch, G. C.; Bazan, G. C. Lewis Acid Adducts of Narrow Band Gap Conjugated Polymers. *Journal of the American Chemical Society* **2011**, *133*, 4632–4644.
113. Takacs, C. J.; Sun, Y.; Welch, G. C.; Perez, L. A.; Liu, X.; Wen, W.; Bazan, G. C.; Heeger, A. J. Solar Cell Efficiency, Self-Assembly, and Dipole–Dipole Interactions of Isomorphous Narrow-Band-Gap Molecules. *Journal of the American Chemical Society* **2012**, *134*, 16597–16606.
114. Ibraikulov, O. A.; Bechara, R.; Chávez, P.; Bulut, I.; Tastanbekov, D.; Leclerc, N.; Hebraud, A.; Heinrich, B.; Berson, S.; Lemaitre, N.; Chochos, C. L.; Lévêque, P.; Heiser, T. Using pyridal[2,1,3]thiadiazole as an acceptor unit in a low band-gap copolymer for photovoltaic applications. *Organic Electronics* **2015**, *23*, 171–178.
115. Wienk, M. M.; Turbiez, M.; Gilot, J.; Janssen, R. A. J. Narrow-Bandgap Diketo-Pyrrolo-Pyrrole Polymer Solar Cells: The Effect of Processing on the Performance. *Advanced Materials* **2008**, *20*, 2556–2560.
116. Li, W.; Hendriks, K. H.; Wienk, M. M.; Janssen, R. A. J. Diketopyrrolopyrrole Polymers for Organic Solar Cells. *Accounts of Chemical Research* **2016**, *49*, 78–85.

117. Liu, F.; Gu, Y.; Wang, C.; Zhao, W.; Chen, D.; Briseno, A. L.; Russell, T. P. Efficient Polymer Solar Cells Based on a Low Bandgap Semi-crystalline DPP Polymer-PCBM Blends. *Advanced Materials* **2012**, *24*, 3947–3951.
118. Zou, Y.; Najari, A.; Berrouard, P.; Beaupré, S.; Réda Aïch, B.; Tao, Y.; Leclerc, M. A Thieno[3,4-c]pyrrole-4,6-dione-Based Copolymer for Efficient Solar Cells. *Journal of the American Chemical Society* **2010**, *132*, 5330–5331.
119. Aïch, B. R.; Beaupré, S.; Leclerc, M.; Tao, Y. Highly efficient thieno[3,4-c]pyrrole-4,6-dione-based solar cells processed from non-chlorinated solvent. *Organic Electronics* **2014**, *15*, 543–548.
120. Small, C. E.; Chen, S.; Subbiah, J.; Amb, C. M.; Tsang, S.-W.; Lai, T.-H.; Reynolds, J. R.; So, F. High-efficiency inverted dithienogermole–thienopyrrolodione-based polymer solar cells. *Nature Photonics* **2011**, *6*, 115–120.
121. Zhou, H.; Yang, L.; Price, S. C.; Knight, K. J.; You, W. Enhanced Photovoltaic Performance of Low-Bandgap Polymers with Deep LUMO Levels. *Angewandte Chemie International Edition* **2010**, *49*, 7992–7995.
122. Zhang, S.; Qin, Y.; Uddin, M. A.; Jang, B.; Zhao, W.; Liu, D.; Woo, H. Y.; Hou, J. A Fluorinated Polythiophene Derivative with Stabilized Backbone Conformation for Highly Efficient Fullerene and Non-Fullerene Polymer Solar Cells. *Macromolecules* **2016**, *49*, 2993–3000.
123. Leclerc, N.; Chávez, P.; Ibraikulov, O.; Heiser, T.; Lévêque, P. Impact of Backbone Fluorination on π -Conjugated Polymers in Organic Photovoltaic Devices: A Review. *Polymers* **2016**, *8*, 11.
124. Liang, Y.; Feng, D.; Wu, Y.; Tsai, S.-T.; Li, G.; Ray, C.; Yu, L. Highly Efficient Solar Cell Polymers Developed via Fine-Tuning of Structural and Electronic Properties. *Journal of the American Chemical Society* **2009**, *131*, 7792–7799.
125. Wang, H.; Yu, X.; Yi, C.; Ren, H.; Liu, C.; Yang, Y.; Xiao, S.; Zheng, J.; Karim, A.; Cheng, S. Z. D.; Gong, X. Fine-Tuning of Fluorinated Thieno[3,4-b]thiophene Copolymer for Efficient Polymer Solar Cells. *The Journal of Physical Chemistry C* **2013**, *117*, 4358–4363.
126. Fei, Z.; Shahid, M.; Yaacobi-Gross, N.; Rossbauer, S.; Zhong, H.; Watkins, S. E.; Anthopoulos, T. D.; Heeney, M. Thiophene fluorination to enhance photovoltaic performance in low band gap donor–acceptor polymers. *Chemical Communications* **2012**, *48*, 11130–11132.
127. Stuart, A. C.; Tumbleston, J. R.; Zhou, H.; Li, W.; Liu, S.; Ade, H.; You, W. Fluorine Substituents Reduce Charge Recombination and Drive Structure and Morphology Development in Polymer Solar Cells. *Journal of the American Chemical Society* **2013**, *135*, 1806–1815.
128. Jo, J. W.; Jung, J. W.; Wang, H.-W.; Kim, P.; Russell, T. P.; Jo, W. H. Fluorination of Polythiophene Derivatives for High Performance Organic Photovoltaics. *Chemistry of Materials* **2014**, *26*, 4214–4220.
129. Li, W.; Albrecht, S.; Yang, L.; Roland, S.; Tumbleston, J. R.; McAfee, T.; Yan, L.; Kelly, M. A.; Ade, H.; Neher, D.; You, W. Mobility-Controlled Performance of Thick Solar Cells Based on Fluorinated Copolymers. *Journal of the American Chemical Society* **2014**, *136*, 15566–15576.
130. Li, Z.; Lin, H.; Jiang, K.; Carpenter, J.; Li, Y.; Liu, Y.; Hu, H.; Zhao, J.; Ma, W.; Ade, H.; Yan, H. Dramatic performance enhancement for large bandgap thick-film polymer solar cells introduced by a difluorinated donor unit. *Nano Energy* **2015**, *15*, 607–615.
131. Facchetti, A. π -Conjugated Polymers for Organic Electronics and Photovoltaic Cell Applications †. *Chemistry of Materials* **2011**, *23*, 733–758.
132. Dou, L.; Liu, Y.; Hong, Z.; Li, G.; Yang, Y. Low-Bandgap Near-IR Conjugated Polymers/Molecules for Organic Electronics. *Chemical Reviews* **2015**, *115*, 12633–12665.
133. Kouijzer, S.; Michels, J. J.; van den Berg, M.; Gevaerts, V. S.; Turbiez, M.; Wienk, M. M.; Janssen, R. A. J. Predicting Morphologies of Solution Processed Polymer:Fullerene Blends. *Journal of the American Chemical Society* **2013**, *135*, 12057–12067.
134. Keshtov, M. L.; Marochkin, D. V.; Kochurov, V. S.; Khokhlov, A. R.; Koukaras, E. N.; Sharma, G. D. New conjugated alternating benzodithiophene-containing copolymers with different acceptor units: synthesis and photovoltaic application. *J. Mater. Chem. A* **2014**, *2*, 155–171.

135. Shuttle, C. G.; O'Regan, B.; Ballantyne, A. M.; Nelson, J.; Bradley, D. D. C.; de Mello, J.; Durrant, J. R. Experimental determination of the rate law for charge carrier decay in a polythiophene: Fullerene solar cell. *Applied Physics Letters* **2008**, *92*, 093311.
136. Foertig, A.; Wagenpfahl, A.; Gerbich, T.; Cheyng, D.; Dyakonov, V.; Deibel, C. Nongeminate Recombination in Planar and Bulk Heterojunction Organic Solar Cells. *Advanced Energy Materials* **2012**, *2*, 1483–1489.
137. Mott, N. F.; Gurney, R. W. *1940 Electronic processes in ionic crystals*.
138. Murgatroyd, P. N. Theory of space-charge-limited current enhanced by Frenkel effect. *Journal of Physics D: Applied Physics* **2002**, *3*, 151–156.
139. Gupta, D.; Katiyar, M.; Gupta, D. An analysis of the difference in behavior of top and bottom contact organic thin film transistors using device simulation. *Organic Electronics* **2009**, *10*, 775–784.
140. Tessler, N.; Roichman, Y. Two-dimensional simulation of polymer field-effect transistor. *Applied Physics Letters* **2001**, *79*, 2987–2989.
141. Klauk, H. Organic thin-film transistors. *Chem. Soc. Rev.* **2010**, *39*, 2643–2666.
142. Kobayashi, S.; Nishikawa, T.; Takenobu, T.; Mori, S.; Shimoda, T.; Mitani, T.; Shimotani, H.; Yoshimoto, N.; Ogawa, S.; Iwasa, Y. Control of carrier density by self-assembled monolayers in organic field-effect transistors. *Nat Mater* **2004**, *3*, 317–322.
143. Pernstich, K. P.; Haas, S.; Oberhoff, D.; Goldmann, C.; Gundlach, D. J.; Batlogg, B.; Rashid, A. N.; Schitter, G. Threshold voltage shift in organic field effect transistors by dipole monolayers on the gate insulator. *Journal of Applied Physics* **2004**, *96*, 6431–6438.
144. Zaumseil, J.; Sirringhaus, H. Electron and Ambipolar Transport in Organic Field-Effect Transistors. *Chemical Reviews* **2007**, *107*, 1296–1323.
145. Fall, S.; Biniek, L.; Odarchenko, Y.; Anokhin, D. V.; de Tournadre, G.; Lévêque, P.; Leclerc, N.; Ivanov, D. A.; Simonetti, O.; Giraudet, L.; Heiser, T. Tailoring the microstructure and charge transport in conjugated polymers by alkyl side-chain engineering. *Journal of Materials Chemistry C* **2016**, *4*, 286–294.
146. Zhang, W.; Smith, J.; Watkins, S. E.; Gysel, R.; McGehee, M.; Salleo, A.; Kirkpatrick, J.; Ashraf, S.; Anthopoulos, T.; Heeney, M.; McCulloch, I. Indacenodithiophene Semiconducting Polymers for High-Performance, Air-Stable Transistors. *Journal of the American Chemical Society* **2010**, *132*, 11437–11439.
147. Venkateshvaran, D.; Nikolka, M.; Sadhanala, A.; Lemaire, V.; Zelazny, M.; Kepa, M.; Hurhangee, M.; Kronemeijer, A. J.; Pecunia, V.; Nasrallah, I.; Romanov, I.; Broch, K.; McCulloch, I.; Emin, D.; Olivier, Y.; Cornil, J.; Beljonne, D.; Sirringhaus, H. Approaching disorder-free transport in high-mobility conjugated polymers. *Nature* **2014**, *515*, 384–388.
148. Vukmirović, N. A comparative study of electronic properties of disordered conjugated polymers. *Physical Chemistry Chemical Physics* **2013**, *15*, 3543–3551.
149. Katsouras, A.; Gasparini, N.; Koulogiannis, C.; Spanos, M.; Ameri, T.; Brabec, C. J.; Chochos, C. L.; Avgeropoulos, A. Systematic Analysis of Polymer Molecular Weight Influence on the Organic Photovoltaic Performance. *Macromolecular Rapid Communications* **2015**, *36*, 1778–1797.
150. Himmelberger, S.; Vandewal, K.; Fei, Z.; Heeney, M.; Salleo, A. Role of Molecular Weight Distribution on Charge Transport in Semiconducting Polymers. *Macromolecules* **2014**, *47*, 7151–7157.
151. Wang, S.; Fabiano, S.; Himmelberger, S.; Puzinas, S.; Crispin, X.; Salleo, A.; Berggren, M. Experimental evidence that short-range intermolecular aggregation is sufficient for efficient charge transport in conjugated polymers. *Proc. Natl. Acad. Sci. U.S.A.* **2015**, *112*, 10599–10604.
152. Vakhshouri, K.; Smith, B. H.; Chan, E. P.; Wang, C.; Salleo, A.; Wang, C.; Hexemer, A.; Gomez, E. D. Signatures of Intracrystallite and Intercrystallite Limitations of Charge Transport in Polythiophenes. *Macromolecules* **2016**, *acs.macromol.6b01086*.
153. Hammond, M. R.; Kline, R. J.; Herzog, A. A.; Richter, L. J.; Germack, D. S.; Ro, H.-W.; Soles, C. L.;

- Fischer, D. A.; Xu, T.; Yu, L.; Toney, M. F.; DeLongchamp, D. M. Molecular Order in High-Efficiency Polymer/Fullerene Bulk Heterojunction Solar Cells. *ACS Nano* **2011**, *5*, 8248–8257.
154. Lou, S. J.; Szarko, J. M.; Xu, T.; Yu, L.; Marks, T. J.; Chen, L. X. Effects of Additives on the Morphology of Solution Phase Aggregates Formed by Active Layer Components of High-Efficiency Organic Solar Cells. *Journal of the American Chemical Society* **2011**, *133*, 20661–20663.
155. van Franeker, J. J.; Turbiez, M.; Li, W.; Wienk, M. M.; Janssen, R. A. J. A real-time study of the benefits of co-solvents in polymer solar cell processing. *Nature Communications* **2015**, *6*, 6229.
156. Wu, P.-T.; Kim, F. S.; Champion, R. D.; Jenekhe, S. A. Conjugated Donor–Acceptor Copolymer Semiconductors. Synthesis, Optical Properties, Electrochemistry, and Field-Effect Carrier Mobility of Pyridopyrazine-Based Copolymers. *Macromolecules* **2008**, *41*, 7021–7028.
157. Biniek, L.; Chochos, C. L.; Leclerc, N.; Hadziioannou, G.; Kallitsis, J. K.; Bechara, R.; Lévêque, P.; Heiser, T. A [3,2-b]thienothiophene-alt-benzothiadiazole copolymer for photovoltaic applications: design, synthesis, material characterization and device performances. *Journal of Materials Chemistry* **2009**, *19*, 4946–4951.
158. Blouin, N.; Michaud, A.; Leclerc, M. A Low-Bandgap Poly(2,7-Carbazole) Derivative for Use in High-Performance Solar Cells. *Advanced Materials* **2007**, *19*, 2295–2300.
159. Zhang, M.; Gu, Y.; Guo, X.; Liu, F.; Zhang, S.; Huo, L.; Russell, T. P.; Hou, J. Efficient Polymer Solar Cells Based on Benzothiadiazole and Alkylphenyl Substituted Benzodithiophene with a Power Conversion Efficiency over 8%. *Adv. Mater. Weinheim* **2013**, *25*, 4944–4949.
160. Sun, Y.; Welch, G. C.; Leong, W. L.; Takacs, C. J.; Bazan, G. C.; Heeger, A. J. Solution-processed small-molecule solar cells with 6.7% efficiency. *Nat Mater* **2011**, *11*, 44–48.
161. Biniek, L.; Fall, S.; Chochos, C. L.; Leclerc, N.; Lévêque, P.; Heiser, T. Optimization of the side-chain density to improve the charge transport and photovoltaic performances of a low band gap copolymer. *Organic Electronics* **2012**, *13*, 114–120.
162. Yang, X.; Loos, J.; Veenstra, S. C.; Verhees, W. J. H.; Wienk, M. M.; Kroon, J. M.; Michels, M. A. J.; Janssen, R. A. J. Nanoscale Morphology of High-Performance Polymer Solar Cells. *Nano Letters* **2005**, *5*, 579–583.
163. Hoppe, H.; Sariciftci, N. S. Morphology of polymer/fullerene bulk heterojunction solar cells. *Journal of Materials Chemistry* **2006**, *16*, 45–61.
164. Jung, J. W.; Liu, F.; Russell, T. P.; Jo, W. H. Medium Bandgap Conjugated Polymer for High Performance Polymer Solar Cells Exceeding 9% Power Conversion Efficiency. *Advanced Materials* **2015**, *27*, 7462–7468.
165. Son, H.-J.; Wang, W.; Xu, T.; Liang, Y.; Wu, Y.; Li, G.; Yu, L. Synthesis of Fluorinated Polythienothiophene- co-benzodithiophenes and Effect of Fluorination on the Photovoltaic Properties. *Journal of the American Chemical Society* **2011**, *133*, 1885–1894.
166. Nketia-Yawson, B.; Lee, H.-S.; Seo, D.; Yoon, Y.; Park, W.-T.; Kwak, K.; Son, H.-J.; Kim, B.; Noh, Y.-Y. A Highly Planar Fluorinated Benzothiadiazole-Based Conjugated Polymer for High-Performance Organic Thin-Film Transistors. *Advanced Materials* **2015**, *27*, 3045–3052.
167. Mueller, C. J.; Gann, E.; McNeill, C. R.; Thelakkat, M. Influence of fluorination in π -extended backbone polydiketopyrrolopyrroles on charge carrier mobility and depth-dependent molecular alignment. *Journal of Materials Chemistry C* **2015**, *3*, 8916–8925.
168. Nguyen, T. L.; Choi, H.; Ko, S. J.; Uddin, M. A.; Walker, B.; Yum, S.; Jeong, J. E.; Yun, M. H.; Shin, T. J.; Hwang, S.; Kim, J. Y.; Woo, H. Y. Semi-crystalline photovoltaic polymers with efficiency exceeding 9% in a ~300 nm thick conventional single-cell device. *Energy Environ. Sci.* **2014**, *7*, 3040–3051.
169. Dong, X.; Deng, Y.; Tian, H.; Xie, Z.; Geng, Y.; Wang, F. Isoindigo-based low bandgap conjugated polymer for o-xylene processed efficient polymer solar cells with thick active layers. *J. Mater. Chem. A* **2015**, *3*, 19928–19935.
170. Zhang, S.; Yang, B.; Liu, D.; Zhang, H.; Zhao, W.; Wang, Q.; He, C.; Hou, J. Correlations among Chemical Structure, Backbone Conformation, and Morphology in Two Highly Efficient Photovoltaic Polymer Materials. *Macromolecules* **2016**, *49*, 120–126.

171. Kao, K. C.; Hwang, W. *Electrical Transport in solids, International series in the science of the solid state*; Electrical Transport in solids, 1981.
172. Tumbleston, J. R.; Collins, B. A.; Yang, L.; Stuart, A. C.; Gann, E.; Ma, W.; You, W.; Ade, H. The influence of molecular orientation on organic bulk heterojunction solar cells. *Nature Photonics* **2014**, *8*, 385–391.
173. Chen, H.-Y.; Yang, H.; Yang, G.; Sista, S.; Zadayan, R.; Li, G.; Yang, Y. Fast-Grown Interpenetrating Network in Poly(3-hexylthiophene): Methanofullerenes Solar Cells Processed with Additive. *The Journal of Physical Chemistry C* **2009**, *113*, 7946–7953.
174. Albrecht, S.; Tumbleston, J. R.; Janietz, S.; Dumsch, I.; Allard, S.; Scherf, U.; Ade, H.; Neher, D. Quantifying Charge Extraction in Organic Solar Cells: The Case of Fluorinated PCPDTBT. *The Journal of Physical Chemistry Letters* **2014**, *5*, 1131–1138.
175. Neher, D.; Kniepert, J.; Elimelech, A.; Koster, L. J. A. A New Figure of Merit for Organic Solar Cells with Transport-limited Photocurrents. *Sci Rep* **2016**, *6*, 24861.
176. Koster, L. J. A.; Mihailetschi, V. D.; Ramaker, R.; Blom, P. W. M. Light intensity dependence of open-circuit voltage of polymer:fullerene solar cells. *Applied Physics Letters* **2005**, *86*, 123509.
177. Shuttle, C. G.; Maurano, A.; Hamilton, R.; O'Regan, B.; de Mello, J. C.; Durrant, J. R. Charge extraction analysis of charge carrier densities in a polythiophene/fullerene solar cell: Analysis of the origin of the device dark current. *Applied Physics Letters* **2008**, *93*, 183501.

Chapter 8: Résumé de la thèse

8 Résumé de la thèse

8.1 Introduction

Plus de 20 ans se sont déjà écoulés depuis que la première cellule solaire de type hétérojonction en volume (BHJ pour « Bulk HeteroJunction ») a été rapportée [1]. Bien que ces cellules aient au début lentement évolué en termes de rendement de conversion énergétique (PCE pour « Power Conversion Efficiency ») [2-4], l'intérêt pour ce domaine a augmenté continuellement. Au cours de la dernière décennie l'efficacité des dispositifs BHJ a connu une forte évolution, atteignant des efficacités remarquables de plus de 10% [5,6]. Cette progression impressionnante doit beaucoup à la conception et au développement de nouveaux matériaux semi-conducteurs organiques ayant des propriétés opto-électroniques optimisées, ainsi qu'à l'optimisation et au contrôle de la morphologie de la couche active. Des copolymères avec une structure quinoïde [7] ou avec une alternance de groupements donneur (D) et accepteur (A) d'électrons [8,9] ont montré de bons résultats dans les cellules solaires car ces deux stratégies de synthèse permettent l'ajustement précis de l'énergie des orbitales moléculaires frontière (FMO pour « Frontier Molecular Orbitals »). En outre, il a été montré que d'autres modifications structurales telles que la planéité de la chaîne principale du polymère, ainsi que la nature et la position des chaînes latérales substituées, influencent les propriétés opto-électroniques des polymères [10,11]. En utilisant ces stratégies, de nombreux matériaux à faible bande interdite ont été synthétisés et utilisés dans des dispositifs photovoltaïques. Cependant, l'ingénierie des FMO des matériaux est loin d'être suffisante pour obtenir des cellules solaires efficaces. Il est bien connu que les semi-conducteurs organiques souffrent généralement de faibles mobilités des porteurs de charge qui dépendent fortement de la microstructure des films minces. De plus, l'auto-organisation des molécules dans les films minces déposés en solution varie fortement selon les matériaux utilisés et est donc difficile à contrôler.

Dans ce contexte, cette thèse se concentre sur l'étude des copolymères à bande interdite étroite dans divers dispositifs tels que les transistors à effet de champ organiques, les diodes à porteur unique limitées par la charge d'espace et les cellules photovoltaïques. Des études détaillées du transport de charges dans des systèmes de différents matériaux sont présentées. Afin de mieux comprendre les observations concernant le transport de charge, la microstructure des films de polymère pur et de mélanges polymère/fullerène a également été étudiée. Tous les polymères

étudiés ont été utilisés avec succès dans des dispositifs solaires de type hétérojonction en volume. Il a été constaté que les copolymères à squelette fluoré qui s'agrègent fortement ont de bonnes performances dans les dispositifs BHJ. Le meilleur rendement obtenu dans des cellules solaires utilisant ces matériaux a été de 9,8%. Tous les polymères ont été synthétisés par un groupe de chimistes de l'Institut de Chimie et Procédés pour l'Energie, l'Environnement et la Santé (ICPEES) sous la direction du Dr Nicolas Leclerc. Les mesures par diffusion des rayons X aux grands angles en incidence rasante (GIWAXS pour « Grazing Incidence Wide Angle X-ray Scattering ») ont été effectuées par le Dr Benoît Heinrich de l'Institut de Physique et Chimie des Matériaux de Strasbourg (IPCMS).

8.2 Copolymères à base de thiéno-pyrroledione (TPD)

Deux copolymères différents à faible bande interdite, basés sur l'unité de thiéno-pyrroledione

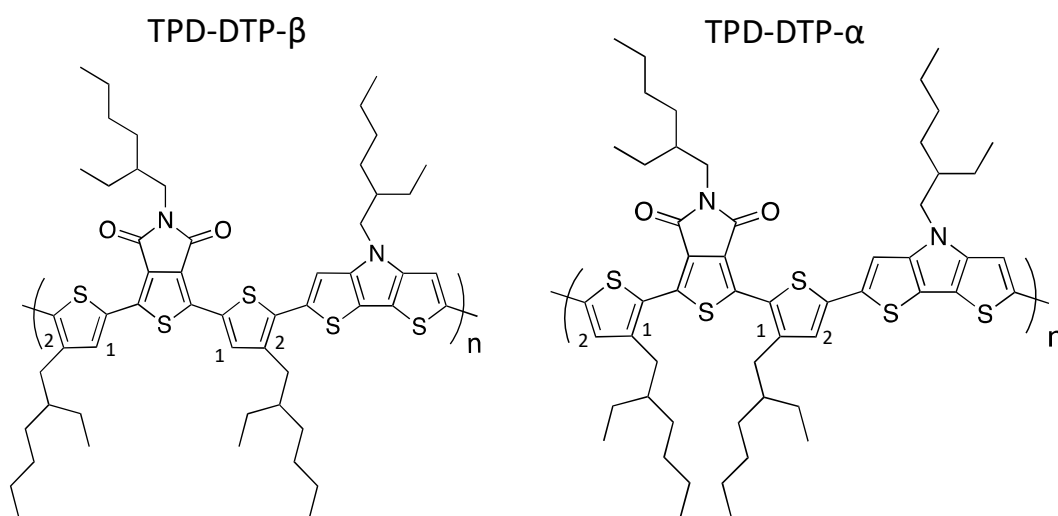


Figure 1: Les structures chimiques des polymères TPD-DTP-β (gauche) et TPD-DTP-α (droite). Les positions 1 et 2 sur les thiophènes correspondent aux α et β, respectivement.

(TPD), acceptrice d'électrons, ont été étudiés en détail. La seule différence entre les deux polymères était la position des deux chaînes latérales éthyl-hexyle (EH) situées sur les thiophènes entourant l'unité TPD (Fig. 1). Pour le premier polymère, les chaînes latérales étaient greffées sur le thiophène en position 2 (β, bêta) (TPD-DTP-β). Pour l'autre, les chaînes latérales EH étaient situées en position 1 (α, alpha) (TPD-DTP-α). Tout d'abord, une étude détaillée du

polymère TPD-DTP- β a été entreprise. Les propriétés de transport de charge du TPD-DTP- β ont été jugées particulièrement intéressantes. La mobilité des trous du TPD-DTP- β dans les transistors organiques à effet de champ (OFET pour « Organic Field-Effect Transistor ») en régime linéaire a notamment montré une dépendance relativement faible en fonction de la tension de grille appliquée (concentration des porteurs de charge). Cette observation n'est pas une tendance générale dans les matériaux organiques désordonnés car la mobilité des porteurs de charge y est réputée dépendre fortement de leur concentration [12]. Le TPD-DTP- α a ensuite été synthétisé sur la base de ces résultats intéressants. Pour le TPD-DTP- α , la mobilité des trous dans les mêmes structures OFET a montré une très forte dépendance en fonction de la tension de grille. En outre, les valeurs de la mobilité des trous du TPD-DTP- α étaient significativement plus faibles que pour le TPD-DTP- β . Les études réalisées pour estimer les mobilités verticales des trous ont révélé la même tendance. Des mesures GIWAXS ont révélé une nature relativement désordonnée pour les deux matériaux. Curieusement, bien que le désordre structural était similaire pour les deux copolymères, le degré de désordre énergétique était tout à fait différent. Les simulations basées sur la DFT (ou « Density Functional Theory ») effectuées sur les dimères ont montré que la position des chaînes latérales alkyles pouvait avoir une forte influence sur la torsion du squelette du polymère seul. Ainsi, pour le TPD-DTP- α la conjugaison du squelette pourrait être rompue par la torsion (48°) due à un possible encombrement stérique entre les chaînes latérales. Cette possible torsion du squelette pourrait à son tour limiter le transport de charge intra-moléculaire. Quant au TPD-DTP- β , l'angle de torsion d'environ 20° ne briserait pas la conjugaison. Ce copolymère pourrait par conséquent être considéré comme étant relativement plan par rapport au TPD-DTP- α . D'après ces résultats nous avons conclu que le désordre énergétique devait être en grande partie contrôlé par la torsion du squelette du polymère seul. Des tendances similaires ont déjà été signalées pour d'autres matériaux où un polymère sans torsion a donné lieu à une mobilité constante, mettant en évidence un très faible désordre énergétique [13]. Les cellules photovoltaïques à base de ces deux copolymères faiblement ordonnés se sont également comportées de manière très différente. Bien que le rendement photovoltaïque n'ait atteint que la valeur de 3,2% pour les dispositifs optimisés basés sur du TPD-DTP- β , cette valeur était très supérieure à la valeur maximale d'environ 0,5% obtenue dans le cas du DPT-DTP- α .

8.3 Copolymère à base de pyridino [2,1,3] thiadiazole

Un nouveau copolymère à faible bande interdite à base de pyridal [2,1,3] thiadiazole comme

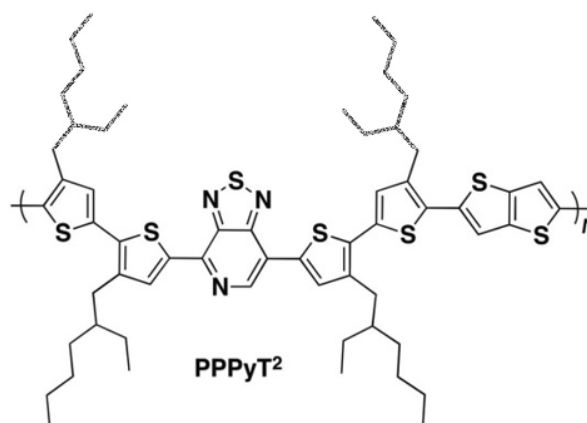


Figure 2: Structure chimique du copolymère PPPyT² à faible bande interdite

unité accepteur a été étudié en détail (Fig. 2) et des études approfondies du transport de charge ont été effectuées. Les études du transport de charge parallèle et perpendiculaire au plan de l'échantillon ont montré une anisotropie élevée. Pour les films de polymère pur, la mobilité des trous dans les diodes à intensité limitée par la charge d'espace (SCLC pour « Space Charge Limited Current ») (direction verticale) étaient inférieure à la mobilité horizontale de près de 2 ordres de grandeur.

De manière intéressante, mélanger du polymère PPPyT² avec du PC [71] BM dans un rapport de 1: 1 a conduit à une mobilité verticale des trous plus grande et a légèrement diminué la mobilité des trous dans les OFETs. En outre, l'introduction de 50% de PC [71] BM dans le film de polymère pur n'a pas perturbé le désordre énergétique. Des mesures GIWAXS ont été réalisées pour comprendre l'auto-organisation structurale du PPPyT² en film pur et en mélange. Les résultats ont révélé la nature semi-cristalline du PPPyT² en film mince et élucidé les observations faites sur le transport de charge dans les films de polymère pur. En particulier, les lamelles cristallines du polymère étaient alignées parallèlement au substrat, avec les chaînes de polymères orientées debout (ou "edge-on"). Dans cette configuration, la direction d'empilement π - π est parallèle au substrat et donne lieu à une forte mobilité à effet de champ. Cette, orientation n'est pas perturbée en présence de PC[71]BM. Ce comportement est cohérent avec l'observation

que le désordre énergétique reste quasiment inchangé après l'ajout de PC[71]BM, mais n'explique pas l'augmentation de la mobilité verticale des trous (mesurée en SCLC) en présence de PC[71]BM. Pour mieux comprendre cette évolution, des mesures d'absorption UV-vis supplémentaires ont été réalisées sur des mélanges polymère:fullerène à l'état solide. Les résultats ont montré l'accroissement des fractions de polymère amorphe après mélange avec du PC[71]BM. La multiplication par presque quatre de la mobilité des trous perpendiculairement au plan a été attribuée à ces fractions amorphes.

En dépit de ses caractéristiques initialement prometteuses du point de vue des FMO, le PPPyT2 n'a pas donné lieu aux performances photovoltaïques attendues. Le PCE maximum des cellules BHJ à base de ce copolymère a atteint la valeur de 4,5% avec un facteur de forme (FF) qui atteignait à peine 50% [14]. Les valeurs relativement faibles de la mobilité des trous perpendiculaire au plan, dues à l'orientation défavorable des lamelles de polymère, est probablement responsable de ce faible facteur de forme et du rendement de conversion qui en découle. Ces travaux ont donné lieu à une publication dans le journal « Organic Electronics ».

8.4 Copolymères à base de di-fluoro benzothiadiazole

Des copolymères semi-conducteurs à bande interdite étroite basés sur des unités benzothiadiazole di-fluorées (PF2) et non fluorées (PF0) ont été étudiés (Fig. 3). Les propriétés optiques, le transport de charge, la microstructure, la recombinaison et les propriétés

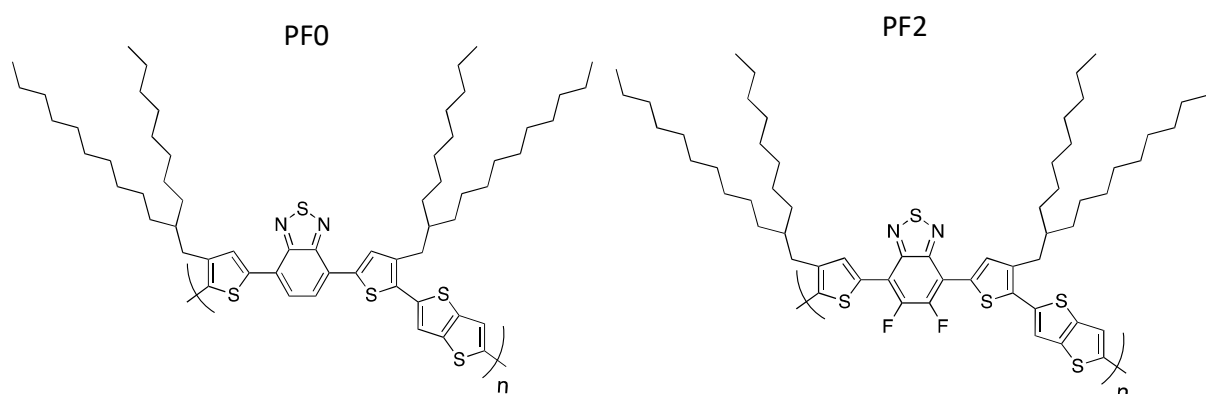


Figure 3: Les structures chimiques polymères fluorées (PF2) et non fluorées (PF0)

photovoltaïques ont été particulièrement explorées. Des mesures UV-Vis ont montré une très

forte dépendance en fonction de la température des propriétés d'agrégation des copolymères fluorés en solution. Cette propriété d'agrégation s'est révélée presque insensible à la variation du poids moléculaire des copolymères. Des études du transport de charge dans des copolymères fluorés de différents poids moléculaires ont été effectuées. Le transport de charge, tant parallèle que perpendiculaire au plan, dans les matériaux purs de tous les copolymères fluorés a montré une anisotropie relativement faible, avec des mobilités de trous et d'électrons équilibrées de l'ordre de $10^{-2} \text{ cm}^2/\text{Vs}$. Les mobilités des trous étaient curieusement insensibles aux différences de poids moléculaires (M_n), ce qui signifie que la connectivité intermoléculaire pourrait être suffisante même pour un copolymère avec le M_n le plus bas. De plus, pour le PF2-HM il a été observé que la présence de près de 60% de PC[71]BM dans les films en mélange avait un effet négligeable sur les mobilités verticales des trous. D'autre part, l'effet du PC[71]BM était renforcé en diminuant M_n . En conséquence, la mobilité perpendiculaire au plan des trous dans des mélanges avec du PF2-LM a diminué d'un facteur presque quatre par rapport à celle du matériau pur. Les résultats GIWAXS pour le PF2-HM et le PF2-MM purs ont montré une microstructure similaire, ce qui signifie que l'auto-organisation en couches minces du copolymère ne dépend pas de M_n . La présence des lamelles à plat et debout (direction d'empilement π - π^* perpendiculaire au substrat) a pleinement confirmé les conclusions précédentes concernant la mobilité équilibrée des trous dans les films de copolymères purs. En outre, les résultats UV-Vis et GIWAXS ont montré que la microstructure des films du mélange PF2-HM:PC[71]BM était principalement contrôlée par le copolymère et n'était pas modifiée de façon significative par la présence du matériau accepteur. Au contraire, les polymères non fluorés n'ont montré aucun comportement d'agrégation en solution, confirmant ainsi le rôle décisif des substituants fluor dans les interactions inter-chaînes des polymères. L'étude du transport de charge a également révélé des différences significatives entre PF2-HM et PF0. En particulier, les mobilités horizontales et verticales des trous dans le PF0 pur ont toutes deux été estimées de l'ordre de $10^{-4} \text{ cm}^2/\text{Vs}$, soit près de deux ordres de grandeur inférieures à celles du PF2. En outre, la mobilité verticale des trous dans le mélange PF0: PC[71]BM (1: 1,5) était inférieure d'un facteur six, ce qui souligne l'influence notable du matériau accepteur dans l'organisation du PF0. Des caractérisations GIWAXS ont été réalisées pour des films à base de PF0 afin de mieux comprendre l'impact de la fluoruration de la colonne vertébrale du copolymère. Il a été constaté que la microstructure des films de PF0 pur était moins ordonné que celle des films de PF2-HM mais avec le même

ensemble d'orientation mélangée des phases lamellaires. Compte tenu d'une récente publication de Fall et al. [12], nous avons pu conclure que les longues chaînes latérales alkyle induisaient une orientation "face-on" des chaînes de polymères (lamelles debout). Curieusement, les distances d'empilement du squelette π -conjugués et les longueurs de corrélation qui ont été estimées étaient voisines pour les deux copolymères, fluoré et non fluoré. Nous avons donc attribué la différence de presque deux ordres de grandeur entre les mobilités 3-D des trous dans les matériaux purs à de plus fortes interactions inter-chaînes dans le polymère et à une cristallinité plus élevée du PF2-HM comparée à celle du PF0. Des mesures GIWAXS sur des films du mélange PF0:PC[71]BM ont montré que la microstructure du PF0 était considérablement perturbée par l'ajout de PC[71]BM. Des caractérisations par microscopie à force atomique (AFM pour « Atomic Force Microscopy ») effectuées sur des mélanges copolymère:PC[71]BM ont également révélé des différences significatives pour les deux matériaux. Alors que le film PF2-MM:PC[71]BM a montré une morphologie nano-fibrillaire bien entremêlée, la morphologie du PF0-PC[71]BM était plutôt granuleuse, avec des domaines relativement plus grands et une séparation des phases plus prononcée. L'étude de la dynamique des porteurs de charge a révélé des mécanismes de recombinaison différents selon le copolymère. Il a été constaté que la recombinaison dans les dispositifs photovoltaïques à base de PF0 en régime de faible concentration des porteurs de charge était principalement limitée par les pièges. En revanche, dans les dispositifs basés sur du PF2-MM, le mécanisme de recombinaison sans piège ou recombinaison bimoléculaire dominait dans toute la gamme étudiée.

Les cellules solaires organiques réalisées en utilisant ces nouveaux polymères fluorés ont montré des rendements de conversion énergétique surprenants avec des FFs élevés. En particulier, une cellule solaire optimisée utilisant le polymère ayant un poids moléculaire d'environ 35 kg/mol a montré un PCE maximum de 9,8% (valeur moyenne de 9,5%). A titre de comparaison, les polymères non-fluorés ont présenté des PCEs bien plus faibles, de l'ordre de 2% (la valeur actuelle du record mondial du PCE d'une cellule solaire organique à jonction unique est d'environ 12%).

8.5 Conclusions

Dans le cadre de cette thèse, des études approfondies du transport de charge, de la morphologie et des comportements photovoltaïques ont été effectuées sur une série de copolymères à faible bande interdite. Bien que le polymère TPD-DTP- β était mal organisé en film mince, il présentait un désordre énergétique relativement faible. En outre, une étude du transport de charge 3-D a montré une anisotropie assez faible des porteurs de charge dans ce polymère, avec des mobilités horizontales et verticales presque identiques. Des calculs DFT ont mis en évidence qu'un degré de torsion élevé du squelette du polymère suffisait pour influencer le transport de charge, et donc les mobilités des porteurs de charge et les propriétés photovoltaïques finales. Néanmoins, les PCEs des dispositifs de type BHJ basés sur le copolymère TPD-DTP- β mal ordonné pouvaient encore atteindre une valeur supérieure à 3%.

D'autre part, un nouveau polymère basé sur une unité accepteur pyridal[2,1,3]thiadiazole a montré une nature semi-cristalline en couche mince. Des domaines cristallins se formaient à partir de lamelles de polymère agrégé avec un empilement π - π dans la direction parallèle au substrat. Du fait de cette orientation à plat des lamelles de polymère, le degré d'anisotropie du transport de charge était relativement élevé. Dans les films de polymère pur, l'étude du transport de charge 3-D a révélé 2 ordres de grandeur de différence entre les mobilités des trous parallèle et perpendiculaire au plan. Malgré ses propriétés initiales prometteuses en termes de niveau d'énergie FMO, les dispositifs finaux en cellules solaires n'ont pas fonctionné comme escompté. Les PCEs des dispositifs photovoltaïques à base de ce matériau n'ont pas dépassé la valeur de 4,5% et étaient principalement limités par les FFs.

Contrairement aux deux matériaux précédents, les copolymères fluorés s'auto-organisaient, avec une nature cristalline relativement élevée. En outre, dans ces matériaux, une fraction élevée des lamelles cristallines du polymère était orientées debout, avec une direction d'empilement π - π perpendiculaire au substrat. Cette orientation des lamelles de polymère a conduit à des mobilités verticales des trous relativement élevées (jusqu'à 10^{-2} cm²/Vs dans les mélanges avec du PC[71]BM). Il a également été constaté que cette direction favorable provenait principalement des longues chaînes latérales. Par conséquent, des cellules solaires avec des PCEs remarquables ont été obtenues en utilisant un polymère fluoré avec de longues chaînes latérales. Les mobilités verticales des trous ont permis d'aller jusqu'à des couches actives relativement épaisses

(≈ 270 nm) pour augmenter la collecte de la lumière sans sacrifier les FFs ($> 70\%$). Un PCE maximum de 9,8% a été atteint en utilisant ce copolymère fluoré.

8.6 Contributions scientifiques

8.6.1 Contributions par affiche

O. A. Ibraikulov, R. Bechara, P. Leveque, N. Leclerc, G. T. Koishiyev and T. Heiser,
Effect of Molecular Weight on the Photovoltaic Performance of a Low band gap Copolymer blended with ICBA, *Material Research Society Spring Meeting and Exhibit (MRS), San-Francisco (USA), April 1-5th, 2013*

O. A. Ibraikulov, R. Bechara, P. Chavez, I. Bulut, N. Leclerc, S. Berson, N. Lemaitre, P. Leveque and T. Heiser,
Using pyridal[2,1,3]thiadiazole as acceptor unit to optimize the opto-electronic properties of a low bandgap copolymer for photovoltaic applications, *7th International Conference on Molecular Electronics (ElecMol'14), Strasbourg (France), August 24-29th, 2014*

8.6.2 Contribution orale

O.A. Ibraikulov, R. Bechara, P. Chavez, I. Bulut, D. Tastanbekov, N. Leclerc, A. Hebraud, B. Heinrich, S. Berson, N. Lemaitre, C.L. Chochos, P. Leveque and T. Heiser,
Charge transport, microstructure and photovoltaic properties of a new low band gap polymer using pyridal[2,1,3]thiadiazole as an acceptor unit, *11th International Conference on Organic Electronics (ICOE 2015), Erlangen (Germany), June 15-17th, 2015*

8.6.3 Publications

O.A. Ibraikulov, R. Bechara, P. Chavez, I. Bulut, D. Tastanbekov, N. Leclerc, A. Hebraud, B. Heinrich, S. Berson, N. Lemaitre, C.L. Chochos, P. Leveque and T. Heiser,
Using pyridal[2,1,3]thiadiazole as an acceptor unit in a low band-gap copolymer for photovoltaic applications, *Org. Electron.* **2015**, 23, 171-178.

N. Leclerc, P. Chavez, O. A. Ibraikulov, T. Heiser and P. Leveque,
Impact of backbone fluorination on π -conjugated polymers in organic photovoltaic devices: A review, *Polymers* **2016**, 8, 11; doi:10.3390/polym8010011

8.7 Références

1. Yu, G.; Gao, J.; Hummelen, J. C.; Wudl, F.; Heeger, A. J. Polymer Photovoltaic Cells: Enhanced Efficiencies via a Network of Internal Donor-Acceptor Heterojunctions. *Science* **1995**, *270*, 1789–1791.
2. Park, S. H.; Roy, A.; Beaupré, S.; Cho, S.; Coates, N.; Moon, J. S.; Moses, D.; Leclerc, M.; Lee, K.; Heeger, A. J. Bulk heterojunction solar cells with internal quantum efficiency approaching 100%. *Nature Photonics* **2009**, *3*, 297–302.
3. Liang, Y.; Wu, Y.; Feng, D.; Tsai, S.-T.; Son, H.-J.; Li, G.; Yu, L. Development of New Semiconducting Polymers for High Performance Solar Cells. *Journal of the American Chemical Society* **2009**, *131*, 56–57.
4. Zhang, F.; Inganäs, O.; Zhou, Y.; Vandewal, K. Development of polymer–fullerene solar cells. *National Science Review* **2016**, *3*, 222–239.
5. Hu, H.; Jiang, K.; Yang, G.; Liu, J.; Li, Z.; Lin, H.; Liu, Y.; Zhao, J.; Zhang, J.; Huang, F.; Qu, Y.; Ma, W.; Yan, H. Terthiophene-Based D–A Polymer with an Asymmetric Arrangement of Alkyl Chains That Enables Efficient Polymer Solar Cells. *Journal of the American Chemical Society* **2015**, *137*, 14149–14157.
6. Liu, Y.; Zhao, J.; Li, Z.; Mu, C.; Ma, W.; Hu, H.; Jiang, K.; Lin, H.; Ade, H.; Yan, H. Aggregation and morphology control enables multiple cases of high-efficiency polymer solar cells. *Nature Communications* **2014**, *5*, 5293.
7. Liang, Y.; Yu, L. A New Class of Semiconducting Polymers for Bulk Heterojunction Solar Cells with Exceptionally High Performance. *Accounts of Chemical Research* **2010**, *43*, 1227–1236.
8. Zhang, Q. T.; Tour, J. M. Alternating Donor/Acceptor Repeat Units in Polythiophenes. Intramolecular Charge Transfer for Reducing Band Gaps in Fully Substituted Conjugated Polymers. *Journal of the American Chemical Society* **1998**, *120*, 5355–5362.
9. Zhou, H.; Yang, L.; You, W. Rational Design of High Performance Conjugated Polymers for Organic Solar Cells. *Macromolecules* **2012**, *45*, 607–632.
10. Wu, J.-S.; Cheng, S.-W.; Cheng, Y.-J.; Hsu, C.-S. Donor–acceptor conjugated polymers based on multifused ladder-type arenes for organic solar cells. *Chem. Soc. Rev.* **2015**, *44*, 1113–1154.
11. Graham, K. R.; Cabanetos, C.; Jahnke, J. P.; Idso, M. N.; El-Labban, A.; Ngongang Ndjawa, G. O.; Heumueller, T.; Vandewal, K.; Salleo, A.; Chmelka, B. F.; Amassian, A.; Beaujuge, P. M.; McGehee, M. D. Importance of the Donor:Fullerene Intermolecular Arrangement for High-Efficiency Organic Photovoltaics. *Journal of the American Chemical Society* **2014**, *136*, 9608–9618.
12. Vissenberg, M. C. J. M.; Matters, M. Theory of the field-effect mobility in amorphous organic transistors. *Physical Review B* **1998**, *57*, 12964–12967.
13. Venkateshvaran, D.; Nikolka, M.; Sadhanala, A.; Lemaire, V.; Zelazny, M.; Kepa, M.; Hurhangee, M.; Kronemeijer, A. J.; Pecunia, V.; Nasrallah, I.; Romanov, I.; Broch, K.; McCulloch, I.; Emin, D.; Olivier, Y.; Cornil, J.; Beljonne, D.; Siringhaus, H. Approaching disorder-free transport in high-mobility conjugated polymers. *Nature* **2014**, *515*, 384–388.
14. Ibraikulov, O. A.; Bechara, R.; Chávez, P.; Bulut, I.; Tastanbekov, D.; Leclerc, N.; Hebraud, A.; Heinrich, B.; Berson, S.; Lemaire, N.; Chochos, C. L.; Lévêque, P.; Heiser, T. Using pyridal[2,1,3]thiadiazole as an acceptor unit in a low band-gap copolymer for photovoltaic applications. *Organic Electronics* **2015**, *23*, 171–178.

Chapter 9: Acknowledgements

9 Acknowledgements

On these last pages of my thesis I would like to express my gratitude to people who were next to me and helped me during these years.

I would like to thank Professor Daniel Mathiot for giving me the opportunity to fulfill this thesis in ICUBE (former InESS) laboratory. Special appreciation and many thanks goes also to all the members of this lab, from technicians and administrative colleagues to researchers, who assisted to provide high level experimental conditions, efficient documental and intellectual support.

I am also very grateful to Dr. Kanat Baigarin and Dr. Galymzhan Koishiyev from Nazarbayev University for providing me with the possibility to continue my thesis when I was back in Astana.

I am very pleased to thank my committee members Professor Stefan Haacke, Dr. Alexander Alekseev, Professor Yvan Bonnassieux and Dr. Uli Wuerfel for taking part in my defense presentation and for interesting, smart questions and discussions. I want to emphasize my special appreciation for the referees Professor Yvan Bonnassieux and Dr. Uli Wuerfel for their time spent on writing the report required by the Doctorate School. I believe that the prospective collaboration with the team in Freiburg under the supervision of Dr. Uli Wuerfel will be very fruitful.

I am deeply indebted to my thesis supervisor, Professor Thomas Heiser, for his fundamental role in this work and without whom the accomplishment of this thesis would not have been possible. He provided me with very high level and invaluable scientific and pedagogical guidance during these years. In his friendly manner he helped me dramatically improve my scientific skills always making me remember that “There are plenty of other things in life apart from you work and Dream of Philosophy”.

I am also very grateful to my co-advisor, Dr. Patrick Lévêque for his very solid, clear and well-structured explanations for various types of questions that I have ever asked him. Also many thanks for providing a guitar from time-to-time. It really helped me a lot especially when I got tired from different types of “writings”.

A very special gratitude goes to a friend of mine, a very first but “small supervisor” in

Strasbourg, Dr. Rony Bechara. Though we couldn't meet in Gare Centrale on the day my first arrival to Strasbourg (I remember that I owe you some euro-coins that you spent for your car parking while waiting me there), he provided invaluable help in the very first days of my presence at the lab in 2012 by acquainting me with the campus, cafeteria and lots of tea/coffee.

I want to cordially thank Dr. Nicolas Leclerc, head of the group of chemists, who supplied me with various interesting polymers. He was always a reliable contact for everything concerning polymer chemistry.

Thanks to all chemical colleagues from ICPEES (former LIPHT), especially to Dr. Ibrahim Bulut and Dr. Patricia Chavez. It was always the best motivation for me to work on new terrific materials synthesized by you.

Thanks to colleagues from ICS, Dr. Laure Biniek and Dr. Amparo Ruiz-Carretero for discussions, courage and support.

Coming back to ICUBE, special thanks goes to my office/floor-mates, Dr. Sadiara Fall for useful discussions on charge transport issues, Tianyan Han who was always there when I forgot to switch off the solar simulator and for chinese milk team and Dr. Ali Azhar Pirzado, for tons of Pakistani food, car for going back home and many pleasant hours. Also thanks to Thomas Regrettier for tea/coffee hours and brainstorming.

Thanks to Dr. Peter Lienert for the .pdf version of important lectures on semiconductor physics, useful suggestions and support. Lectures helped me to remember the things back.

Many thanks to Caroline Eckert for help with the translation of thesis summary into French, organization of group meetings, assistance and contribution to Organic Electronic group in different ways and to Marina Urban for the patience assistance with formal documents.

I am grateful to the technical staff of the laboratory: Nicolas Zimmermann, Stephane Roques, Sebastian Schmitt, Nicolas Colin, Jeremy Bartringer and Florent Dietrich. Thanks a lot to all of you for providing technical assistance during these years.

Thanks to my colleagues from Solar energy laboratory, National Laboratory Astana, especially my colleague Damir Aidarkhanov for discussions on many different topics which sometimes could be other than science, lots of tea and support.

Thanks to Dr. Stephane Mery and Dr. Benoit Heinrich from IPCMS institute who supported

this work in various ways.

I would also like to thank my school-mates and friends for their immutable support though most of them are far away from where I am and haven't seen them for years, for their faith in me that I always felt.

Last but not least I want to express my special gratitude to the people who this thesis is dedicated to: my mother, my grandmother, close relatives and my girls: wife Assel and daughters Amina, Safinur. Thank you for being there, for all the good times we shared, for your love, inspirations and support throughout the years.

Olzhas A. Ibraikulov

Strasbourg, France

December 5th, 2016